Some aspects of proton dynamics in squaric acid crystal using pseudo-spin formalism

by

Vijigiri Vikas

PHYS07201404018

Institute of Physics, Bhubaneswar

A thesis submitted to the
Board of Studies in Physical Sciences
In partial fulfillment of requirements
for the Degree of

DOCTOR OF PHILOSOPHY
of
HOMI BHABHA NATIONAL INSTITUTE

December, 2020

Homi Bhabha National Institute

Recommendations of the Viva Voce Committee

As members of the Viva Voce Committee, we certify that we have read the dissertation prepared by Mr Vijigiri Vikas entitled "Some aspects of proton dynamics in squaric acid crystal using pseudo-spin formalism", and recommend that it may be accepted as fulfilling the dissertation requirement for the Degree of Doctor of Philosophy.

AmJayannavar

Chairman - Prof Arun M Jayannavar Date: 22. 6. 2021

Saptarshi Mandal

Guide /Convener - Dr. Saptarshi Mandal Date: 23/06/2021

Co-guide (if any) Date:

23/06/21

Examiner - Prof. Arnab Sen Date:

Member 1 - Prof Biju Raja Sekhar Date: 23.6.21

Member 2 - Dr. Arijit Saha Arijit Saha Date: 23/06/2021

Final approval and acceptance of this thesis is contingent upon the candidate's submission of the final copies of the dissertation to HBNI.

I/We hereby certify that I/we have read this thesis prepared under my/our direction and recommend that it may be accepted as fulfilling the thesis requirement.

Date: 23.06.2021

Place: Bhubaneswar

Saptarshi Mandal

Co-guide (if applicable) **Guide**

STATEMENT BY AUTHOR

This dissertation has been submitted in partial fulfillment of requirements for an advanced degree at Homi Bhabha National Institute (HBNI) and is deposited in the Library to be made available to borrowers under rules of the HBNI.

Brief quotations from this dissertation are allowable without special permission, provided that accurate acknowledgement of source is made. Requests for permission for extended quotation from or reproduction of this manuscript in whole or in part may be granted by the Competent Authority of HBNI when in his or her judgment the proposed use of the material is in the interests of scholarship. In all other instances, however, permission must be obtained from the author.

Vikas
Vijigiri
Vijigiri Vikas

DECLARATION

I, hereby declare that the investigation presented in the thesis has been carried out by me. The work is original and has not been submitted earlier as a whole or in part for a degree / diploma at this or any other Institution / University.

Vikas
Vijigiri
Vijigiri Vikas

List of publications arising from the thesis

Publications

- Vikas Vijigiri, Saptarshi Mandal, Classical mean-field, spin-wave, and perturbative continuous unitary transformation analyses of the squaric acid system H_2SQ, *Phys. Rev. B* **98**, 224425 (2018).
- Vikas Vijigiri , Saptarshi Mandal, Dipole-dipole interaction induced phases in hydrogen-bonded squaric acid crystal, *Journal of Physics: condensed matter* Volume 28, Number 32 (2020).
- Vikas Vijigiri, Ashis K Nandy, Saptarshi Mandal, Quantum Monte Carlo analysis of role of interlayer coupling in an organic squaric acid crystal, *In preparation*, (2020).

Conferences

- Recent trends in condensed matter physics (RTCMP);
  Bose Institute, Kolkata, West Bengal, India; (September 27- october 2, 2017)
- PRL conference on condensend matter physics(PRLCCMP-18);
  Physical Research Laboratory (PRL), Ahmedabad, Gujarat, India; (March 16-19, 2018)

Vikas Vijigiri

Vijigiri Vikas

ACKNOWLEDGEMENTS

First and foremost, I love to thank my family especially mom and dad for their unconditional spiritual support throughout my career and right through scripting of this dissertation. I am indebted to them for all my life.

I wish to shower my praises and thank my supervisor, Dr. Saptarshi Mandal, not just for guiding me academically as a mentor but also on a personal level. I thank him for his kind and generous disposition and the frequent assistance of my Ph.D. work and related studies. His clear ideas, motivation, patience, and dynamism helped me in the entire time of research and writing of this thesis. I never could have thought up of having a better guide and mentor for my Ph.D. study. The discussions I had with him had a deep impact both on the understanding of my research subject and also the philosophical aspect.

Along with my supervisor, I would like to extend my thankfulness to the rest of my doctoral committee, Prof. Arun M. Jayannavar, in motivating me to keep going regardless of the situation. I thank Prof. Biju Rajasekhar and Dr. Arijit Saha not only for their intuitive remarks and inspiritment but also for the tough questions which motivated me to broaden my research from various viewpoints. I thank Prof. S. D. Mahanti, I haven't seen a professor with so much enthusiasm and encouragement that he can give to any person he talks to.

I am deeply grateful to Prof. Julian Vidal for giving his time to discuss a method that is part of this thesis, where I gained some conceptual insights and the newer ways of implementing them. I owe him big time. I am grateful to Sounak Biswas who was my lone acknowledger, the stimulating discussions I had with him had a profound impression on my understanding of a certain problem. I remember those motivating days where we worked closely to sort out the difficulty.

Last but not least, I want to thank all my friends, juniors especially Ritam, faculty, colleagues, computer staff of IOP, and all of whom we had all the fun in the last five years, lots of memories and experiences to cherish. I thank all for being part of my life.

Contents

List of Figures

List of Tables

CHAPTER 5

Conclusion

In this thesis, using pseudo-spin formalism we analyze a strongly correlated proton network system, namely, squaric acid (H_2SQ). To explore the system analytically, we map our system to a suitable quantum spin-1/2 system. Then using techniques such as pCUT and quantum Monte Carlo, we determine the spectrum in both low and high-fields. We also distinguish each phase and obtain the phase diagram at both zero and finite-temperatures and fields. The model Hamiltonian we use in this thesis is the extended version of Ising lattice gauge theory in (2+1) dimensions. The additional terms account for the intramolecular coupling and dipole-dipole interaction consisting of next next-nearest neighbor interactions. The motivation for such modeling historically comes from the vertex-based models [75]. The gauge term may be understood to be originated primarily because of the interaction mediated by the π-electrons in C_4O_4 by the rearrangement of π-bonds. Further details describing the possible mechanism, and the effective vertex model can be found in Ref. [75].

First, we analyze the model within the classical limit where the quantum spins are replaced by the classical vectors. Using the quench mean-field approximation we obtain the classical ground states in each regime corresponding to the cases of the presence and absence of dipole-dipole interaction. We find that in the absence of dipole-dipole interaction strength, the system remains disordered, that is to say, there exists a macroscopic set of classical ground states connected by a gauge transformation (in quantum version). Within the degenerate manifold, each configuration corresponding to a symmetric arrangement of H_2SQ was shown to be connected to other ground states using a non-local gauge transformation. The contours covering the gauge-transformation operators are given in the form of closed loops. The classical groundstate can also be thought of as the dimer-coverings on the lattice. With each dimer representing a pair of antiparallel spins. When the dimer-decomposition is done systematically throughout the lattice, one can notice that there is the natural formation of loops and the flipping of those loops lead to another groundstate within the same manifold. It may be noted that especially, each degenerate configuration could be a symmetric arrangement of the crystal that could be detected in the inelastic Raman scattering experiments. Nevertheless, the obtained set of classical groundstates is now analyzed for their stability under the quantum fluctuations where the individual protons are subjected to the external field (pressure in experiments) increasing the tunneling rate of protons. At sufficiently large fields one can understand that the tunneling is of so high rate (1THz) that the proton mean-position is at the center of the double-well potential. When every proton is in this state, this phase usually corresponds to the high-field conventional paraelectric phase.

Nevertheless, in the absence of dipole-dipole interaction when the field term accounting for such quantum fluctuations was turned on, it is shown to exhibit that for finite-fields there is no lifting of the degeneracy. That is to say, there is no quantum order-disorder phenomenon taking place. This can be attributed to the fact that for small-fields, the model Hamiltonian was shown to map to non-interacting anyons of kitaev's toric code model and that the interactions among the anyons may be required to the lifting of such degeneracy in our model. Our spin-wave (quantum fluctuations around classical ground states) in the high-field limit also showed a closing of one-quasi particle magnon gap at the critical boundary, besides, not only the gap closes but also we see that a quadratic nature of dispersion being entering into linear behavior corresponding to the antiferroelectric phase as the strength of dipole-dipole interaction is increased. Moreover, the order of the phase transition is understood to be of second-order.

Next, we calculate the the effect of quantum fluctuations on the classical groundstates in the low-field as well, our results show that the nature of dispersion in the antiferroelectric phase being anti-symmetric around the high-symmetry point of X. Importantly, the spectrum was found to be gapped for all values of couplings considered. This shows that the nature of excitations might correspond to the robust nature of the AFE phase. We also found that the spectrum is different for fourfold global orientations of dipole-moments within the AFE phase. The dispersion for the case of dipole orientations along two orthogonal directions shows a minimum at X-high symmetry point. While the dipoles pointing along the other unit vector spanning the lattice shows a minimum at M-high symmetry point. We suggest that the difference in the spectrum around the X-high symmetry point could well be detected in experiments. Lastly, to improve our results on the critical points obtained from the linear-spin wave results, we consider the system in high-field limit and perform a continuous unitary transformation to diagonalize the many-body Hamiltonian in the particle conserving number operator basis. It may be noted that the low-field limit is shown to have an inequidistant spectrum thereby limiting our study to the cases of high-field. However, it was that when the gauge coupling strength J_0 is equal to J_1 the system maps exactly to the TCM but with a qualitative difference in the nature of excitations. Since we have an additional interaction (J_1) that may restrict the movement of gauge excitations (or charge excitations) in our model.

Next, we move on to analyzing the system under finite-temperatures. Specifically, we are interested in understanding the role of quantum fluctuations together with the thermal fluctuations on the above-mentioned groundstates. It is interesting to see because not all the ice-rule states carry the same energy and that the temperature might lift the states to higher excited states and while the field may be thought of as a barrier connecting the degenerate set of groundstates. We use a stochastic series quantum Monte Carlo technique and perform a simulation with both the quantum and thermal fluctuations turned on in the system. However, simulating the system using the existing percolation-based algorithm for such a diverging degenerate system found to be inefficient. We, therefore, improvise a loop algorithm that we already found in the form of dimer-coverings. We see that the algorithm naturally avoids any apparent spin-freezing. The efficiency of the algorithm to other similar systems was also estimated elsewhere. Nevertheless, we see that when the system is subjected to these around a particular contour of temperature and field values, it is shown to host three distinguished phases, 1) the AFE phase at lower temperatures (and fields) 2) an intermediate liquid-like state (at intermediate fields and temperatures) 3) the conventional paraelectric phase (at higher fields). The existence of a liquid-like state has been found by estimating the order parameter that detects the local ice-rule ordering. Moreover, the IS manifests itself by an anomalous peak in the specific heat that vanishes with the system size. To locate the critical point, we also estimate the binder cumulant. From the analysis of order-parameters, specific heat, and binder points, we see that the system first undergoes a second-order phase transition to a liquid-like intermediate state upon increasing the temperatures and pressures. Later, for larger temperatures, the IS states crossovers to the conventional paraelectric phase without accounting for any phase transition that is a characteristic of a disorderedness of the IS liquid-like state.

Later, using the above-mentioned analysis we also chart the phase diagram in the $T-K$ plane, our results for the critical boundary showed to be linear for small field and temperature values. However, the linear behavior starts deviating for large fields. It may be noted that the linear critical boundary is in agreement with the experiments. However, we note that there exists a discrepancy as the linearity is maintained throughout the boundary in the $T-K$ plane in experiments in contrast to our results. We believe that the linearity of the critical boundary might depend on the interlayer coupling. Indeed, in the follow-up of this work, we consider the interlayer coupling in our simulations. However, we use the imaginary-time Monte Carlo method to tackle the complexity of the 4D model Hamiltonian where we map the current 3D Hamiltonian including the interlayer coupling to a classical Hamiltonian with just Ising variables on the 4D Hamiltonian, we use a similar algorithm as in the case of 2D version carried in the stochastic series expansion method. However, besides those, we use a Swendsen-Wang type cluster algorithm along the imaginary-time direction. Using the same order parameters as used in the 2D case, our results for the current model with additional interlayer coupling showed that when the interlayer coupling considered is of antiferromagnetic type, we see that the quasi-2D layers still host the AFE phase at lower temperatures, however with a difference that when the strength of the interlayer coupling is increased we see that the intermediate liquid-like state starts disappearing. Contrastingly, when an FM nature of interlayer is coupling is considered both the AFE phase and intermediate liquid-like phase are shown to be extended for higher fields and temperatures, unlike the antiferromagnet case. Additionally, we also consider the disorder case where we see that both the phase seem to disappear when the strength of interlayer coupling in this case increased. This is also confirmed from the specific heat curves, where the anomalous peak is shown to vanish in the disorder case. Not only this, but we also determine the dipole-dipole imaginary-time correlation function and found that the deconfined phase shown to vanish regardless of the nature of interlayer coupling. Based on this we conclude that the AFM type coupling could be more plausible comparing with the experimental results. However, despite these, the linearity of the critical boundary in the $T-P$ plane couldn't be reproduced. We believe that the discrepancy might be due to the transverse nature of the model. Most of the transverse field models are shown for such avalanche critical boundary at large fields. We conclude that this thesis has offered scope of understanding the H-bond systems and their phase transitional aspects based on pseudo-spin formalism. However, there there is a much bigger scope for improvements as far as the exploring of the squaric acid using the Hamiltonian considered. For example, a more rigorous estimation of dispersion and dynamical structure factor in the disordered dipole case could be an important direction of investigation from the experimental point of view. A more rigorous calculation of pCUT also could provide more understanding of the material in the low-field regime. Moreover, density functional analysis for the realistic paramater space of the exchange interaction strengths are needed as far as squaric acid is concerned. Also, from the numerical perspective, a more efficient algorithm in the case of finite dipole-dipole interactions are to be important addition of the present study. A possible future endeavors include the mean-field treatment of the gauge term decomposed into pairs of two-body interactions. For example, the dimer covering on lattice found in low-field can be effectively used to decouple the four-body Ising gauge term within the Schwinger-boson formalism.

SUMMARY

Hydrogen-bond (H-bond) systems are quite ubiquitous, particularly in organic compounds. Traditionally, they are well-known for their dielectric properties coming from the spontaneous ferroelectricity they exhibit below the curie temperature, T_c [1, 2, 3, 4, 5]. Some of them are also very light in weight and could be made easily portable [6]. Technologically, they are one of the alternatives to non-volatile random access memory (FeRAM) devices currently in the market. H-bond compounds can be abundantly found in the universe ranging from as small as DNA to water to as big as Saturn. Nevertheless, these systems are also of fundamental interest especially from the condensed matter physics perspective that arises from the *quantum nature* of protons [6, 7]. A very immediate application of this leads to an inherent relation between the H-bond and the quantum spin-1/2 systems since the configuration of protons can be mapped to pseudo-spin-1/2 variables replacing the protons. In this dissertation, we use such a pseudo-spin formalism to estimate various physical quantities of a well-known H-bond system, namely, squaric acid.

While the focus of this decade is on quantum magnetism, the studies on the H-bond crystals were as old as the study of magnetic materials which dates back to the early 1940s. *Bernal* and *Fowler* had first shown that the configuration of protons in some of these systems were found to satisfy *Ice-rules* (analogous to two-in two-out in spin-ice) [8]. It is now understood that the ice-rules states are the lowest energy configurations in many H-bond systems. The strong ferroelectric nature arising in these strongly correlated proton systems is an outcome of such ice-rule ordering [3, 5]. There have been vast interests in these materials in trying to understand the material properties both from technological and scientific perspectives. Since these systems could serve us in realizing the quantum effects at a macroscopic scale. Also as an alternative in understanding several exotic phenomena related to quantum spin-1/2 systems that include spin-ices, spin-liquids with fractionalized excitations [9, 10]

to name a few.

Recently, one of the most looked out H-bond system from the fundamental physics point of view is the *squaric acid* crystal with stoichiometric formula $H_2C_4O_4$ (also abbreviated as H_2SQ with SQ being referred to *square* shape of the C_4O_4 molecules [11]). It is known that the crystal structure of H_2SQ is a quasi-2D stacked layered monoclinic below the critical temperature $T_c \approx 371K$ [11]. Moreover, below T_c, it was found to have ordered (antiferroelectric) configuration of protons. In the ordered phase, each proton is located on either side of the double-well potential minima of $O-O$ ions causing local ferroelectricity [12]. That is to say, the maximum probability of locating the proton is in one of the double-well minima. For temperatures above T_c, it is at the center of the H-bond, causing local paraelectricity [12]. It may be noted that the driving thermodynamic parameters to cause local ferroelectricity and paraelectricity at each site are the temperature and pressure. In this dissertation, we try to understand the proton's several ordering and its implications under quantum (field or pressure in experiments) and thermal fluctuations (temperature). Broadly, we find various phases characterized by proper order parameters where we estimate accurate critical-points (or boundaries) using pseudo-spin formalism. Below, we briefly summarize the works carried in this dissertation.

First, we study (analytically) a model Hamiltonian that is used to describe H_2SQ and whose dynamics is governed by (i) a gauge-invariant ($\mathcal{Z}_2$) four-spin plaquette interaction (J_0), (ii) Ising-like intramolecular interaction (J_1), (iii) a dipole-dipole interaction (J_2), and (iv) an external transverse Zeeman field K. We restrict our discussion to the case where ($J_0 > J_1 > J_2$), while K can be taken arbitrarily. The model described by J_0 and K (Ising lattice gauge theory in (2+1) dimensions (ILGT)) is well-known to host a deconfined phase. The application of an external magnetic field (given by a strength K) drives the deconfined phase to a confined phase (CDT). We first perform the mean-field calculations to obtain and identify groundstate (classical) configurations and determine the value of

K_c for which such a transition happens when the intramolecular interaction term (J_1) is turned on. The other set of groundstates are obtained by identifying a gauge-transformation connecting all these groundstates. Further, we find that the role of J_1 is to stabilize the deconfined phase by reducing the classical groundstate degeneracy. Moreover, all the groundstates without the dipole-dipole interaction term in the low-field limit were found and are represented as singlet pairs or dimers whose z-component projections of spins are anti-aligned to satisfy the restricted ice-rule. Our mean-field results indicate that the classical groundstate remains degenerate extending for finite small values of K. However, in the presence of the dipole-dipole term J_2, we see that the local degeneracy is lifted to yield fourfold globally ordered (antiferroelectric) groundstate that is independent of system size. We give the exact expression of degeneracies in all the regimes under the low-field limit. Later, we perform the spin-wave analysis by investigating the role of quantum fluctuations over these large set of classical degenerate groundstate for $J_2 = 0$ and also for the case of globally ordered groundstate for $J_2 \neq 0$. We find that at the quadratic level the local degeneracy is not at all removed and no order from disorder phenomenon was observed unlike the classically driven order-disorder case [7]. That is, all the set of classical groundstates were found to be stable even when a finite but small on-site perturbation is turned on, consistent with the mean-field findings. Indeed, we have shown that there exists a macroscopic number of conserved quantities that enable a gauge transformation among the degenerate groundstate manifold causing this absence of order-disorder phenomenon.

For finite J_2, the spin-wave (SW) dispersion over the fourfold globally ordered groundstates were, in general, found to be gapped, quadratic, and asymmetric (around X and R high-symmetry points) for all values of K. However, when an SW analysis was performed in the low-field limit and for $J_2 \neq 0$, although we see that the dispersion is generally symmetric and quadratic in nature, yet there are certain parameter regimes where the spectrum becomes gapless and linear. This happens particularly near the phase boundary of the ferroelectric to paraelectric phase transition (FT). It may be appropriate to mention that the true quantum ground state for $J_2 = 0$ is a nontrivial one due to the presence of extensive degeneracy in this regime. However, the spin-wave analysis for $J_2 \neq 0$ is expected to be more realistic given that quantum groundstate is an ordered state. To improve the earlier results based on spin-wave analysis, we have performed perturbative calculations based on Continuous Unitary Transformations (pCUT) to analyze the system in the large field limit ($K \gg J_0, J_1, J_2$). In this limit, the ground state consists of all spins aligned along x-direction with single spin-flip excitations. We estimate the one-particle gap in this limit and compare it with the spin-wave results obtained earlier. Though the pCUT analysis has improved the estimation of groundstate energy and one-particle gap as determined by spin-wave analysis, the closeness of results in the two different approaches seems to point out that the results are realistic in this limit. Our study also predicts the nature of excitations for finite J_2 and in the high-field limit. Finally, the model was discussed to show the dual mapping of ILGT to Kitaev's toric code model (TCM) also for the case of J_1 turned on.

Until now, we have studied the effect of an external field (K) upon the various classical groundstate. We understand that the field, K, acts as a barrier connecting these degenerate groundstate driven by quantum fluctuations. Contrastingly, temperature helps in randomizing these barriers by populating the higher excited states that violate ice-rule and thereby destroying the quantum groundstate. In the subsequent work, we study the finite-temperature (T) and field (K) phase diagram ($T - K$ plane) of proton's several orderings of H_2SQ crystal using quantum Monte Carlo (QMC) [13]. In other words, we aim at understanding the intricate connection between the quantum (field) and thermal (temperature) fluctuations upon the classical groundstate or the ice-rule states. Using an improvised loop algorithm within the stochastic series expansion (SSE) quantum Monte Carlo method, for finite but small values of J_2, we find two distinct phases as we increase the temperature and magnetic-field [13]. One of the phases is the $\prod_f$, the phase with long-range ferroelectric order (low-T and low-K) followed by an intermediate state with strong local correlations, that is, a quantum liquid-like state $\prod_{ql}$. We see that the transition to $\prod_f$ manifests a very small anomalous peak in the specific heat with a strong dependence of critical temperature on the strength of dipole-dipole interaction. The presence of this small peak is attributed to the absence of macroscopic degeneracy in the presence of dipole-dipole interaction and re-entrance of such degeneracy to some extent at small temperatures and fields [13] due to the competition between the locally degenerate ice-rule term, J_1, and the globally ordered term, J_2.

In all the above-mentioned analyses, we have considered a geometry that did not take into account the stacked layered configuration of the H_2SQ crystal, that is, the interlayer coupling was ignored validated by earlier experiments. In the last work, we study a model Hamiltonian for H_2SQ using the Suzuki-Trotter (imaginary-time) path integral Monte Carlo method. The 2D version of the same model Hamiltonian (a Z_2 gauge-invariant one describing the ice-rule-dominated physics) was earlier studied and was shown to host an (i) deconfined, (ii) antiferroelectric, and an (iii) intermediate-liquid-like phase. Here, in our 3D version, we introduce an additional interaction along the interlayers where we consider all the possible scenarios of the nature of the interlayer coupling constant, J_3 (Antiferromagnetic (AFM), Ferromagnetic (FM), and Disordered) to analyze our model. Our results primarily show a strong dependence of the underlying phases with the nature of interlayer coupling, and a moderate dependence of it with the strength of J_3 compared to the intralayer dipole-dipole interaction strength J_2. Our results on the dynamic structure factor also reveal features corroborating the existence of an intermediate-liquid-like state with the appearance of two length-scales in the dynamic structure factor. We conclude that the AFM coupling nature of J_3 could be more close to experiments as we observe a robust anomalous peak in the specific heat curves and at the temperatures near the re-entrance point of the quantum liquid-like state.

CHAPTER 1

Squaric acid crystal

1.1 Introduction

Hydrogen bond (H-bond) systems are arguably one of the most fundamental systems one may ever encounter in their daily life. They are responsible for a wide range of phenomena seen in nature. For example, 1D molecular bridges consisting of several water molecules are fundamental to proton transfer processes in enzyme catalysis [14] and membrane water channels [15]. The mechanism of such concerted proton transfers is of great biological interest [16]. Similarly, water molecules confined inside carbon nanotubes have been investigated as an ideal model system of proton conduction along water wires [17, 18], and the presence of tunneling-assisted concerted proton tunneling between molecules in cyclic water hexamers in ice has recently been demonstrated both experimentally [19] and theoretically. However, they display numerous puzzling properties, notable ones include the anomalous boiling and freezing point, abnormal viscosities, unusual density of water at 4°C, the negative expansion coefficient of water-ice to name a few. Most of the anomalous properties are associated with materials having the H-bonds. It is believed that the characteristic role of the *quantum* *nature of protons* in these materials may be responsible for the anomalous properties. Furthermore, it is of fundamental interest in understanding the implications of the *quantum nature of protons* from a condensed matter physics perspective. Specifically, from the perspective of the ferroelectric state arising due to order-disorder phenomenon of protons taking place in many H-bond solids when the temperature (and (or) pressure) is lowered. There are various applications of organic ferroelectrics in technology in the form of actuators, sensors, (FeRAM), in digital circuits like FeFET's. And recently, in designing new electrically ordered materials by thorough maneuvering of the molecular structures (crystals) where the H-bonds can be purposefully segregated. There are also diverse technological applications of these materials that display polarized ordering of charges that make them be also used in ceramic capacitors, pyroelectric detectors, piezoelectric transducers, and sonars [20]. H-bond materials are also vastly researched keeping in view of the possible realization of new kinds of functionality, for example, multiferroics, and with the discovery of the ferroelectricity beyond room temperature [21] it has only drawn more attention both from the theory and experimental point of view.

The quantum nature of protons can serve as a basis for realizing quantum effects at a macroscopic scale [1, 2, 22]. Primarily, several phenomena emerging from the quantum nature such as localization-delocalization, zero-point motion, quantum tunneling are pivotal to the comprehension of the properties of these materials. It is believed that the zero-point motion of protons could play a vital role in structural phase transition due to its coupling with the lattice degrees of freedom. Theoretically, to study the phase transitional aspects and other physically measurable properties, one generally maps the position of the hydrogen (protons) ions to pseudo-spin variables. In other words, the phenomenology used to describe the physical properties concerning the phase transitional aspects in some of the H-bond systems are based on the pseudo-spin modeling. And depending on the properties of the particular material, for example, geometry, the shape of the double-well potential, the nature of proton-proton interactions, and other secondary interactions (e.g: molecular field) one may usually map the configurational dynamics of proton (H-bond) system into a suitable quantum spin system, for example, a spin ice-system [23].

Basic difference between the proton and spin systems

The microscopic difference between the proton and the spin systems is that the former exhibits a symmetry-breaking phenomenon in the crystal structure, for example, monoclinic to tetragonal. That is to say, usually, a change in symmetry associated with the corresponding space group is observed. Not only that sometimes a change in the symmetry (structure) is also accompanied by the transition from the ordered ((anti)ferroelectric (AFE)) phase of protons to the disordered phase (paraelectric (PE)). Also, the ordering of protons usually requires collective displacements of atoms to accomplish the symmetry breaking. However, on the other hand, the spin systems only require certain strong spin-spin exchange interactions between the moments located on lattice sites (or edges) to undergo a magnetic phase transition without any structural change.

Squaric acid

One of the H-bonded system that we study in this thesis is the squaric acid. The stoichiometric formula for squaric acid is $H_2C_4O_4$. The crystal structure of squaric acid consists of simple planar C_4O_4 groups bonded via H-bonds to four neighboring C_4O_4 molecules in the layered *ac*-plane perpendicular to the b-axis (also known by *unique* axis, i.e, *hkl*(010) or the plane perpendicular to the quasi-2D geometry). The schematic arrangement of planar C_4O_4 molecules within a layer is shown in Fig. 1.2. The corresponding H-bonding parameters at $121°C$ above the transition temperatures $T_c \sim 100°C$ are $H - O = 1.536(5)$Å, $O - O = 2.548(2)$Å, $O - H = 1.014(4)$Å. The H-bond bond angle is $O - H \cdots O = 176.2(6)$ [11]. Similarly, below the transition temperatures they are, $O - O = 2.554$Å and $H \cdots O = 1.034$Å, the $O - H \cdots O$ H-bond angle is $177.5°$ [24]. On an average, the bond lengths within the C_4O_4 unit are $C - C$ 1.500Å, $C = O$ 1.229Å, $C - O$ 1.288Å & 1.462Å and $C = C$ 1.414Å [24]. Because of the small differences in the bond lengths of C-C bonds within

C_4O_4 molecule the geometrical arrangement is not a perfect square. However, since the differences in them are relatively small (~ 0.05Å) compared to the absolute values of bond-lengths we, therefore, for most of the theoretical purposes approximate it to be a perfect square. For this purposes, the squaric acid is also referred to as H_2SQ (SQ referring to the square arrangement of C_4O_4) more often than $H_2C_4O_4$. For simplicity, hereby, we use the shorthand abbreviation, H_2SQ, to refer to squaric acid untill stated explicitly.

Basic understanding of H_2SQ

H_2SQ has recently become a matter of interest simply because of its planar geometry, striking similarities with water-ice and also for the presence of first-order phase transition. Pioneered by *Sammuelsen* and *Semmingsen*, early x-ray and neutron scattering [25] studies have revealed the crystal structure of $H_2C_4O_4$ where it is at first known to undergo a second-order antiferroelectric structural phase transition about $100°C$ at a normal pressure of one atm. Though the transition was initially believed to be of second-order, the subsequent studies re-established it to be of first-order [26, 27], largely due to the discontinuities observed in the order parameters [28, 29, 30, 31, 32, 33]. Moreover, the ^1H NMR spectroscopy on H_2SQ showed both the displacive [34, 35, 36, 37] as well as order-disorder features present at the transition temperature, T_c [38]. An unusual S-shaped variation of interatomic distance versus temperature was observed. Since at the transition point the material is seen to undergo a continuous distortive structural change accompanied by a magnetic transition, for this reason, this phase transition is sometimes also referred to as antiferrodistortive or antiferroelastic transition. Furthermore, the lower temperature phase is recognized to be a monoclinic one with $P2_1/m$ associated space-group symmetry while the high-temperature phase is of tetragonal structure with an approximate four-fold rotational and screw symmetry (w.r.t axes parallel to the unique axis, i.e, the *hkl*(010) plane) belonging to I_4/m symmetric space group [39, 40].

Quasi-2D structure

Low values in the critical exponent of the order parameter (f_i = 0.14 & 0.17) of H_2SQ observed in the experiments of the optical birefringence [39, 29] and neutron scattering [41] showed to manifest a characteristic of two-dimensional transition as mentioned early [42]. For this reason we at first consider only the quasi-2D structure ignoring the weak interlayer coupling. Furthermore, it is widely believed that the nature of protons in H_2SQ has a strong effect on the order parameters [39, 40] that indicate a possible 2D transition. For instance, a large variation in transition temperatures upon deuteration is observed, which is known as the *Ubbelohde effect* [43, 44] and is observed only within the intraplane region. It is believed that more understanding of the quasi-2D structure may come from the microscopic details regarding the origin of geometrical isotope effect [45, 46], though it may be challenging, yet it could very well be helpful to decipher the role of strong proton-proton correlations. Nonetheless, from the perception of displacements of protons, the H_2SQ is inferred to be comprising of planar 2D antiferroelectric layers (proton ordering) stacked alternately along the unique axis (b-axis) below the critical temperature [40]. The details regarding the 3D-structure of H_2SQ are dedicated in chapter 4.

Temperature-pressure studies

As indicated, the zero-point motion of protons in H_2SQ within the ac-plane (intraplane) play a crucial role in understanding the distortive phase transition as already mentioned. A further hint of the possibility of proton tunneling and it's role in such distortive phase transition may also be understood from the Raman-scattering [25, 39, 47, 48, 49], second harmonic generation [50], neutron-diffraction [51], experiments such as thermogravimetry and differential scanning calorimetry [52] and most significantly from the pressure-temperature related studies. Since $O - H \cdots O$ being the most mechanically weakest bond, upon the application of external pressure to H_2SQ it is expected that the pressure will significantly affect the phase transition. Indeed, the effect of pressure on transition temperatures up to 1.4 GPa [12] were reported and were shown to greatly alter the transition temperatures (T_c). For instance, high-pressure measurements by *Nelmes et al* on the crystal structure using x-ray diffraction (up to 4.7 GPa) and neutron diffraction (up to 3 GPa) [53] revealed that the H_2SQ undergoes a monoclinic to tetragonal transition at the critical pressure of P_c = 0.75 GPa and at room temperature (a pressure-induced phase transition) [53]. Moreover, the transition temperature was found to linearly vary with anisotropic pressure (uniaxial stress along the unique axis perpendicular to the ac-plane) to 0.7 GPa with corresponding slope $\mathrm{dT}_c/\mathrm{dp} = -106$ K GPa^{-1} [54], which is unusually much larger than the observed value for KDP. In addition, the dielectric properties [55] and elastic constants studied up to 2 Kbar [49] for H_2SQ showed a large anomaly in strain along both the ac- and b-axis. Similarly, the stress dependence of shear-type rigid layer mode [56] were studied to show that the temperature and stress have the same effects for the acoustic mode in the low-temperature phase as that of the optical mode in the disordered phase. It may be noted that all these studies recognized the tunneling motion of protons and strongly suggests to have an impact of it in the phase transition.

Raman spectra

Other experimental results include the comparison of infrared spectra with that of Raman spectra [57]. It was found that the vibrational Davydov splitting was high for the external modes coming from the interlayer interaction, while it was small for the internal modes of the C_4O_4 molecule [57]. Based on this, it was suggested that the interactions between the interlayers acts only between the H-bonds of adjacent layers and that is highly localized in the regions near the H-bonds. We use this result for modeling the interlayer interaction and understand the role of different types of interlayer coupling on phase transition in chapter 4.

Similarly, vibrational [36, 58] and infrared studies [59, 60] have suggested not only that the H_2SQ exhibits strong H-bond nature, the H-bonds in H_2SQ could also add more stability giving such a compact 2D structure. It was found that the molecular structure of C_4O_4 in both the ordered and disordered phases were essentially the same [61]. It is because the lattice vibrations were observed to obey selection rules in both phases while on the other hand the intramolecular vibrations were seen not obeying the selection rules [61] in the high-temperature (or pressure) phase. Moreover, in Raman-scattering experiments except for the 83 cm^{-1} not every line that existed in the low-temperature monoclinic phase continued to be present in the high-temperature disordered phase. It was suggested that the lines that strictly correspond to the symmetry exists in the ordered phase but remains forbidden in the tetragonal phase. Combinedly, all the mentioned results only indicate that the local arrangement of C_4O_4 molecules still possess the low-temperature symmetry carrying to the disordered phase. This is also favored by the conclusions drawn from the contemporary neutron scattering experiments [48].

Possibility of double phase transition in H_2SQ

Besides, reports were suggesting that the H_2SQ could undergo a double phase transition, the second phase transition being a locally ordered state with strong molecular-correlations at higher temperatures much above $T_c = 371K$. It was observed that sharp features of short-range ordering were seen in the measurements of high-resolution Neutron Magnetic Resonance (NMR) along with ^{17}O Nuclear Quadrupole Resonance (NQR) spectrometry at temperatures much above antiferrodistortive phase transition [62, 63]. Further heating to higher temperatures almost believed to lead to a phase transition at about $420K$ coming from the measurements of ^1H NMR on H_2SQ crystals [64]. However, this is not favored by the Raman-scattering analysis [64], as there were no [52] substantial evidences found regarding the second phase transition near $420K$ [64]. Instead, it was suggested that it is the molecular symmetry $(m - C_{1h})$ that persisted till $473K$ with the thermal decomposition temperature of H_2SQ crystal around $566K$ [65]. More details of this will get clear from chapter 3 where (within our model) we show that there may be only single phase transition to locally ordered strong correlated phase followed by conventional paraelectric phase via a smooth crossover transition.

Proton-proton interaction probe

Analysis on the proton-proton exchange interaction in H_2SQ showed that the critical index, $\beta = 0.14$, is significantly lower than the obtained value from mean-field approximation, i.e, 0.5 [66]. Based on this discrepancy, it is understood that the interactions might be of short range [66]. Moreover, a mechanism involving the double bond configurations of the molecule was adjudged. The chemical composition (alternating single and double bonds) is understood to make the π electrons itinerant within each C_4O_4 molecule such that the information about the proton position is transmitted through the C_4O_4 residue from oxygen to oxygen [66]. Such interaction was believed to be of the range of a molecule exchange interaction, due to electron wave function overlap, thereby disregarding the secondary (weak) dipolar interactions. Thus, the interaction of protons can be understood mediated by the C_4O_4 molecules.

1.1.1 Theoretical proceedings

Here in this section, we discuss few important theoretical works that have been used earlier. Each work discussed here eventually lead to a model that we consider in this thesis. To start with, early theoretical works include a simplistic atomic model of harmonic oscillators used to explain the isotope effect of KH_2PO_4 [23]. It was showed that the ferroelectric transition could only happen if the strength of dipole-dipole interactions between various proton displaced dipoles (transformed into frequencies) is greater than the tunneling rate of the protons in the low energy levels of vibrational degrees of freedom [23]. Based on that, the temperature dependence of the spontaneous polarization was obtained predicting the existence of T_c below which the (anti)ferroelectric phase transition occurs [5]. Similarly, other studies include the transverse-field pseudo-spin Ising model where a bound for transition temperature in between $200°C$ and $600°C$ was first predicted. [67]

Next, to explain the same isotope effect *Tokunaga and Matsubara* [4] introduced the models similar to *Slater*'s [1] and *R.Blinc*'s [23] theory, but with a supposition that the ferroelectric ordering in this material is presumably of the collective coordination of the displacement of ions, the interactions between protons and oxygen ions, and the proton tunneling. In other words, they have considered a model that is not purely a pseudo-spin model but the spins are coupled to phonon degrees of freedom. The theory aimed to explain the discrepancy of no or minimal Isotope effect in spontaneous polarization [68]. In a similar way, when a bilinear coupling between the displacements of the electron shell of the neighboring P_4O_4 molecules and the proton tunneling motion was considered. It was showed that nonlinear aspects of polarization arise in the crystal [69] due to such coupling with lattice degrees of freedom.

Apart from the other theories, Hydrostatic pressure studies were also used to explain the Isotope effect in H_2SQ by collecting the T_c under numerous pressures and with uniaxial stress applied in the direction perpendicular to the 2D layers. It was showed that when the distance $(2R^H)$ for H_2SQ is stretched to $2R^D$ of its deuterated version, the transition temperature T_c^H of H_2SQ were observed to coincide with T_c^D of D_2SQ. Moreover, the Isotope effect upon deuteration observed that the slopes of the transition curves in the $T-P$ plane didn't alter much for the protonated and deuterated versions [48]. Nevertheless, hydrostatic pressure studies are also being investigated actively, for instance, it is worth mentioning that there are recent studies related to the hydrostatic pressure dependence of water-ice where the authors in Ref. [70] using quantum simulations have shown a thermal phase transition happening in the water-ice induced by high pressures ($\sim$10GPa). The study draws motivation from various perspectives such as the modeling of compressed ice in the interiors of stars and the evolution of solar planets (e.g: Uranus and Neptune) and exoplanets and so on. It may be noted that hydrostatic studies always favored the order-disordered mechanism of ferroelectric phase transition.

Role of geometry

To probe the role of geometry in H_2SQ, again an atomic model comprising of kinetic and potential energy terms consisting of two oxygens atoms and a hydrogen was considered. The hydrogen in $O-H\cdots H$ was assumed to interact through the interatomic potential of the three-particle system [7].

Following early results, the model was expanded to include the quantum effects of the proton by a modified interatomic Morse potential. It was found that the effect of geometry is largely prevalent in a narrow range of the interatomic distances R_{O-O} ($R_1 < R_{O-O} < R_2$) [7]. That is, the regions where tunneling motion is seen in the domain of (R_1, R_2) were identified. In other words, a quantification was made on the dependence of tunneling motions of protons (deuterons) on the interatomic distances.

Order-disorder transition

Organic H_2SQ is notable not only for its (anti)ferroelectric properties but also for its light weightness and eco-friendly nature. After the quantum nature of proton motion in a double-well potential was established [23, 7] by investigating the observed anomalies in infrared and NMR spectroscopy, subsequently, the collective motions of protons were studied [71, 4]. Following this, a theory of phase transition in terms of an effective Hamiltonian was formulated [4], which includes dipole-dipole interaction. In general, many theories with different mechanisms have been put forward trying to explain the above-mentioned properties, of all the prominent ones which have been gaining significance since then is based on the order-disorder phenomenon. A good description of the order-disorder type phase transition on ferroelectric and antiferroelectric phases can be found in Ref. [5]. Besides, several experimental observations regarding the (anti)ferroelectric properties were also explored in other H-bonded ferroelectrics [22, 2, 72, 73].

Early studies also incorporated the lattice distortion effects into the order-disorder mechanism to explain the thermal antiferrodistortive phase transition within the mean-field approximation. Physical properties like dielectric susceptibility, specific heat [32], the elastic constant of the lattice were shown to be in qualitative agreement with the experiments. It may be noted that only in order-disorder-based theories, one usually maps a proton system to a pseudo-spin system with a thumb rule that the number of double-well minima for a proton placed at a given site, i, should be equal to the sum of the expectation value of S^z of pseudo-spin operator of S. With regards to this, the most widely used pseudo-spin models are the transverse field Ising model (TFIM), frustrated TFIM with nearest, next nearest, next next nearest-neighbor interactions, etc. However, in this thesis, instead of a TFIM-like model, a Hamiltonian consisting of $\mathcal{Z}_2$ gauge-invariant interactions (four-body) accounting for the ice-rules (IR) is investigated. In brief, the motivation to consider such a four-body Hamiltonian comes from the cooperative rearrangement of proton configuration within a unit molecule. In the following paragraphs, we discuss the early important theories in a systematic order.

Remarkable improvement of results on H_2SQ were seen when strongly coupled lattice-distortions [74, 42, 7] are included in pseudo-spin (e,g: TFIM models) modelling. The complete model with these lattice-distortions included was shown to be in reasonable agreement with the experimental findings. However, despite the improvements, few discrepancies between theory and experiments were found as far as the anomalous parts of the elastic and the dielectric constant are concerned [74, 42]. Based on that, there was a suggestion of a four-spin cluster theory in further improving the results [42, 75, 76] and an attempt was made to unify all the possible mechanisms [77]. Moreover, a simple analysis using the TFIM model showed that the exchange coupling though might not be the exact microscopic origin mimicking the proton system yet it could well explain the isotope effect [7].

Similarly, the presence of characteristic twofold structures below the transition temperatures, T_c [42] was explained in a mean-field approximation where it is shown that only by including the antiferroelectric interlayer interaction, the quasi-two-dimensional proton network in H_2SQ may exhibit a phase transition of first or second-order. The order of phase transition was observed to be strictly dependant on the model parameters [42]. The reason for such strict dependence may arise from the strong proton correlations within the quasi-2D layers. Moreover, within the pseudo-spin model, the higher value of T_c in H_2SQ was attributed to the fact that the rearrangement in proton configuration may lead to the larger increase in energies in the electronic structure of C_4O_4. It was also suggested that the low values of entropy at transition temperature, very low dependence of temperature with dielectric constant above T_c and the steep decrease in elastic constant and the dielectric constant just below T_c may be closely related to the unusual nature of transition at T_c in H_2SQ.

The importance of tunneling motion of protons in H_2SQ

There is a major difference between the H_2SQ and the rest of the H-bond materials. This has to do with the observed values of slopes of the temperature-pressure dependence curve dT_c/dp for the proton and deuterated versions. The values are not close to zero, i.e, the changes in dT_c/dp are close to zero for H_2SQ. While it is very different for KH_2PO_4 with the corresponding changes around $dT_c^P/dp = -46$ to $dT_c^D/dp = -24K/GPa$ for protonated and deuterated versions. This along with the large Isotope effect in T_c together made to infer that the tunneling motion of proton may not be necessary. As the large differences in the H-bond distances were presumed to be sufficient to explain it. However, *Matsushita* made a note on Isotope effect in H-bond crystals [7]. A graph was plotted for the empirical relation between R_{O-H} and R_{O-O} of many H-bond crystals with a restriction on H-bond angle, i.e, $\langle O - H \cdots O \rangle 170^\circ$. Then a theory was described to explain the characteristic behavior of the distribution of these interatomic distances with a 1D Morse potential containing the features of double-well potential. Within the model the theory established the relation of interatomic distances versus transition temperatures, T_c. A detailed description of the correlation between $O - O$ and the $O - H$ distance distribution was given. Moreover, a systematic comparison of the tunneling motions and the effect on the equilibrium positions of proton and deuteron as a function of R/r_0 was made. This concludes the early theoretical works, with an idea that tunneling motion is crucial in determining the phase transition in H_2SQ, and one cannot avoid the order-disorder mechanism to provide the platform in explaining the quantum phase transition occurring in H_2SQ.

Tautomerism

First-principle calculations could offer different perspectives in knowing the underlying interactions in H_2SQ. It may be noted that the proton-proton interactions may be primarily mediated by the alternating double-bonds in C_4O_4 by the process of π delocalization and the cooperative rearrangement of protons [21], also known as *Tautomerism*. The tautomerism helps the polarized molecules

(C_4O_4) to reorient themselves with four possible global orientations for a dipole, i.e, with symmetry of four-fold [21]. The (anti)ferroelectricity could then be achieved by the transfer of protons in a single-component molecule through this mechanism of tautomerism. Indeed, when the spontaneous polarization and hysteresis were measured, it was founnd to have very large dipole moments. The following *controlled yet spontaneous way* of inducing ferroelectricity leads to exhibit the highest spontaneous polarization (20 $\mu C\ cm^{-2}$) despite of its small molecular size [21]. This could have been only possible by the tautomerism mechanism. Accurate measurements of polarization were obtained from the the state of art first principle *ab intio* calculations using the Berry phase formalism rather than the conventional way of the vector sum of the dipoles. The detailed analysis of the above room temperature ferroelectricity and the mechanism of the efficient topological π switching (tautomerism) in the organic crystal-like H_2SQ can be found in Ref. [21].

Abinitio calculations

To probe parameter independent analysis of the phase transition, *ab initio* calculations [78, 79, 80, 81] were performed for H_2SQ. It was found that the AFE to FE phase transition can take place by varying the applied electric field E [82]. It is reported that with the help of an external electric field, the direction of the local polarization vector can be aligned in a total of eight distinct directions. Of them, two metastable ferroelectric phases have been identified along with their crystal structures [82]. Consistent with the previous studies [21], the largest spontaneous polarization has been obtained which is relatively higher than the organic ferroelectrics known till today [82]. Electric polarization amplitudes of the FE-α and FE-β phases were indirectly estimated to be 16.4 and 23.2$\mu C/cm^2$, respectively, based on the experimental AFE structure [11] since the detailed crystal structures of FE phases were not determined. Such high values of polarization amplitudes are now believed to be originating from the mechanism of the rearrangement of π electron delocalization and concerted proton transfer/displacements. The estimated value for the FE-α phase was shown to be in reasonable agreement with the experimental value of 10.5$\mu C/cm^2$ [21]. It highlighted the shortcomings of the point charge model.

The path integral molecular dynamics (PIMD) simulations employed with Density Functional Theory (DFT), nuclear quantum effects coming from the neighboring O-atoms [79, 78, 83] were estimated. The proton transfer barrier obtained by various density functional is evaluated and found that the best agreement was obtained for vdW-DF$_2$ functional. The use of the same functions in PIMD simulations revealed a very large influence of nuclear quantum effects [79, 78]. In other words, cooperative proton tunneling along H-bonding chains was found to be facilitated by synchronous quantum tunneling of several protons for short simulation times. The early results are successful in explaining the isotope effect, i.e, $\Delta T_c > 150K$. Yet it is reported that the absolute T_c values which are significantly lower than experimental results could not be accounted for. Similarly, the nature of the phase transition was found to be continuous instead of first order [79].

1D Molecular chain model

In the absence of any prototypical microscopic modeling of H_2SQ the models comprising of 1D molecular chain coupled weakly along the intraplane and interplane directions were found to be efficient. For instance, using the weakly coupled one-dimensional Ising chains and by fitting the exchange interaction parameters with the experimentally obtained results of the molecular correlations it was shown that the transition temperature is around $412K$. The closeness of the calculated T_c with that of $371K$ was highlighted. It was also found that the correlations lengths vary anomalously with temperature. Likewise, a model having two orthogonal interpenetrating H-bonding chains in H_2SQ effectively described by decoupled chains of 1D were introduced [79, 78, 83]. The significance of this model is that the generalization could be done to more complex H-bond structures. However, one may note that the realistic simulations for few H-bond ferroelectrics are challenging for several reasons. First, an accurate theoretical description is needed that describes the H-bonds between the molecules, the proton transfer barriers, and, in many cases, weak Van der Waals bonding between molecules or layers of the material. Second, to explain the collective nature of proton ordering in

H_2SQ it is suggested to use extended simulation cells containing several molecular units along the H-bonding directions [78, 83]. Third, thermal and nuclear quantum effects such as tunneling and zero-point motion must be taken into account. This has to do with the finite-temperature phase transition and the quantum mechanical nature of the proton. A more complete description of the theoretical approach employed and tests performed to establish its accuracy is given in the Ref. [78, 83].

1.1.2 Significance of studying H_2SQ

Finally, we note that the systems with ice-rule constraints are shown to exhibit no long-range ordering (LRO) down to zero-temperature, with ionic defects similar to the magnetic monopoles being the elementary excitations [73, 84, 85, 86, 87]. The ice-rules generally leads to frustration in the system where all the configurations in the low-energy sector are degenerate, this was discussed early by Pauling in the early 1930s [88]. While the quantum effects of the water-ice and spin-ice still attract interest, recent studies on water-ice systems have revealed an interesting phenomenon of coherent quantum tunneling in the low temperatures leading to $U(1)$ quantum spin-liquid like groundtstate with fractionalized spinon and gauge field excitations [84, 73, 85, 86, 87, 10].

Earlier works [72] include the investigation of finite-temperature phase diagram in the $T - P$ plane. It was shown that a phase transition from the AFE (antiferroelectric) to PE (paraelectric) phase occurs. The paraelectric phase is sustained at zero-temperature above some critical pressure P_c. In this thesis, we use a model Hamitonian that was recently been gaining importance. Chern et al [89] have studied a similar model Hamiltonian for such a system and obtained a phase diagram numerically using the quantum Monte Carlo (QMC) technique at zero-temperature. The model Hamiltonian at zeroth order consists of a quartic spin (on a plaquette) interaction with a strength J_0. The quartic interactions were also considered in the relevant XXZ models as well [90]. When the Hamiltonian is studied in the presence of a magnetic field characterized by the parameter K, the system shows a confinement-deconfinement phase transition. There is also a proposal for the detection of the deconfined charges to verify certain lattice gauge theories [91]. Nevertheless, the complete model includes a next-nearest neighbor Ising-type interaction with strength J_1 and a dipole-dipole interaction $J_2 < J_1$. Usually, the presence of J_2 causes the ferroelectricity in these materials. The model was shown to exhibit both confinement-deconfinement transition (CDT) and ferroelectric quantum phase transition (FT) for an appropriate set of parameters of the model Hamiltonian. The details of it are discussed in chapter 2.

1.2 Phenomenology of pseudo-spin formalism

In the previous section 1.1, we have mentioned the mapping between pseudo-spins and the proton tunneling in H-bond systems. Here, we describe the formalism which later becomes useful to understand in mapping it to the suitable quantum spin systems for H_2SQ, for example, Ising gauge theories. It is to be noted that, throughout this dissertation, we use pseudo-spin formalism as our basis of analytical and computational method to investigate various of H_2SQ. As indicated in the previous subsection, the mapping is not new to H_2SQ, it has been previously formulated to study the ferroelectric properties of other H-bonded organics as well. Inspired by vertex-based models [92, 93, 94, 95, 96], KH_2PO_4 was one of the earlier system studied by a simple TFIM with the kinetic term proportional to $\sigma_i^z\sigma_j^z$ mimicking the configurational energy of two protons located at site i, j. The term mapping may be understood as the mapping (from spatial (protons) to magnetic moment (spin) degrees of freedom) of their respective energies, i.e, for H-bonded solids the configurational energy caused by the local ordering of protons ($\vec{P} = q\vec{d}$, where $\vec{P}$ is the dipole (displacement) vector of the proton) [97, 98] is equivalently and effectively described by exchange interaction of σ^z variables in the pseudo-spin language with the Ising-type interaction $\propto \sigma_i\sigma_j$. It may be appropriate to note that the initial studies were based on the quantum version of the ball-spring model with vibrational energies linking to the energies of the proton motion. Nevertheless, here the dipole moment vectors (displaced

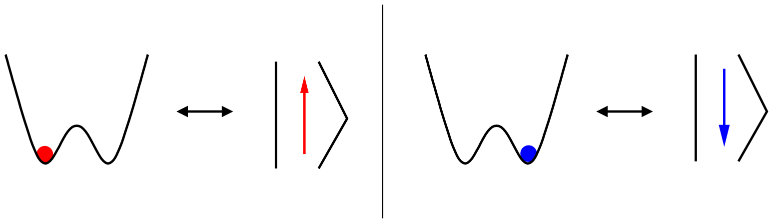

Figure 1.1: Schematic diagram showing the mapping between the protons in a double-well potential of $O - O$ bond and the pseudo-spin 1/2 variables. The notation and sign convention of the spins are described below in sec. 1.3

protons) could be understood as σ^z's with the interaction of proton-proton now being represented as the interaction between two spin-1/2's. It is to be noted that the mapping mechanism provided is not an exact mathematical transformation and may not have been possible without the quantum nature of the proton. The key aspect to be aware of is that because of the fundamental equivalence in the quantum mechanical behavior of protons and spins, it is understood that there is no loss of generality in such mapping. That is to say, similar physics could also be realized with the pseudo-spin formalism [74, 42], but with a difference in the observables that are to be estimated in the calculations. Nevertheless, many theories that now describe H-bond solids are based on pseudo-spin formalism. For KH_2PO_4, the energetics of protons may be effectively described as,

$$\mathcal{H} = -J_0 \sum_{\langle ij \rangle} \sigma_i^z \sigma_j^z - K \sum_i \sigma_i^x, \tag{1.1}$$

a simple TFIM model with J_0, the interaction strength proportional to the dipole-dipole energy typically in the units of meV. The field term (K) is accounted for the fact that the tunneling of the protons between the double-well potential is now represented by the non-commuting operator, σ^x, responsible for quantum fluctuations in the system. Intuitively, it may be thought of imparting the quantum fluctuations whose action is to flip the dipole (local ferroelectricity) created by the H-bond. The crucial aspect in designing an effective pseudo-spin Hamiltonian comes from the nature of the kinetic term that is the exchange coupling, which is dictated by the physical properties of the material, specifically related to its geometry, structure, and underlying fundamental interactions. Intriguingly, this simple model was successful in describing the quantum order-disorder phenomenon in KH_2PO_4 in the late 1980s by *Matshushita et al.* This was also one of the early theories which studied phase transition in H-bonded organics. Following this, many later studies had come up with more complex interactions covering various H-bond solids. Most of the theories were based on pseudo-spin formalism that have been constructed from the vertex-models with a restriction on each vertex. Specifically at each vertex the ordering is not random but is subjected to satisfy the ice-rules (exactly two hydrogen ions approach oxygen out of four hydrogen ions [1, 88, 99, 100, 101]). The constraint that is analogous to the well-known two-in and two-out configurations in spin-ice pyrochlores and other frustrated systems [102]. However, these ice-rules dictate the phenomenology of order-disorder transition in H-bond solids.

Out of all, studies on H_2SQ crystal are primarily important because of its ordered proton configurations and also for the underlying physics that is strongly favored to be due to the order-disorder phenomenon mechanism specific to H_2SQ. This may be naively understood to be because of the ice-rule states that are being obeyed in these materials could be lifted to give an ordered state by dipole-dipole interactions around the vacuum, as mentioned in section 1.1. H_2SQ is one of the very few organics which possess such property. In the next section 1.3, we discuss the details of the interactions in the H_2SQ crystal and give its suitable Hamiltonian.

1.3 Quantum pseudo-spin model for squaric acid

In the previous section 1.2, we have discussed the mapping of a H-bonded system to a relevant quantum spin-1/2 system given the basic underlying proton-proton interactions with KH_2PO_4 as the example. Here we discuss the construction of a model Hamiltonian describing the dynamics of proton-proton interactions in H_2SQ using the same rules of the formalism. However unlike KH_2PO_4 the nature of proton-proton interactions are much diverse in H_2SQ, this has to do with the C=C π-bond nature of the the C_4O_4 molecules. It is believed that the interactions between the protons within

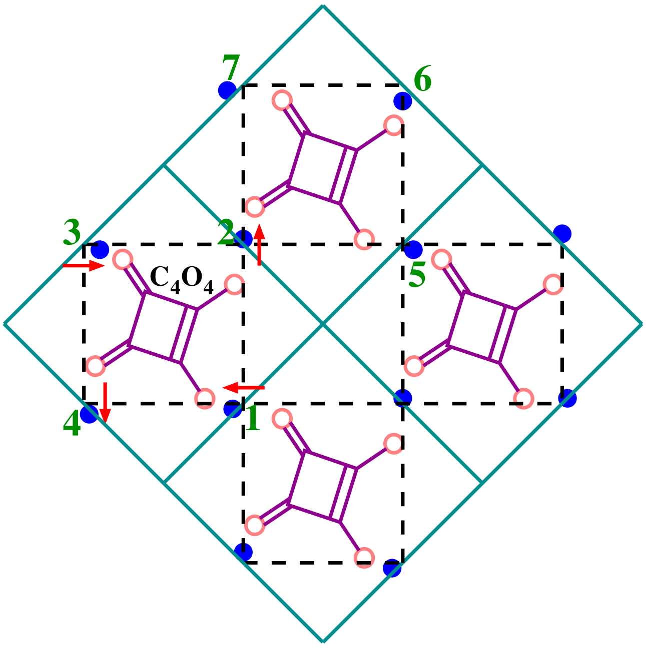

Figure 1.2: Illustration of part of a layer in H_2SQ crystal, the blue dots represent the protons and the small pink circles represent the oxygen atoms forming a quasi-2D configuration of the H-bond network, one of the C_4O_4 molecular unit is shown and labeled. The dashed brown lines show the physical lattice and the solid cyan lines form the lattice on which the model is built on. The indices shown represent the corresponding spins as shown in Eq. (1.3).

a C_4O_4 molecule is mediated by this π-bond realizing the potential ferroelectricity at lower temperatures and lower pressures and the ice-rule type physics. The model of H_2SQ is motivated by the experimental realization of ferroelectricity and the vertex-based model [99, 75]. For elaborate details regarding the vertex-modeling of the present system, the reader may refer to Ref. [99, 75].

Since in a ferroelectric state all the molecules have the same configuration of protons surrounding it, i.e, two neighboring protons are nearer to the molecule, as a consequence, a C=C double bond is established between the C-atoms close to the protons. Following this mechanism, one may simply assume that the interaction of protons is mediated by the C=C double bond within the groundstate at low-T and P, i.e, the ferroelectric state with neighboring protons in the same state (closer to C_4O_4) [75]. With this in hand, one may now construct the higher excited states starting with the obtained groundstate. At an instant, if one proton closer to C_4O_4 is tunneled to *farther* (flipping the pseudo-spin) the change in total energy is now $2E'$ ($E' > 0$) as shown in Fig. 1.3. The molecule acquires a net negative charge and the energy of the state is higher as it does not satisfy the local ice-rules. Using similar arguments one may construct all the other higher excited states with a rule

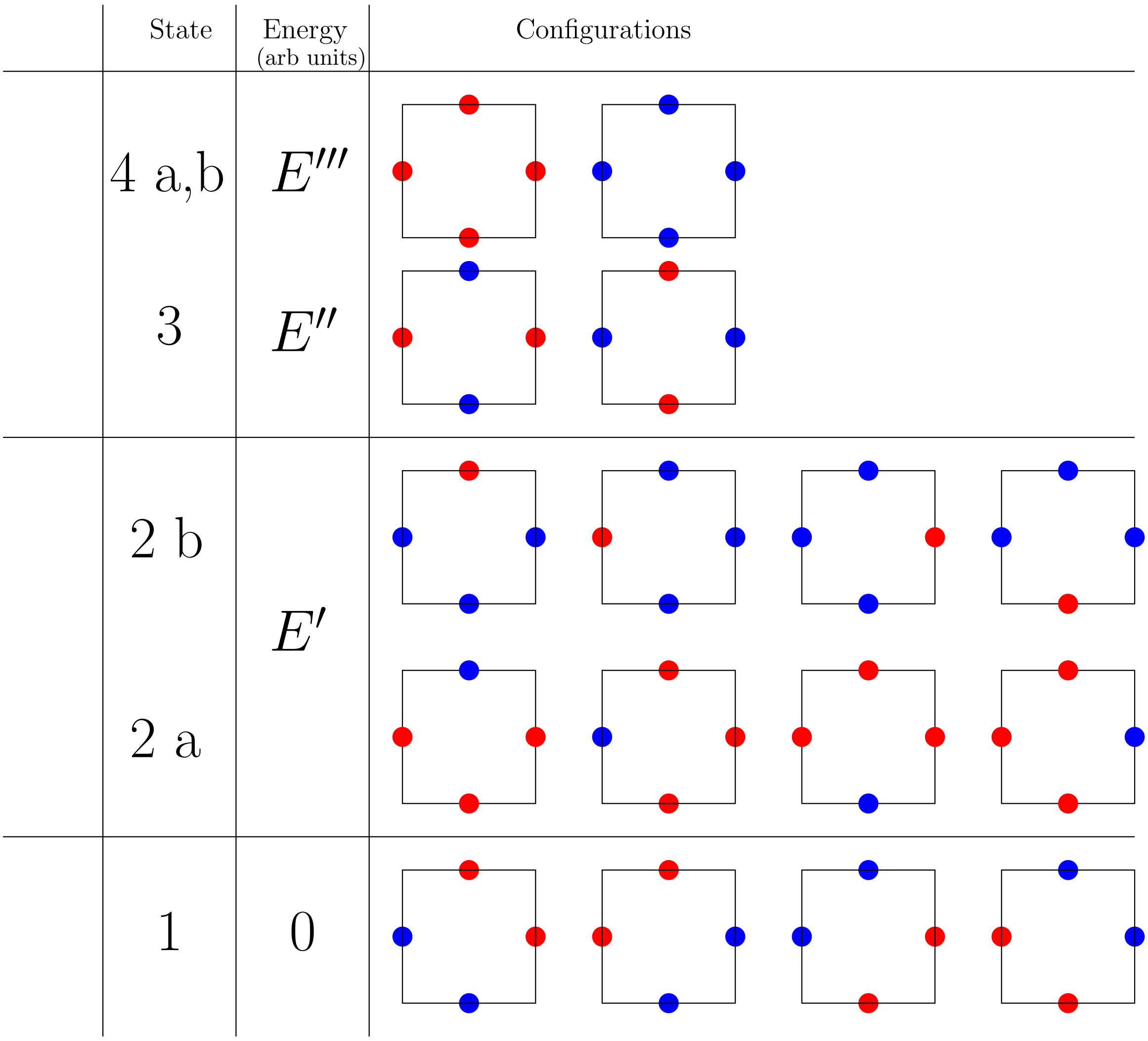

Figure 1.3: Schematic diagram showing all possible states and their corresponding energies that arise due to proton-proton correlations in the H_2SQ. The model used is a vertex-based model and the local states are shown in the column of configurations. The blue (red) dots represent the spin-up (spin-down) degrees of freedom.

that one has to construct states subsequently starting with an ordered state as mentioned above. All the configurations and their corresponding energies are charted out in Fig. 1.3.

The next question that arises is to what degree the proton-proton correlations seems to exist. It is shown in Ref. [99] that the protonic configuration of a layer could be imagined to be built up by independent orthogonal and parallel linear Ising spin chains. Consider a fully ordered layer, in which all molecules are in the same groundtstate, and assume that one certain proton is shifted from a molecule to its neighbor (Fig. 1.3). By this process, one configuration with three close protons (state 2 a) and one configuration with one close proton (state 2 b) is generated. The energy of the three molecules in Fig. 1.4 then is $2E'$. Assume that in the next step a proton is shifted from the configuration 2 a to the neighboring molecule (Fig. 1.4). As a consequence, molecules are generated off the types 2 a, 2 b, 3 and the total energy of the configuration is $2E' + E''$. Since the energy of state 3 is higher than that of the groundstate, i.e, $E'' > 0$, this energy is larger than that of the preceding configuration. Clearly, the latter configuration could be reached from a fully ordered groundstate only via the first configuration. It is reasonable to assume that the second configuration, as well as all other configurations with higher energy, are thermally not populated to any substantial extent. Thus, disregarding these higher excited states one is left with a model of linear chains. Violations of the ice-rule give rise to excited states (ionic defects). Whereas the lowest excited state may be considered as an excited state realized within some chain by the higher states interactions are realized within the linear chains as well as between orthogonal linear chains. In the schematic representation of Fig. 1.4, the chains are parallel to the diagonals of the squares. Since the lowest excited defect configuration is given by molecules in the configurations 2 a, 2 b we may assume for our model that defect states occur only within the chains without influencing protons of other chains. Consequently, we may look at the molecular planes as a network of independent linear Ising spin chains oriented along with two orthogonal directions in the crystal. By J_1 we denote the interaction between neighboring protons in the chains. Although the present argument starts from the fully ordered groundstate it is expected to apply approximately also to the region above T_c because the strong in-plane ice-rule type interactions give rise to a considerable in-plane order also in this temperature region. A more quantitative information of the linear spin chain Ising model can be derived from the vertex models discussed [75]. One then associates a pseudo-spin variable $\sigma_i = \pm 1$ to each proton bond between the C_4O_4 molecules. Consequently the states of the protons on a given molecule C_4O_4 are denoted by the pseudo-spin variables σ_1^z, σ_2^z, σ_3^z, σ_4^z where the subscripts label the spins in the order shown in Fig. 1.2. The sign of the spin vector σ_i^z is defined to be positive if its projection is positive on some arbitrary but fixed coordinate system. So for example the state 4 a in Fig. 1.3 may be given by σ_1^z = + 1, σ_2^z = -1, σ_3^z = -1, σ_4^z = + 1. The energy $E(\alpha)$ of a

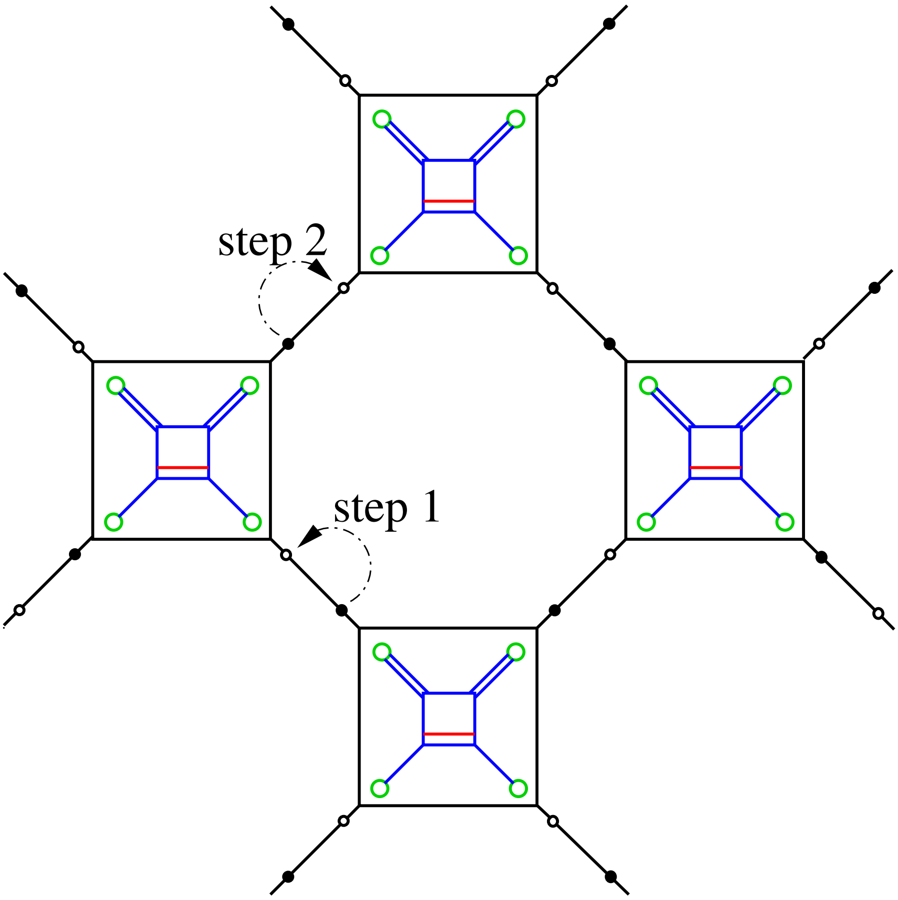

Figure 1.4: I, Referring to the ice-rule configuration of the corresponding pseudo-spin system and for proton system where the net dipole moment of the molecule is finite, $P^x = 1, P^y = 0$. II, Showing one of the ice-rule configurations but the net dipole-moment here is zero, $P^x = 0, P^y = 0$. III, Same but with non-zero dipole moment and neither pointing along x nor y, $P^x = 0.5, P^y = 0.5$.

vertex at a lattice site α, then can be written as [75],

$$\mathcal{E}(\alpha) = -J_0\sigma_1^z\sigma_2^z\sigma_3^z\sigma_4^z - J_1(\sigma_1^z\sigma_3^z + \sigma_2^z\sigma_4^z) - J'(\sigma_1^z\sigma_2^z - \sigma_2^z\sigma_3^z + \sigma_3^z\sigma_4^z + \sigma_4^z\sigma_1^z), \tag{1.2}$$

where $J_1 = (4E' - (E'' + E'''))/8.$, $J_2 = (E''+E''')/8$, $J_3 = (E'' - E''')/8$, Thus, E is determined by nearest and next-nearest neighbor two spin interactions and by four spin interactions. The total energy of the lattice is then simply given by $\mathcal{H} = \sum_{i=1}^{N} \mathcal{E}(i)$.

1.3.1 Ice Rules: The Ising gauge J_0 and the Intramolecular coupling J_1

It is worth mentioning again that the early trends included the studies which considered the proton system strongly coupled to the lattice distortions, i.e, the phonons, to study the order-disorder phenomena of the (anti)ferroelastic behavior below an (anti)ferrodistortive transition. However, later the same results of (anti)ferroelectric transition were shown even without considering such phonons-protons coupling, the realization in the theory comes from the phase diagram in the $T-P$ plane. The common aspect in all such models is that the groundstate is highly degenerate with each configuration representing a disordered copy of the proton system satisfying the ice-rules. This motivates us to consider one such Hamiltonian incorporating all the ice-rule states as its zeroth-order dynamics and is given by the Eq. (1.3) . The Hamiltonian is the straightforward extension of the equation (Eq. (1.2)) from the preceeding section. It is known that the Hamiltonian described by the Ising gauge term alone has a structure with 16 different configurations per plaquette (Fig. 1.3). Importantly, the configurations are shown in Fig. 1.3 and in the first row of Fig. 1.3 refers to the configurations with two-up and two-down configurations, i.e, the ice-rules, while the second row in Fig. 1.3 refers to the non-ice-rule state but also a groundstate (classical) in the Ising lattice gauge theory (ILGT). This is not the desired one because we need only those states which satisfy the ice-rules and simultaneously also as our lowest energy states of H_2SQ. The non-ice-rule states refers to excited states with ionic defects. The distinct aspect of the H_2SQ is that this is naturally rectified by the intramolecular coupling term in the system which removes this ambiguity of removing certain non-ice-rule states as our lowest energy states. This question is addressed in details in the chapter 2. For brevity, the Fig. 1.3 shows the excited state which is a ionic defect since the net charge of the molecule is not zero. Nevertheless, till now, we were able to model our H_2SQ system concerning the ice-rule properties. In the next section 1.3.2, we discuss our model concerning the dipole-dipole interaction (J_2) which explain the ferroelectric properties.

1.3.2 The dipole-dipole interaction

Until now we have discussed the modeling of H_2SQ involving the terms J_0, J_1, and J'. In Fig. 1.3 for $J' = 0$ the lowest energy state is given by state 1. This is a state where all the molecules can be in any one of the four given local ordered states (see bottom row in Fig. 1.3). In otherwords, we have a set of randomly oriented dipoles spanning the entire lattice. It is natural to think that the interaction between the dipoles is inevitable. Indeed, to realize a antiferroelectric ordering in H_2SQ, reasonably one could argue that a minimal model also accounts for the dipole-dipole interaction regardless of the strength of it. We will see later in chapter 2 that indeed a very small J_2 is enough to drive the order-disorder transition in the system. However, this is not the case always as we shall see later in chapter 3. This establishes our model with J_0 being the Ising gauge term accounting to the 16 possible configuration of proton within a plaquette which along with J_1 imposes the restricted ice-rules with each having only finite dipole moment and finally J_2 describing the physics of dipole-dipole interactions.

It may be appropriate to mention that there are other possible models explaining the same ice-rule dominant physics in H_2SQ. For example, *Ishizuka et al* [103] has used the complex TFIM model with multiple interactions, J_1, J_2, and J_3 where the couplings are given along the nearest, next-nearest neighbor and next next-nearest interaction on a square lattice as a model to describe the H_2SQ. Note that the spins within this model are located on the lattice sites. Similarly, in 2014, *Chern et al* [89] has used the model explained above in Eq. (1.2) [99] except for the nearest neighbor diagonal hopping, J', that has been not taken into account. This is an extended version of ILGT in (2+1) dimensions but with additional interaction J_1 and J_2. Here the spins are located on the edges of the dual lattice as shown in Fig. 1.2. In this thesis, we use the Hamiltonian as used in Ref. [89] as a model to analyze the H_2SQ system. We now write the Hamiltonian and discuss the phenomenology of the dipole-dipole term derived from the properties of H_2SQ, and is given by,

$$H = H_0 + H_1 + H_2, \tag{1.3}$$

where H_0, H_1 and H_2 are respectively given by

$$H_0 = J_0 \sum_p \sigma_1^z \sigma_2^z \sigma_3^z \sigma_4^z - K \sum_i \sigma_i^x, \tag{1.4}$$

$$
\begin{aligned}
H_1 &= J_1 \sum_p (\sigma_1^z \sigma_3^z + \sigma_2^z \sigma_4^z), && (1.5)\\
H_2 &= -J_2 \sum_{\langle AB \rangle} \vec{P}_A \cdot \vec{P}_B, && (1.6)
\end{aligned}
$$

where σ_i^α's are the Pauli matrices, P_A and P_B are the dipole moment vectors of molecule A and B (see Fig. 1.2) respectively and the components of them are defined as follows,

$$
\begin{aligned}
P_{(A,B)x} &= (\pm)\frac{1}{4}(\sigma_1^z + \sigma_2^z - \sigma_3^z - \sigma_4^z), && (1.7)\\
P_{(A,B)y} &= (\pm)\frac{1}{4}(\sigma_2^z + \sigma_3^z - \sigma_1^z - \sigma_4^z), && (1.8)
\end{aligned}
$$

where (+) is for molecule A and (-) is for molecule B. The summation of indices p runs over all the plaquettes of the dual lattice (red) and i runs over all the spins in the dual lattice and $\langle AB \rangle$ indicates the nearest neighbor dipole-dipole interaction.

1.4 Overview

We have started with a brief introduction on the significance of H-bonded systems and the motivation of studying H_2SQ followed by the early experimental details revealing the crystal structure and the associated intertwined (structural and charge) phase transition. Numerous experimental works regarding the microscopic details of the phase transition were presented. For instance, a brief discussion on coherent and incoherent Raman scattering, infrared spectra, and x-ray diffraction studies from various authors was presented. It is known that the crystal structure of H_2SQ can be understood of stacked quasi-2D layers with weakly coupled interplane interactions of Van der Waals type. As a consequence of ice-rules dynamics, strong intraplane proton-proton correlations are believed to be inherently present. In the low-temperature or pressure, the ordering of protons within the intraplane network was experimentally found to be antiferroelectric and while the 2D layers were stacked antiferroelectrically along the *unique-axis*. We briefed that the studies established the nature of the phase transition to be of the first-order and the corresponding symmetry in the respective phases being identified. Another interesting aspect of H_2SQ was also discussed regarding the case of double phase transition with the second one occurring above the first, however, it is later found to be a crossover as suggested by the NMR and NQR experiments. Theoretically, this is also favored by one of our early studies [13]. The details of which are presented in chapter 4.

Despite going through a discontinuous phase transition the core molecular structure of the C_4O_4 was found to remain intact as observed in the Raman scattering experiments. And the only change observed was in the rearrangement of C_4O_4 molecules, the protons, and the lattice parameters such as the interatomic spacings, unit cell dimensions, etc. The temperature-pressure related studies have been presented to show that the interatomic spacing decreases with the increase of external pressure. This in turn makes the proton having a higher tunneling rate with a mean position at the center of the H-bond, which is a paraelectric phase. Nevertheless, following the early experimental works on the Isotope effect of H_2SQ, several possible mechanisms such as tunneling motion of protons, a coupling of it with lattice distortions were taken into account to explain the phase transition. Indeed, both the displacive [34, 35, 36, 37] and order-disorder features were seen present as analyzed from the NMR spectroscopy and infrared studies. However, the first-principles calculations suggest to be favoring more of order-disorder type [5, 31, 26].

Later, followed by experimental details of earlier studies, all the important theoretical works trying to explain the known experimental results were briefly presented. Although it seems no concrete conclusion could be made about the exact possible mechanism describing the physics of H_2SQ, one may favor the order-disorder mechanism for its range of applicability and the success of it and more specifically being favored from the *ab-initio* calculations [82, 79, 78]. Specifically, looking from the perspective of anomalous properties, it may be noted that the phenomenon of order-disorder transition are purely based on the pseudo-spin formalism of spins but with a constraint, that is, *Ice-rules* imposed on the pseudo-spins. Although, it has remarkable success when the distortion effects are also included, yet on the other hand the recent results based on pure pseudo-spin models predicting the existence of ferroelectric phase transition and the quantum paraelectric state fascinated to explore H_2SQ along the mechanism of order-disorder phenomenon where a pure pseudo-spin model is analyzed disregarding the phonon coupling. Indeed, the dielectric properties, the correlation lengths in the (anti)ferroelectric phase estimated by quantum Monte Carlo were closely matched with experimental findings [89]. Finally, based on the mechanism of proton rearrangement and given the ice-rule type dynamics in the crystal and the phenomenology involving various configurations of ice-rules, a theory similar to the Ising lattice gauge theory (ILGT) in (2+1) dimensions and the basic details of each term coming from the experiments were presented and discussed. In this thesis, we use this extended version of ILGT to arrive at all our results.

Briefly, in the upcoming chapters, we first present the model and the methods and describe our results obtained for the zero-temperature calculations using various methods using the Hamiltonian in Eq. (1.3). Later, In chapter 3, we present the detailed method of QMC and present the various physical quantities calculated in our finite temperature (and field) analysis. The phase diagram was also presented and discussed in detail. And in chapter 4, using the Suzuki-Trotter path integral Monte Carlo method, we simulate the extended 3D model of the Hamiltonian Eq. (1.3) with the newly introduced interlayer coupling constant as the independent parameter. Within the realm of linear-spin wave theory, we estimate the off-diagonal xx correlation function for a 2D version of Hamiltonian.

CHAPTER 2

Classical groundstates, symmetry, and excitations

2.1 Classical model

We consider the minimal model satisfying the phenomenological ice-rules with various competing interactions that include the Ising gauge term J_0, intramolecular term J_1, and dipole-dipole coupling J_2. All the diagonal interactions reflect the strong proton-proton correlations that are in play in squaric acid crystal. Here, we discuss the classical groundstates obtained from the mean-field analysis of the model Hamiltonian given by Eq. (1.3). Glancing at the Hamiltonian one can naively identify the classical groundstates, however, the same cannot be understood when a magnetic field, K, is turned on. In other words, we are interested in finding the disorder-order (if any) phenomenon associated with the given Hamiltonian upon applying the field K. For this, the quantum spin-1/2 system given by the Pauli matrix $\sigma_i^\alpha \epsilon SU(2)$ will be now replaced by classical spin system S_i^α belonging to $SO(3)$ group. Later, we perform the spin-wave calculations on the groundstates. The Hamiltonian can be rewritten as,

$$
\begin{aligned}
H_0 &= -\frac{1}{4} J_0 \sum_{\langle i i_1 i_2 i_3 \rangle} S^z_{i_1} S^z_{i_2} S^z_{i_3} S^z_{i_4} - K \sum_i S^x_i && (2.1)\\
H_1 &= \frac{1}{2} J_1 \sum_p (S^z_1 S^z_3 + S^z_2 S^z_4) && (2.2)\\
H_2 &= -\frac{1}{2} J_2 \sum_{\langle AB \rangle} \vec{P}_A \cdot \vec{P}_B && (2.3)
\end{aligned}
$$

where S^{α}_i's are the classical spins, the coefficients 1/4, 1/2 are accounted for double-counting since a given spin is linked to two subplaquettes (A, B), and also each plaquette accounts for two horizontal and vertical links. Therefore, while doing a summation over single spin sites we encounter the gauge term four times after expanding the summation for the finite lattice as in Eq. (2.1). The P_A and P_B are the dipole moment vectors of molecule A and B respectively and the components of them are defined as follows (see Fig. 1.2),

$$
\begin{aligned}
P_{(A,B)x} &= (\pm)\frac{1}{4}(S^z_1 + S^z_2 - S^z_3 - S^z_4) && (2.4)\\
P_{(A,B)y} &= (\pm)\frac{1}{4}(S^z_2 + S^z_3 - S^z_1 - S^z_4) && (2.5)
\end{aligned}
$$

where (+) is for molecule A and (-) is for molecule B. Note that the sign convention used here is not unique. The summation of indices p runs over all the plaquettes of the dual lattice (red) and i runs over all the spins in the dual lattice and $\langle AB \rangle$ indicates the nearest neighbor dipole-dipole interaction.

The parameter space of the Hamiltonian H is three-dimensional with J_0 being the largest followed by J_1 and J_2 in magnitude. While K can be varied. The $J_0 (> 0)$ gives rise to $\mathcal{Z}_2$ gauge-invariance and the intermolecular coupling term J_1 gives rise to the ice-rules. Let us briefly discuss the consequences of various terms in the above Hamiltonians. The first terms in H_0 can easily be satisfied by suitably aligning spins along the $\pm$ z-axis such that each plaquette exactly contains an even number of up-spins and even number of down spins. The groundstate manifold of the first term consists of two subsets. A square plaquette can have all four spins up (or down) or it might have exactly two spins up and two down spins. The first configuration is termed as parallel configuration (PC) and the second one is known as ice-rule configuration (IRC). If one considers a torus having $\mathcal{N}_x$ and $\mathcal{N}_y$ plaquette in x and y direction respectively then there are $\mathcal{D} = 2^{\mathcal{N}_x \mathcal{N}_y}$ degenerate groundstates for the first terms in the Hamiltonian which implies an entropy density per plaquette is 4. However, for a variant model on a square lattice, the IRC degeneracy has been exactly worked out [104] and is equal to $(3/2)^{1.5}$ per spin. Nevertheless, here the J_1 terms remove the parallel configurations in a plaquette and make the ice-rule configurations the true groundstate configurations. One interesting question that one might be interested in is whether, in the absence of J_1, the quantum fluctuation selects one of those (PC, IRC) as the true groundstate manifold. One can consider the parallel configuration as the defect in ice-rule configurations. The spin-wave theory suggests that there is no removal of groundstate degeneracy between ice-rule and non-ice-rule configurations. The external field, that is, K brings in frustration in the tendency to align along the $\pm$ z-direction. As large K, all the spins are eventually aligned along the x-directions. One of our motivations to understand the classical version of the model was to investigate these transitions from a highly degenerate classical configuration to an ordered phase where spins are along the x-axis. The terms in H_1 and H_2 bring in additional complexity mainly by lifting the groundstate degeneracy generated by the first term in H partially. The effect of the H_1 term on the groundstate degeneracy has already been discussed. The dipole-dipole interaction represented by H_2 eventually removes all local degeneracy causing a ferroelectric alignment of electric dipoles associated with each plaquette. However, there are four global degenerate states in this case which will be discussed later in detail [3]

2.2 Mean-field analysis

Generally, for classical Heisenberg-type interactions, one resorts to Luttinger-Tisza method [105] to find the classical groundstates. However, the limitation of this approach is confined to only Bravais lattices, though for non-Bravais lattices, it may give important leads to possible groundstate spin configurations [106]. The presence of four-spin interactions limits us from using such analytical methods. Owing to this reason, we examine numerically the groundstate spin configurations. We notice that the Hamiltonian can be rewritten in the following form [107]: $H = \sum_i h_i^z S_i^z + h_i^x S_i^x$, where for a given spin component S_i^α, h_i^α denotes the local field component along α axis. The minimum energy configuration of spins is then obtained by aligning the S_i^α to the negative α axis. Usually, one starts from a random configuration of [S_i^α,0] yielding a configurations of [h_i^α,0] and a total energy $E[S_i^\alpha, 0]$.The distribution [h_i^α,0] yields a new configuration of spins [S_i^α,1] and new total energy of the system $E[S_i^\alpha, 1]$. In the above, the index "$0''$ or "$1''$ denotes the steps in numerical iterations. We continue this process until $E[S_i^\alpha, n] \equiv E[S_i^\alpha, n+1]$ (see Fig. 2.3 for a schematic understanding). We have performed numerical simulations over a lattice of dimension 256×256 and checked for sufficient initial configurations. Noticeably, we have found that the groundstate has a one-to-one corresponds to the groundstate configurations of the first terms of H_0. Importantly, the only difference is that the spins have now a finite and constant component of S_i^x, which changes as a function of K [108]. Since the calculations are strictly done for the zero-temperature case and given that the system is closed, thus minimizing free energy is equal to minimizing the total energy of the system. Therefore, the saddle point can be found simply by $\partial E[S^\alpha, n]/\partial S_i^\alpha(\alpha = x, y) = 0$. Then the mean-field equations governing the groundstate dynamics are given by,

$$\begin{aligned}\mathcal{H}_{\mathrm{mf}} &= \sum_i -\frac{1}{4} J_0 \sum_i (S_{i_1}^z S_{i_2}^z S_{i_3}^z + S_{i_4}^z S_{i_5}^z S_{i_6}^z) S_i^z \\ &\quad + \frac{1}{2} J_1 \sum_p (S_{i_1}^z + S_{i_5}^z) S_i^z - \frac{J_2}{4s} \sum_{j=1}^{4} \left(P_{B_j}^x + P_{B_j}^y + P_{A_j}^x + P_{A_j}^y \right) S_i^z\end{aligned}$$

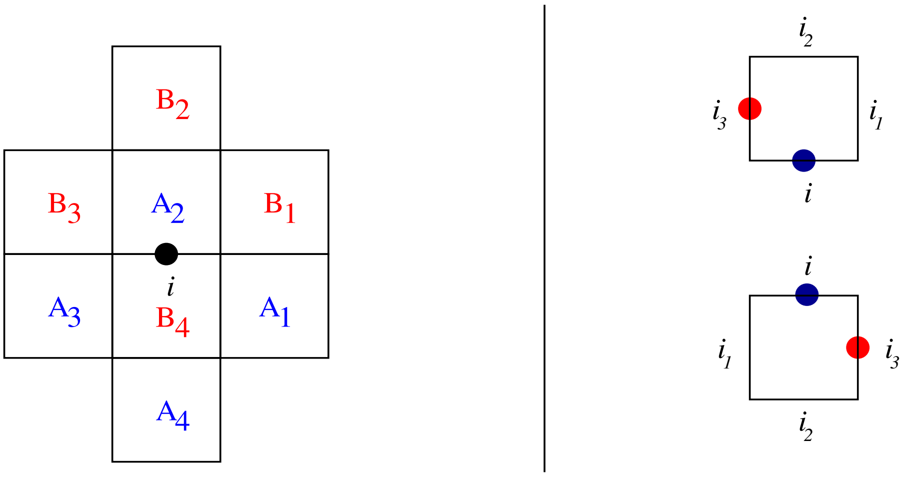

Figure 2.1: a) Lattice showing the plaquette indices $A_\alpha, B_\alpha(\alpha = 1, 2, 3, 4)$ used as the convention for Eqs. (2.13) - (2.14). This is exactly the cluster size whose local molecular fields influences the orientation of spin i. The indices represent the spins with which the spin i is interacting.

$$\begin{aligned}
& -K\sum_i S_i^x, \\
= & \sum_i -\frac{J_0}{4}\Bigg((S^z_{i_1}S^z_{i_2}S^z_{i_3}+S^z_{i_4}S^z_{i_5}S^z_{i_6}) \\
& +\frac{J_1}{2}(S^z_{i_1}+S^z_{i_5}) - \frac{J_2}{4s}\sum_{j=1}^{4}(P^x_{B_j}+P^y_{B_j}+P^x_{A_j}+P^y_{A_j})\Bigg)S^z_i - K\sum_i S^x_i \\
= & \sum_i\Bigg(-\frac{J_0}{4}\Big[(S^z_{i_1}S^z_{i_2}S^z_{i_3}+S^z_{i_4}S^z_{i_5}S^z_{i_6}) \\
& +\frac{J_1}{2}(S^z_{i_1}+S^z_{i_5}) - \frac{J_2}{16s}\sum_{j=1}^{4}(P^x_{B_j}+P^y_{B_j}+P^x_{A_j}+P^y_{A_j}\Big]S^z_i - KS^x_i\Bigg), \qquad (2.6)
\end{aligned}$$

We can rewrite the above equation in the following form,

$$\begin{aligned}
\mathcal{H}_{\text{mf}} &= \sum_i\Big(h^z_i S^z_i - KS^x_i\Big) \qquad (2.7) \\
&= \sum_i\Big(h^z_i S^z_i + h^x_i S^x_i\Big), \qquad (2.8)
\end{aligned}$$

With the mean-field parameters, $h_i^{z,x}$, at each site i can be identfied clearly as,

$$\begin{aligned}
h^z[S^z_i, n] = & -\frac{J_0}{4}\Big[(S^z_{i_1}S^z_{i_2}S^z_{i_3}+S^z_{i_4}S^z_{i_5}S^z_{i_6}) \\
& +\frac{J_1}{2}(S^z_{i_1}+S^z_{i_5}) - \frac{J_2}{16s}\sum_{j=1}^{4}(P^x_{B_j}+P^y_{B_j}+P^x_{A_j}+P^y_{A_j}\Big]. \qquad (2.9)
\end{aligned}$$

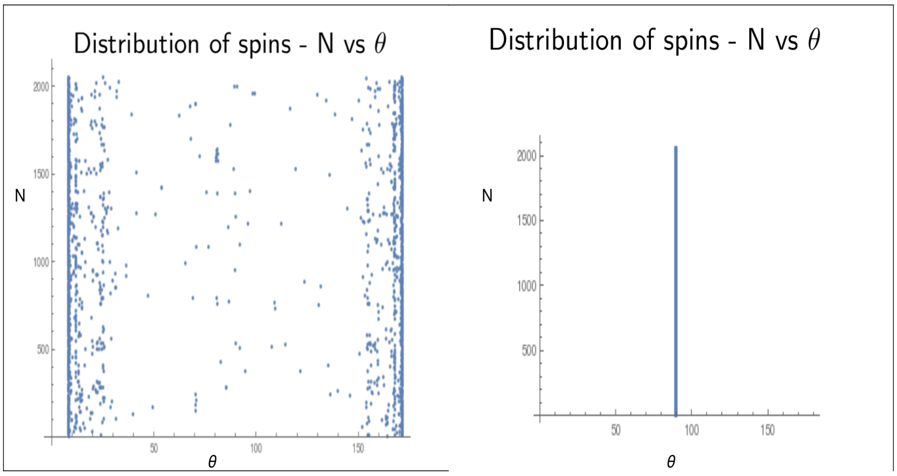

Figure 2.2: (Color online) The distribution of N spins over all θ values. The left panel figure corresponds to the case of low-field mean-field results obtained for a system of 256×256 lattice. We can see from the figure that, the relative orientations $\lambda_i \cos(\theta_i)$ fall on two vertical lines. One correponds to negative z-projection and the other with a positive projection.

By expanding the dipole terms, $P^{x,y}_{A_j,B_j}$, we obtain the mean-field expression completely expressed in terms of spins which the i^{th} spin is interacting with,

$$\begin{aligned} h^z[S^z_i, n] &= \sum_{\square\in i}\left(\frac{J_0}{4s^3}S^z_{i_1}S^z_{i_2}S^z_{i_3} + \frac{J_1}{2s}S^z_{i_2}\right) + \frac{J_2}{8s}\Big((S^z_{i_5} - S^z_i) + (S^z_{i_{11}} - S^z_{i_{13}}) + \\ &\quad (S^z_{i_2} - S^z_{i_{22}}) + (S^z_{i_{36}} - S^z_{i_{34}}) - (S^z_{l_5} - S^z_l) - (S^z_{l_{11}} - S^z_{l_{13}}) - (S^z_{l_2} - S^z_{l_{22}}) - \\ &\quad (S^z_{l_{36}} - S^z_{l_{34}})\Big), \qquad (2.10) \\ h^x[S^x_i, n] &= -K. \qquad (2.11) \end{aligned}$$

Where i_α's indices correspond to the neighboring spins which the i^{th} spin is interacting with. In practice, one first performs the spin projection along z and x and then followed by the energy minimization by reorienting these projections angles (θ_i's) along the fields $h^{x,z}$. One may have to be also extra cautious in determining these mean-field equations as any given spin is linked to two different subplaquettes A, B. Indeed, the summation in the first term within the brackets is performed over these two subplaquettes for which the given spin (i) belongs to. The local fields, $h^{x,z}$ and the spin components satisfy the usual normalized relations, $h_i = [(h^z_i)^2 + (h^x_i)^2)]^{0.5}$, $S_i = [(S^z_i)^2 + (S^x_i)^2]^{0.5}$

such that the total energy of the system now is simply given by the innerproduct,

$$E[S_i, n] = \sum_i \vec{h}_i \cdot \vec{S}_i. \tag{2.12}$$

with the decomposition, the energy (2.10) can be represented by $E[S_i^{\alpha}, n] = \sum_i h_i^{\alpha} S_i^{\alpha}$. However, In terms of the dipole-dipole terms $P^{x,y}$ the same Eq. (2.10) can be rearranged as,

$$h^z[S_i^z, n] \;=\; \sum_{\square \in i} \left(\frac{-J_0}{4s^3} S_{i_1}^z S_{i_2}^z S_{i_3}^z + \frac{J_1}{2s} S_{i_2}^z \right) - \frac{J_2}{4s} \sum_{j=1}^{4} \left(P_{B_j}^x + P_{B_j}^y + P_{A_j}^x + P_{A_j}^y \right). \tag{2.13}$$

It is to be noted that due to the existence of different modes of polarization, for example, x, y, we, therefore, have two inequivalent links, that is, the spins located on the horizontal and vertical links respectively. The equations given so far are valid for spins on the horizontal links, with a slight variation the similar equation for the spins on vertical links are given as,

$$h^z[S_i^z, n] \;=\; \sum_{\square \in i} \left(\frac{J_0}{4s^3} S_{i_1}^z S_{i_2}^z S_{i_3}^z + \frac{J_1}{2s} S_{i_2}^z \right) + \frac{J_2}{4s} \sum_{j=1}^{4} \left(P_{B_j}^y + P_{A_j}^x - P_{B_j}^x - P_{A_j}^y \right). \tag{2.14}$$

Now, to proceed further one has to minimize the energy $E[S_i, n]$, generally, this is done by reorienting these spins along these fields $h^{x,z}$. The flowchart describing the method is shown in Fig. 2.3. Next, we solve these equations on a parallel environment using openMP for system sizes ($L_x = 64, 96, 128, 256$). The basis states were obtained for various K-values, following which the quantities of interest like groundstate energy is obtained. In the next section, we discuss in detail the groundstates obtained from our analysis. Later, based on the arguments of the mean-field ansatz we extend our analysis to conclude true quantum groundstates for the model without dipole-dipole interaction, $J_2 = 0$ and for nearly zero magnetic field strength K. These are particularly important because this enables the use of gauge-transformation that connects various degenerate groundstates of the Hamiltonian.

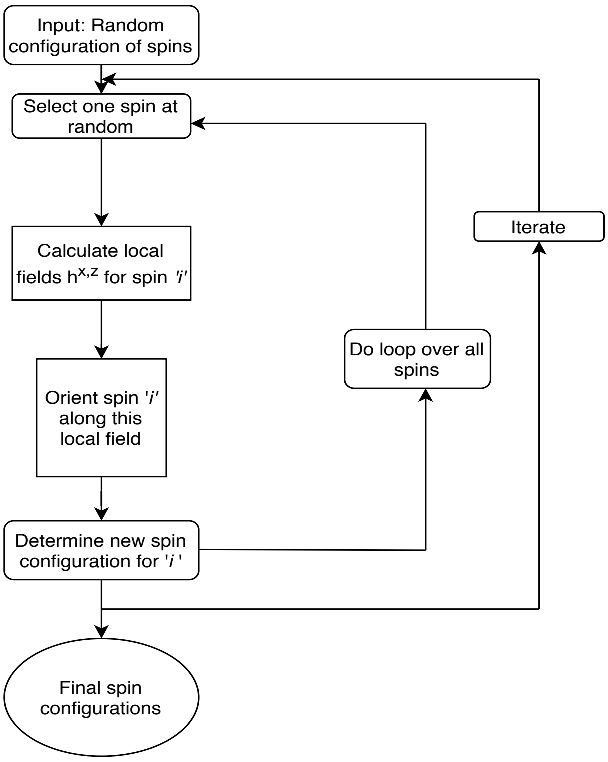

Figure 2.3: Flowchart showing the conceptual implementation of mean-field method on a computer.

2.2.1 Groundstates

The groundstate energy is strictly characterized by the parameter θ_i, the classical spin projection angle. From the above mean-field analysis an affirmation of the groundstates is confirmed and in conjunction with the arguments based on the Lagrange multiplier method, the groundstate for the Hamiltonian, in general, can be represented by a dimer form as,

$$\vec{S}_i = S(\lambda_i \cos\theta \mathbf{e_z} + \sin\theta \mathbf{e_x}), \tag{2.15}$$

Where λ_i could be ± 1 in tune with the groundstate configurations of H_0 for $K = 0$. We do not consider a component along s_y due to the classical nature of spins where the interactions are only given in terms of z with no y-component interactions. This argument is valid only in the classical case. The value of θ depends on K, J_1, and J_2. For $K = 0$, we have $\theta = 0$. This θ takes the role of our order parameter. From the mean-field ansatz represented by Eq. (2.10), the groundstate energy of

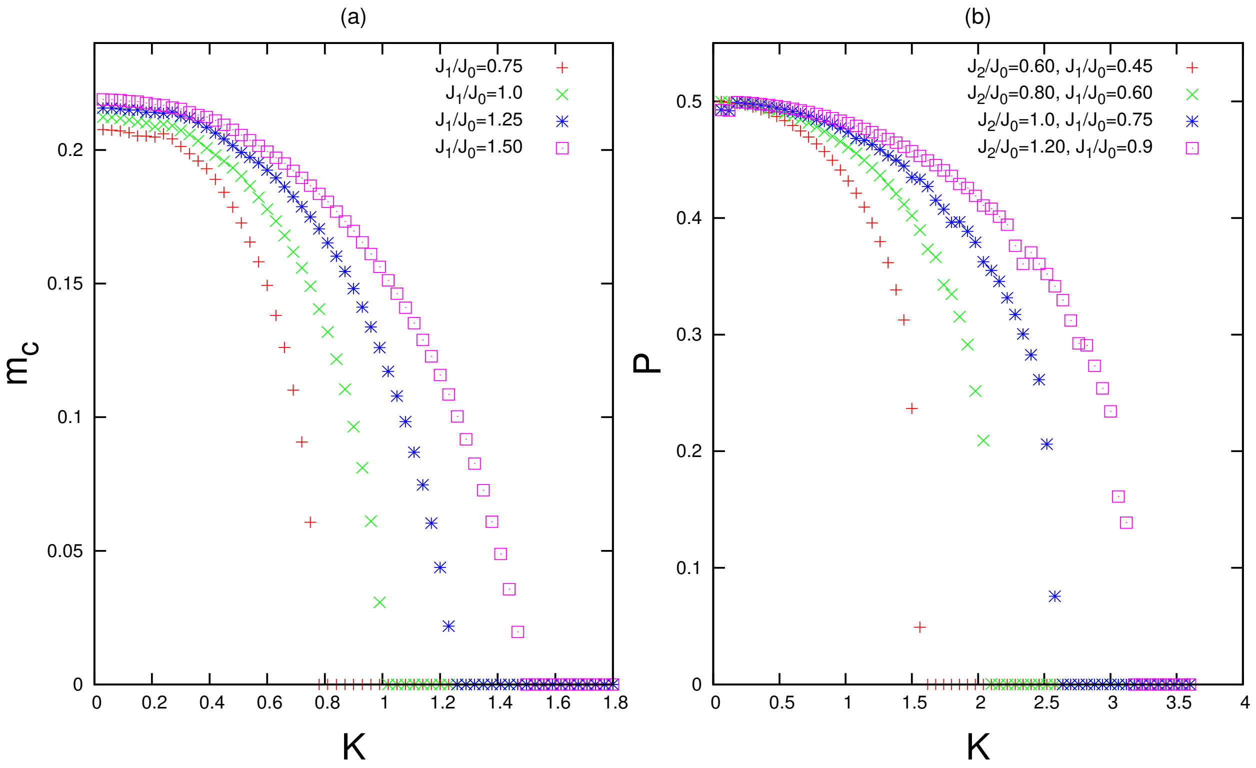

Figure 2.4: Variation of the parameters, that is, staggered magnetization per site m_c (Left) and polarization moment P (Right) per plaquette as a function of magnetic field K is shown for different parameter regimes and for multiple relative strengths of J_1 and J_2. a) m_c is calculated for the case where $J_2 = 0$ and b) polarization for $J_2 \neq 0$. The system size used for this computation is 96×96.

the system can be written as follows:

$$E_{cl} = -\frac{1}{2} J_0 S^4 N \cos^4\theta - J_1 S^2 N \cos^2\theta - KSN \sin\theta - 2J_2 S^2 N \cos^2\theta. \tag{2.16}$$

Minimizing E_{cl} with respect to θ, we obtain θ_C. This groundstate energy has been compared with the $E_x = -KN$, which denotes the energy corresponding to the state where all spins are aligned along x-direction. For a given J_0, J_1, J_2, there exists a K_c such that if $K \leq K_c$ then $E_{cl} < E_x(\theta_C)$ with $\theta_C \leq \pi/2$. Fig. 2.5 shows the numerically obtained values of θ_C in $K - J_1$ plane for various values of J_2. As evident from Fig. 2.5, the value of K_c linearly increases with J_1, which is expected. As one increases the values of J_2, K_c further takes higher values.

To consolidate our results we also estimate the quantities which may be thought of as order parameters in the classical system that are used to distinguish the paraelectric phase from that of the long range-ordered phase. But here the bigger motive is to see the effect of the role of absolute values

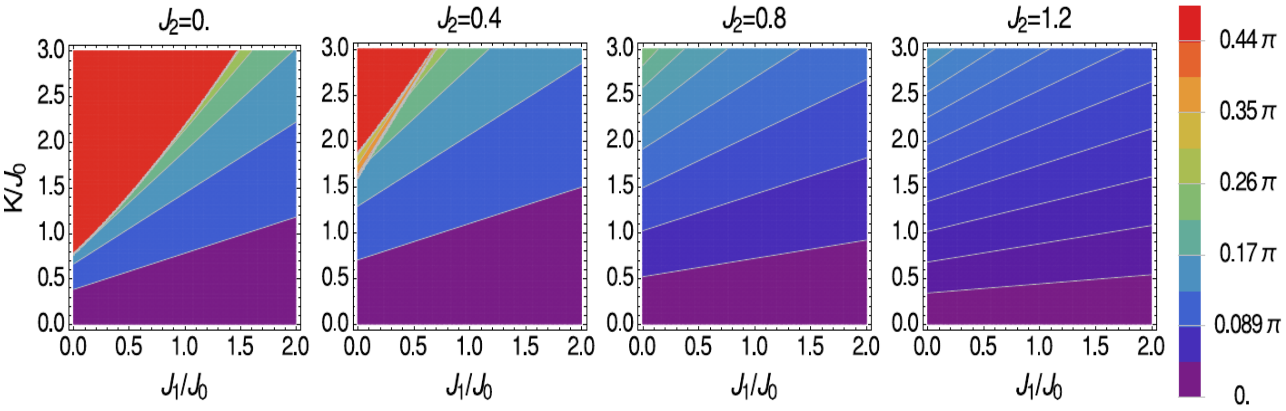

Figure 2.5: Contour plot of θ_C in the $K - J_1$ plane for various values of J_2. The red region denotes an ordered phase where all the spins align in x-direction. Various other shaded regions (except red) denote a disordered phase where the z components of spins are disordered.

of J_1, J_2 on K_c. The expression for staggered magnetization is $m_c = \frac{1}{N_s}\sum_i(-1)^i S_i^z$. Similarly, for $P = \frac{2}{N_s}\sum_i(-1)^i P_i^x$. From the Fig. 2.4(a), we can observe that the variation of m_c is continuous and the spacing of K_c for $J_1/J_0 = 0.75$ to 1.0 is the same as that of the values 1.25 and 1.5. Similar behaviour can be seen for polarization as shown in Fig. 2.4(b) in the finite dipole-dipole coupling case for $J_2/J_0 = 0.60, J_1/J_0 = 0.45$, $J_2/J_0 = 0.80, J_1/J_0 = 0.60$, $J_2/J_0 = 1.0, J_1/J_0 = 0.75$, $J_2/J_0 = 1.20, J_1/J_0 = 0.9$.

Let us summarize our results for classical groundstate configurations. For all the parameter values, there is a θ_C for $K \leq K_c$ that defines the groundstate configurations according to Eq. (2.16). The groundstate has finite degeneracy in the presence of J_0, J_1. For $J_1 = J_2 = 0$, the degeneracy is $2^{N_x N_y + 1}$ and for $J_2 = 0$, the degeneracy is $2^{N_x + N_y}$. For both J_1 and J_2 nonzero, the degeneracy is reduced to four as described in Fig. 2.8. For large $K > K_c$, all the spins get aligned along the x-axis corresponding to $\theta_C = \pi/2$. Now we are in a position to discuss the relative stability of the groundstate spin configurations against the quantum fluctuation as prescribed by the linear spin-wave theory. Our specific interest is to search for a possible order-disorder driven lifting of groundstate degeneracy in the absence of dipole-dipole interaction. In the presence of dipole-dipole interaction, we are interested to find the nature of low-lying excitations as the manifestation of competing ferromagnetic and antiferromagnetic ordering in orthogonal direction for various values of the external field.

2.3 Gauge Symmetry and degeneracy

In this section, we elaborately discuss the groundstate degeneracy counting due to the first term of the Hamiltonian given in Eq. (2.1). There are eight groundstate configurations for a single plaquette term among the possible sixteen states. However, once we start filling the neighboring plaquettes, it imposes constraints on the number of possible states for a given plaquette. However, a complete understanding of such enumeration is possible in this case. To give proof, for simplicity, we first consider a 4×4 system with periodic boundary conditions in both directions and show explicitly that the groundstate degeneracy is $2^{4\times4+1}$. In Fig. 2.6 we have shown counting of the groundstate degeneracy for a 4×4 system in two different ways of satisfying the groundstate configuration for each plaquette. On the left, we start the counting from the extreme left down the corner and proceed toward the right toward the down right corner. The number of ways in which a given plaquette can be filled to comply with the groundstate constraint is mentioned inside the plaquette itself. Next, we move one row up and again start from the extreme left plaquette. This procedure is repeated until all the plaquettes are filled up according to the groundstate constraint. The total number of states is $X=2^{17}$. On the right, we show another way of counting and reaching the same number as explained in the caption of Fig. 2.6. We mention that to count the number of ways in which a given plaquette can be filled up (once its neighboring plaquettes are already filled up), we need to take into account the following observations.

1. If for a given plaquette, all the spins are available, there are eight possible ways to fill that plaquette.
2. If one spin of a given plaquette is already determined, then only four possible ways are left.
3. If two spins of a given plaquette are already determined, only two choices are left.
4. If three sides of a given plaquette are determined, only one choice is left.

If we denote by $S_{i,j}$ the number of ways a given plaquette (i,j) can be filled up, then we have for the above procedure:

$$S_{1,1} = 8,\ S_{j,1} = 4(1 < j < N_x),\ S_{N_x,1} = 2, \tag{2.17}$$

$$S_{j,2} = 4(1 < j < N_y), \tag{2.18}$$

$$S_{i,j} = 2(1 < i(j) < N_x(N_y)), \tag{2.19}$$

$$S_{1,N_y} = 2,\ S_{i,N_y} = 1(1 < i \leq N_x). \tag{2.20}$$

The total degeneracy $\mathcal{D}$ could be found by the product of all $S_{i,j}$. A straightforward calculation yields $\mathcal{D} = 2 \times 2^{N_x+N_y}$. We notice that this estimation does not depend upon the thermodynamic limit and is valid for any small system with periodic boundary conditions. In the right panel of Fig. 2.6, we showed a different way of filling up states in a 4×4 square lattice. We start filling diagonally from right to left. The blue numerals show the sequences of filling up the plaquette terms and the black numerals show the number of ways one can fill up a given plaquette. The plaquettes with no numerals are automatically filled up to their neighboring plaquettes. It is very easy to find an explicit expression for this way of counting as given in Eq. (2.17) to Eq. (2.20) and we leave it as an exercise to the interested reader. It may be noted that this way of counting fails to yield the groundstate degeneracy for ice-rule configurations as, without all up or down spin configurations, there is an unequal number of choices once two sides of a given plaquette are filled up. The existence of $2^{N_xN_y+1}$ number of degenerate states can be easily understood by the presence of the many conserved quantities which form a closed group $\mathcal{G}$. The members of the group are constructed as follows. At each vertex of a square lattice, one can define a quantity $\mathcal{A}_i = \prod \sigma_j^x$, where the index "j" runs through the four links connected to that vertex "i". One can check that any $\mathcal{A}_i$ and any arbitrary product of any number of $\mathcal{A}_i$ commutes with the J_0 term in the Hamiltonian. However, due to the constraint $\prod \mathcal{A}_i$, all the $\mathcal{A}_i$'s are not independent. This leaves us a total of $\sum_m {}^{(N_xN_y-1)}C_m = 2^{N_xN_y-1}$ independent group elements.

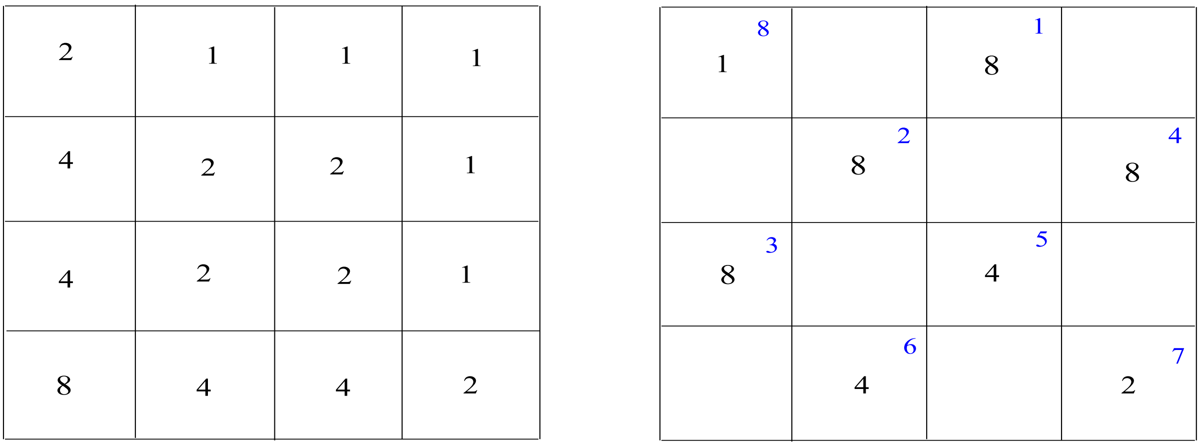

2	1	1	1
4	2	2	1
4	2	2	1
8	4	4	2

8 1		1 8	
	2 8		4 8
3 8		5 4	
	6 4		7 2

Figure 2.6: On the top left, we have shown the number of ways a given plaquette for a 4×4 square lattice can be filled up to satisfy the groundstate constraint. (Right) We have shown a different way of counting as explained in the text.

Apart from this, two independent global Wilson loop operators commute with the above-mentioned group element. They are called $\Gamma_h = \prod \sigma^y_{h_i}$ and $\Gamma_\nu = \prod \sigma^y_{\nu_i}$. Here, h_i runs over all the vertical links along x-direction. The vertical links are chosen from the opposite sides of squares of a given row. Similarly, v_i runs over all the horizontal links along y-direction. As before, the horizontal links are chosen from the opposite sides of squares of a given column. Though there are N_x and N_y number of horizontal and vertical lines, only one on each of these lines in a given direction yields an independent group element. Taking into these two global conserved quantities, we end up with a total number of $2^{N_x N_y + 1}$ conserve quantities.

Similarly, one can calculate degeneracy for finite J_1 but with $J_2 = 0$. One can easily find the rules for the number of ways a plaquette can be filled up. The rules for counting the number of ways a given plaquette can be filled in is the following. For example, if all the sides of a square are available, then it can be filled up in four ways. Once a given side of a plaquette is determined, there are only two choices left to be filled up. If the two adjacent sides of the square are filled up, then only one choice is available, however, if the opposite sides of the square are filled in, there exist two choices. One can easily find that [by having similar Eq. (2.17) to Eq. (2.20)] the degeneracy for finite J_1 is $2^{N_x + N_y}$. The fact that there exists a $2^{N_x + N_y}$ number of degenerate states in the presence of J_1 can be understood by similar consideration of conserved quantities in the presence of only the J_0 term. $\mathcal{A}_i$'s no longer remain conserved in the presence of J_1 term, however, Γ_h and Γ_ν remain conserved. Apart from this, $\Gamma_{h/\nu}$, constructed parallel to the horizontal or vertical direction becomes independent thus making it a total of $2^{N_x+N_y}$ conserved quantities. This explains the degeneracy of $2^{N_x+N_y}$.

2.4 Spin-wave excitations

We notice that, in general, spins are quantized in an arbitrary direction (as evident from classical analysis), which we call the local axis represented by x'/z'. The global axis will be represented by x/y. Any spin has the following decomposition:

$$\vec{S}_r = \mathbf{e}_x S_r^x + \mathbf{e}_z S_r^z. \tag{2.21}$$

Here, the index "r" indicates the position of a given site. Now, we perform an orthogonal coordinate transformation (from x, y, z to x', y', z') around y axis such that one axis of the new coordinate system gets aligned along the local moment direction at every site:

$$\begin{aligned} S_r^x &= S_r^{x'} \cos \lambda_i \theta_C - S_r^{z'} \sin \lambda_i \theta_C, & (2.22) \\ S_r^z &= S_r^{x'} \sin \lambda_i \theta_C + S_r^{z'} \cos \lambda_i \theta_C. & (2.23) \end{aligned}$$

The expressions for $S'_{x/z}$ in terms of the bosonic operators are given below:

$$S_r^{x'} = s - a_r^\dagger a_r, \;\; S_r^{z'} = \sqrt{s/2}(a_r^\dagger + a_r). \tag{2.24}$$

We have specifically chosen the above representation as our interest is to investigate the phase boundary where the spins align mostly along x-direction, where $\mathbf{a}_\mathbf{r}^\dagger$ and $\mathbf{a}_\mathbf{r}$ represent the creation and annihilation operators of a magnon at site r.

2.4.1 High-field limit, $K \gg J_0, J_1, J_2$ & $\theta_0 = \pi/2$

The groundstate in this limit is a trivial one with all the spins pointing towards the x. To obtain the magnon-spectrum and to check the stability of the classical groundstates, the Holstein-primakoff transformation (2.24) is substituted into the Hamiltonian 2.1 with the groundstate (all oriented along x-direction) now being explicitly embedded into it. The Hamiltonian now reads as,

$$\begin{aligned}
\mathcal{H}_{sw} \;=\; & \sum_{\square} \Big[- J_0 \sqrt{s/2}^4 \big[\left(a_i^\dagger + a_i\right) \left(a_{i_1}^\dagger + a_{i_1}\right) \left(a_{i_2}^\dagger + a_{i_2}\right) \left(a_{i_3}^\dagger + a_{i_3}\right) \big] \\
& + J_1 \sqrt{s/2}^2 \big[\left(a_i^\dagger + a_i\right) \left(a_{i_1}^\dagger + a_{i_1}\right) + \left(a_{i_2}^\dagger + a_{i_2}\right) \left(a_{i_3}^\dagger + a_{i_3}\right) \big] \Big] \qquad (2.25) \\
& - \frac{J_2}{16} \sum_{\langle AB \rangle} \sqrt{s/2}^2 \Big[((a_i + a_i^\dagger) + (a_{i_1} + a_{i_1}^\dagger) - (a_{i_2} + a_{i_2}^\dagger) - (a_{i_3} + a_{i_3}^\dagger))_A \\
& \times ((a_i + a_i^\dagger) + (a_{i_3} + a_{i_3}^\dagger) - (a_{i_2} + a_{i_2}^\dagger) - (a_{i_1} + a_{i_1}^\dagger))_B \Big] - K \sum_i (s - a_i^\dagger a_i). \\
& \qquad (2.26)
\end{aligned}$$

Expanding the above Eq. (2.25), we get,

$$\begin{aligned}
\mathcal{H}_{sw} \;=\; & \sum_i \Big[- J_0 \sqrt{s/2}^4 \big[(a_{i_1} a_{i_2} a_{i_3} a_i^\dagger + a_i a_{i_2} a_{i_3} a_{i_1}^\dagger + a_{i_2} a_{i_3} a_i^\dagger a_{i_1}^\dagger \\
& + a_i a_{i_1} a_{i_3} a_{i_2}^\dagger + a_{i_1} a_{i_3} a_i^\dagger a_{i_2}^\dagger + a_i a_{i_3} a_{i_1}^\dagger a_{i_2}^\dagger + \\
& a_{i_3} a_i^\dagger a_{i_1}^\dagger a_{i_2}^\dagger + a_i a_{i_1} a_{i_2} a_{i_3}^\dagger + a_{i_1} a_{i_2} a_i^\dagger a_{i_3}^\dagger + a_i a_{i_2} a_{i_1}^\dagger a_{i_3}^\dagger \\
& + a_{i_2} a_i^\dagger a_{i_1}^\dagger a_{i_3}^\dagger + a_i a_{i_1} a_{i_2}^\dagger a_{i_3}^\dagger + a_{i_1} a_i^\dagger a_{i_2}^\dagger a_{i_3}^\dagger \\
& + a_i a_{i_1}^\dagger a_{i_2}^\dagger a_{i_3}^\dagger + a_i^\dagger a_{i_1}^\dagger a_{i_2}^\dagger a_{i_3}^\dagger + a_i a_{i_1} a_{i_2} a_{i_3}) \big] \Big] \\
& + J_1 \sum_i \left(\sqrt{s/2}^2 a_{i_1} a_i^\dagger + a_i a_{i_1}^\dagger + a_i^\dagger a_{i_1}^\dagger + a_{i_3} a_{i_2}^\dagger + a_{i_2} a_{i_3}^\dagger + a_{i_2}^\dagger a_{i_3}^\dagger + a_i a_{i_1} + a_{i_2} a_{i_3} \right) \\
& - \frac{J_2}{16} \sum_{\langle AB \rangle} \sqrt{s/2}^2 \Big[((a_i + a_i^\dagger) + (a_{i_1} + a_{i_1}^\dagger) - (a_{i_2} + a_{i_2}^\dagger) - (a_{i_3} + a_{i_3}^\dagger))_A \\
& \times ((a_i + a_i^\dagger) + (a_{i_3} + a_{i_3}^\dagger) - (a_{i_2} + a_{i_2}^\dagger) - (a_{i_1} + a_{i_1}^\dagger))_B \Big] - K \sum_i (s - a_i^\dagger a_i), \qquad (2.27)
\end{aligned}$$

where the braces in the J_2 term, $()_{A(B)}$, denotes the four links/indices on plaquettes $A(B)$ as defined by the polarization $P^{x(y)}_{A(B)}$. At this point, one may either mean-field decompose the four-body interaction term (for example, $a_i a_j a^\dagger_k a_l$) into the following two: $\langle a_i a_j\rangle a^\dagger_k a_l + a_i a_j \langle a^\dagger_k a_l\rangle - \langle a_i a_j\rangle\langle a^\dagger_k a_l\rangle + \cdots +$ all possible decompositions, however, here we only consider the bilinear terms and do not pursue the other direction. With the virtue of that, clearly the J_0 accounts to all four-body interaction terms. And in the linear spin-wave theory approximation, the J_0 terms clearly does not enter into the calculations of the stability of ground state in the high-field limit. Therefore, in this limit, the J_0 term can be regarded as secondary interaction. The Hamiltonian in this approximation scheme can be given as,

$$\begin{aligned}\mathcal{H}_{sw} &= \sum_i J_1 \sqrt{s/2}^2 (a_{i_1} a^\dagger_i + a_i a^\dagger_{i_1} + a^\dagger_i a^\dagger_{i_1} + a_{i_3} a^\dagger_{i_2} + a_{i_2} a^\dagger_{i_3} + a^\dagger_{i_2} a^\dagger_{i_3} + a_i a_{i_1} + a_{i_2} a_{i_3}) \\ &-\frac{J_2}{16} \sum_{\langle AB\rangle} \sqrt{s/2}^2 \Big[((a_i + a^\dagger_i) + (a_{i_1} + a^\dagger_{i_1}) - (a_{i_2} + a^\dagger_{i_2}) - (a_{i_3} + a^\dagger_{i_3}))_A \\ &\times((a_i + a^\dagger_i) + (a_{i_3} + a^\dagger_{i_3}) - (a_{i_2} + a^\dagger_{i_2}) - (a_{i_1} + a^\dagger_{i_1}))_B\Big] - K\sum_i (s - a^\dagger_i a_i).\end{aligned} \tag{2.28}$$

Next, since in the high-field case we see the translational invariance of the spin-configurations, we then can Fourier transform the a_i variables to a_k as $a_i = \frac{1}{N}\sum_{\vec{k}} a_{\vec{k}} \exp(-i\vec{k}\cdot\vec{r})$, substituting the transformed boson operators into the above equation yields a Hamiltonian of various orders in a. Within the linear regime we neglect the higher order terms beyond the order 2, that is, $\mathcal{O} \sim a_1 a^\dagger_2 a_3 a^\dagger_4, a_1 a^\dagger_2 a^\dagger_4, \cdots$. The Hamiltonian then is given by,

$$\begin{aligned}\mathcal{H}_{sw} &= \sum_i \sum_k J_1 \sqrt{s/2}^2 \Big(a_{i_1} a^\dagger_i e^{\mathrm{ik}\cdot r_{i_1} - \mathrm{ik}\cdot r_i} + a_i a^\dagger_{i_1} e^{\mathrm{ik}\cdot r_i - \mathrm{ik}\cdot r_{i_1}} + a^\dagger_i a^\dagger_{i_1} e^{-\mathrm{ik}\cdot r_i - \mathrm{ik}\cdot r_{i_1}} \\ &+ a_{i_3} a^\dagger_{i_2} e^{\mathrm{ik}\cdot r_{i_3} - \mathrm{ik}\cdot r_{i_2}} + a_{i_2} a^\dagger_{i_3} e^{\mathrm{ik}\cdot r_{i_2} - \mathrm{ik}\cdot r_{i_3}} \\ &+ a^\dagger_{i_2} a^\dagger_{i_3} e^{-\mathrm{ik}\cdot r_{i_2} - \mathrm{ik}\cdot r_{i_3}} + a_i a_{i_1} e^{\mathrm{ik}\cdot r_i + \mathrm{ik}\cdot r_{i_1}} + a_{i_2} a_{i_3} e^{\mathrm{ik}\cdot r_{i_2} + \mathrm{ik}\cdot r_{i_3}}\Big) \\ &-\frac{J_2}{16} \sum_{\langle AB\rangle} \sqrt{s/2}^2 a^\dagger_i e^{-\mathrm{ik}\cdot r_i} - a^\dagger_{i_1} e^{-\mathrm{ik}\cdot r_{i_1}} - a^\dagger_{i_2} e^{-\mathrm{ik}\cdot r_{i_2}} \\ &+ a^\dagger_{i_3} e^{-\mathrm{ik}\cdot r_{i_3}} + a_i e^{\mathrm{ik}\cdot r_i} - a_{i_1} e^{\mathrm{ik}\cdot r_{i_1}} - a_{i_2} e^{\mathrm{ik}\cdot r_{i_2}} + a_{i_3} e^{\mathrm{ik}\cdot r_{i_3}}.\end{aligned} \tag{2.29}$$

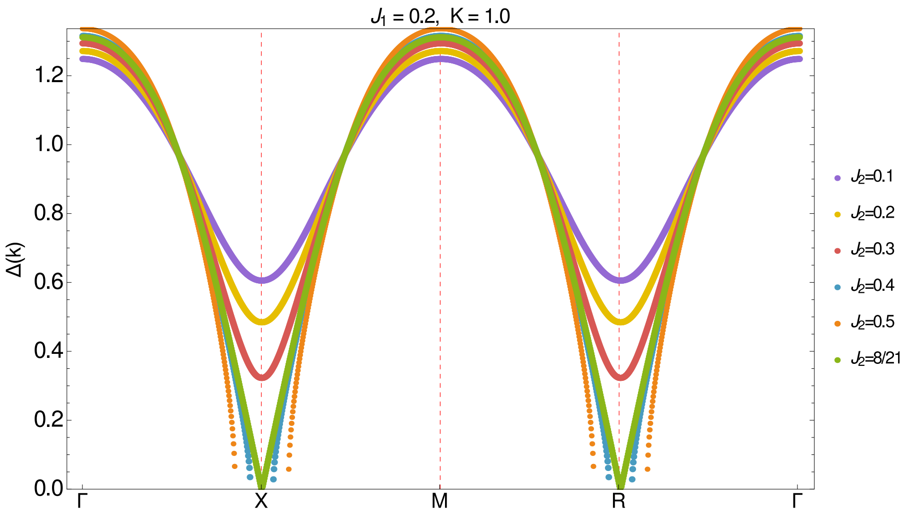

Figure 2.7: Plot showing the dispersion in the high-field case where quadratic behavior slowly converges to a linear behavior at the second-order critical line given by $K = 2sJ_1 + \frac{21}{8}sJ_2$. The various symmetry point used in the above figure is as follows: Γ = $(0, 0)$, X = $(\pi, 0)$, $M = (\pi, \pi)$, and $R = (0, \pi)$. The same convention applies to all plots used in this dissertation.

Using the identity $\sum\limits_i e^{i(k-q)\cdot r_i} = \delta_{k,q}$, the above Eq. (2.29) can be transformed to,

$$\mathcal{H}_{sw} = N\sum_k \left[\xi_k a_k a_k^\dagger + \frac{\gamma_k}{2}(a_k a_{-k} + a_{-k}^\dagger a_k^\dagger)\right] + C_0 + \mathcal{O}(a^3) + \mathcal{O}(a^4), \tag{2.30}$$

where $C_0 = KSN$ and is the classical energy upon which the first term has the information of the first excited state dispersion in k-space, and $\xi_k = \gamma_k + K - \frac{SJ_2}{8}$, and

$$\gamma_k = \frac{-s}{4}\left[J_2(2p_k^2 - 1) - 4(J_1 + J_2)p_k\right], \tag{2.31}$$

where $p_k = \cos(k_x + k_y)\cos(k_x - k_y)$. Now, the Hamiltonian is easily diagonalizable and upon doing that we obtain the eigen energies regarding the magnon spectra as given by,

$$E_k = \sqrt{\xi_k^2 - \gamma_k^2}. \tag{2.32}$$

In the Fig. 2.7 we show the spectrum plotted for parameters $J_1 = 0.2, K = 1.0$ and varying J_2 from 0.1 to 0.5. To qualitatively decipher the linearity seen in the dispersion curves obtained for

$J_2 = 8/21$ we expand the spectrum around the minima, that is, X (or R) high-symmetry point. We consider the following decomposition ($k_x = -\pi/2 + \delta_x, k_y = \pi/2 + \delta_y$). Replacing the following Eqs. (2.32) and expanding the terms γ_k, p_k. We obtain,

$$\begin{aligned} \xi_k &= -\frac{1}{2} J_2 s \cos^2(\delta_x - \delta_y) \cos^2(\delta_x + \delta_y) - J_1 s \cos(\delta_x - \delta_y) \cos(\delta_x + \delta_y) \\ &\quad - J_2 s \cos(\delta_x - \delta_y) \cos(\delta_x + \delta_y) + \frac{J_2 s}{4} + K - \frac{\mathrm{sJ}_2}{8}, \end{aligned} \tag{2.33}$$

similarly,

$$\begin{aligned} \gamma_k &= -\frac{1}{2} J_2 s \cos^2(\delta_x - \delta_y) \cos^2(\delta_x + \delta_y) - J_1 s \cos(\delta_x - \delta_y) \cos(\delta_x + \delta_y) \\ &\quad - J_2 s \cos(\delta_x - \delta_y) \cos(\delta_x + \delta_y) + \frac{J_2 s}{4}, \\ p_k &= -\cos(\delta_x - \delta_y) \cos(\delta_x + \delta_y), \end{aligned} \tag{2.34}$$

substituting the above equations into the spectrum (Eq. (2.32)),

$$\begin{aligned} E_{\delta_x,\delta_y} &= (-\frac{1}{4} s \left(J_2 \left(2\cos^2(\delta_x - \delta_y) \cos^2(\delta_x + \delta_y) - 1\right) + 4(J_1 + J_2) \cos(\delta_x - \delta_y) \cos(\delta_x + \delta_y)\right) \\ &\quad + K - \frac{\mathrm{sJ}_2}{8})^2 - \frac{1}{16} s^2 (J_2 \left(2\cos^2(\delta_x - \delta_y) \cos^2(\delta_x + \delta_y) - 1\right) \\ &\quad + 4(J_1 + J_2) \cos(\delta_x - \delta_y) \cos(\delta_x + \delta_y))^2. \end{aligned} \tag{2.35}$$

Since, δ_x, δ_y are small, therefore, $\cos(a) \approx 1 - a^2/2$ can be approximated. Substituting this approximation along with the smallness of δ (such that $\mathcal{O} \sim \delta^4$ are neglected) in the above equation and simplifying further yields,

$$E_{\delta_x,\delta_y} = \tilde{K}_1^{1/2} \sqrt{\tilde{K}_2 + 4(J_1 + 2J_2)|\delta_x^2 + \delta_y^2|^2}, \tag{2.36}$$

which can be simply rewritten as,

$$E_{\vec{\delta}} = \tilde{K}_1^{1/2}\sqrt{\tilde{K}_2 + 4(J_1 + 2J_2)|\vec{\delta}|^2}. \tag{2.37}$$

Here, $\tilde{K}_1 = K - \frac{sJ_2}{8}$, $\tilde{K}_2 = (K - 2sJ_1 - \frac{21}{8}sJ_2)$. With this Eq. (2.37) one can see that for all the values of $J_{1,2}, K$ the spectrum remains gapped with low-energy quadratic behavior in the dispersion curves except at the second-order transition point as obtained by $K_c = 2sJ_1 + 21/8J_2$. The spectrum at this point becomes linear and gapless, indicating a possibility to find the groundstate for higher J_2 which is the antiferroelectric case. This also shows that the transition for smaller values of J_2 the system behaves quite differently from the one with relatively higher values of J_2. This can be attributed to the fact that the gapped spectrum is implicative of the degeneracy in the groundstate manifold in the absence of dipole-dipole interaction J_2, with the excitations being gapped and discrete. When J_2 is increased and approaches the antiferroelectric ordered state, the spin-wave spectrum becomes linear and gapless as expected. And as one increases the value of J_2 further we see that the $\tilde{K}_2$ changes to negative in the sign where the spectrum becomes imaginary (2.37). The same can be deciphered from the Fig. 2.7 shown in dotted lines near the $X(R)$ high-symmetry points where there are no states available with the gap $\Delta(k)$ being undefined. It is to be noted that for sufficiently large J_2 one needs to perform the SW analysis on a different groundstate. In the next section, we calculate the SW spectrum in the low-field in the ordered ferroelectric case.

2.4.2 Low-field limit, $J_2 = 0$ & $J_1 \gg K$

The approach in this limit is different from that of the above analysis. This is due to the fact that for small fields and for $J_2 = 0$, the groundstate is exponentially degenerate. Since the translational invariance, in general, is lost we, therefore, employ a slightly variant approach away from the Fourier transform. We stick to the real space and perform the calculations based on the dynamic matrix formalism to check the stability of each degenerate groundstate explicitly. Whether or not the degeneracy

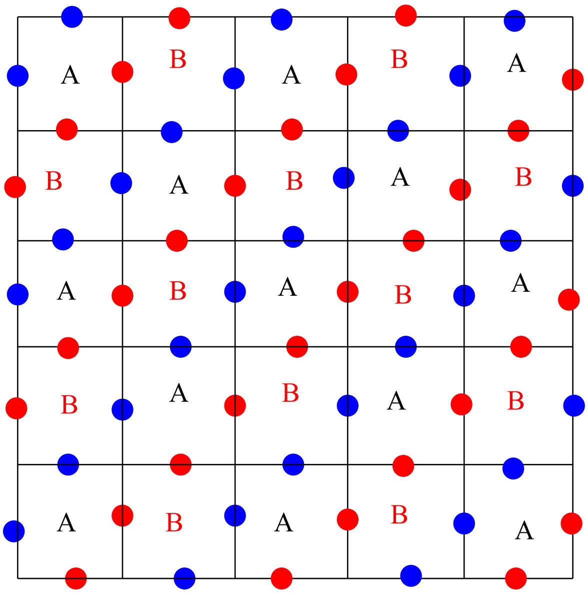

Figure 2.8: One of the four degenerate groundstates that exists for finite J_2 is shown in the above figure. The red dots represent up spins and the blue dots represent down spins. Taking the mid points of the lower left square as the origin, the position of up spins and down spins can be written as $\vec{\mathcal{R}}_{\text{up}} = -\tilde{\mathbf{e}}_{\mathbf{y}} + \mathbf{m_1}\tilde{\mathbf{a}} + \mathbf{n_1}\tilde{\mathbf{b}}$, $\vec{\mathcal{R}}_{\text{down}} = -\mathbf{e}_x + m_2\vec{a} + n_2\vec{b}$ where $\vec{a} = \mathbf{e}_x/2 - \mathbf{e}_y/2$, $b = -\mathbf{e}_x/2 + \mathbf{e}_y/2$. The second degenerate groundstate is obtained by up ↔ down transformation. The third and fourth groundstates could be obtained by rotating the spin configurations of first and second by $\pi/2$.

is being lifted at the linear order is a matter of importance as the higher orders may give a clue of the possible mechanism of the strong interactions of the quasi-particles in the low-energy scale. Moreover, the quantum order-disorder phenomenon is crucial in determining the physics of the Hamiltonian for the pure quantum version if the degeneracy is lifted. We note that this is also a case where the degenerate groundstate is a state with randomly oriented dipoles with each molecule/plaquette being oriented either along $\pm x$ or $\pm y$. The dynamic matrix is generally given by [109, 110],

$$i\frac{\partial\psi}{\partial t} = [\psi, \mathcal{H}] = \mathcal{D}\psi, \tag{2.38}$$

where the fields ψ is given by,

$$\psi^\dagger \equiv [a_1^\dagger \;\; a_2^\dagger \;\; \cdots a_N^\dagger \;\; a_1 \;\; a_2 \;\; \cdots a_N]. \tag{2.39}$$

From the Hamiltonian in Eq. (2.1) the above expression for dynamical matrix $\mathcal{D}$ can be found as,

$$\begin{aligned}
\mathcal{H}_{lf} \;=\; & \sum_i \frac{J_0 s^4}{4}\big(\cos^4(\theta)\lambda_i\lambda_{i_1}\lambda_{i_2}\lambda_{i_3}S^z_iS^z_{i_1}S^z_{i_2}S^z_{i_3} + \sin^4(\theta)S^x_iS^x_{i_1}S^x_{i_2}S^x_{i_3} + \sin(\theta)\cos^3(\theta)\lambda_i\lambda_{i_1}\lambda_{i_2}S^x_{i_3}S^z_iS^z_{i_1}S^z_{i_2} \\
& + \sin(\theta)\cos^3(\theta)\lambda_i\lambda_{i_1}\lambda_{i_3}S^x_{i_2}S^z_iS^z_{i_1}S^z_{i_3} + \sin(\theta)\cos^3(\theta)\lambda_i\lambda_{i_2}\lambda_{i_3}S^x_{i_1}S^z_iS^z_{i_2}S^z_{i_3} \\
& + \sin(\theta)\cos^3(\theta)\lambda_{i_1}\lambda_{i_2}\lambda_{i_3}S^x_iS^z_{i_1}S^z_{i_2}S^z_{i_3} \\
& + \sin^2(\theta)\cos^2(\theta)\lambda_i\lambda_{i_1}S^x_{i_2}S^x_{i_3}S^z_iS^z_{i_1} + \sin^2(\theta)\cos^2(\theta)\lambda_i\lambda_{i_2}S^x_{i_1}S^x_{i_3}S^z_iS^z_{i_2} \\
& + \sin^2(\theta)\cos^2(\theta)\lambda_{i_1}\lambda_{i_2}S^x_iS^x_{i_3}S^z_{i_1}S^z_{i_2} + \sin^2(\theta)\cos^2(\theta)\lambda_i\lambda_{i_3}S^x_{i_1}S^x_{i_2}S^z_iS^z_{i_3} \\
& + \sin^2(\theta)\cos^2(\theta)\lambda_{i_1}\lambda_{i_3}S^x_iS^x_{i_2}S^z_{i_1}S^z_{i_3} + \sin^2(\theta)\cos^2(\theta)\lambda_{i_2}\lambda_{i_3}S^x_iS^x_{i_1}S^z_{i_2}S^z_{i_3} \\
& + \sin^3(\theta)\cos(\theta)\lambda_iS^x_{i_1}S^x_{i_2}S^x_{i_3}S^z_i + \sin^3(\theta)\cos(\theta)\lambda_{i_1}S^x_iS^x_{i_2}S^x_{i_3}S^z_{i_1} \\
& + \sin^3(\theta)\cos(\theta)\lambda_{i_2}S^x_iS^x_{i_1}S^x_{i_3}S^z_{i_2} + \sin^3(\theta)\cos(\theta)\lambda_{i_3}S^x_iS^x_{i_1}S^x_{i_2}S^z_{i_3}\big) \\
& \sum_i \frac{J_1 s^2}{2}\big(\cos^2(\theta)\lambda_i\lambda_{i_2}S^z_iS^z_{i_2} + \cos^2(\theta)\lambda_{i_1}\lambda_{i_3}S^z_{i_1}S^z_{i_3} + \sin^2(\theta)S^x_iS^x_{i_2} + \sin^2(\theta)S^x_{i_1}S^x_{i_3} \\
& + \sin(\theta)\cos(\theta)\lambda_iS^x_{i_2}S^z_i + \sin(\theta)\cos(\theta)\lambda_{i_1}S^x_{i_3}S^z_{i_1} + \sin(\theta)\cos(\theta)\lambda_{i_2}S^x_iS^z_{i_2} + \sin(\theta)\cos(\theta)\lambda_{i_3}S^x_{i_1}S^z_{i_3}\big) \\
& + \sum_{i_{AB}} \frac{J_2 s}{16}\big(S^z_{i_A}S^z_{i_{B_i}}\lambda_{i_A}\lambda_{i_B}\cos^2(\theta) - S^z_{i_{A_1}}S^z_{i_{B_i}}\lambda_{i_B}\lambda_{i_{A_1}}\cos^2(\theta) - S^z_{i_{A_2}}S^z_{i_{B_i}}\lambda_{i_B}\lambda_{i_{A_2}}\cos^2(\theta) \\
& + S^z_{i_{A_3}}S^z_{i_{B_i}}\lambda_{i_B}\lambda_{i_{A_3}}\cos^2(\theta) - S^z_{i_A}S^z_{i_{B_1}}\lambda_{i_A}\lambda_{i_{B_1}}\cos^2(\theta) + S^z_{i_{A_1}}S^z_{i_{B_1}}\lambda_{i_{A_1}}\lambda_{i_{B_1}}\cos^2(\theta) \\
& + S^z_{i_{A_2}}S^z_{i_{B_1}}\lambda_{i_{A_2}}\lambda_{i_{B_1}}\cos^2(\theta) - S^z_{i_{A_3}}S^z_{i_{B_1}}\lambda_{i_{A_3}}\lambda_{i_{B_1}}\cos^2(\theta) \\
& - S^z_{i_A}S^z_{i_{B_2}}\lambda_{i_A}\lambda_{i_{B_2}}\cos^2(\theta) + S^z_{i_{A_1}}S^z_{i_{B_2}}\lambda_{i_{A_1}}\lambda_{i_{B_2}}\cos^2(\theta) \\
& + S^z_{i_{A_2}}S^z_{i_{B_2}}\lambda_{i_{A_2}}\lambda_{i_{B_2}}\cos^2(\theta) - S^z_{i_{A_3}}S^z_{i_{B_2}}\lambda_{i_{A_3}}\lambda_{i_{B_2}}\cos^2(\theta) \\
& + S^z_{i_A}S^z_{i_{B_3}}\lambda_{i_A}\lambda_{i_{B_3}}\cos^2(\theta) - S^z_{i_{A_1}}S^z_{i_{B_3}}\lambda_{i_{A_1}}\lambda_{i_{B_3}}\cos^2(\theta) - S^z_{i_{A_2}}S^z_{i_{B_3}}\lambda_{i_{A_2}}\lambda_{i_{B_3}}\cos^2(\theta) \\
& + S^z_{i_{A_3}}S^z_{i_{B_3}}\lambda_{i_{A_3}}\lambda_{i_{B_3}}\cos^2(\theta) - \sin(\theta)S^x_{i_{B_1}}S^z_{i_A}\lambda_{i_A}\cos(\theta) - \sin(\theta)S^x_{i_{B_2}}S^z_{i_A}\lambda_{i_A}\cos(\theta) \\
& + \sin(\theta)S^x_{i_{B_3}}S^z_{i_A}\lambda_{i_A}\cos(\theta) + \sin(\theta)S^x_{i_{B_i}}S^z_{i_A}\lambda_{i_A}\cos(\theta) + \sin(\theta)S^x_{i_A}S^z_{i_{B_i}}\lambda_{i_B}\cos(\theta) \\
& - \sin(\theta)S^x_{i_{A_1}}S^z_{i_{B_i}}\lambda_{i_B}\cos(\theta) - \sin(\theta)S^x_{i_{A_2}}S^z_{i_{B_i}}\lambda_{i_B}\cos(\theta) \\
& + \sin(\theta)S^x_{i_{A_3}}S^z_{i_{B_i}}\lambda_{i_B}\cos(\theta) + \sin(\theta)S^x_{i_{B_1}}S^z_{i_{A_1}}\lambda_{i_{A_1}}\cos(\theta) + \sin(\theta)S^x_{i_{B_2}}S^z_{i_{A_1}}\lambda_{i_{A_1}}\cos(\theta) \\
& - \sin(\theta)S^x_{i_{B_3}}S^z_{i_{A_1}}\lambda_{i_{A_1}}\cos(\theta) - \sin(\theta)S^x_{i_{B_i}}S^z_{i_{A_1}}\lambda_{i_{A_1}}\cos(\theta)
\end{aligned}$$

$$
\begin{aligned}
&+\sin(\theta)S^x_{iB_1}S^z_{iA_2}\lambda_{iA_2}\cos(\theta)+\sin(\theta)S^x_{iB_2}S^z_{iA_2}\lambda_{iA_2}\cos(\theta)\\
&-\sin(\theta)S^x_{iB_3}S^z_{iA_2}\lambda_{iA_2}\cos(\theta)-\sin(\theta)S^x_{iB_i}S^z_{iA_2}\lambda_{iA_2}\cos(\theta)-\sin(\theta)S^x_{iB_1}S^z_{iA_3}\lambda_{iA_3}\cos(\theta)\\
&-\sin(\theta)S^x_{iB_2}S^z_{iA_3}\lambda_{iA_3}\cos(\theta)+\sin(\theta)S^x_{iB_3}S^z_{iA_3}\lambda_{iA_3}\cos(\theta)\\
&+\sin(\theta)S^x_{iB_i}S^z_{iA_3}\lambda_{iA_3}\cos(\theta)\\
&-\sin(\theta)S^x_{iA}S^z_{iB_1}\lambda_{iB_1}\cos(\theta)+\sin(\theta)S^x_{iA_1}S^z_{iB_1}\lambda_{iB_1}\cos(\theta)+\sin(\theta)S^x_{iA_2}S^z_{iB_1}\lambda_{iB_1}\cos(\theta)\\
&-\sin(\theta)S^x_{iA_3}S^z_{iB_1}\lambda_{iB_1}\cos(\theta)-\sin(\theta)S^x_{iA}S^z_{iB_2}\lambda_{iB_2}\cos(\theta)+\sin(\theta)S^x_{iA_1}S^z_{iB_2}\lambda_{iB_2}\cos(\theta)\\
&+\sin(\theta)S^x_{iA_2}S^z_{iB_2}\lambda_{iB_2}\cos(\theta)-\sin(\theta)S^x_{iA_3}S^z_{iB_2}\lambda_{iB_2}\cos(\theta)\\
&+\sin(\theta)S^x_{iA}S^z_{iB_3}\lambda_{iB_3}\cos(\theta)-\sin(\theta)S^x_{iA_1}S^z_{iB_3}\lambda_{iB_3}\cos(\theta)-\sin(\theta)S^x_{iA_2}S^z_{iB_3}\lambda_{iB_3}\cos(\theta)\\
&+\sin(\theta)S^x_{iA_3}S^z_{iB_3}\lambda_{iB_3}\cos(\theta)-\sin^2(\theta)S^x_{iA}S^x_{iB_1}+\sin^2(\theta)S^x_{iA_1}S^x_{iB_1}+\\
&\sin^2(\theta)S^x_{iA_2}S^x_{iB_1}-\sin^2(\theta)S^x_{iA_3}S^x_{iB_1}-\sin^2(\theta)S^x_{iA}S^x_{iB_2}+\sin^2(\theta)S^x_{iA_1}S^x_{iB_2}\\
&+\sin^2(\theta)S^x_{iA_2}S^x_{iB_2}-\sin^2(\theta)S^x_{iA_3}S^x_{iB_2}+\sin^2(\theta)S^x_{iA}S^x_{iB_3}-\sin^2(\theta)S^x_{iA_1}S^x_{iB_3}\\
&-\sin^2(\theta)S^x_{iA_2}S^x_{iB_3}+\sin^2(\theta)S^x_{iA_3}S^x_{iB_3}+\sin^2(\theta)S^x_{iA}S^x_{iB_i}-\sin^2(\theta)S^x_{iA_1}S^x_{iB_i}\\
&-\sin^2(\theta)S^x_{iA_2}S^x_{iB_i}+\sin^2(\theta)S^x_{iA_3}S^x_{iB_i}\Big).
\end{aligned}
\tag{2.40}
$$

Here, we have rotated the local z-orientation of spins onto the global coordinate system $S^{x,z\prime}$ (see Eqs. (2.23)). For simplicity, we drop the symbol $\prime$ in the above Eq. (2.40). Now, we can transform the current Hamiltonian into a bosonic one using the HP transformation (see Eq. (2.24)). After performing this, we note that the Eq. (2.40) is too long to be given here, instead we give it in Appendix A. In the commutator given in Eq. (2.38) only those terms contribute which the bosonic operator (or the spin) is interacting with. Therefore, after performing the calculations by neglecting higher-order terms ($\mathcal{O} \sim aa^\dagger aa$) we obtain the simple relation for the elements of the dynamic matrix, $\mathcal{D}$ as,

$$
\mathcal{D}_{ii} = 2J_0 s^3\cos^4\theta + 2J_1 s\cos^2\theta + K\sin\theta, \tag{2.41}
$$

$$
\mathcal{D}_{ij} = -\lambda_i\lambda_j J_0\frac{s^3}{2}\sin^2\theta\cos^2\theta + \delta\frac{sJ_1}{2}\sin^2\theta, \tag{2.42}
$$

here the coefficients $\lambda_i^{\prime}s$ are the coefficients obtained from the mean-field analysis as given in Eq. (2.15). And $\delta = 1$ if i, j are associated to same plaquette and are either along one of the two orthogonal direction in the lattice spanned by n_1, n_2, else $\delta = 0$. Now, diagonalizing the dynamic matrix containing the information of the energies of the excited states, we obtain the gap equal to $0.4581(4)$ for $J_0 = 1$, $J_1 = 0.2$, $K = 0.2$, and $\theta = 0.06691(5)$, the value is very close to the one obtained from the spin-wave analysis done for the globally ordered ferroelectric groundstate (see Fig. 2.8). This is possible because the groundstates (groundstate) for $J_2 \neq 0$ are subsets of the groundstate for the case $J_2 = 0$ as detailed in Fig. 2.8. We explicitly check the same for all the degenerate groundstates on a 4×4 lattice. Our results showed the same value of gap for all the 256 ground states considered, indicating that there is no lifting of degeneracy upon switching on-field K. Precisely, the action of the symmetry operator inverses the signs of λ_i, consistent with the groundstate constraint that the spin-wave spectrum remains unchanged. A possible physical interpretation is that a coherent spin-flip or proton-tunneling process associated with each vertex of the plaquette. In a real system, this should correspond to a certain symmetry of the local potential profile created on the bonds associated with each vertex. One simple way to understand this is that as the potentials are not purely one dimensional (as viewed idealistically) but three dimensional, it creates a constraint that the motion of one proton affects the other coherently across the vertex of the effective lattice. However, to get an exact understanding, one needs to perform an ab initio study, which is beyond the scope of the present thesis. Though the above calculation is done for small values of the field and in the quadratic approximation, we think our results are valid in higher-order (for example, quadratic order) as suggested by the effective Hamiltonian formulation in Sec. 2.6.

2.4.3 Low-field case, $J_2 \neq 0$

Untill now we have performed SW calculations in high-field limit and to some extent in low-field for the degenerate case. Here, using the same HP transformation, we perform the same around the groundstates that are ordered antiferroelectrically along $\pm x$ or $\pm y$. As mentioned earlier one can represent the ferroelectric case as a case of ordered dimer configurations, the Hamiltonian after substituting Eqs. (2.24) into Eq. (2.1), we get,

$$\begin{aligned}
\mathcal{H}_{lf}^{ferro} &= \sum_{\square}\Big[-J_0 \times \\
&\quad ((\lambda_1 \cos\theta(s - a_1^\dagger a_1) + \sqrt{s/2}\sin\theta(a_1^\dagger + a_1))(\lambda_2 \cos\theta(s - a_2^\dagger a_2) + \sqrt{s/2}\sin\theta(a_2^\dagger + a_2)) \\
&\quad (\lambda_3 \cos\theta(s - a_3^\dagger a_3) + \sqrt{s/2}\sin\theta(a_3^\dagger + a_3))(\lambda_4 \cos\theta(s - a_4^\dagger a_4) + \sqrt{s/2}\sin\theta(a_4^\dagger + a_4)) + \\
&\quad J_1((\lambda_1 \cos\theta(s - a_1^\dagger a_1) + \sqrt{s/2}\sin\theta(a_1^\dagger + a_1))(\lambda_3 \cos\theta(s - a_3^\dagger a_3) + \sqrt{s/2}\sin\theta(a_3^\dagger + a_3)) \\
&\quad +(\lambda_2 \cos\theta(s - a_2^\dagger a_2) + \sqrt{s/2}\sin\theta(a_2^\dagger + a_2))(\lambda_4 \cos\theta(s - a_4^\dagger a_4) + \sqrt{s/2}\sin\theta(a_4^\dagger + a_4))\Big] - \\
&\quad \frac{J_2}{16}\sum_{\langle AB\rangle}\Big[\\
&\quad (\lambda_1 \cos\theta(s - a_1^\dagger a_1) + \sqrt{s/2}\sin\theta(a_1^\dagger + a_1)) + \lambda_2 \cos\theta(s - a_2^\dagger a_2) + \sqrt{s/2}\sin\theta(a_2^\dagger + a_2)) \\
&\quad -\lambda_3 \cos\theta(s - a_3^\dagger a_3) + \sqrt{s/2}\sin\theta(a_3^\dagger + a_3)) - \lambda_4 \cos\theta(s - a_4^\dagger a_4) + \sqrt{s/2}\sin\theta(a_4^\dagger + a_4))_A \\
&\quad \times(\lambda_1 \cos\theta(s - a_1^\dagger a_1) + \sqrt{s/2}\sin\theta(a_1^\dagger + a_1)) + \lambda_4 \cos\theta(s - a_4^\dagger a_4) + \sqrt{s/2}\sin\theta(a_4^\dagger + a_4)) \\
&\quad -\lambda_2 \cos\theta(s - a_2^\dagger a_2) + \sqrt{s/2}\sin\theta(a_2^\dagger + a_2)) - \lambda_3 \cos\theta(s - a_3^\dagger a_3) + \sqrt{s/2}\sin\theta(a_3^\dagger + a_3))_B\Big].
\end{aligned} \tag{2.43}$$

Since the antiferroelectric is a subset of groundstate for J_0, thus we see that $\lambda_1\lambda_2\lambda_3\lambda_4 = 1$, whereas the product involving two site λ's do vary depending upon which global drection the dipoles are pointing to. However, using the Fourier transform and considering only the terms upto quadratic level in a's, we get,

$$\begin{aligned}
\mathcal{H}_i &= N\sum_k\left[\varepsilon_k a_k^\dagger a_k + \frac{\tilde{\gamma}_{i,k}}{2}(a_k^\dagger\ \dagger_{-k} + a_k a_{-k})\right] \\
&\quad -\frac{1}{2}J_0 s^4 N\mathcal{C}_\theta^4 - (J_1 + 2J_2)s^2 N\mathcal{C}_\theta^2,
\end{aligned} \tag{2.44}$$

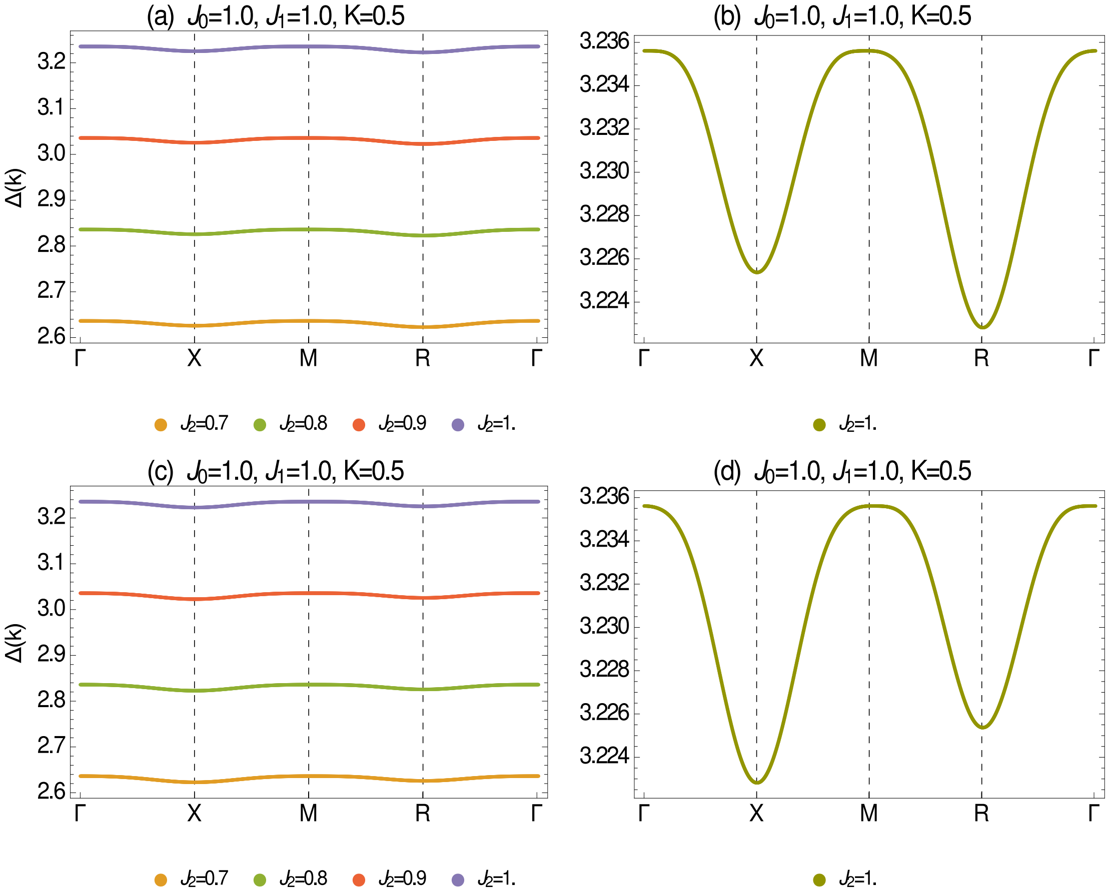

Figure 2.9: Spin-wave dispersion in the low-field limit of K in the ordered antiferroelectric phase. The upper right panel (b) shows the spectrum for the first and second degenerate ground states as mentioned in Fig. 2.8. Similarly, the lower right panel (c) shows the spectrum for the third and fourth groundstates. The upper (a) and lower left columns (d) show the variations of the spectrum for different values of J_2.

where ε_k and $\tilde{\gamma}_{i,k}$ are given by,

$$\varepsilon_k = \gamma_k + 2s^3 J_0 \mathcal{C}_\theta^4 + 2sJ_1 \mathcal{C}_\theta^2 - \frac{J_2 s}{s}\mathcal{S}_\theta^2, \tag{2.45}$$

$$\tilde{\gamma}_{i,k} = \mathcal{S}_\theta^2\big[\gamma_k + s^3 J_0 \mathcal{C}_\theta^2[2\chi_i q_k + p_k]. \tag{2.46}$$

Here, the index i in the Hamiltonian refers to four degenerate groundstates as described in Fig. 2.8. χ_i can take values 1(-1) for $i = 1, 2(3, 4)$, and the p_k is defined as in Eq. (2.34), $q_k = \sin k_x \sin k_y$, and the terms $\mathcal{C}_\theta$ and $\mathcal{S}_\theta$ stand for $\cos\theta$ and $\sin\theta$, respectively. Following the earlier analysis of expanding the gap around the minima, X, we find that the spectrum is gapped and quadratic for all values of K

and J_2, and the expression for the gap reads as,

$$\Delta_k = \zeta_0\sqrt{\zeta_1 + \zeta_2\rho^2}, \tag{2.47}$$

where,

$$\begin{aligned}
\zeta_0 &= 2s^3\left(J_0\mathcal{C}^4_{\theta_0} + \frac{\tilde{J}_{12}}{s^2}\mathcal{C}^2_{\theta_0} - \frac{J_2}{16s^2}\mathcal{S}^2_{\theta_0}\right)0.5, && (2.48)\\
\zeta_1 &= 2J_1\left(s\mathcal{C}^2_{\theta_0} - \frac{s}{2}\mathcal{S}^2_{\theta_0}\right) + 8s^3J_0\mathcal{C}^4_{\theta_0} \\
&\quad -(2\chi+1)\frac{s^3J_0}{2}\mathcal{C}^2_{\theta_0}\mathcal{S}^2_{\theta_0} - \frac{15s}{8}J_2\mathcal{S}^2_{\theta_0}, && (2.49)\\
\zeta_2 &= \frac{\mathcal{S}^2_{\theta_0}}{2}\left[4s(J_1+3J_2) + 2s^3\chi J_0\mathcal{C}^2_{\theta_0}\right]. && (2.50)
\end{aligned}$$

In the above $\tilde{J}_{12} = J_1 + 2J_2$, $\mathcal{C}^2_{\theta_0} = \cos\theta_0$, and $\mathcal{S}^2_{\theta_0} = \sin\theta_0$. Here the only relevant constant is ζ_1 which is to be solved numerically and simultaneously with the equation that minimizes the total energy given in Eq. (2.16). The results for few parameter values are shown in Fig. 2.9 where one finds the quadratic variation of dispersion. Also, the dispersion is asymmetric around M which shows that the low-energy bosonic excitation is directional. In the left of Fig. 2.9, the spectrum is plotted for different values of J_2 where the variation of it is seen to be equidistant as we vary J_2 uniformly. Contrasting to the results of the high-field limit is that the degeneracy of gap minimum found at X and R points is removed for small values of K. Thus the gap difference, $\Delta = \Delta_X - \Delta_R$, where Δ_X and Δ_X is the gap at X and R points respectively which are important quantities can be measured experimentally.

2.5 Dual mapping to Kitaev-model

In section 2.4.2, we have mentioned the absence of any quantum (field K) order-disorder phenomenon in the system. We saw that at least for few orders of magnetic field and within the realm of LSWT, the degeneracy is never lifted. Here, we show a connection to the findings and corroborate the same by mapping the present Hamiltonian (Eq. (1.3)) to the toric code model (TCM) [111] in the low-field limit $J_0 \gg K$ and $J_{1,2} = 0$. We use a simple perturbative approach and apply an additional magnetic field along the transverse direction y such that $k_y \ll J_0$. We show that the model can be mapped to the non-interacting anyon model. We switch from $S^{z/x}$ variable to $\sigma^{z/x}$ without any loss of generality:

$$\mathcal{H} = -J_0 \sum_{\square} \sigma_1^z \sigma_2^z \sigma_3^z \sigma_4^z - K_x \sum_i \sigma_i^x - K_y \sum_i \sigma_i^y. \tag{2.51}$$

Where K_x, K_y are the transverse fields and σ^α's are the Pauli matrices. Now, consider the following $SO(2)$ transformation: $\sigma_i^x = \cos\theta \sigma_i^{x'} - \sin\theta \sigma_i^{y'}$ and $\sigma_i^y = \sin\theta \sigma_i^{x'} + \cos\theta \sigma_i^{y'}$. Substituting these equations into the above Hamiltonian, the transverse field part of it gets transformed into:

$$-\sum_i \left(\sigma_i^{x'} [K_y \sin\theta + K_x \cos\theta] + \sigma_i^{y'} [K_x \sin\theta - K_y \cos\theta] \right). \tag{2.52}$$

Since, θ being a parameter of choice, we can let take any contour. Specifically, we choose the contour $\tan\theta = \frac{K_y}{K_x}$ such that the second term including the $\sigma_i^{y'}$ vanishes. The model then reduces to a simple transverse field model with the gauge term, and is given by,

$$\mathcal{H} = -J_0 \sum_{\square} \sigma_1^{z'} \sigma_2^{z'} \sigma_3^{z'} \sigma_4^{z'} - K_x' \sum_i \sigma_i^{x'}, \tag{2.53}$$

where $K_x' = K_x / \cos\theta$. We now use the standard perturbation theory to arrive at the first nontrivial correction at fourth order. The effective Hamiltonian at that order can be found by using the formula:

$$\mathcal{H}_{\text{eff}}^{(4)} = \mathcal{P}(\mathcal{H}_1 \mathcal{D})^3 \mathcal{H}_1 \mathcal{P}, \tag{2.54}$$

$$\mathcal{D} = -\frac{1-\mathcal{P}}{\mathcal{H}_0 - E_0}, \tag{2.55}$$

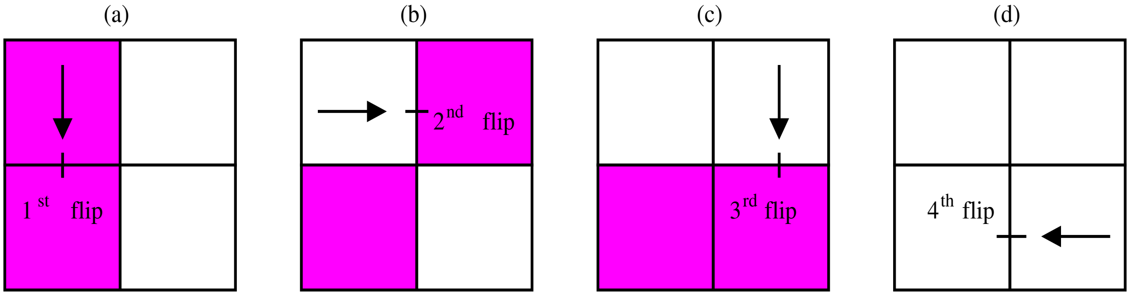

Figure 2.10: Schematic depiction of Eq. (2.57). The thick bar (−) denotes the action of σ_x operator on that site. The sequence of action of σ_i^x operators on the lattice as per the Eq. (2.62)

where, $P = \prod_{\Box} \frac{1}{2}(\mathbb{1} + \Box)$ is the groundstate projection operator, the symbol, $\Box$, represents the short-hand notation for the plaquette term, $\sigma_1^z\sigma_2^z\sigma_3^z\sigma_4^z$, that is, the elementary interaction on a unit square plaquette, and $\mathcal{H}_1$ is the perturbed Hamiltonian, here, the transverse field term. After expanding all the terms, we find,

$$
\begin{aligned}
\mathcal{H}_{\text{eff}}^{(4)} = & -\prod_{\Box}\frac{1}{2}(\mathbb{1}+\Box)\big(K_x\sum_i\sigma_i^x\big)\left(\frac{\mathbb{1}-\prod_{\Box}\frac{1}{2}(\mathbb{1}+\Box)}{H_0-E_0}\right)\big(K_x\sum_j\sigma_j^x\big)\left(\frac{\mathbb{1}-\prod_{\Box}\frac{1}{2}(\mathbb{1}+\Box)}{H_0-E_0}\right) \\
& \big(K_x\sum_k\sigma_k^x\big)\left(\frac{\mathbb{1}-\prod_{\Box}\frac{1}{2}(\mathbb{1}+\Box)}{H_0-E_0}\right)\big(K_x\sum_l\sigma_l^x\big)\prod_{\Box}\frac{1}{2}(\mathbb{1}+\Box).
\end{aligned}
\tag{2.56}
$$

Using the commutation relation $\{\sigma_i^x, \sigma_j^z\} = 2\delta_{ij}$, and moving the $\mathcal{P}$ operator to the right of the equation with the help of the Eq $\mathcal{P}\mathcal{D} = 0$, the only contributing term can be given by,

$$
\begin{aligned}
\mathcal{H}_{\text{eff}}^{(4)} = & -K_x^4\sum_{\{+\}}\sum_{+}\left[\sigma_\alpha^x\left(\frac{\mathbb{1}}{H_0-E_0}\right)\sigma_\beta^x\left(\frac{\mathbb{1}}{H_0-E_0}\right)\sigma_\gamma^x\left(\frac{\mathbb{1}}{H_0-E_0}\right)\right. \\
& \left.\times\sigma_\delta^x\prod_{\Box}\frac{1}{2}(\mathbb{1}+\Box)\right].
\end{aligned}
\tag{2.57}
$$

Where $\alpha, \beta, \gamma, \delta$ represent the indices of spins located on the four edges of a vertex $+$ (see Fig. 2.10). The indice $\{+\}$ sums over the terms one can arrive at the same effective Hamiltonian in 4! different ways at every site $+$. But this comes with different prefactor after the action of $(H_0 - E_0)^{-1}$ term, one such sequence is depicted in Fig. 2.10. One can also understand from the permutations and combinations coming from the rearrangement of σ_α^x, σ_β, σ_γ^x, σ_δ^x spins. Next, using the orthonormality relation $\langle n|m\rangle = \delta_{mn}$ and inserting the completeness relation, $\sum\limits_{n} |n\rangle\langle n)| = \mathbb{1}$ (where n is no. of quasi-particle (qp) excitations represented in second quantization notation in accord with pCUT) at appropriate locations, the equation simplifies to,

$$\begin{aligned}\mathcal{H}_{\text{eff}}^{(4)} &= -K_x^4 \sum_{\{+\}} \sum_{+} \Bigg[\sigma_\alpha^x \left(\frac{\mathbb{1}}{H_0 - E_0} \right) (\sum_p |p\rangle\langle p|) \sigma_\beta^x \left(\frac{\mathbb{1}}{H_0 - E_0} \right) \\ &\quad \times (\sum_q |q\rangle\langle q|) \sigma_\gamma^x \left(\frac{\mathbb{1}}{H_0 - E_0} \right) (\sum_r |r\rangle\langle r|) \sigma_\delta^x \Bigg[\prod_{\Box} \frac{1}{2}(\mathbb{1} + \Box) \Bigg] (\sum_s |s\rangle\langle s|) \Bigg]. \qquad (2.58)\end{aligned}$$

After the action of the $(H_0 - E_0)^{-1}$ operator on the n-qp number basis, we get,

$$\begin{aligned}\mathcal{H}_{\text{eff}}^{(4)} &= -K_x^4 \sum_{\{+\}} \sum_{+} \Bigg[\sigma_\alpha^x \left(\frac{\mathbb{1}}{H_0 - E_0} \right) \left(\sum_p |p\rangle\langle p| \right) \sigma_\beta^x \left(\frac{\mathbb{1}}{H_0 - E_0} \right) \\ &\quad \times \left(\sum_q |q\rangle\langle q| \right) \sigma_\gamma^x \left(\frac{\mathbb{1}}{H_0 - E_0} \right) \left(\sum_r |r\rangle\langle r| \right) \sigma_\delta^x |0\rangle\langle 0| \Bigg]. \qquad (2.59)\end{aligned}$$

Since, $\Bigg[\prod\limits_{\Box} \frac{1}{2}(\mathbb{1} + \Box) \Bigg] (\sum\limits_s |s\rangle\langle s|) = |0\rangle\langle 0|$, we get,

$$\begin{aligned}\mathcal{H}_{\text{eff}}^{(4)} &= -K_x^4 \sum_{\{+\}} \sum_{+} \Bigg[\sigma_\alpha^x \left(\sum_p \frac{\mathbb{1}}{E_p - E_0} |p\rangle\langle p| \right) \sigma_\beta^x \left(\sum_q \frac{\mathbb{1}}{E_q - E_0} |q\rangle\langle q| \right) \\ &\quad \times \sigma_\gamma^x \left(\sum_r \frac{\mathbb{1}}{E_r - E_0} |r\rangle\langle r| \right) \sigma_\delta^x |0\rangle\langle 0| \Bigg]. \qquad (2.60)\end{aligned}$$

Next, rearranging the scalars $\langle p|\sigma_\beta^x|q\rangle$, we get,

$$\mathcal{H}_{\text{eff}}^{(4)} = -K_x^4 \sum_{\{+\}} \sum_{+} \Bigg[\sigma_\alpha^x \left(\sum_{p,q,r} \frac{\langle p|\sigma_\beta^x|q\rangle}{E_p - E_0} \frac{\langle q|\sigma_\gamma^x|r\rangle}{E_q - E_0} \frac{\langle r|\sigma_\delta^x|0\rangle}{E_r - E_0} |p\rangle\langle 0| \Bigg]. \qquad (2.61)$$

Clearly, the two channels of non-zero contributing combination of the matrix elements is given by,

$$\langle p|\sigma_\beta^x|q\rangle\langle q|\sigma_\gamma^x|r\rangle\langle r|\sigma_\delta^x|0\rangle \quad \sim \quad \langle 2|\sigma_\beta^x|2\rangle\langle 2|\sigma_\gamma^x|2\rangle\langle 2|\sigma_\delta^x|0\rangle \text{ (channel 1)} \qquad (2.62)$$

$$\langle 2|\sigma^x_\beta|4\rangle\langle 4|\sigma^x_\gamma|2\rangle\langle 2|\sigma^x_\delta|0\rangle \text{ (channel 2)}. \tag{2.63}$$

One knows that the cost of creating two gauge charges can be given from all the 4! combinations as,

$$\sim 4\left[4\times\left(\frac{1}{2J_0 * 2J_0 * 2J_0}\right)+2\times\left(\frac{1}{2J_0 * 4J_0 * 2J_0}\right)\right]. \tag{2.64}$$

The outer prefactor '4' comes from the fact that the initial excitation can be created at any of the four sites. Within the brackets the prefactor of the first (second) are due to the four (two) different ways of creation and annihilation of excitations around the vertex, $+$, through channel 1(2) Eq. (2.62) respectively. The next step is very straightforward where the Eq. (2.66) can be effectively described as,

$$\mathcal{H}^{(4)}_{\text{eff}} = -\frac{5K_x^4}{16J_0^3}\sum_{+}\left[|0\rangle\langle 0|\left[\sigma^x_\alpha\sigma^x_\beta\sigma^x_\gamma\sigma^x_\delta\right]|0\rangle\langle 0|\right]. \tag{2.65}$$

Comparing with the standard theory of Brillouin-Wigner form, $PH^4_{\text{eff}}P$, we get the correction at the fourth order as,

$$\mathcal{H}^{(4)}_{\text{eff}} = -\frac{5K_x^4}{16J_0^3}\sum_{+}\left[\sigma^x_\alpha\sigma^x_\beta\sigma^x_\gamma\sigma^x_\delta\right]. \tag{2.66}$$

This proves the result and establishes the connection between lattice the model here and the toric code model. Note that the result for the Kitaev model differs from the present case where we get a coefficient of $1/16$ in the former case as opposed to $5/16$ in the latter.

2.6 Perturbative Continuous unitary transformations

Introduction

The Hamiltonian as represented by Eq. (1.3) and the following equations represent a quantum interacting spin system, which is not generally solvable exactly. Generally, one follows various analytical schemes depending on their interest in a specific aspect of the model or the suitability of the model to the method itself. For example, for a one-dimensional nearest-neighbor interacting spin system, the Jordan-Wigner transformation [112] is a very good starting point for analytical solutions. For two-dimensional and higher-dimensional systems, slave fermion/boson methods are applied in general, and often mean-field approximations are followed [113]. Though there are exceptions, for example, the Kitaev model [114, 115], which represents an exactly solvable model even in three dimensions [116]. As mentioned before, in this section, we use pCUT [117, 118, 119, 120, 121] (perturbative continuous unitary transformation) in our model whenever applicable. We are motivated by the fact that, unlike slave boson/fermion formalism, we do not have to use mean-field approximations, which often do not represent the true groundstates. On the other hand, few properties like the gap and one-particle spectrum can be calculated to a very high order of perturbations as shown in previous studies [111]. Another important aspect of pCUT is the sequential derivations of effective Hamiltonian at higher-order within a given particle sector. The prerequisite of applicability of pCUT is the equidistant spectrum, which we have in the limit $K \gg J_0, J_1, J_2$ where the groundstate is given by the spins aligned along the x axis and excitations are given by spin-flip excitations. We use pCUT to obtain an accurate measure of the one-particle gap and one-particle dispersion and compute the effective Hamiltonian up to reasonably high order. We compare our results of the gap with previous Monte Carlo studies [89] and find a very good comparison. Our one-particle dispersion should also be useful to verify the low-energy excitations beyond spin-wave approximations. Before we start the application of pCUT, we first map the spin- Hamiltonian as given in Eq. (1.1) onto the effective bosonic operator formalism. Since the groundstate in the high-field limit is where all the spins are aligned along x-axis, we, therefore, transform our global z-basis along with the groundstate orientation of spin as given in Eq. (2.23) (with θ_C replaced by $\pi/2$) and subsequently use Eq. (2.24). The resulting Hamiltonian has quadratic and as well as quartic interaction, which amounts to an interacting Hamiltonian. We aim to transform the resulting Hamiltonian to a unitarily equivalent Hamiltonian, H_{eff}, through a unitary transformation. Specifically, we follow Ref [121] where the block-band diagonality of the Hamiltonian is preserved with the choice of quasiparticle (QP) conserving infinitesimal generator $\eta(l)$ given by Wegner. We request the reader to follow the Ref. [117, 118, 119, 120, 121] for further pedagogical review.

Basics

As we are interested in the spectrum and the phase diagram that can be analyzed from the DLog-Pade analysis of one-particle gap, we, therefore, approach the same from the high-field limit. Since in this limit, the spectrum is trivially equidistant with magnonic excitations. The results are obtained up to order 6 beyond which as we will see problems persisting with RAM limit arise which thus limit our perturbative expansion.

The method of pCUT is based on the unitary transformation of Hamiltonian on a quasi-particle number basis as a low-energy effective field theory of a many-body system described by the quasi-particles. Insightful physics can be understood with the help of a quasi-particle picture, especially in the low-energy limit. Within the precision limits (of the 10^{-5}), one may approach the perturbative expansion of CUT's in the qp-basis where one benefits by performing the pCUT to higher orders. However, for very high precisions non-perturbative expansion seems to be an inevitable choice for a qualitative scenario. Here in the following section we introduce the pCUT method and discuss the main ideas and methodology shortly and rationally. Noticingly, for the current Hamiltonian (1.3) we will show that even order six is indeed sufficient to arrive at the qualitative results where we compare with the lower orders results systematically. Interested readers may refer to Ref. [122, 123, 124, 125, 126] for indepth discussions on pCUT.

We start with the basic notations useful for the discussions comprising quasi-particles states. Let Q be the quasi-particle number operator for the eigenbasis $\{|n\rangle\}$, while $n \in \mathbb{N}$ and $|n\rangle$ denotes an n-particle state:

$$Q|n\rangle = n|n\rangle. \tag{2.67}$$

With the above equation, we usually require the creation (or annihilation) operators $T_m = T^{\dagger}_{-m}$ (where $m \in \mathbb{N}$) that alters the local number of quasi-particles in a state by m:

$$T_m|n\rangle = \begin{cases} |n+m\rangle, & \text{for } m+n \geq 0, \\ 0, & \text{for } m+n < 0, \end{cases}$$

following which a very important correspondence can be drawn and given below as,

$$[Q, T_m] = mT_m, \tag{2.68}$$

this can be verified by acting the operators in the eigenbasis of Q. A more compact way of representing the T_m operators can be given by a compact k-tuple indice, $m_i \in \mathbb{Z}$ as given by,

$$\mathbf{m} = (m_1, m_2, m_3, ..., m_k), \tag{2.69}$$

$$|\mathbf{m}| = k, \tag{2.70}$$

$$M(\mathbf{m}) = \sum_{i=1}^{k} m_i. \tag{2.71}$$

Then the notation for $T(m)$ operators goes as follows:

$$T(m) \quad = \quad T_{m_1}T_{m_2}T_{m_3}...T_{m_k}. \tag{2.72}$$

Using this, the Eq. (2.68) can be generalized to:

$$[Q, T(m)] \quad = \quad \sum_{i=1}^{k} m_i T(\mathbf{m}) = \mathbf{M}(\mathbf{m})\mathbf{T}(\mathbf{m}). \tag{2.73}$$

2.6.1 Continuous unitary transformation

As far as the diagonalization method is concerned, most often, when we are dealing with a many-body Hamiltonian, there is a very strict limit in sizes of the systems limited up to few spins (e.g: 4×4). Thus, the motivation of using the pCUT is to diagonalize the Hamiltonian in the unitarily (particle conserving) transformed basis thereby decoupling the particle sub-spaces. This enables us faster calculations saving enormous time and memory. It can be easily noted that in the particle conserving basis the Hamiltonian is given in the block-band diagonal form [121]. At times, perturbative expansion can be a powerful tool especially when the spectrum is equidistant even in cases where the perturbing parameter (or unperturbed) is complex with multiple parameters [127]. In that case, one can reach up to very high orders of expansion. However, the most significant aspect of the pCUT's is that the results are valid even in the thermodynamic limit ($N \to \infty$). Wegner [121, 120] initially proposed the idea of continuous unitary transformation (CUT) which has been successfully tested on a 1D n-orbital model in the thermodynamic limit. Similar works have been carried in high-energy physics through an optimized perturbation theory [122].

Usually, CUT's can be approximated by an infinite sequence of discrete unitary transformations. Nevertheless, one can conveniently parametrize the same transformation by a parameter 'l' that runs from 0 to ∞ such that,

$$
\begin{aligned}
H(l=0) &= H, && (2.74)\\
H(l>0) &= U(l)H(0)U^{\dagger}(l), && (2.75)
\end{aligned}
$$

here, H is the untransformed (or original Hamiltonian) and $U(l)$ is the unitary transformation which at present is not explicitly given. One can formulate the flow equations by differentiating both the sides of Eq. (2.74) as follows:

$$
\begin{aligned}
\frac{d}{dl}H(l) &= \left[\frac{d}{dl}U(l)\right]H(0)U^{\dagger}(l) + U(l)H(0)\left[\frac{d}{dl}U^{\dagger}(l)\right] && (2.76)\\
&= \left[\frac{d}{dl}U(l)\right]U^{\dagger}(l)H(l) + H(l)U(l)\left[\frac{d}{dl}U^{\dagger}(l)\right] && (2.77)\\
&= [\eta(l), H(l)], && (2.78)\\
\eta(l) &= [\frac{d}{dl}U(l)]U^{\dagger}(l) = -U(l)[\frac{d}{dl}U^{\dagger}(l)], && (2.79)
\end{aligned}
$$

we have used the identity $U^{\dagger}(l)U(l) = \mathbb{1}$ in the second line. Note that at this point one is free to choose a generator $\eta(l)$ of his choice depending on the problem but with a constraint of antihermiticity coming due to the Eq. (2.77). Nonetheless, usually one is desired to have a block-band diagonal form Hamiltonian under $l \to \infty$ limit. The effective Hamiltonian should be obtained as follows:

$$
H_{\text{eff}} = \lim_{l\to\infty} H(l), \tag{2.80}
$$

where H_{eff} conserves the total number of quasi-particles. In order to have the Hamiltonian in a block-band diagonal structure we require the following condition:

$$
[Q, H_{\text{eff}}] = 0. \tag{2.81}
$$

Because of Eq. (2.78), one probable option for the generator is

$$\eta(l) \quad = \quad [Q, H(l)]. \tag{2.82}$$

Unless the right-hand side of Eq. (2.82) don't vanish, $H(l)$ is subjugated to Eq. (2.78). In case the RHS equals to zero, there is a stop of flow equation where the $H(l)$ converges to its $l \to \infty$ limit. This choice of generator was initially proposed by Mielke [124] and generalized by Knetter and Uhrig [118]. The generator also preserves block diagonality of the initial Hamiltonian. The generalized generator is given by its matrix elements as:

$$\eta_{ij}(l) = \text{sgn}(q_{i,i} - q_{j,j})h_{ij}(l) = \begin{cases} h_{ij}(l), & \text{for } q_{i,i} > q_{j,j}, \\ -h_{ij}(l), & \text{for } q_{i,i} < q_{j,j}, \\ 0, & \text{for } q_{i,i} = q_{j,j} \end{cases} \tag{2.83}$$

where $h_{ij}(l)$, $\eta_{ij}(l)$ are the corresponding elements of a matrix of $\eta(l)$, and $H(l)$ in the eigenbasis of Q and $q_{i,i}$ is the total number of particles currently in the state $|i\rangle$.

To get the final flow equations in the form of coupled differential equations, Eq. (2.78) can be discretized which can be iteratively solved under certain approximations [121, 128, 129, 130, 131]. This establishes the CUT on the Hamiltonian. Note that the coefficients are obtained once before the start of calculations of groundstate and n-qp gap, and are specific to the problem considered.

2.7 pCUT flow equations

Most general representation of perturbation can be given by

$$H = H_0 + \lambda V, \tag{2.84}$$

where the spectrum of H_0 is known beforehand, and V denotes perturbation term with λ defining the strength of the perturbation. At this point, it should be noted that the perturbative approach is not unique and there are more than a couple of methods to arrive at the perturbative solutions of the flow equations. For instance, a series ansatz can be invoked directly to solve the flow equations numerically, e.g: Runge-Kutta methods [132]. Our emphasis, however, will be on the other approach that becomes the pCUT method and which is apt for the problem of magnonic dispersion at high-field limits. Nevertheless, there are few constraints as far as the applicability of pCUT is concerned. The following conditions must be satisfied in order for a pCUT transformation to be applied:

(i) Unpertubed Hamiltonian H_0 must have a spectrum that is discrete and also bounded from below.

That is to say, H_0 can be given by a matrix with finite or semi-infinite dimensions. Regarding notational purposes, the quantized energy levels (discrete) are labeled by $\epsilon_i (i \in \mathbb{N})$ where the elementary excitations energies are given by $\Delta\epsilon_i = \epsilon_i - \epsilon_0$.

(ii) The unperturbed spectrum should be equidistant, in other words, there should exist $\Delta\epsilon$ so that in general underlying excitation can be simply given as

$$\Delta\epsilon_i = n_i \Delta\epsilon, \tag{2.85}$$

where $n_i \in \mathbb{N}$. It is useful to set $\Delta\epsilon = 1$ such that the energy required to excite the elementary is equal to the number of quasi-particles. In the purview of the discussion, H_0 now exactly becomes the number of qp, Q itself, defined in Eq. (2.67).

(iii) The number of states the perturbation V can connect is bounded and is represented by the sum at zeroth order as

$$V = \sum_{m=-N}^{m=+N} T_m, \tag{2.86}$$

the T_m alters the quasi-particle number in the system by m, as shown in Eq. (2.6).

Despite the constraints mentioned above regarding the applicability of pCUT's, yet one still finds numerous models where the pCUT's are successfully applied. Few examples include the arena of low-dimensional quantum magnets including the frustrated systems, spin-ladder, supersolids, nuclear physics as well as stabilizer codes and also cluster Hamiltonians including topologically-ordered spin models [108, 111, 119, 133, 134, 135, 136, 137, 138, 139, 140, 141, 142], to name a few.

Following the approaches of Knetter, Uhrig, and Stein [118, 123] we curtail the problem consisting of flow equations to the one of a differential equations system that are highly coupled. Then a generic numeric algorithm to obtain the solution recursively is briefed. The details regarding the algorithm and implementation details are given in Appendix A. Given the nature of commutation algebra of the generator Eq. (2.78), a more familiar ansatz regarding the Hamiltonian that consists of the flow-dependent part, viz. $V(l)$ is given by:

$$V(l) \;=\; \sum_{k=1}^{\infty} \lambda^{k-1} \sum_{|\mathbf{m}|=k} F(l;\mathbf{m}) T(\mathbf{m}). \tag{2.87}$$

While the first sum runs over the order of perturbation the second one is performed covering all combinations of k-tuples of $m_i \leq N$ where $N \in \mathbb{N}$. The undetermined function $F(l;\mathbf{m})$ are evaluated as following. We regard the matrix elements of $H(l)$ in the eigenbasis of quasi-particle conserving part, that is, Q as,

$$\langle n_i | H(l) | n_j \rangle \;=\; \langle n_i | Q + \lambda V(l) | n_j \rangle = q_{i,j} + \lambda \nu_{i,j}, \tag{2.88}$$

$$\langle n_i | T(\mathbf{m}) | n_j \rangle \;=\; t_{i,j}(\mathbf{m}). \tag{2.89}$$

Since Q is diagonal in the $|n\rangle$ basis, we therefore dont see any 'l' dependence of it. Using the Eqs. (2.88) and Eq. (2.83), the $\eta(l)$ can be expanded in T operators as,

$$\begin{aligned}
\langle n_i|\eta(l)|\eta_j\rangle &= \eta_{i,j}(l) && (2.90)\\
&= \mathrm{sgn}(q_{i,i}-q_{j,j})(q_{i,j}+\lambda\nu_{i,j}(l)) && (2.91)\\
&= \mathrm{sgn}(q_{i,i}-q_{j,j})\lambda\nu_{i,j}(l) && (2.92)\\
&= \sum_{k=1}^{\infty}\lambda^k\sum_{|\mathbf{m}|=k}F(l;\mathbf{m})\mathrm{sgn}(q_{i,i}-q_{j,j})t_{i,j}(\mathbf{m}). && (2.93)
\end{aligned}$$

In Eq. (2.92) we invoke the Q operators diagonal property. With the help of Eq. (2.81) we can simplify the above equation further by removing the unperturbed Hamiltonian within the generator:

$$\begin{aligned}
M(\mathbf{m})T(\mathbf{m}) &= [Q,T(\mathbf{m})], && (2.94)\\
M(\mathbf{m})t_{i,j}(\mathbf{m}) &= [Q,T(\mathbf{m})]_{i,j} && (2.95)\\
&= (q_{i,i}-q_{j,j})t_{i,j}(\mathbf{m}), && (2.96)\\
\mathrm{sgn}[M(\mathbf{m})]t_{i,j}(\mathbf{m}) &= \mathrm{sgn}(q_{i,i}-q_{j,j})t_{i,j}(\mathbf{m}). && (2.97)
\end{aligned}$$

Using Eq. (2.93) and Eq. (2.97), the generator can be given by:

$$\eta(l) = \sum_{k=1}^{\infty}\lambda^k\sum_{|\mathbf{m}|=k}F(l;\mathbf{m})\mathrm{sgn}(M(\mathbf{m}))T(\mathbf{m}). \qquad (2.98)$$

Substituting the solution for $\eta(l)$, and the ansatz solution of $V(l)$ in the flow Eq. (2.78), ($\frac{s}{sl}Q=0$):

$$\begin{aligned}
\frac{d}{dl}H(l) &= \lambda\frac{d}{dl}V(l) && (2.99)\\
&= \lambda[\eta(l),V(l)]-[Q,\eta(l)] && (2.100)\\
&= \lambda[\eta(l),V(l)]-\sum_{k=1}^{\infty}\lambda^k\sum_{|\mathbf{m}|=k}F(l;\mathbf{m})\mathrm{sgn}(M(\mathbf{m}))\underbrace{[Q,T(\mathbf{m})]}_{M(\mathbf{m})T(\mathbf{m})}.\,. && (2.101)
\end{aligned}$$

$\mathbf{m}_1$	$\mathbf{m}_2$
(m_1)	$(m_2, ..., m_k)$
(m_1, m_2)	$(m_3, ..., m_k)$
$\vdots$	$\vdots$
$(m_1, ..., m_{k-1})$	(m_k)

Next, we put the ansatz Eq. (2.87) solution of $V(l)$, and sorting the RHS in ascending order of λ of Eq. (2.99)

$$\begin{aligned}\sum_{k=1}^{\infty}\sum_{|\mathbf{m}|=k}\frac{d}{dl}F(l;\mathbf{m})T(\mathbf{m}) &= \sum_{\substack{k_1,k_2\\|m_1|=k_1\\|m_2|=k_2}}\lambda^{k_1+k_2}F(l;\mathbf{m}_1)F(l;\mathbf{m}_2)\mathrm{sgn}[M(\mathbf{m}_1)][T(\mathbf{m}_1),T(\mathbf{m}_2)]\\ &\quad-\sum_{\substack{k\\|\mathbf{m}|=k}}\lambda^{k}F(l;\mathbf{m})|M(\mathbf{m})|T(\mathbf{m}). \qquad (2.102)\end{aligned}$$

The algebraic functions $F(l;\mathbf{m})$ can be evaluated over coupled differential equations by matching coefficients in Eq. (2.101) and Eq. (2.102):

$$\begin{aligned}\frac{d}{dl}F(l;\mathbf{m}) &= -|M(\mathbf{m})F(l;\mathbf{m})+\\ &\quad\sum_{\substack{\{\mathbf{m}_1,\mathbf{m}_2\}=m\\|\mathbf{m}|=2}}(\mathrm{sgn}[M(\mathbf{m}_1)]-\mathrm{sgn}[M(\mathbf{m}_2)])F(l;\mathbf{m}_1)F(l;\mathbf{m}_2). \qquad (2.103)\end{aligned}$$

The summation in the last term of the above equation runs through all possible partitions of $\{\mathbf{m}_1,\mathbf{m}_2\} = \mathbf{m}$, along with the constraint $|\mathbf{m}| = k$ can be given by: To make the equation look neater, we do the following simple rotation:

$$F(l;\mathbf{m}) = \exp^{-|M(\mathbf{m})|l} f(l;\mathbf{m}). \qquad (2.104)$$

We then get,

$$\begin{aligned}\frac{d}{dl}f(l;\mathbf{m}) &= \sum_{\substack{\{\mathbf{m}_1,\mathbf{m}_2\}=\mathbf{m}\\|\mathbf{m}|\geq 2}}\exp\left(|M(\mathbf{m})|-|M(\mathbf{m}_1)|-|M(\mathbf{m}_2)|\right)l\\ &\quad\mathrm{sgn}[M(\mathbf{m}_1)]-\mathrm{sgn}[M(\mathbf{m}_2)]f(l;\mathbf{m}_1)f(l;\mathbf{m}_2). \qquad (2.105)\end{aligned}$$

The flow equations are highly recursive and let us evaluate the coefficients $f(l;\mathbf{m})$, with $|\mathbf{m}| = k$, starting with functions evaluated for all $|\mathbf{m}| < k$ with the following initial conditions from $V(0)$ as:

$$F(0;\mathbf{m}) = \begin{cases} 1, & \text{for} \quad |\mathbf{m}| = 1 \quad \text{and} \quad m \in \{0, \pm 1, \pm, ..., \pm N\}, \\ 0, & \text{else.} \end{cases} \tag{2.106}$$

As our interest lies in $\rightarrow \infty$ limit, for the matter of convenience it is better to introduce the coefficients $C(\mathbf{m})$ such that:

$$C(\mathbf{m}) = \lim_{l\rightarrow\infty} F(l;\mathbf{m}). \tag{2.107}$$

Now, once the coefficients are evaluated according to the Eq. (2.105), the effective Hamiltonian in the particle (quasi) conserving basis can be exactly given by taking the limit $l \rightarrow \infty$ as:

$$\lim_{l\rightarrow\infty} H(l) = H_{\text{eff}} = Q + \sum_{k=1}^{\infty} \sum_{\substack{\mathbf{m}=k \\ M(\mathbf{m})=0}} C(\mathbf{m})T(\mathbf{m}). \tag{2.108}$$

It should be noted that the only surviving coefficients of the function F are the ones that satisfy the condition of a fixed total number of quasi-particles in the system, and the functions are given in the exponential form with a negative exponent that is proportional to l (such as $e^{-1/2l}$). We can see that the term vanishes in the $l \rightarrow \infty$ limit. This also proves the effective Hamiltonian being block-diagonal in the quasi-particle number basis. We notice that the coefficients $c(m)$ do not depend on the problem at sight. Though the exact number of coefficients that contribute to the problem can strictly depend on the perturbed Hamiltonian, the coefficients themselves are not. For example, 3rd order process in the groundstate sector, $\langle 0|T_{-2}T_0T_2|0\rangle$, has the coefficient C_{-202} that is constant regardless of the Hamiltonians. Whether or not such a coefficient appears in the process is decoded by the perturbing Hamiltonian. However, if one has a Hamiltonian that does not meet the 3-point criteria mentioned in section 2.7, one may employ an alternate approach as developed by Krull et al [132] where the constraints are not necessary to be invoked with the H_{eff} can be evaluated numerically for every new problem. This has to do with the equidistant nature of the spectrum. However, in the next section, we review the linked-cluster theorem used to compute the physical quantities on a computer.

2.7.1 Series expansions on finite graphs

pCUT's are famous for their one of the strong properties that the results obtained are valid even in the thermodynamic limit. It may be noted that this is not the only the case with short-ranged perturbation when the quasi-particle excitations created are local in real space but also can be generalized to long-range interactions [143, 144, 145, 146]. However, if the effective Hamiltonian is given in terms of summation over elementary interactions of short-range type, a following powerful scheme of evaluating the physical quantities on a finite-lattice or graphs emerges, that is, the linked-cluster expansions. Here we shall briefly describe the recipes of one of the series expansion methods implemented in our calculations. Nevertheless, interested readers can resort to various literature on the means of evaluating groundstate energy, n-particle dispersions (usually it is one or two-particle), and the green functions. For details regarding the linked-cluster expansion derivation and its smooth emergence from pCUT is given in Appendix A, here we discuss the implementation details of the series expansion method used in our calculations [125, 119, 147].

To tackle the linked-cluster calculations of a given quantity based on the merits and demerits of the problem considered, there are three various cluster expansion methods. They are:

(i) Linked-cluster expansion

Also known as the white graph expansion method. It is enough to identify and perform calculations on certain irreducible topological graphs embedding the lattice. Contributions coming from the various topological cluster as well their corresponding embedding numbers have to be determined. The task of determining the embedding numbers can be performed efficiently by invoking the pegs in holes algorithm proposed by Oitmaa et al [148]. After that, the perturbation expansion of P is obtained by a proper summation of results with their corresponding embedding numbers using Eq. (2.110). Though the following method reduces memory usage and time considerably, the method might still become challenging when the number of relevant topological graphs increase exponentially depending on the problem.

(ii) Single periodic cluster

In an earlier time, this method has been used extensively because of the simplicity it offers. Another advantage of this method is that a generic code can be used without the prior needs of any particular model. This generic code can produce all possible graphs automatically rendering a great advantage to the users. One generally has less work to do when dealing with this method. The only precaution, however, one has to take care of is the minimal size of the lattice, which should be large enough that the finite-size effects do not surface. The minimal size of the lattice does strictly depend on the lattice structure, the effective Hamiltonian, and the perturbation order. This approach has its advantages and disadvantages. However, apart from its success, it suffers from certain shortcomings such as the number of intermediate terms that might go beyond reach thereby limiting the perturbation order. It is still the very simplest one to implement on a computer and one doesn't need to identify the set of irreducible topological graphs.

(iii) Finite-lattice method

An approach that has its roots in both the above methods. It has been developed by Neef and Enting [149] for square lattice for specific models such as the classical Ising model. Later, Dusuel [147] et al has generalized the methods to quantum systems. Within its applicability, this is the most efficient and optimized method in the current scenario. The fundamental concept that defines the method is that one has to consider only subcluster $C_{m\times n}$ with $m \times n$ sites. Crucially, the embedding numbers can be found algebraically here without much effort. The total number of topological graphs is also drastically reduced. From the Eqs. (2.109) and Eq. (2.110) we get,

$$P(\Gamma)/N = \sum_{m\leq n} L(\Gamma, C_{m\times n})W(C_{m\times n}), \tag{2.109}$$

$$W(C_{m\times n}) = P(C_{m\times n}) - \sum_{\substack{m'\leq m\\ n'<n}} \sum_{\substack{m'<m\\ n'=n}} W(C_{m'\times n'}), \tag{2.110}$$

the summation in the second term runs through all m' and n' such that $\mathbf{C}_{m'\times n'}$ can be embedded in $\mathbf{C}_{m\times n}$ with $\mathbf{C}_{m'\times n'} \neq \mathbf{C}_{m\times n}$. For a square sized cluster, the lattice constant in Eq. (2.110) is equal to one, while the rectangular lattice it is two. The number of embeddings N_{emb} of a rectangular cluster $\mathbf{C}_{m\times n}$ in a square lattice. Usually,

$$N_{\text{emb}} = \begin{cases} 2mn, & \text{if} m \neq n, \\ m^2, & \text{if} m = n. \end{cases} \tag{2.111}$$

Then the lattice constant can be simply obtained by the relation: N_{emb}/mn. It can be noted that the Eq. (2.109) and (2.110) are completely valid in the thermodynamic limit. Nevertheless, in computer simulations, a finite-order maximal m and n can be found such that the above sums become limited. Usually, it is limited by the perturbation order. Then appropriate summation has to be performed to obtain the final result for the extensive quantity, P. However, details regarding this method and implementations on quantum systems such as the Toric code model in a field. Other geometries have also been explored for example the triangular lattices [150]. Attempts have been made to extend the approach to higher dimensions [151]. With this, we end the discussion on the methodology of pCUT. In the next section, we discuss some of the results obtained using the pCUT in various limits.

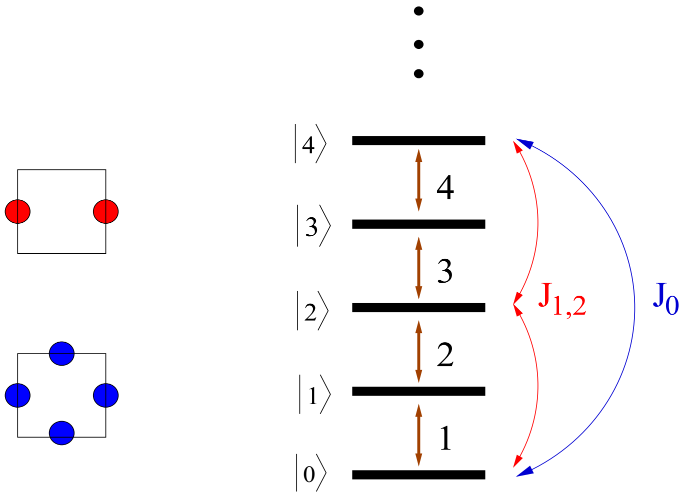

Figure 2.11: (Color Online) The left column shows a cartoon picture of a process where the action of $T_{2(4)}$ [red(blue)] upon the groundstate of 0-quasiparticle (QP) subspace produces 2-QP (above) and 4-QP (below). The right column shows a simple connection of the perturbing parameters connecting the different QP levels of the unperturbed Hamiltonian.

2.8 Results

2.8.1 pCUT in High-field limit $K \gg J_{0,1}$

In this case, the Hamiltonian boils down to:

$$H_x = -K \sum_i \sigma_i^x, \tag{2.112}$$

here, i is summed over all individual spins, and we know the groundstate is the one where all spins are aligned along x, that is, $| \uparrow\uparrow \cdots \uparrow\rangle_x$ with equidistant magnonic spectrum. Thus we rotate the basis to incorporate the z-axis along the field direction K. The system satisfies the criteria (i) and (ii) of sec. 2.7. We then perturb the system with $J_{0,1,2}$ operators rotated into the optimal basis. We know the total cost of energy to flip a spin is proportional to $2K$. We then perform calculations of the groundstate and one-particle dispersion, however, before that we give away the expressions for creation (or annihilation) operators. The derivation goes by substituting the representation Eqs. (2.24) and Eq. (2.23) with $\theta_C = \pi/2$ into the Hamiltonian (1.3). Then collecting the terms that are proportional to local creation (or annihilation) of quasi-particles, the exact expressions can be found as:

$$\begin{aligned}
T_0 &= J_0 \sum_{\square} [a_1 a_2 a_3^\dagger a_4^\dagger + a_1 a_2^\dagger a_3 a_4^\dagger + a_1 a_2^\dagger a_3^\dagger a_4 + h.c] \\
&+ J_1 \sum_{\square} [a_1 a_3^\dagger + a_2 a_4^\dagger + h.c] \\
&+ \frac{J_2}{8} \sum_{\langle AB \rangle} [a_2 a_4^\dagger + a_3 a_7^\dagger + a_1 a_5^\dagger + a_2 a_6^\dagger - a_3 a_7^\dagger - a_1 a_7^\dagger - a_4 a_6^\dagger + h.c], \qquad (2.113) \\
T_2 &= J_0 \sum_{\square} [a_1^\dagger a_2 a_3^\dagger a_4^\dagger + a_1^\dagger a_2^\dagger a_3 a_4^\dagger + a_1^\dagger a_2^\dagger a_3^\dagger a_4 + a_1 a_2^\dagger a_3^\dagger a_4^\dagger] \\
&+ J_1 \sum_{\square} [a_1^\dagger a_3^\dagger + a_2^\dagger a_4^\dagger] \\
&+ \frac{J_2}{8} \sum_{\langle AB \rangle} [a_2^\dagger a_4^\dagger + a_3^\dagger a_7^\dagger + a_1^\dagger a_5^\dagger + a_2^\dagger a_6^\dagger - a_3^\dagger a_7^\dagger - a_1^\dagger a_7^\dagger - a_4^\dagger a_6^\dagger], \qquad (2.114) \\
T_4 &= J_0 \sum_{\square} [a_1^\dagger a_2^\dagger a_3^\dagger a_4^\dagger]. \qquad (2.115)
\end{aligned}$$

In the above expression, the parameters J_0, J_1, and J_2 are now reduced constants where the S prefactor from the HP transfromation (2.24) is absorbed into the exchange constants as follows: $J_0 \to J_0 \frac{S^2}{4}$, $J_{1,2} \to \frac{S}{2}$ and the numbering scheme is according to Fig. 1.2. The conjugate operators ($T^\dagger$) can be found from the simple relation: $T_n^\dagger = T_{-n}$. We present the calculation of groundstate energy on the finite lattice up to 1$^{\text{st}}$ order, here the effective Hamiltonian in the optimal basis is given as:

$$H^0_{\text{eff}} = -NK + 2KQ, \qquad (2.116)$$

$$H^1_{\text{eff}} = T_0. \qquad (2.117)$$

Here N is the number of spins in the lattice (single lattice method), Q is the operator as described in sec. 2.81. To normalize the unperturbed energy that is required to flip one particle, we set the magnetic field $K = 1/2$. Given the operator structure Eq. (2.116) we now perform the groundstate energy by making a substitution of $Q = 0$ as:

$$e_0^{(0)} = -K = -\frac{1}{2}. \qquad (2.118)$$

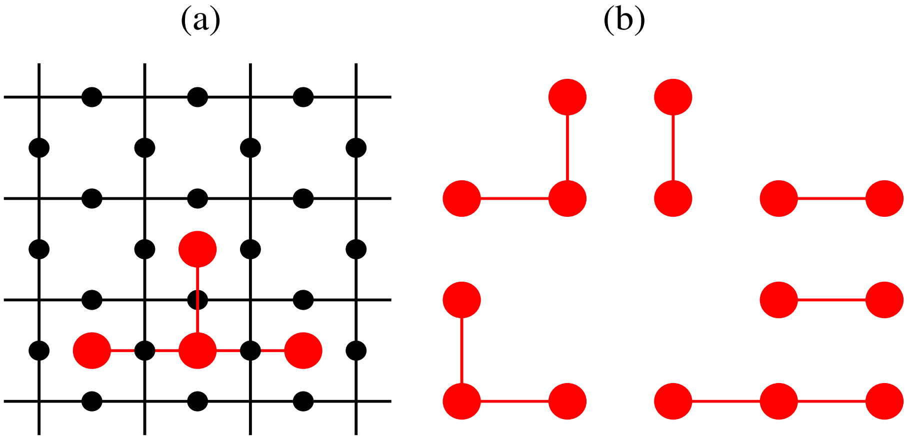

Figure 2.12: (a) Example showing the connected four-plaquette graph on a square lattice for a local Hamiltonian, where each plaquette excitation is produced by a single spin-flip operator. This is shown for the case of low-field limit, where the excitations are the elementary plaquettes with gauge charges carrying the charge of -1. Note that the excitations are produced in pairs (in low-field limit only) with plaquettes adjacent to each other [this relates to n = 2 in (2.109)]. (b) Various subgraphs corresponding to the cluster in (a). Individually subgraphs containing no less than two sites, because n = 2.

Similarly, at first order, we can compute the matrix elements as follow:

$$\langle 3\times 3|T_0|3\times 3\rangle \;=\; -\frac{1}{8}J_0^2-\frac{1}{2}J_1^2. \tag{2.119}$$

Some of the processes come from the gauge term J_0 and some from the intramolecular coupling term J_1. However, it is to be noted that the term with only gauge term J_0 can be mapped to a transverse field Ising system [152] with the couplings of both the models being inversely related. The strong coupling of one system maps on to the weak coupling in the dual model and vice versa. The fact that the number of effective operators usually in the high-field makes the computations limited to effectively lower orders. A valid argument makes up the fact that due to better convergence of the gap even at order 6 it is reasonable to consider the following limit, especially when the low field-limit is quite complex. The implementation tools and the tools to analyze the one-particle gap especially the *DLog-Pade* approximants are given in Appendix A.

All the effective operators for Hamiltonian (1.3) are now obtained, and once the flow equation coefficients C_m are calculated electronically, we then substitute them correspondingly and evaluate the groundstate and one particle sector according to the equation:

$$
\begin{aligned}
E_0 &= \langle 0|H_{\text{eff}}|0\rangle, && (2.120)\\
\omega(k) &= \langle k|H_{\text{eff}} k\rangle - E_0. && (2.121)
\end{aligned}
$$

Here the momentum carrying the information of the lattice is given by, $|k\rangle = \sqrt{2/N}\sum_j \exp i\vec{k}.\mathbf{r_j}|j\rangle$ where j is the lattice site and $\mathbf{r_j}$ is the relative position vector of site j. The origin of the coordinate system is set on the lattice site number 0. So any hopping's position vector is relatively given from this origin site '0'. The groundstate energy and the one particle gap which can be found at Γ-point in the given limit is found to be as:

$$
\begin{aligned}
e_0 = \; & \frac{1}{2} - \frac{1}{8}J_0^2 - \frac{1}{384}J_0^4 - \frac{41}{393216}J_0^6 - \\
& \frac{1}{2}J_1^2 - \frac{1}{2}J_0J_1^2 - \frac{9}{32}J_0^2J_1^2 - \frac{3}{16}J_0^3J_1^2 - \frac{47525}{442368}J_0^4J_1^2 \\
& -\frac{1}{8}J_1^4 - \frac{1}{2}J_0J_1^4 - \frac{32957}{32768}J_0^2J_1^4 - \frac{61}{512}J_1^6, \qquad (2.122)
\end{aligned}
$$

$$
\begin{aligned}
\Delta(\Gamma) = \; & 1 - \frac{1}{2}J_0^2 + \frac{3}{32}J_0^4 - \frac{1711}{27468}J_0^6 + 2J_0J_1 + 2J_1 \\
& -\frac{1}{8}J_0^2J_1 - \frac{3}{4}J_0^3J_1 + \frac{67}{576}J_0^4J_1 + \frac{8131}{13824}J_0^5J_1 \\
& -\frac{3}{4}J_0^2J_1^2 - \frac{7}{2}J_0^3J_1^2 - \frac{111013}{36864}J_0^4J_1^2 + J_0J_1^3 + \frac{317}{128}J_0^2J_1^3 \\
& -\frac{13361}{4608}J_0^3J_1^3 - \frac{10207}{3072}J_0^2J_1^4 + \frac{79}{128}J_0J_1^5. \qquad (2.123)
\end{aligned}
$$

A standard analysis for the gap Δ using DLog-Pade approximants for different parameters values of J_1 and our calculation confirms that, indeed, the phase transition of CDT in $J_1 - K$ plane for $J_2 = 0$ is of second-order consistent with the Ref. [89] as shown in Fig. 2.14, where we presented the phase diagram from confined to deconfined phase transition in $K - J_1$ plane. The phase boundary is obtained from the one-particle dispersion equation. We used cumulative DLog-Pade approximants

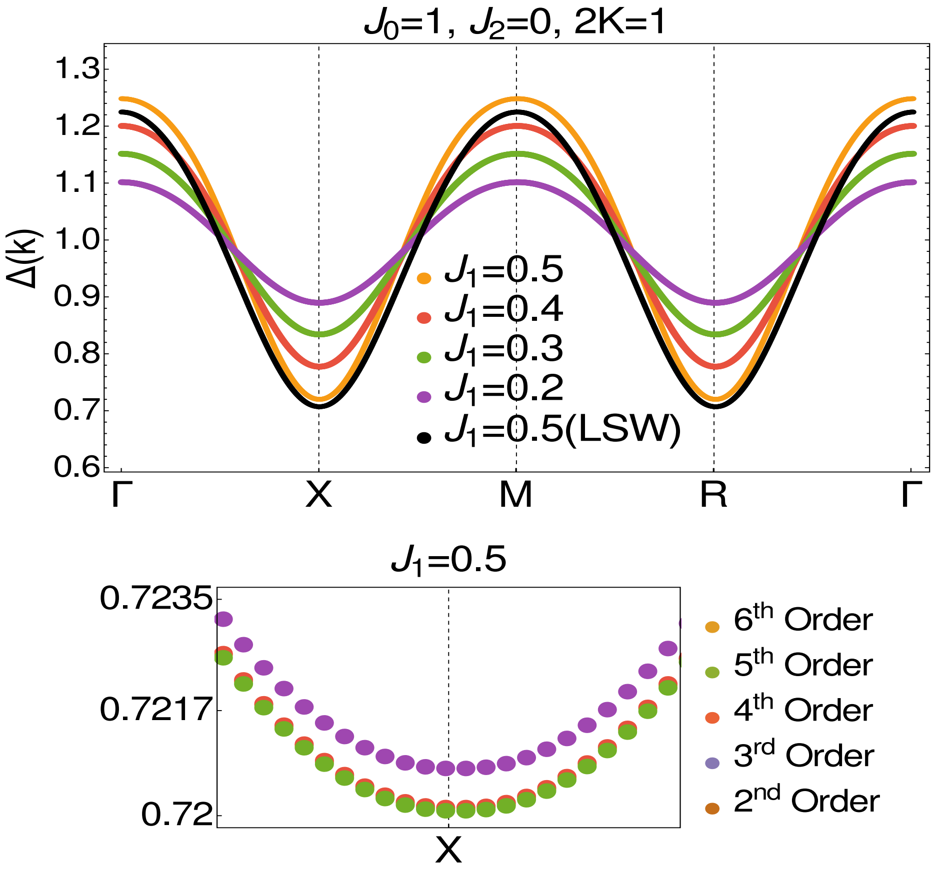

Figure 2.13: Spectrum as obtained from pCUT up to sixth order. The black line is the result obtained from spin-wave calculations. (Bottom) Zoomed spectrum around X points (extended very little toward the left to Γ point and at right to M point). We also present plots obtained at a different order of pCUT for a $J_1 = 0.5$, which shows that they are converging.

(Dlog-Pade[2,3] and Dlog-Pade[3,2]) to obtain the phase diagram because the order of expansion is relatively lower. It may be mentioned that for $J_1 = 0$ the Hamiltonian is a (2+1) quantum Ising gauge Hamiltonian [89] with critical point located at $K_c = 0.325$, here noticeably, for $J_1 = 0$, the obtained value is $0.3506(8)$. The closeness of the K_c obtained from pCUT to that of the value obtained in QMC entails the success of pCUT for this system. Note that when $J_1 = 0$, J_0 does not become a free parameter $(J_0 = 16)$ where J_0 itself becomes the tuning parameter. The small inaccuracy in the critical value is due to the relatively low order of expansion. Remember that the Ising gauge term J_0 does not even appear in spin-wave calculations at quadratic order, unlike the present case where the J_0 term is safely incorporated by pCUT at all orders. In Fig. 2.13, we have plotted the dispersion as obtained from pCUT and compared it with the spin-wave spectrum obtained earlier, which matches each other very well to leading order. We conclude this section with the observation that the one-

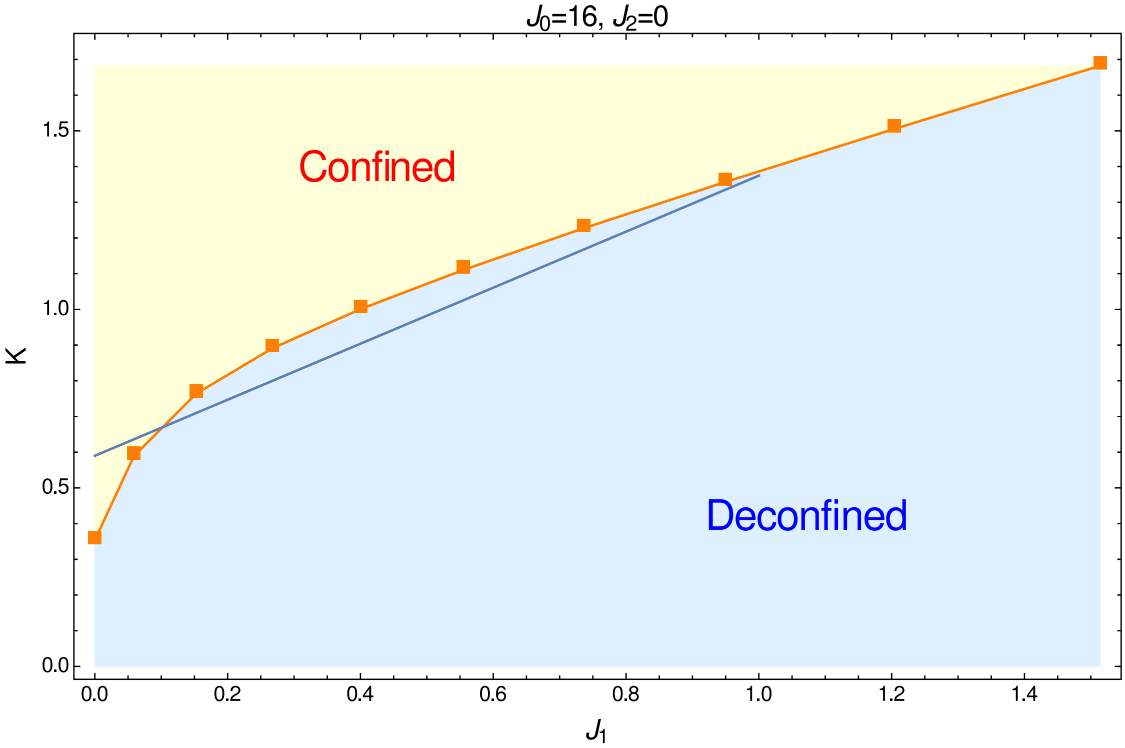

Figure 2.14: The above figure shows the phase boundary between confined and deconfined phases as obtained by the DLog-Pade[2,3] approximate analysis of pCUT at order six as derived by the expansion series given in Eq. (2.123) for the gap. The blue line is a linear fit of the data.

particle excitation spectrum as obtained in pCUT agrees well with the spin-wave spectrum obtained in Sec. 2.4. Moreover, the gap obtained in pCUT smoothly vanishes along the phase transition line signifying the transition as a second-order phenomenon.

2.8.2 pCUT application: High-field limit $K \gg J_{0,1}$ & $J_2 \neq 0$

In this section, we present the results of groundstate energy per spin and the one-particle dispersion for $J_2 = 0$. We could perform it in fourth-order as the number of intermediate states increases due to the non-local nature of dipole-dipole interaction. Nevertheless, the obtained expression helps determine its critical behavior qualitatively. As in the above case, the groundstate is the state where all the spins are oriented along the field direction and the single-spin flips are the elementary excitations with 2K cost of energy, hence setting $K = 1/2$ we obtain the groundstate energy and one-particle dispersion as

	T_0	$T_{\pm 2}$	$T_{\pm 4}$
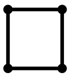	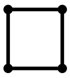	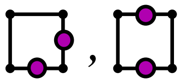 , . . .	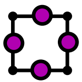
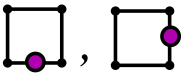 , . . .	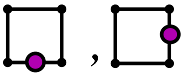 , . . .	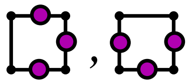 , . . .	
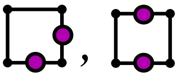 , . . .	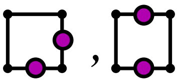 , . . .	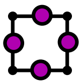	
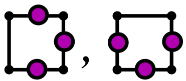 , . . .	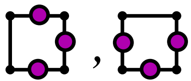 , . . .		
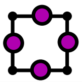	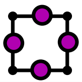		

Table 2.1: The operators T_n acting on the real space unit lattice is shown above. However, not all but only a few possible states are mentioned as represented by $\cdots$. The first column from left is the input state and the action of T_0, T_2, and T_4 are shown in the corresponding column under the respective operators. For T_0, it is column 1 and so on. Here, each process has different matrix elements as evident from the different exchange coupling strengths present in the perturbing Hamiltonian, that is, J_0, J_2 and J_3. Note that the operators like T_1 and T_3 do not contribute as the structure of perturbing Hamiltonian don't contain such terms.

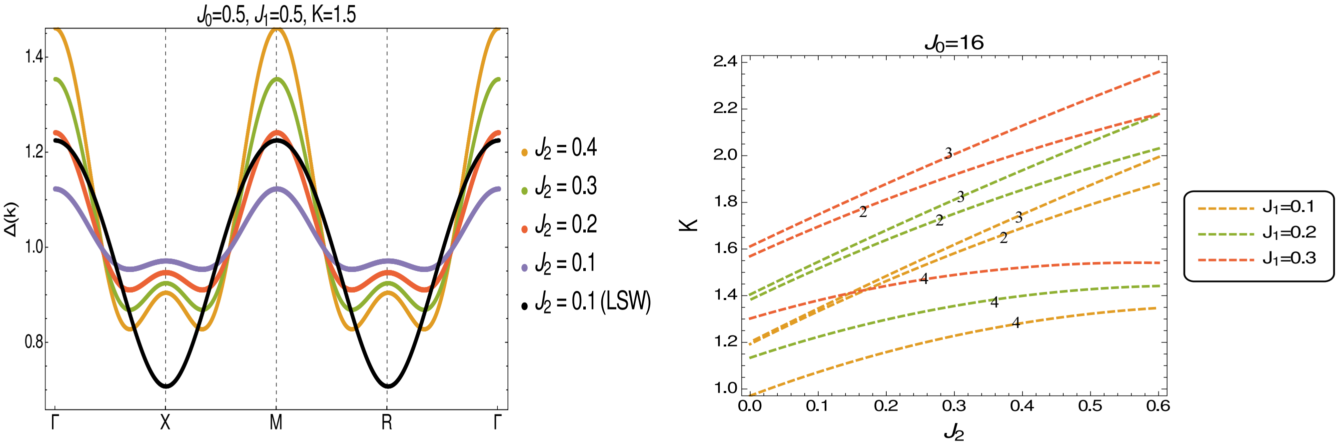

Figure 2.15: (Left) One-particle dispersion as obtained from pCUT. The above results are also compared with the spin-wave spectrum (the black plot). The additional peaks and the shifting of the minima around the X and R high-symmetry points in the pCUT results suggest the appearance of paraelectric ordering [89] by broken symmetry in the presence of finite J_2. Note that the additional peaks were not observed in the spin-wave calculation. (Right) The paraelectric to ferroelectric phase transition critical line extended over the $J_2 > 0$ region is shown above. It is evident as we increase the value of J_2 , the magnitude of the critical line for K_c also increases, which suggests that the dipole-dipole interaction extends the deconfined phase of J_1 to a ferroelectric phase for finite $J2$.

$$\begin{aligned} e_0 \;=\; & -\frac{1}{2}-\frac{1}{8}J_0^2-\frac{1}{384}J_0^4-\frac{1}{2}J_1^2-\frac{1}{2}J_0J_1^2-\frac{9}{32}J_0^2J_1^2-\frac{1}{8}J_1^4 \\ & -\frac{1}{2}J_1J_2-\frac{1}{2}J_0J_1J_2-\frac{9}{32}J_0^2J_1J_2-\frac{3}{8}J_1^2J_2-\frac{3}{4}J_0J_1^2J_2 \\ & -\frac{1}{4}J_1^3J_2-\frac{3}{8}J_2^2-\frac{1}{8}J_0J_2^2-\frac{39}{256}J_0^2J_2^2-\frac{33}{32}J_1J_2^2 \end{aligned}$$

$$-\frac{3}{2}J_0J_1J_2^2-\frac{155}{64}J_1^2J_2^2-\frac{15}{32}J_2^3-\frac{9}{16}J_0J_2^3-\frac{207}{64}J_1J_2^3-\frac{2859}{2048}J_2^4. \tag{2.124}$$

Similarly, the computation on one-particle yields:

$$\begin{aligned}\Delta \;=\;& 1+2J_1-\frac{1}{2}J_0^2+\frac{3}{32}J_0^4+2J_0J_1-\frac{1}{8}J_0^2J_1-\frac{3}{4}J_0^3J_1\\ &-\frac{3}{4}J_0^2J_1^2+J_0J_1^3+J_0J_2-\frac{3}{8}J_0^3J_2+J_1J_2+\frac{5}{2}J_0J_1J_2\\ &+\frac{105}{64}J_0^2J_1J_2+\frac{3}{4}J_1^2J_2+3J_0J_1^2J_2+\frac{1}{2}J_1^3J_2\\ &+\frac{11}{8}J_2^2+\frac{41}{16}J_0J_2^2-\frac{29}{128}J_0^2J_2^2+\frac{45}{16}J_1J_2^2\\ &+\frac{233}{16}J_0J_1J_2^2+\frac{71}{8}J_1^2J_2^2+\frac{9}{4}J_2^3+\frac{297}{32}J_0J_2^3\\ &\frac{535}{32}J_1J_2^3+\frac{553}{64}J_2^4.\end{aligned} \tag{2.125}$$

In the present case, due to the increasing demand for computing power, we could only perform pCUT up to fourth order, however, we still find that the gap vanishes here as well within some parameter range. However, this is fully consistent with the fact that switching on J_2 triggers a ferroelectric phase as obtained in the previous study [89], which has excitations as a single dipole changing its orientation costing a finite gap. Nevertheless, for brevity, we have tried to solve Eq. (2.125) for Δ= 0 to obtain the value of K_c near the phase transition. The ferroelectric phase transition critical line extended over the $J_2 > 0$ region is obtained suggesting a second-order phase transition. In the right panel of Fig. 2.15, we have shown the phase boundary extended in the $J_2 - K$ plane for various values of J_1. The numerics attached with the plots denote the orders of pCUT calculation. Within the pCUT limit of the parameter value J_2, the magnitude of the critical line for K_c suggests that the dipole-dipole interaction is a weak interaction which only extends the deconfined phase of J_1 to a ferroelectric phase for finite J_2 as obtained for finite J_2. Note that for the present case of $J_2 = 0$, the standard extrapolation schemes were not used due to the low order of expansion comparably. Despite the low order, the convergence is quite good suggesting pCUT is effective when the parameter strength J_2 is comparatively smaller than the Ising gauge term and K, J_0. Also, in Fig. 2.15, we have plotted the dispersion as obtained from pCUT. We see that additional peaks appear in the dispersion when compared to spin-wave dispersion. One important contrasting difference from the previous case is that the difference between the spin-wave theory and pCUT are quite significant, this may be due to the strong magnon-magnon interactions which are quite evident from the nature of dipole-dipole interaction, as it contains the next next nearest neighbor Ising type interactions. And the additional peaks signify the emergence of the paraelectric phase, which is a consequence of the symmetry breaking phenomenon manifested in the system. Our results for gap and one-particle dispersion will have experimental consequences and can be verified. As of now, we have given an extensive account of the Hamiltonian in Eq. (1.3) where $K \gg J_0$.

2.9 Chapter summary

To summarize, in this chapter, we have performed an extensive analytical study of a model H_2SQ system. Our work builds on the model proposed earlier [89, 99]. To start with, we have mentioned the various terms in the Hamiltonian and their physical origin. At the zeroth level, the model Hamiltonian has only a plaquette term that harbors a deconfined phase. The application of an external magnetic field (given by a strength K) drives the deconfined phase to a confined phase. We have determined the value of K_c for which such a transition happens. The role of intramolecular coupling J_1 and dipole-dipole interaction J_2 on such a transition has been investigated. We have shown that the role of J_1 and J_2 is to stabilize the deconfined phase by reducing the degeneracy. A groundstate without the dipole-dipole interaction term in the low-field case was found and can be represented as a singlet pair or dimers whose z-component projections of spins are anti-aligned to satisfy the restricted ice rules. Thus the classical groundstate remains degenerate for small values of K as shown by mean-field ansatz. In the presence of the dipole-dipole term J_2, the local degeneracy is removed to yield four degenerate groundstates with global symmetry independent of system size. Then the role of quantum fluctuations has been investigated over these large classical degenerate groundstates for $J_2 = 0$. Noticeably, we have found that at the quadratic level the local degeneracy is not at all removed and there is no order from disorder phenomena unlike the classically driven order-disorder case [42]. We have shown that there exists a macroscopic number of conserved quantities which enables a gauge transformation among the degenerate groundstate manifolds causing this absence of order-disorder phenomena. For finite J_2, we have found the spin-wave dispersion for the four global degenerate groundstates and found that, in general, the spectrum is gapped and quadratic for small values of K, except for certain parameters where the spectrum becomes gapless and linear. This happens particularly near the phase boundary of the confinement to the deconfinement phase transition. Our formula for the spin-wave dispersion and measure of the gap will be useful for future experiments. It may be pertinent to mention that the true quantum groundstate for $J_2 = 0$ is a nontrivial one due to its frustrated nature of the interaction. As a first step, at this limit, we have performed spin-wave approximations over classical groundstates. Though we can not expect to reach the true quantum groundstates, we think that the spin-wave fluctuations give us a reasonable estimate towards that. However, a more in-depth study is needed for exploring the nature of true groundstates, and unfortunately, as we have seen pCUT cannot be applied in this regime. On the other hand, the spin-wave analysis for $J_2 = 0$ is expected to be more realistic given that the quantum groundstate is ordered. To give more meaning to our study, we have applied pCUT to analyze the system in the large field limit ($K J_0, J_1, J_2$) where the groundstate consists of all spins aligned along x-direction with single spin-flip excitations. Though the pCUT analysis has improved the estimation of groundstate energy and one-particle gap as determined by spin-wave analysis, the closeness of results in the two different approaches seems to point out that the results are realistic in this limit. Our study also predicts the nature excitations as shown in Fig. 2.15 for finite J_2. However, one needs to perform a DFT study to confirm the exact values of parameters needed to fit the experiment. To complete, we have also briefly discussed the limit where $K \gg J_0$ and showed its inherent connection to the toric code model [115, 114] at the fourth-order of perturbation.

CHAPTER 3

Finite temperature analysis on quasi-2D squaric acid

3.1 Introduction

This chapter discusses in detail the finite-temperature phase diagram and the details of the associated quantum phase transition using the stochastic series expansion (hereafter referred to as SSE) quantum Monte Carlo (QMC) method. A robust numerical recipe in exploring the equilibrium properties of strongly correlated quantum systems that are analytically otherwise inefficient to solve. In the previous chapter, we have found and analyzed the lowest energy Ising states that contribute to the groundstate properties of the H_2SQ. A zero-temperature phase diagram was then obtained. Here, we extend our analysis to obtain a finite-temperature and finite-field phase diagram investigating the role of both the quantum and thermal fluctuations upon the obtained lowest energy Ising states. Specifically, we are interested to understand the intricate connection between the entropy arising from the degeneracy of ice-rules and the fluctuations in them caused by temperatures (or fields) as mentioned. However, simulating the current Hamiltonian is non-trivial. Even with the absence of any sign problem, as we shall see even ferromagnetic multispin interactions do pose a challenge in sampling the configuration space. Before discussing the results, we briefly describe the method of SSE and algorithms previously used [153] for transverse field models and the problems percolation-based decomposition of the Hamiltonian approach suffers. With the discussion of it, we then improvise a new way of decomposing the gauge term in the Hamiltonian which helps in naturally avoiding the spin freezing at lower temperatures and fields for $J_{1,2} = 0$. Using this newly improvised algorithm and sophisticated parallel tempering technique (for faster equilibration) we then describe the interplay of the thermal and quantum fluctuations on the Ice-rules dominant physics in H_2SQ system and the critical phenomenon associated with it by estimating the properties specific to the H-bonded systems, especially of H_2SQ. Interested readers may refer to Ref [154, 155, 156, 157] for a detailed analysis of the SSE QMC method from a broader perspective. In the next subsequent section, we will discuss about the derivation of the formalism of SSE QMC [158].

3.2 SSE representation of the partition function

The pivotal step in determining the SSE Quantum Monte Carlo method is based on expansion of the Hamiltonian of a quantum lattice spin system with it's exponential part of the partition-function being rewritten in powers of ($\beta\mathcal{H}$) as,

$$\mathcal{Z} = \mathrm{Tr}(e^{-\beta\mathcal{H}}) = \sum_{n=0}^{\infty} \frac{(-\beta)^n}{n!} \mathrm{Tr}(\mathcal{H}^n), \tag{3.1}$$

where $\beta = 1/(k_B T)$ is the temperature inverse. Now, the Hamiltonian $\mathcal{H}$ can be broken down into bond(b) or plaquette($\square$) operators as follows:

$$\mathcal{H} = -\sum_{b(\square)} H_{b(\square)} - \sum_{i} H_i, \tag{3.2}$$

the elementary bond (plaquette) operators $b(\square)$ labels the two (multi)-spins (say $b = (i, j)$) bond (plaquette) connecting the sites i and $(i, j, k, ...)$ containing in a single unit bond (plaquette). Note the minus sign that is conventionally followed in the SSE method. For instance, the bond (plaquette) term can be $H_b = \sigma_i^z\sigma_j^z$ ($\sigma_1^z\sigma_2^z\sigma_3^z\sigma_4^z$ of the gauge term). In our case, we have divided the diagonal operators decomposed in the form of elementary bonds (plaquette) interactions $\mathcal{H}_{b(\Box)}$, while the off-diagonal operators are decomposed as elementary non-interacting sites, that is, $\mathcal{H}_i$.

Once the Hamiltonian is completely decomposed into such elementary interaction fashion, It is useful to rewrite the term under the trace(Eq. (3.1)) in power series of Hamiltonian as,

$$\mathcal{H}^n \equiv (-\sum_{\Box} H_\Box - \sum_i H_i)^n = \sum_{S_n}(-1)^n \prod_{i=1}^{n} H_{\alpha_i}, \tag{3.3}$$

where $\{S_n\}$ represents the set of operator string S_n consisting of the sequences(that is products) of operators including diagonal($H_\Box$) and off-diagonal(H_i) operators. The terms arises by expanding out the sum in Eq. (3.3): $S_n = \{[\alpha_1], [\alpha_2], [\alpha_3], \cdots [\alpha_n]\}$ with α_i denoting the label of various types of commuting($\Box$) or non-commuting(i) operators. By writing the trace operation in Eq. (3.1) in the computation basis $|\alpha\rangle = |S_1^z, S_2^z, \cdots, S_N^z\rangle$ of tensor product states of eigenstates of S_i^z, we collect for the partition function sum where the equation reads as,

$$\mathcal{Z} = \sum_{n}^{\infty} \frac{(-\beta)^n}{n!} \sum_{\{S_n\}} \sum_{\{\alpha\}} \langle\alpha|(-1)^n \prod_{i=1}^{n} H_{a_i}|\alpha\rangle, \tag{3.4}$$

here, both the sums involved can run over all sequences of operators $\{S_n\}$ and all basis states $\{|\alpha\rangle\}$ respectively. We have deliberately decomposed the Hamiltonian $\mathcal{H}$ with a minus sign such that it cancels with the minus sign infront of inverse temperature (β).

Above all, one must choose the plaquette operators such that H_{a_i}'s action on $|\alpha\rangle$, that is, a given basis state returns multiple of some other state (basis) $|\beta\rangle$

$$H_{a_i}|\alpha\rangle \propto |\beta\rangle, \tag{3.5}$$

that isn't a superposition of states. A mark on the nomenclature: In the equation $|\alpha_1\rangle = H_{a_i}|\alpha\rangle$ we say that H_{a_i} propagates the initial state $|\alpha\rangle$ to the state $|\alpha_1\rangle$. The direction which the operator string S_n expands is called as the imaginary-time or propagation direction, in correspondence to the Feynmann's formalism of path integrals in statistical mechanics to which the SSE formalism is very nearly associated. It is helpful to define the states that are propagated along the imaginary-time and that are normalized $|\alpha(p)\rangle$ as attained after the application of the first p plaquette operators in the operator sequence as:

$$|\alpha(p)\rangle \propto \prod_{i=1}^{p} H_{a_i}\alpha(0)\rangle. \tag{3.6}$$

Next, if the trace operation in Eq. (3.4) can be calculated analytically, the partition function, $\mathcal{Z}$, then can be rewritten as a summation of computable weights as,

$$\mathcal{Z} = \sum_{n=0}^{\infty}\sum_{\{S_n\}} W(S_n), \tag{3.7}$$

here, $W(S_n)$ is the relative probability (weight) of creating a sequence, S_n, and the evaluation of expectation value happens by sampling over all sequences. In the year 1992, Handscomb [159] was the first to propose such a new Monte Carlo scheme, which, however, the original scheme was exclusively suited to the ferromagnet coupling of Heisenberg model [159, 160] as well as a few other systems. It can be seen that in almost every case the trace operation in Eq. (3.4) could not be estimated analytically. It is, therefore, necessary to importance sample in addition over a basis of states $\{|\alpha\rangle\}$. This way leads us to the broader scheme generalizing Handscomb's initial method. This is currently the most extensively applicable Stochastic Series Expansion (SSE) scheme [161, 155]. One may notice that with this generalizing scheme of sampling over basis states, the method nearly draws parallels with the approach of path integral continuous imaginary-time in an analytically exact way [162, 163].

To conclude, the SSE style of depicting the partition function is

$$\mathcal{Z} = \sum_{n=0}^{\infty} \sum_{\{|\alpha\rangle\}} \sqsupseteq(\alpha, S_n) \tag{3.8}$$

$$= \sum_{\{\mathcal{C}\}} \sqsupseteq(\mathcal{C}), \tag{3.9}$$

while configuration's weight

$$\sqsupseteq(\alpha, S_n) = \frac{\beta^n}{n!} \prod_{p=1}^{n} \langle \alpha(p) | H_{l_p} | \alpha(p-1) \rangle, \tag{3.10}$$

is given by the product of matrix elements of all the plaquette (bond) operators in the operator sequence, S_n. In the current Monte Carlo simulation in practice one needs to sample over effective configuration space $\{C\}$ of tensor products between the space of operator strings, $\{S_n\}$, and the set of initial spin states $\{|\alpha\} = \{|S_1^z(0), S_2^z(0), ..., S_N^z(0)\rangle\}$ at propagation step $p = 0$, that is, $\{C\} = \{S_n\} \otimes \{|\alpha\rangle\}$. A central property of the above formalism is that, running the simulation from an initial state $|\alpha\rangle$, the sequence consisting of operators, S_n, describes purely a sequence of configurations $|\alpha_1\rangle, \alpha_2\rangle$,... everything associated to the computational basis, and so that $|\alpha_1\rangle = H_{a_1}|\alpha\rangle$, $|\alpha_2\rangle = H_{a_2}|\alpha_1\rangle$,... Consequently, the spin states that are propagated not necessarily be stored since this knowledge is superfluous. Moreover, the weights $\sqsupseteq(\alpha, S_n) = ...\langle \alpha_2 | H_{a_2} | \alpha_1 \rangle \langle \alpha_1 | H_{a_1} | \alpha \rangle$ can be evaluated easily as products of matrix elements of plaquette (bond) operators consisting only spins the perturbing elementary Hamiltonian contains.

3.3 SSE Monte Carlo Update procedure

Before going to the sampling scheme used in SSE, we need to note that the memory for any numerical simulation is finite and thus one may have to trim the series expansion in the operator string S_n to some upper cutoff length, say $n_{\text{max}} \equiv \mathcal{L} \sim N\beta$. Usually, the typical size of n depends on the Hamiltonian and the temperature with lower ones having the higher cutoff lengths. The error of truncation vanishes exponentially with n_{max}. This can be understood from the expression of specific heat as well, $C_v = -\beta^2 \frac{\partial}{\partial \beta}\langle E\rangle = \langle n^2\rangle - \langle n\rangle^2 - \langle n\rangle$. We know that when $T \to 0$, C_v should approach zero. Then from the above relation of specific heat we have $\langle n^2\rangle - \langle n\rangle^2 = \langle n\rangle$, in words, the variance of n is $\langle n\rangle$ so that the variation of distribution decays exponentially above some order $n \sim N\beta$.

The fixed length scheme can be simply understood from the perspective of operator strings of same size $\mathcal{L}$ each, where we imbed a total of $\mathcal{L} - n$ identity operators at random locations into the operator sequence such that the total length now is extended to length $\mathcal{L}$. The position of the identity operators at $\mathcal{L} - n$ locations in the 'n' length operator sequence is entirely stochastic. Thus the configuration space is enhanced. However, the equivalent operator strings $S_{\mathcal{L}}$ of $n(S_{\mathcal{L}})$ that can be generated by simple permutations of the identities in the operator strings can be given as $\frac{\mathcal{L}!}{n(S_{\mathcal{L}})!(\mathcal{L}-n(S_{\mathcal{L}}))}$. The numerator comes by permuting the $\mathcal{L}$ operators which then has to be divided by a factor $n(S_{\mathcal{L}})!$ by taking into consideration that permutation of non-trivial operators is strictly rejected and by $(\mathcal{L} - n(S_{\mathcal{L}}))!$ permutation of identities does not alter the sequence. Therefore, one divides by this factors to return to the initial size of the configurational space and arrive at

$$\mathcal{Z} = \sum_{S_{\mathcal{L}}}\sum_{|\alpha\rangle} \frac{\beta^{n(S_{\mathcal{L}})}}{n(S_{\mathcal{L}})!} \frac{n(S_{\mathcal{L}})!(\mathcal{L} - n(S_{\mathcal{L}}))!}{\mathcal{L}!} \langle\alpha| \prod_{i=1}^{\mathcal{L}} H_{a_i} |\alpha\rangle \tag{3.11}$$

$$= \sum_{S_{\mathcal{L}}}\sum_{|\alpha\rangle} \frac{\beta^{n(S_{\mathcal{L}})}}{\mathcal{L}!} (\mathcal{L} - n(S_{\mathcal{L}}))! \langle\alpha| \prod_{i=1}^{\mathcal{L}} H_{a_i} |\alpha\rangle. \tag{3.12}$$

Here the summation involving $\{S_{\mathcal{L}}\}$, takes all permutable strings of operators with repetitions. Within the sequence, equivalent strings of operator that has the same sequence of non-trivial operators are also included. The cut-off length $\mathcal{L}$ that is determined for a given temperature and size of the system is adjusted during the equilibration time of the simulation until it converges to a large enough value appropriate to the system in hand.

3.3.1 SSE Sampling

In a way to efficiently sample the partition function in Eq. (3.4) we need to change a bit on the operator sequence $S_{\mathcal{L}}$ and the input trial (initial) state $|\alpha\rangle \equiv |\alpha(0)\rangle$ which is stored. We note that the modifications made in stored states are dependent, since a change in the operator string affects the states propagating along the imaginary-time thus also affecting the input state. Every update is required to satisfy some configurational conditions for the emerging latest configuration to have a weight that is non-zero. One should note that the sum involved in the partition function in Eq. (3.4) is nothing but a trace operation that constraints to have periodic boundary conditions in imaginary-time direction and therefore the condition $|\alpha(0)\rangle = |\alpha(\mathcal{L})\rangle$. Consider the Hamiltonian in our case:

$$\begin{aligned} \mathcal{H} &= \sum_{\square} H_{\square} + \sum_i H_i, && (3.13)\\ H_{\square} &= -J_0 A_{\square} + J_1 B_{\square} - J_2 \sum_B \vec{P}_{\square} \cdot \vec{P}_B, && (3.14)\\ H_i &= -K\sigma_i^x. && (3.15) \end{aligned}$$

A useful way of decomposing the current Hamiltonian is:

$$\begin{aligned} H_0 &= \mathbb{1} && \text{Identity operator,} && (3.16)\\ H_{\square} &= J_0 - J_0\sigma_1^z\sigma_2^z\sigma_3^z\sigma_4^z && \text{plaquette operator,} && (3.17)\\ H_{\square}^1 &= J_1 - J_1(\sigma_1^z\sigma_3^z + \sigma_2^z\sigma_4^z) && J_1 \text{ bond operator,} && (3.18)\\ H_{i,j}^+ &= J_2 - J_2(\sigma_i^z\sigma_i^z) && \text{bond operator with + sign before } J_2, && (3.19)\\ H_{i,j}^- &= -J_2 + J_2(\sigma_i^z\sigma_i^z) && \text{bond operator with minus sign before } J_2. && (3.20) \end{aligned}$$

Note the artificial induction of the constants J_0, J_1, and J_0 into the Hamiltonian to make the matrix element positive definite.

1. **Diagonal update:** During each operator sequence step p, if there is no diagonal operator al-

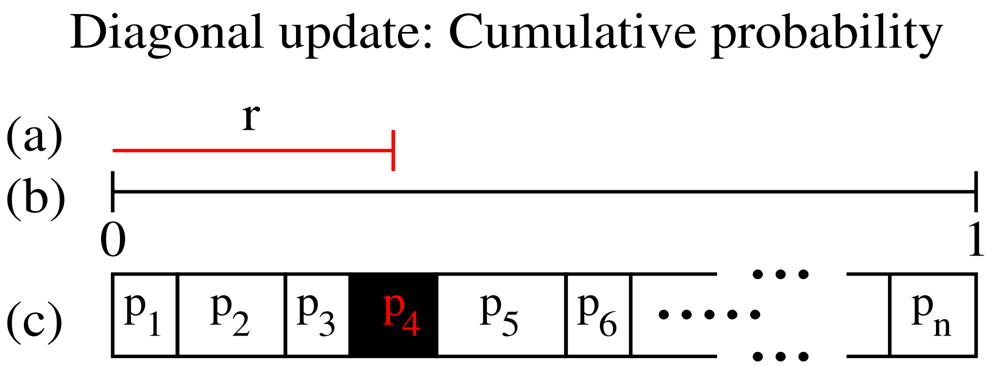

ready inserted, then using the acceptance probability given in Eq. (3.21) a decision is made whether or not to insert a diagonal operator into the operator string $S_{\mathcal{L}}$. On the other hand, if an operator (diagonal) is already present then again using the removal probability (see Eq. 3.21) a decision is made [See Fig. 3.1] whether or not to remove it. The following update changes the total number of non-trivial operators in the operator string, that is, the expansion order n, and thus the energy of the system also gets changed, since the energy of the SSE configuration is $E = -\langle n\rangle/\beta$. However, the initial $|\alpha(p-1)\rangle$ is not changed (See Fig. 3.1). The associated Metropolis acceptance probabilities for insertion and removal of a diagonal operator obtained by dividing the weights of a configuration before and after the insertion (or removal) is given by:

$$
\begin{aligned}
P(\mathbb{1} \to H_{\gamma_i}) &= \min(1, \frac{\sum \sqsupseteq_{\text{new}}}{\sqsupseteq_{\text{new}}}) = \min(1, \frac{\beta(NK + 2|J_i|)}{\mathcal{L} - n}), && (3.21)\\
P(H_{\gamma_i} \to \mathbb{1}) &= \min(1, \frac{\sqsupseteq_{\text{new}}}{\sum \sqsupseteq_{\text{new}}}) = \min(1, \frac{\mathcal{L} - n + 1}{\beta(NK + 2|J_i|)}). && (3.22)
\end{aligned}
$$

Here, γ_i refers to the Hamiltonian operator types as mentioned in Eqs. (3.16) such that γ_0 corresponds to identity operator and so on. Note that, the corresponding change in the expansion order $n \to n \pm 1$ leads to a contribution of a prefactor $\beta^{\pm}\frac{(\mathcal{L}-n\pm 1)!}{(\mathcal{L}-n)!}$ multiplying the ratio between the matrix element one of the identity operator H_0 and the coefficient given in the denominator (3.21) of the non-zero matrix elements. It is to be noted that the probabilities do not depend on the propagated state $|\alpha(p)\rangle$. Once all the probabilities of the corresponding operators have

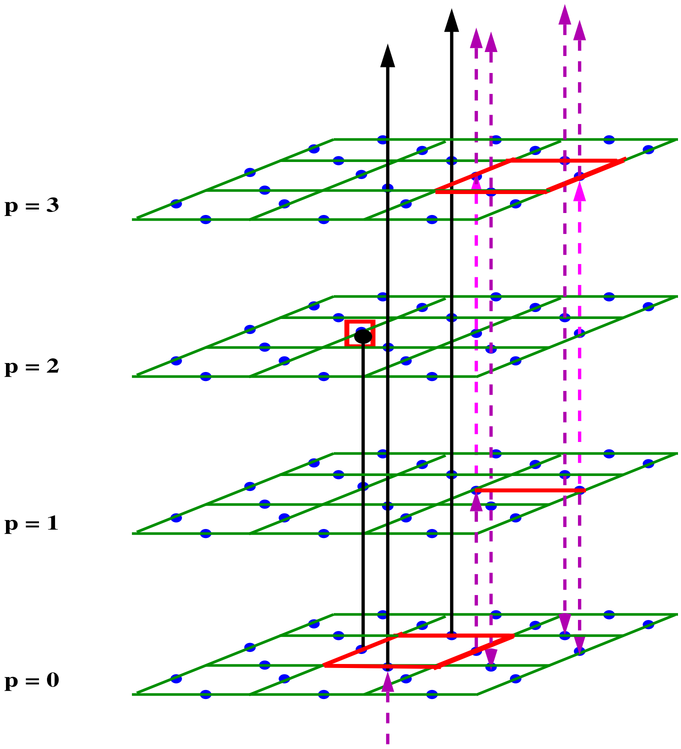

Figure 3.1: (a-c) The cumulative probabilities that are to be compared with a random number r for the insertion or removal of diagonal operators. The below panel shows the schematic of multibranch cluster update on a 2D lattice. The upward direction($p = 0, 1, 2...$) is the imaginary-time direction where the state at $p = 0$ is evolved into $|\alpha(p)\rangle$. Note the diagonal operators showed (red color plaquettes) and the off-diagonal operators represented as squares.

been identified, we insert them based on the cumulative probability: $P_j = \sum_0^j P_j / \sum_0^{N_t} P_j$, where N_t is the number of operator types present in the decomposed Hamiltonian.

2. **Off-diagonal update:** This is an update where in contrast to a diagonal update, the expansion order, n, do not get changed, rather an exchange between the operator types occurs (i.e from identity to the one the γ_i operators and so on) during equilibration. To be precise, the diagonal operators which have been inserted in the diagonal update (above), are converted into off-diagonal operators utilizing a loop or cluster update, which may also modify the initial state $|\alpha(0)\rangle$ and thus the magnetization in the SSE configuration. For systems with Heisenberg interactions, the loop updates are the only way to deal with them as they are one of the few updates that change the topology of the imaginary-time evolution without changing the magnetization which is and should be conserved in Heisenberg systems. Now, the removal of a diagonal

operator does not need any condition to be satisfied, however, for the insertion of a diagonal operator, a criterion based on the positivity of the matrix element $\sqsupseteq_\Box$ needs to be fulfilled. For example, consider the Hamiltonian with only the gauge term J_0, we then get the matrix element $\sqsupseteq_\Box = \langle \sigma_1^z(p+1)\sigma_2^z(p+1)\sigma_3^z(p+1)\sigma_4^z(p+1)\rangle | H_\Box | \langle \sigma_1^z(p)\sigma_2^z(p)\sigma_3^z(p)\sigma_4^z(p)\rangle$ to be either $2J_0$ or 0 making them positive and usable as relative probabilities in the importance sampling scheme. Therefore, the diagonal operator $H_\Box$ can only be inserted at a plaquette that satisfy the constraint of $\sigma_1^z(p)\sigma_2^z(p)\sigma_3^z(p)\sigma_4^z(p) = 1$ for $J_0 > 0$. Similarly, if we include the J_1 term the insertion probabilities get modified accordingly.

3.4 Percolation based multibranch cluster update

This is an off-diagonal update which is followed by the diagonal update. From the Eqs. (1.3) and (3.16) one might realize that there are various ways of performing the off-diagonal update, where the constant operators, $H_0 \equiv \mathbb{1}$ and spin-flip operators, $H_i = \sigma_i^x$, are exchanged. In this process, no change in the expansion order, n, is while the initial state $|\alpha(0)\rangle$ could get updated resulting in a net change in magnetization without changing the energy $E = -\langle n \rangle/\beta$ (since n doesn't get changed).

One of the simplest ways of replacing the identity and the flipping operators (such as transverse fields) is the local update, where a cluster is restrained to individual sites and extends only in the imaginary-time, however, this approach suffers from critical slowing near the quantum critical points with long autocorrelation times. Therefore, we directly stick to the discussion on the non-local updates, that is, the cluster updates. It is a well-known fact that cluster algorithms usually fasten Monte Carlo dynamics with relatively much shorter autocorrelation times than the local updates, particularly near the critical boundaries where critical slowing is typical.

The superiority of the cluster updates can be understood from the proper analytical observation, that is, from the Fortuin-Kasteleyn transformation. A mapping from the ferromagnetic Potts model to a corresponding bond percolation problem (see [164] for detailed review) was first performed. It may be noted that the resulting configurations from the percolation models after every sweep is independent of the previous configurations, thus making simulation very efficient with the autocorrelation times that are exactly zero.

The characteristic principle involved in the construction of the multibranch cluster is that the cluster is usually randomly shaped in space and imaginary-times. And the weight of the new configuration obtained after flipping every spin in the cluster must be non-zero to maintain detailed balance. In schematic Fig. 3.1 examples of cluster formation with certain shape is shown. However, a resulting configuration with non-zero weight is obtained only when all the spins connected to the plaquette (bond) are flipped simultaneously with corresponding vertex weights given according to Eq. (3.16). This results in clusters extending both along the spatial and propagation direction. Particular branches of the cluster are stopped when it encounters an off-diagonal (flipping) or constant operators. The final cluster formation rules are depicted in Fig. 3.2(a-c)): An entrance leg of an incoming cluster branch entering into a vertex is shown by a dashed arrow; each one spins is flipped dictated by the rules shown in Fig. 3.2(a-c)); finally, outgoing arrows in Fig. 3.2(a)) depict new cluster branches. Requisite to the cluster formation is the linked vertex list (doubly or multiply) [157, 153], which couples the legs of vertices across imaginary-time. Interested readers can further refer to Ref. [153] for a quick review on the SSE implementation and Sect. 3.3.1 for a representative example of how one number of the vertex legs in a computer simulation stored as linked lists. Nevertheless, the construction of a cluster can be elucidated in the following steps. Initializing a cluster involved picking one of the legs of the n non-trivial vertices in the operator string $S_{\mathcal{L}}$ at random with the corresponding spin of the entrance leg that is to be flipped. At this step, depending on the type of vertex to which the leg is connected different necessary operation is to be taken. For example, if the legs are connected to a vertex consisting of a diagonal operator, then the cluster extends to at all legs of the vertex (see Fig. 3.2(a)). In other words, this means that except for the current leg, all the other legs emanating from the vertex are put onto a stack that is to be picked later serially as new entrance legs. On the other hand, if the entrance leg is connected to a constant or the vertex containing the off-diagonal operator, in that case only the spin corresponding to the entrance leg is flipped. Because of this a change from H_0 to H_i, and vice versa is seen. Further, there are no additional legs to be added to the cluster at this point resulting in a termination of the cluster branch. This way, all the legs in the stack are processed until none is remaining in the stack. At this point, the cluster formation gets terminated and is complete. In Sec. 3.5 particulars for a systematic application of the multibranch cluster update are provided for a case that does not consider a longitudinal field (coupling to S_i^z) where a cluster is always flipped since no net change in the configurational weight is seen: because, the matrix element of the Ising plaquette (bond) operators does not depend on the absolute orientation of the spins and is not affected when both the spins are flipped simultaneously, on the other hand, the weight corresponding to the matrix elements of the constant and transverse (spin-flip) operators are both equal to K and therefore exchanging among them do not change the weight.

It may be noted that, in contrast to the loop update of Sec. 3.5, the cluster formation is entirely deterministic given the operator sequence. This makes it easier to construct all the clusters spanning the entire lattice of spatial and imaginary-time and also flipping each cluster independently of probability 1/2, as in the classical version of Swendsen-Wang (SW) algorithm [165]. Moreover, in the classical limit [165] of $K = 0$ where M number of imaginary-time slices collapse to a single time slice, the current cluster construction rules just coincide with the classical SW algorithm. Each cluster as said is to be flipped randomly and this can be decided even before the construction of the cluster. In any case, even if a decision of cluster was made not to flip, the cluster construction should continue fully so that a marking of visited vertex legs can be made for future construction of new entrance legs corresponding to a new cluster. One may also analyze the distribution of cluster sizes, where the cluster size is defined as the number of legs $n_{\text{legs}} = n_{2-\text{leg}} + n_{4-\text{leg}}$ that belong to a cluster.

The quantum cluster only changes the initial state $|\alpha(0)\rangle$ whenever a cluster branch winds around the boundary in imaginary-time. Also, to identify branches winding the imaginary-times, one may

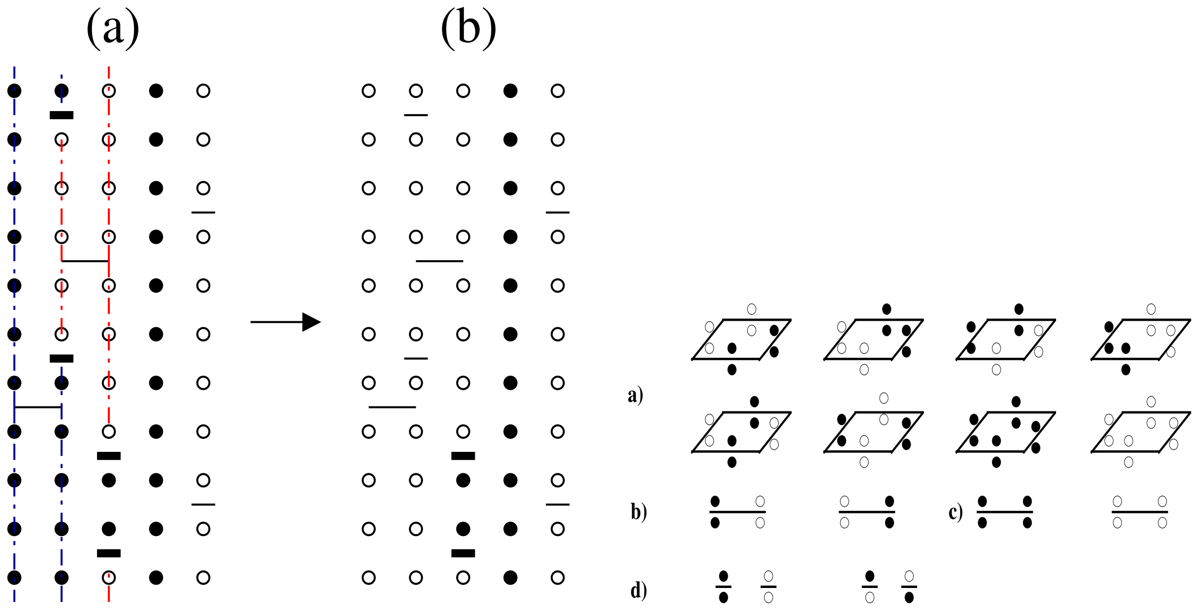

Figure 3.2: (Left) Schematic representation of the quantum cluster off-diagonal update for a chain of five spins. In the left columns, a cluster shown in the red cluster is flipped to a configuration shown in the right column. The entire lattice can be decomposed into sets of disjoint clusters that have to be flipped deterministically. Note that the configuration weights before and after flipping are essentially the same, therefore, they have to be flipped with a probability of 1/2. The cluster construction is shown also ensures the constraint of periodic boundary conditions in the imaginary-time direction is obeyed. (Right) Distinct vertices that could be encountered during the cluster update as represented by the Eq. (3.16).

mark the direction of the cluster growth along the linked vertex list as ”up” or ”down”. Then, the winding branch corresponds to an increase (decrease) of the leg numbers when going ”down” (”up”).

Finally, a single Monte Carlo step (MCS) consists of a full sweep of diagonal updates, followed by the off-diagonal update involving the construction of linked vertex list and an SW type quantum-cluster update. Where in quantum cluster update all clusters are constructed and flipped with heat-bath probability 1/2. And, free spins that do not belong to any cluster can be flipped with probability 1/2.

Unfortunately, the percolation-based approach becomes inefficient significantly due to the diverging degeneracy (with system size) that is carrying with the gauge-term, J_0. The approach suffers critically from the slowing down and therefore a loss of ergodicity is seen. The problem in the current method has to do with the plaquette term J_0 where we flip all the spins in a plaquette once the corresponding operator is encountered in the multicluster branch. However, we see below that a smart way of approaching the current system is to decompose the gauge term further into two parts. The details of which will be explained in the next section. More details regarding this can be found in Ref. [164].

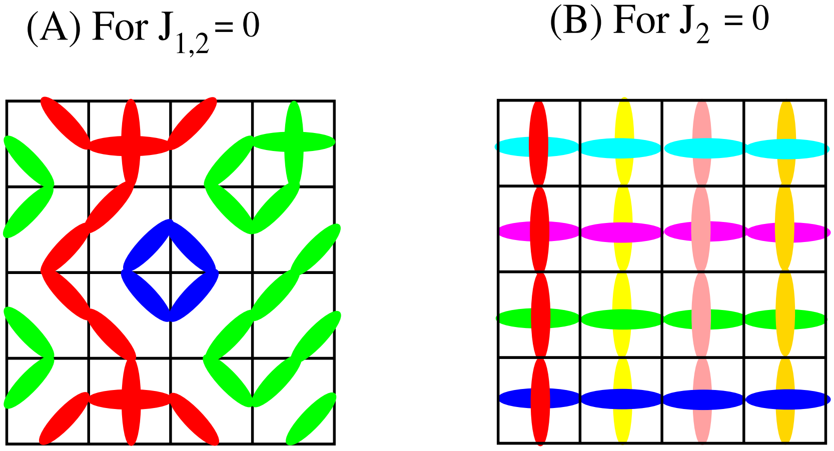

Figure 3.3: Schematic showing the natural formation of loops after decomposing the Hamiltonian into a set of dimers covering the entire lattice. Each dimer is connected to a neighboring dimer until it meets the initial one forming a loop. Different colors of the loop corresponding to different Swendsen-Wang clusters that need to be flipped independently with probability 1/2. Notice the contours of the loop for $J_1 \neq 0$ case (Fig. (B)), they are nothing but the non-local gauge operators found in chapter 2. However, it may be noted that depending on the Hamiltonian one has to incorporate accordingly the contours that will lead to an efficient sampling scheme.

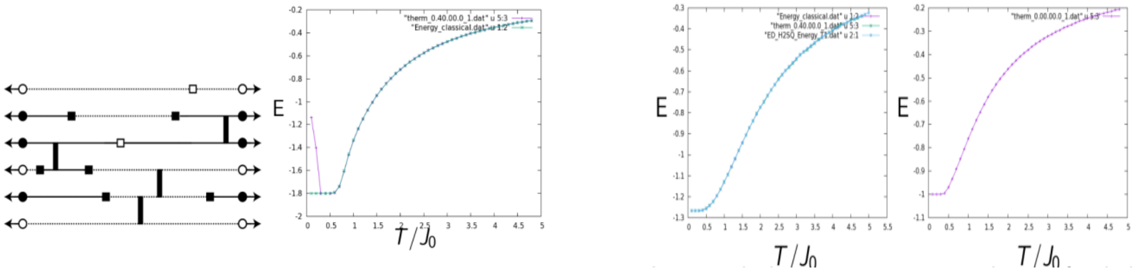

Figure 3.4: The left panel shows the results of total energy per spin versus temperature as calculated from SSE QMC (blue) using the unimproved quantum cluster update, and also from the Exact diagonalization analysis (purple). The discrepancy between them can be seen at lower temperatures. In the right panel, we show that this discrepancy is removed after the improvisation of the quantum cluster algorithm briefly discussed in sec. 3.5.

3.5 Plaquette based quantum-cluster update

Earlier methods relied on constructing the clusters based on a *link-decomposition* of Hamiltonian found to be inefficient [164], despite being tried in various forms by constructing the clusters along τ-dimension (imaginary-time). Nevertheless, here we use a variant of a recently developed micro-canonical cluster algorithm (quantum cluster update) where it uses the plaquette decomposition of the Hamiltonian within the framework of stochastic series expansion (SSE) pioneered by Sandvik and others [153, 166, 167, 168, 169, 170, 171, 164, 161]. Clusters are constructed based on a plaquette percolation process with the the notion of *premarked motifs* which act as a flag in determining how it connects the legs of all diagonal plaquette operators 'living on' various planes of imaginary-time direction. Once all clusters are constructed, each can be independently flipped with probability 1/2 within a Swendsen-Wang type implementation. Here in the present study, we have employed and improvised an algorithm within the stochastic series expansion Monte Carlo method [164]. Readers interested in the details regarding the efficiency and performance of the algorithm compared to the percolation-based algorithm can find here [164] for an 'odd' Ising gauge Hamiltonian with antiferromagnetic Ising exchange term. The major difference in the design of the algorithm is that the choice of premarked motifs differ for each system with complicated interactions or frustration, where intuition or little prior knowledge of the equilibrium ensemble is a bonus for improving the algorithm further, this is also where we had implemented our idea to investigate the Hamiltonian we considered.

Since three distinct regions are corresponding to three different parameters J_0, J_1, J_2, we thus identify different premarked motifs choice as shown in Fig. 3.5. In Fig. 3.5(a), we provide the cartoon picture of pre-marked motif for a general plaquette four-body interaction signified by finite J_0 and $J_{1,2} = 0$. In Fig. 3.5(a), we show a privileged single site premarked motifs. It is easy to find that four such choices are corresponding to four sites in a given plaquette. In Fig. 3.5(b) and (c), we represent in the pink shaded region, the sites whose spins are to be flipped. They all correspond to the single site premarked motif described in Fig. 3.5(a) and (d), we represent the choice of having two sites as the preferred premarked motifs. There are two such choices.

For $J_1 \neq 0$, $J_2 = 0$, the only choice of premarked motifs are shown in Fig. 3.5(d) where two frustrated bonds (only those with one parallel to the other) are required to be on each plaquette which corresponds to eigenvalue $4J_0 + 4J_1$, while configurations with four or zero frustrated bonds have eigenvalue zero and hence corresponding plaquette operators do not appear in the operator string. Our choice of the motif in the $J_2 \neq 0$ case also consists of two privileged diagonal sites among the

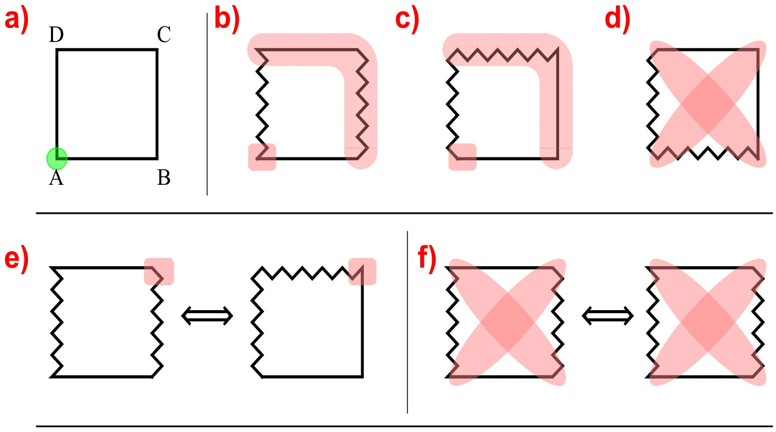

Figure 3.5: Various choices of cluster decomposition rule for premarked motifs are shown in (a)-(d). In (e) and (f) we show the distributions of parallel and anti-parallel bonds corresponding to the above choices. The zigzag lines indicate the bonds consisting pair of antiparallel spins, the frustrated bonds, and unfrustrated bonds correspond to solid lines.

four that make up a spatial plaquette as in Fig. 3.5(d). Thus each spatial plaquette has two distinct possible motifs. The motif on a given spatial plaquette determines the cluster decomposition of plaquette operators at that location in the following way: if only one frustrated bond touches the two privileged site, the four legs corresponding to these two sites are assigned to a priori different cluster, and the other four legs make up the other cluster. If the privileged site is touched by two or zero frustrated bonds, then the four legs corresponding to the privileged site and its diagonally opposite site are assigned to one cluster, and the other four legs are assigned to a different cluster (which could in principle merge with the other cluster at a future step in the cluster construction).

We observe that in the case of $J_1 = 0$ there is no apparent spin-freezing thus making the algorithm much more efficient in this regime. However, despite improvising the sophisticated algorithm to work in the case $J_1 \neq 0$, we see some apparent spin freezing at low temperatures, and hence to avoid that we also invoke the replica-exchange method with temperatures ranging from 0.05 to 1.0. We use system sizes varying from L = 24 to 32 ($N = 2L^2$) with a standard 1×10^7 iterations for equilibration and 1×10^7 for measurements. Results are divided into six bins to estimate statistical errors by the variance among the bins.

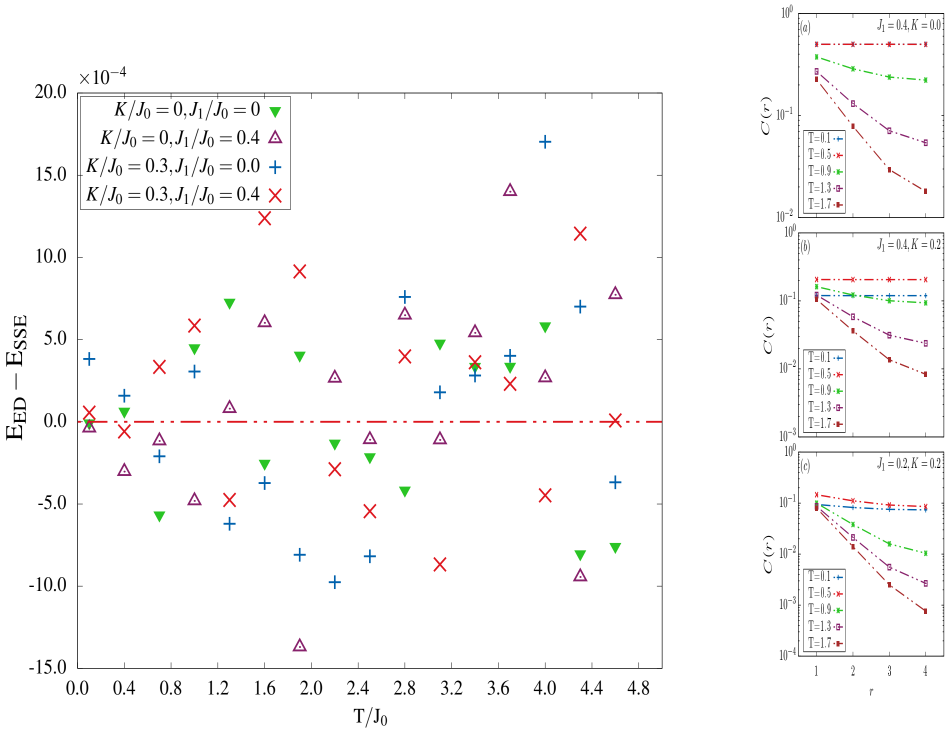

Figure 3.6: (Left) The match between the configurational energies after convergence between exact diagonalization technique and the current SSE method after using the improvised algorithm as discussed in Sec. 3.5. (Right) The correlations function $C(r)$ calculated as a function of r by equally averaging over all the classical groundstates for zero and finite transverse fields.

3.6 Physical Quantities: Probing the liquid-like state

Given the wide scope of our model which might host different phases depending on the relative magnitude of the model parameter and temperature as well, we introduce the relevant parameters in detail. This will help us to identify each phase as well as to distinguish from each other without ambiguity. At very high temperature $T > J_i$, one generally expects a paraelectric phase where the dipole moments associated with each plaquette are disordered. The paraelectric to ferroelectric phase transition (due to dipole-dipole interaction term J_2) as we lower the temperature is characterized by the order parameter P which is nothing but the electronic polarization and the associated susceptibility χ_P. They are defined as below,

$$P = \frac{1}{N}[|S(0,\pi)|^2 + |S(\pi,0)|^2]^{1/2}, \tag{3.23}$$

$$\frac{\chi_P}{N} = \beta[\langle P^2 \rangle - \langle P \rangle^2], \tag{3.24}$$

where $S(\mathbf{k})$ is the static spin-structure factor given by

$$S(k) = \frac{1}{N}\sum_{i,j}^{N} S_i^z S_j^z \exp(-\mathbf{k}\cdot\mathbf{r}_{ij}). \tag{3.25}$$

To locate the critical temperature associated with this paraelectric to the ferroelectric phase transition, we use the Binder Cumulant analysis, where the Binder parameter Q_P [172] is given as

$$Q_P = \left(1 - \frac{\langle P^4 \rangle}{8\langle P^2 \rangle^2}\right). \tag{3.26}$$

Apart from the presence of paraelectric and ferroelectric phases, at low temperatures, and for small values of J_2, the dipole-dipole interaction strength, the groundstate is dominated by states determined by J_0 and J_1. In this situation, the groundstate manifold is dictated by the states which satisfy the local 'ice-rules'. In a quantum mechanical sense, this is a quantum liquid state. To distinguish this state from the usual paraelectric states, we need to define an order parameter that can successfully establish the presence of this state which should differentiate it from the usual paraelectric phase and ferroelectric phase. To this end, we define the parameter ρ which detects the local ice-rules state on a plaquette, i.e, the partially disordered locally-correlated liquid-like paraelectric phase,

$$\rho = \frac{1}{N}\sum_{p} I(p), \tag{3.27}$$

where $I(p) \rightarrow 1$, if the given plaquette P is in one of the local four-fold degenerate ice-rule states with finite-molecular polarizations or finite-dipole moment and similarly $I(p) \rightarrow -1/3$ otherwise. The details regarding the assigning of the particular values for $\rho_\Box$ are detailed in chapter 4. To further corroborate the results of phase transition and crossover points we also estimate the susceptibility corresponding to ρ by calculating their fluctuations as given by,

$$\frac{\chi_P}{N} = \beta[\langle \rho^2 \rangle - \langle \rho \rangle^2], \tag{3.28}$$

where the crossover from the disordered but correlated dipoles into a paraelectric phase can as well be detected in the specific heat measurements as shown in Fig. 3.7(e)-(f) We know from the earlier studies [173, 174] that the presence of dipole-dipole interaction (the J_2 term in the Hamiltonian in equation (3.13) induces a ferroelectric order. In the absence of J_2, the groundstate is highly degenerate. The degeneracy for $J_1 = 0$ is exponential though with J_1 it is proportional to the peripheral size of the system. On the other hand, the global ferroelectric order is fourfold degenerate. Thus we see that the effect of temperature on the system might be very intricate due to the energy cost for low energy excitations due to competing interactions as well as due to the degeneracy of the groundstate manifold for each parameter. This necessitates examining the order parameter P and ρ both. Interestingly we find that they do not follow each other as we increase the temperature. Correspondingly, the susceptibility also shows contrasting behavior. We first discuss the temperature dependence of P and ρ followed by the corresponding susceptibility.

3.6.1 Temperature dependence of P and ρ

The general behavior as evident from the QMC simulation suggests that as we turn on the temperature the ferroelectric order parameter denoted by P sharply decreases for a very small value of temperature. However, this decrease seems to be a two steps process. We call the first phase of decrease of P as the quantum liquid states and the higher temperature counterpart as a usual paraelectric phase. The P shows a shoulder like a hump at the transition from quantum liquid-like states to paraelectric states. In Fig. 3.7(a) and (b), we have shown the variation of P in blue points for $J_0 = 1.0$, $J_1 = 0.5$, $J_2 = 0.020, 0.024$. The presence of quantum liquid-like states is apparent from the temperature variation of ρ as presented in blue points in Fig. 3.7(c) and (d). We observe that ρ

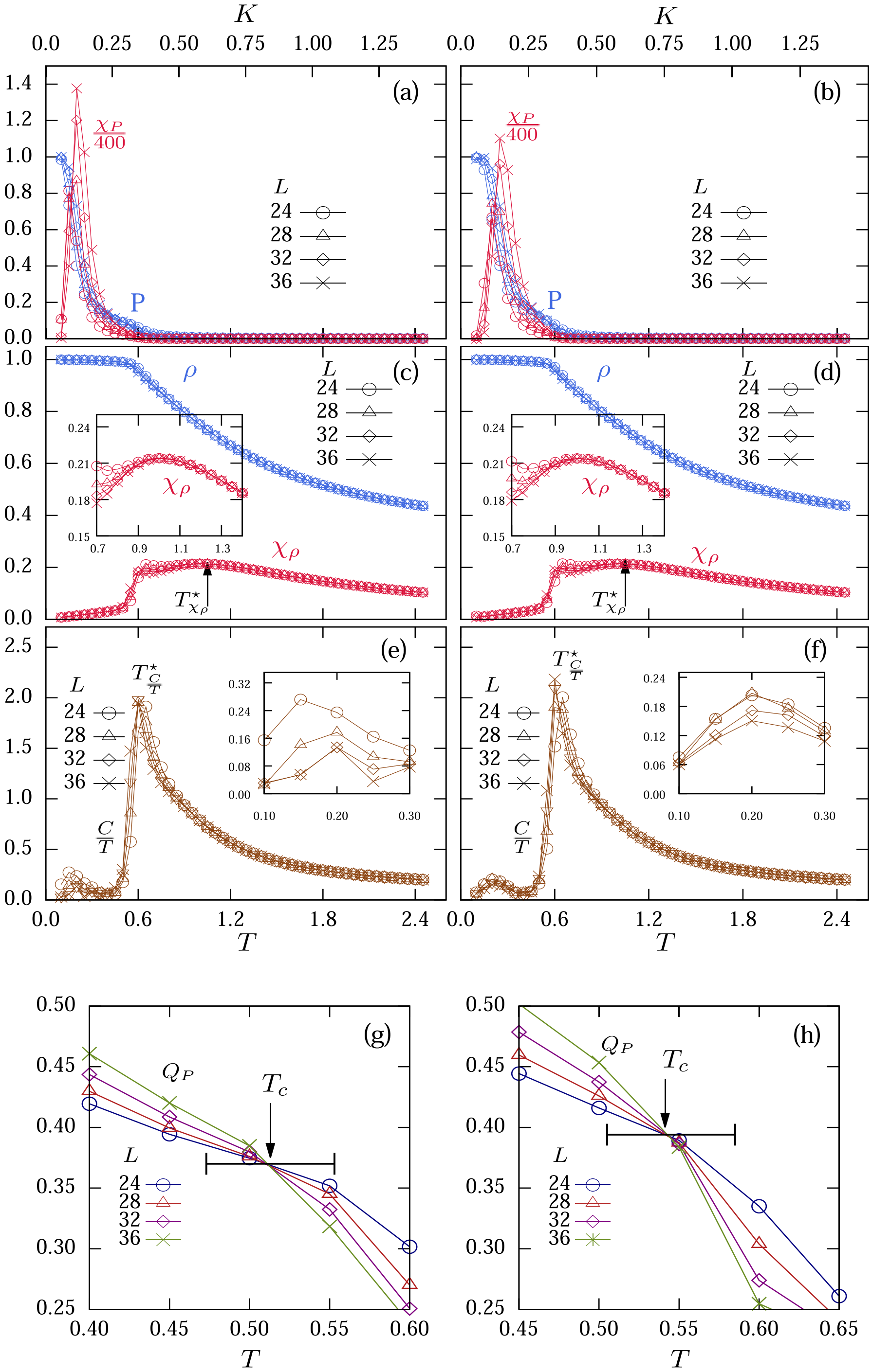

Figure 3.7: In panel (a) and (b) the red points and the blue points show the plot for χ_P and P. Similarly, in (c) and (d), we present ρ and χ_ρ by red and blue points respectively. In (e) and (f), specific heat divided by temperature (C/T) has been shown. Binder parameter has been shown in panel (g) and (h). In all the plot, various points denote different system size as shown. All the results are calculated along the contour $K/T = \tan(\theta)$ where $\theta = \pi/6$. For a detailed description of the above, we refer to Sec. 3.6. The parameter values used in the figures are $J_0 = 1.0$, $J_1 = 0.5$ with $J_2 = 0.020$ for left panel and $J_2 = 0.024$ for right panel.

is almost constant throughout this quantum liquid-like state and decreases monotonically when the system yields to a paraelectric state. Thus the order parameter P and ρ suggest that as we increase

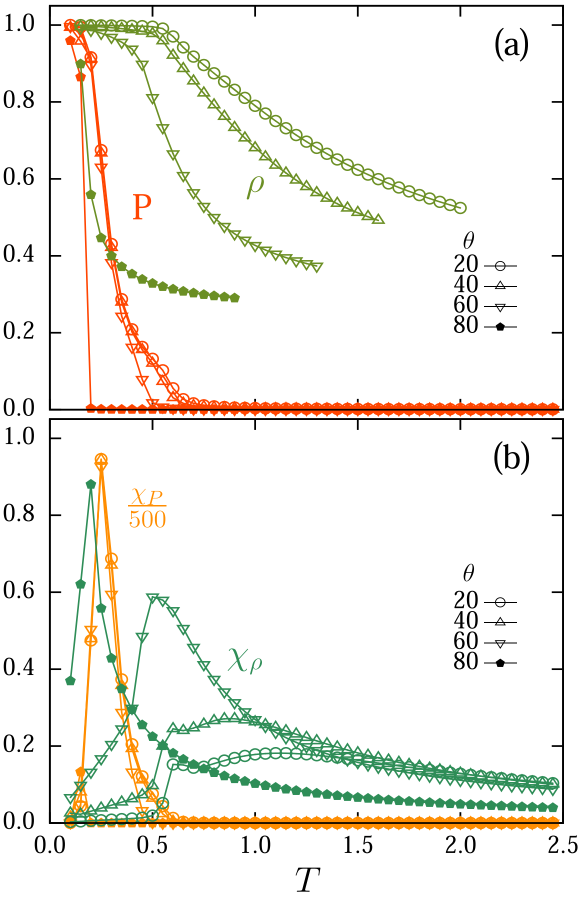

Figure 3.8: In the upper panel we show the temperature dependence of order parameter and ice-rule parameter ρ by the orange and green points respectively. The corresponding susceptibility has been plotted in the lower panel with the same color convention as the upper plane. Note that in the above 2D plot each graph denotes a specific line in the $T-K$ plane. Each line is represented by the corresponding slope of the line θ. For the details of the plot refer to the text in Sec 3.6.

the temperature from zero, the system starts from the ferroelectric phase, moves to an intermediate quantum-liquid-like state, and finally reaches a pare-electric phase. In the upper panel of Fig. 3.8 we have shown by orange and green points more plots for the behavior of P and ρ respectively for various values of θ in the $T-K$ plane. It shows that for large values of θ, P and ρ decreases more rapidly than the small values of θ. This indicates that pressure and temperature have the opposite effect on the system. The pressure denoted by K tends to stabilize the ferromagnetic and the intermediate quantum liquid-like state.

3.6.2 Susceptibility χ_P and χ_ρ and specific heat C/T

The susceptibility obtained due to P is shown in Fig. 3.7(a) and (b) by red points which shows a jump at the transition from ferroelectric phase to quantum liquid-like states. This suggests that ferroelectricity is almost destroyed at this transition. However the susceptibility corresponding to ρ, that is χ_ρ, shows a very interesting feature. Initially, it is almost zero, increases very slowly until the temperature reaches near the transition from quantum liquid-like states to the paraelectric states. At this transition the χ_ρ jumps at a higher value and remain almost constant up to a certain temperature which we call T_ρ and after this, χ_ρ decreases monotonically. The specific heat at a very large temperature shows monotonically decreasing behavior characteristic to the usual paraelectric phase but at low temperature, it shows two peaks of different magnitude as denoted in Fig. 3.7(e) and (f). The largest peak appears at the transition of quantum liquid-like state and we denote this temperature by $T^\star_{C/T}$. However, the sharp nature of the peak indicates a possible order-disorder phenomenon where the degeneracy seems to be uplifted to some extent. Below this temperature specific heat shows another small peak at where the P starts to decrease from the initial constant value for small T. The peak height of this smaller one tends to decrease with the increase of system size as denoted in the inset of Fig. 3.7. In the lower panel Fig. 3.8, we have shown the behavior of χ_P and χ_ρ for various values of θ in the $T-K$ plane in orange and green plots respectively. It shows that for large values of θ, P and ρ have sharper peaks and also they decrease more rapidly compared to the small values of θ. It suggests that the stability of the intermediate liquid-like the state is enhanced by increasing the K/T ratio. This may be attributed to the fact that the increase of K results in enhancing the bandwidth of the system resulting in decreasing the thermal effect.

3.6.3 Binder cumulant and critical temperature

In the foregoing discussion, we have already introduced the two critical temperatures. The largest one is the $T^\star_{\chi_\rho}$ which is signified by the step-like jump from almost zero values of χ_ρ to a higher value. Below this temperature, we observed another critical temperature signified by the largest jump in the specific heat at the transition to the paraelectric phase from the quantum liquid-like state. This temperature is denoted by $T^{\star}_{C/T}$. Our analysis for the Binder cumulant as shown in Fig. 3.7(g,h) shows that the actual phase transition is very near to the $T^{\star}_{C/T}$ and we denote this temperature as T_c. As for as our numerical results and analysis are concerned, $T_c = 0.56(47)$ and $0.56(03)$. for $J_2 = 0.020$ and 0.030 respectively. The corresponding $T^{\star}_{C/T}$ is obtained as $0.060(03)$ and $0.61(40)$ respectively.

3.6.4 Phase diagram

The numerical results presented above suggest the presence of three phases as we increase the temperature. The first one is the ferroelectric phase which survives for very small temperatures and extends up to T_c as obtained from Binder cumulant. We call this phase $\prod_f$. The jump in the specific heat signified by $T_{C/T}$ is a little higher than the T_c. Above the T_c there is a presence of a complex quantum liquid-like state which extends up to some critical temperature T_{χ_ρ}. This phase is very intriguing as long as the behavior of the order parameter is concerned and we call this phase as $\prod_{ql}$. After T_{χ_ρ}, the normal paraelectric phase develops with no residual quantum correlation between the dipole moments. The above three critical temperatures defined above depend on the values of J and the K. It is instructive to present the above three phases in a contour plot in the $T-K$ plane and this is presented in Fig. 3.9. The results are shown for different J_2 strengths in the $T-K$ plane. For the case where $J_2 = 0$ the system shows a crossover transition from quasi macroscopic degenerate liquid-like state to a completely disordered state, with the crossover temperatures shifting to higher temperatures with J_1 as expected. However, even for J_2 very small, the system orders ferroelectrically (the region below T_c, orange circles), the region between the T_c and T_{χ_ρ} belongs to the liquid-like state.

It is interesting to note that the scaling behavior of the critical boundary shows unique characteristics, the boundary does not extend into the liquid-like region rapidly but rather slowly indicating that the dependence of T_c with J_2 is complex with a lower dynamic exponent than the model having

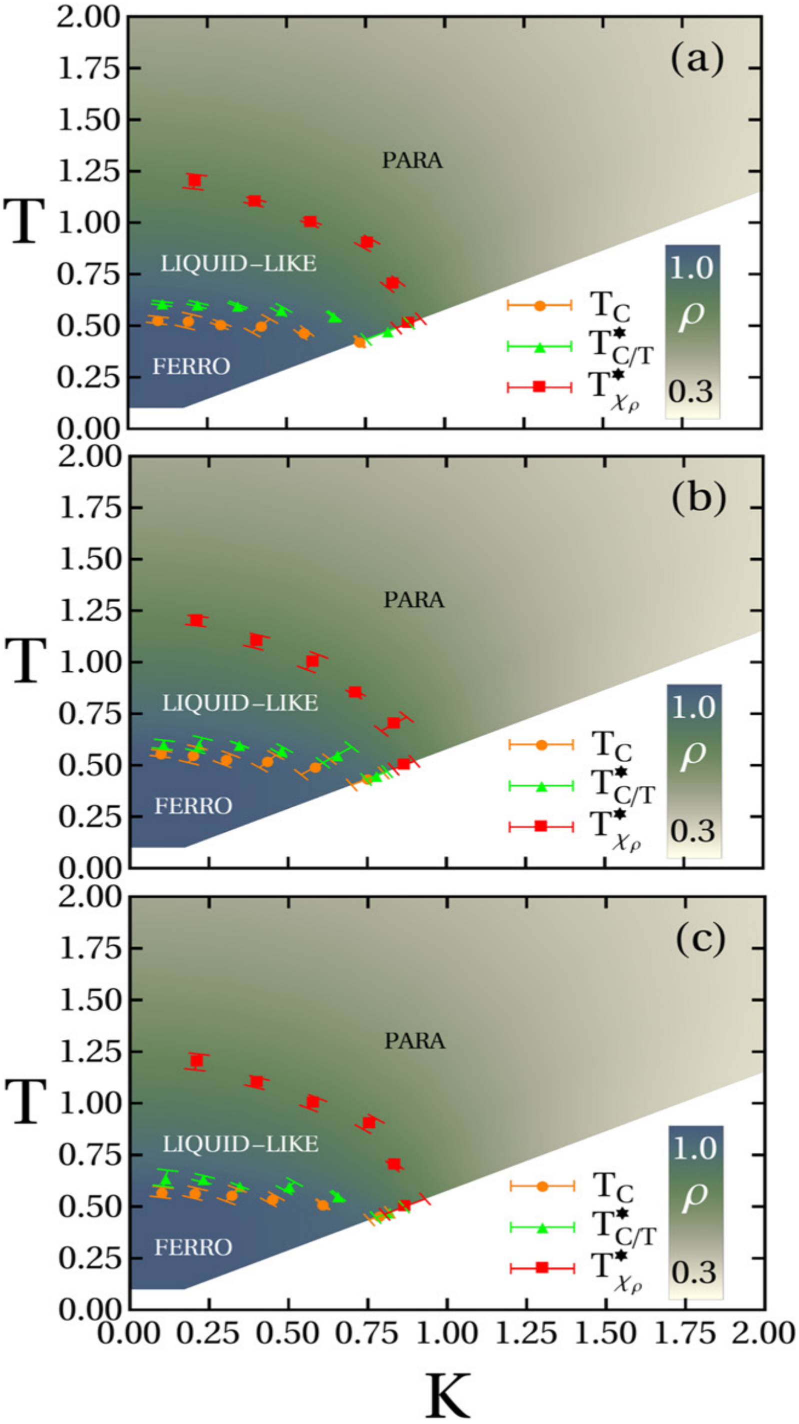

Figure 3.9: Phase diagram showing the critical and crossover points, the Figs. (a)-(c) correspond to the values $J_2 = 0.020$, $J_2 = 0.024$, $J_2 = 0.028$ respectively. The orange dots indicate the critical points for Ferro to liquid-like transition obtained from the binder analysis, green triangles indicate the cross over points $T_{C/T}$ obtained from the C/T curve, while the red squares indicate the T_{χ_ρ} obtained from χ_ρ.

only two-body interactions [103]. Another aspect is that the ratio of thermal energy (T_c) to that of J_2 is also less. We believe that the colossal enhancement of T_c with J_2 is related to the lifting of quasi macroscopic degeneracy. The above finding could be confirmed by experiment in conjunction

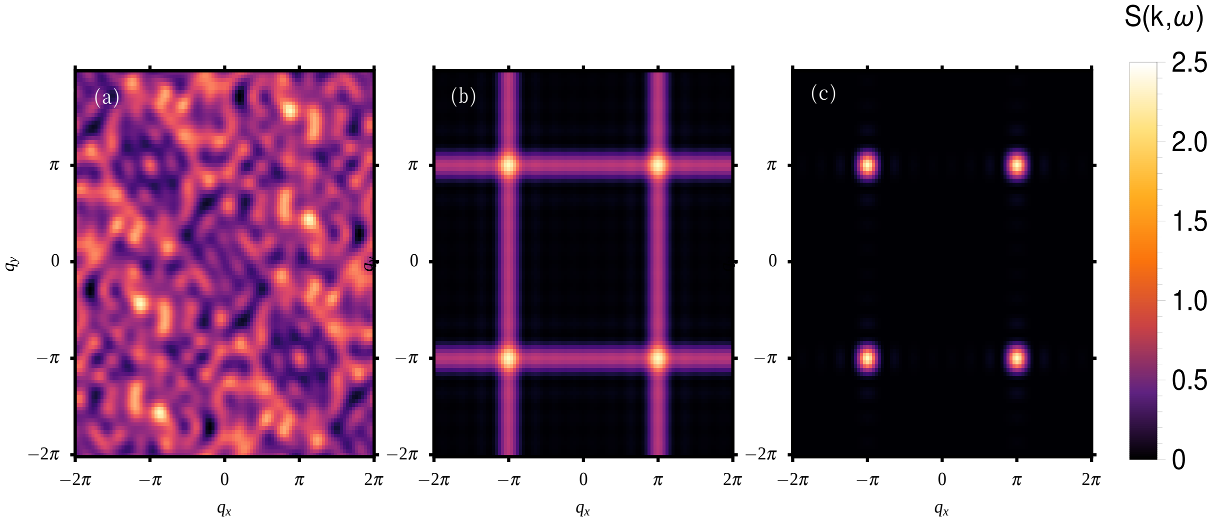

Figure 3.10: The static structure factor $S(\mathbf{k})$ calculated in three different parameter regimes. The subfigure (a) is estimated for the completely disordered case of $J_{1,2} = 0$, while (b) is estimated for the case of disordered dipole when J_1 is finite with J_2 still zero. Finally, subfigure (c) is estimated for a global ordered case of ferroelectric ordering in the lattice.

with a first principle study yielding an estimation of the parameter of the model Hamiltonian. It is interesting to note that all the phase transitions that we observe are not of first-order but rather like second-order especially the transition from $\prod_f$ to $\prod_{ql}$. On the other hand, the transition from $\prod_{ql}$ to $\prod_p$ is a smooth crossover. The phase $\prod_{ql}$ and $\prod_f$ suggests quite an interesting behavior of ρ and C/T. Let us begin with $\prod_f$ first. At $T = 0$, the system is in a ferroelectric state with global groundstate degeneracy of four. As we increase the temperature, the ferroelectric order parameter P decreases rapidly but ρ remains constant and besides, we observe a small peak in C/T. This suggests that the global ferroelectric order reduces into the domain of ferroelectric clusters and also includes the presence of other states not contributing to P but consistent with ice rules. The possibility of the presence of these additional states explains the small peaks in C/T which also decreases as we increase the system size. As far as the phase $\prod_{ql}$ is concerned, we observe the steady decrease of the ice rule order parameter ρ which suggests that the excitations now include the non-ice rule states as expected. However, the quantum correlation is not lost completely until the critical temperature T_{χ_ρ} is reached.

3.6.5 Static structure factor

To have a basic understanding of the Hamiltonian, we also estimate the static structure factor (SSF) in our Monte Carlo calculations. We note that to calculate any spin-spin correlation function, the operator loop in SSE have to go twice. Making the problem intractable. If we have a Hamiltonian with uniform J_0, J_1, J_2 one may invoke the translational invariance. So, the SSF can be estimated by,

$$\begin{aligned} S^{zz}(\vec{k}) &= \sum_{i,j} \sigma_i^z \sigma^j \exp(i\vec{k}(\cdot \mathbf{R_i} - \mathbf{R_j}), \\ &= \sum_{i,j} \sigma_i^z \exp(i\vec{k}(\cdot \mathbf{R_i})\sigma^{\mathbf{j}} \exp(\mathbf{i\tilde{k}}(-\mathbf{R_j}), \\ &= \sum_{i} \sigma_i^z \exp(i\vec{k}(\cdot \mathbf{R_i}) \sum_{\mathbf{j}} \sigma^{\mathbf{j}} \exp(\mathbf{i\tilde{k}}(-\mathbf{R_j}), \\ &= \left| \sum_{i} \sigma_i^z \exp(i\vec{k}(\cdot \mathbf{R_i}) \right|^{\mathbf{2}}. \end{aligned} \tag{3.29}$$

Now, the computational cost to estimate the SSF is reduced from N^2 operations to N. We plot the results of it in Fig. 3.10. The Fig. 3.10(a) is obtained for the values of $J_{1,2} = 0$, we see that the SSF is distributed all over the momenta in $k_x - k_y$ plane. And the system can take any momenta. This is possible when the system does not show any order. Because in a disordered state, many degenerate configurations with no translational invariance overlap to give such widely distributed momentum. However, when we turn on J_1, we see four lines crossing at four points corresponding to the $M-$high symmetry point (specifically at $(-\pi, \pi), (\pi, \pi), (\pi, -\pi), (-\pi, -\pi)$). The lines indicate that the S^{zz} quasi-particles can still have finite correlations corresponding to a disordered case but with a degeneracy lesser than the case of $J_1 = 0$ (Fig. 3.10(a)). Now, when a finite J_2 is turned on, the system has only four possible states (see Fig. 3.10(c)). This also testifies the results obtained in chapter 2 that the J_2 interaction breaks the symmetry that is present in the cases of $J_2 = 0$ with a diverging degeneracy.

3.7 Chapter summary

We have considered a model where at zeroth order there is a four-spin Ising gauge like the interaction of protons in the pseudo-spin formalism. Earlier results on the model showed that the system hosts a deconfined phase for $J_2 = 0$ [173] at zero temperature. We use the model here to extend the phase diagram along the finite temperature axis. Our results show ice-rule-dominated strong proton-proton correlations to be the main physics of the system. Motivated by experiments and the previous studies, the phase diagram in the $T-K$ plane suggests that the qualitative shape of the critical boundary T_c is closer to a linear behavior for small field strength consistent with the experimental results [32, 29, 62], though at large pressure, T_c and T does not behave linearly in contrast to experimental results where one finds a complete linear behavior for all ranges of applied pressure. Another aspect that we find in our study is the difference between T_c and T which remains constant throughout all pressure ranges, which to our opinion is a remarkable success of our study. However, our results indicate a possible second-order phase transition in contrast to experiments. This deviation with experiments might be reconciled by considering the interlayer coupling or more complicated couplings to lattice distortions, which are neglected in our model. The temperature dependence of the interaction parameter can not be ruled out as well. The anomalous specific heat peak at low temperature in the ferroelectric phase is due to the formation of a cluster of ferroelectric domains. The height of the peak reduces with the increase of system size suggesting that for a small system, the domain size is comparable to the system itself. The fact that the height of this anomalous peak as well as the critical temperature depends on the strength of dipole-dipole interaction renders the squaric acid system an interesting system for experimental confirmation of the same.

Another important aspect is the nature of the phase diagram in the $T-K$ plane which is linear for small and intermediate values of K and for large values of K it becomes elliptical. We think the distinct feature of our results shows that a four-spin interaction at the zeroth order is more realistic.

Also in the present model, the dependence of degeneracy of groundstate manifold is different from the two-spin Hamiltonian. For example, at the zeroth order, four spin interaction includes non-ice rule states as well (all spin-up and all spin-down in a given plaquette) ice-rule states. The diagonal Ising-like interaction reduces the macroscopic groundstate degeneracy to be proportional linearly to the system dimension. However, for the two-body case, the degeneracy is still macroscopic. We believe that this might be the reason that the present study is more closure to the experimental realization.

To summarize, we have studied the finite-temperature phase diagram of proton dynamics of the squaric acid system. The study offers a unique opportunity to examine the competition between quantum fluctuation and thermal fluctuation and the effect of the intricate groundstate degeneracy of such a system. The model Hamiltonian we considered involves a four-spin interaction which renders the present study an interesting one because of successfully solving the model as well as to qualitatively reproduce the experimental findings.

In our endeavor to study such a Hamiltonian in Eq. (1.3) involving four-spin interaction, we used SSE quantum Monte Carlo involving an improvised version of loop update algorithm which efficiently overcomes the problem of ergodic sampling in some parameter regimes. Our theoretical study successfully detected the quantum liquid-like intermediate state before the appearance of the conventional paraelectric state as we increase the temperature. The ferroelectric state which exists before the liquid-like quantum state is characterized by its colossal dependence of T_c concerning J_2, the dipole-dipole interaction. In the intermediate liquid-like state, the local correlations governing the ice-rule constraints are still valid to a large extent. While the experimental phase diagram in the $T-K$ plane, the phase transition shows a linear behavior for all K, we find the linear behavior for small and intermediate values of K. Thus though our results fall short of full experimental confirmation, still it is quite an improvement concerning the earlier theoretical study so far. Also, the phase transition from the ferroelectric phase to a quantum liquid-like state is sharper which reasserts that the model is considered here is more practical as far as the squaric acid system is concerned. For further improvement of our results, a first-principle calculation would be helpful to establish the correct Hamiltonian as well as fixing the realistic parameters. In addition to this, the interlayer coupling should be considered to fill the gap between the theoretical and experimental studies.

CHAPTER 4

Role of interlayer coupling

In the previous chapter, we have presented the quantum and thermal effects on H_2SQ considering the quasi-2D nature of the material. Here, in this chapter, we focus on the realistic nature of the material considering the interlayer coupling between the 2D layers placed one above the another with the adjacent ones slightly displaced alternatively along the plane parallel to the layers. An aspect concerning squaric acid is the role of interlayer coupling. Earlier experimental results have revealed low values of the critical exponent for order parameter (f_i= 0.17 and 0.14) as obtained from the measurements of the optical birefringence [39] and of the neutron scattering [41] respectively. Based on the analysis of the critical exponent, it was shown that H_2SQ exhibits a characteristic of a two-dimensional transition. Despite this fact, the thing however to be noticed that it is still not clear as to how the layers have been stacked antiferroelectrically. In other words, the nature and the role of interlayer coupling are not addressed rigorously. Also, theoretically, the three-dimensional nature of the material was not strictly accounted for as far as the squaric acid is concerned.

An important insight about the interlayer coupling comes from the experiment by *Nakashima et* *al* [57] suggesting that the interlayer interaction acts between the hydrogen bonds of adjacent layers and is localized in the region near the H-bonds. Following this, a theory has been put-forth [175, 75] suggesting that the interlayer coupling may be a reason for such high T_c and for a phase transition to happen. Put together, as to what role the interlayer coupling may play in phase transition is still an open question. In this chapter, we present some elementary analysis regarding the interlayer coupling on H_2SQ.

4.1 3D-Model Hamiltonian

It is already mentioned in the introduction that the crystal structure of H_2SQ consists of quasi-2D layers stacked one above the other with each alternating layer displaced slightly along the horizontal direction (see Fig. 4.1(a)). It is also known that despite its 3D structure, the material predominantly manifests its two-dimensional behavior. Specifically, low values of the critical exponent for order parameter (f_i= 0.17 and 0.14) obtained respectively from measurements of the optical birefringence [39] and of the neutron scattering [41], were found to have a characteristic of a two-dimensional transition. This poses a question as to how the layers have been stacked antiferroelectrically and what might be the role of interlayer coupling. However, from the experiments of *Nakashima et al*, [57] one thing we know is that the interlayer interaction acts only between the hydrogen bonds of adjacent layers and is localized in the region near the H-bonds. Following this, a theory has been put-forth suggesting that the interlayer coupling may be the reason for high transition temperatures, T_c, and for a phase transition to happen [176] in H_2SQ.

Most of the theories that have been put forward were based on the order-disorder mechanism dictating the ice-rules type physics in the low-temperature monoclinic phase. It may be noted that the order-disorder mechanism could be best explained by mapping the proton system to a quantum spin system comprising pseudo-spins. Here, the protons are represented by pseudo-spin variables corresponding to a suitable quantum spin Hamiltonian. Within the model, when only the quasi-2D nature was taken into account, the material was shown to host three different phases. As indicated, they are, 1) Antiferroelectric (AFE), 2) Quantum liquid-like (intermediate-liquid-like), and 3) Deconfined phase.

Apart from the fact that in a given layer, the dipoles (molecular polarization) are antiferroelectrically ordered, it is also known that the layers that are stacked are also of antiferroelectric order along the interlayer axis [6]. Due to this fact, one may believe that the interlayer interaction to be of antiferromagnetic. However, in the present work, we show that even in cases that include disorder or ferromagnet, the material could support antiferroelectrically stacked configurations. Besides, the distortion of lattice at the critical point also could point out the non-uniformity of the interlayer coupling. We, therefore, consider the non-uniform nature of interlayer coupling J_3 in our simulations and analyze the effect of interlayer on the quasi-2D phases. We use the pseudo-spin formalism and employ the discrete version of the path-integral continuous-time quantum Monte Carlo technique to arrive at our results [177]. To distinguish three different phases, we estimate various quantities such as the order parameters similar to what has been used in chapter 3, i.e, the order parameter describing antiferroelectric phase (P), the ice-rule order parameter ρ, and the imaginary-time correlation function c_τ as a function of the transverse field, K. We believe that the study of interlayer coupling is important as a sufficient interlayer interaction strength could lead to concerted proton tunneling between the interlayers dictating an alternative physics. The complete 3D Hamiltonian with the interlayer coupling is given by,

$$\begin{aligned} \mathcal{H} &= -J_0 \sum_{\Box} \hat{A}_{\Box} + J_1 \sum_{\Box} \hat{B}_{\Box} - J_2 \sum_{\langle AB \rangle} \hat{\vec{P}}_A \cdot \hat{\vec{P}}_B \\ &\quad + J_3 \sum_{L,i} \sigma^z_{L,i} \sigma^z_{L+1,i} - K \sum_i \sigma^x_i, \end{aligned} \tag{4.1}$$

$$\mathcal{H} = \mathcal{H}_{\text{2D}} + J_3 \sum_{L,i} \sigma^z_{L,i} \sigma^z_{L+1,i}. \tag{4.2}$$

In the above $\hat{A}_{\square} = \sigma_1^z\sigma_2^z\sigma_3^z\sigma_4^z$, the indices 1,2,3,4 correspond to the indices of four spins on the links (green lines in Fig. 4.2) of a given plaquette ($\square$) taken counterclockwise starting from the lower horizontal link($-$) (see Fig. 4.2). The indices 1, 3, and 2, 4 are designated to be diagonally opposite to each other. Similarly, $\hat{B}_{\square} = (\sigma_1^z\sigma_3^z + \sigma_2^z\sigma_4^z)$. $\hat{P}^x_{A,B} = \pm\frac{1}{4}(\sigma_1^z + \sigma_4^z - \sigma_2^z - \sigma_3^z)$, $\hat{P}^y_{A,B} = \pm\frac{1}{4}(\sigma_1^z + \sigma_2^z - \sigma_3^z - \sigma_4^z)$ are the dipole-moment vectors for A, B subplaquettes as illustrated in Fig. 4.2. As revealed in experiments, we note that the 2D layers are not stacked exactly one above the other, indeed a finite shear displacement is seen alternatively among the adjacent layers (see Fig. 4.2(a)-(c)). However, as the interlayer interaction is located near the H-bonds, we, therefore, consider the J_3 interaction to be of short-range (adjacent layers) composed of simple two-spin Ising interactions.

We here consider the coupling J_0 as the largest among all the couplings as before. And until stated explicitly, for all the simulations carried throughout this work, we fix the value of J_0 equal to 1. We note that the absolute value of the couplings doesn't qualitatively change the results obtained, since it is the relative coupling strengths that are important for a qualitative description. The four competing local interactions in Eq. (4.2) except the Zeeman term are associated with different proton dynamics (see sec. 1.3 for more details). There are eight degenerate *ice-rule* configurations with the lowest energy within a plaquette. Some of the ice-rule states have finite molecular polarization and some have zero molecular polarization. It may be noted that the model described by the strong coupling term J_0 alone and the external field K_x is nothing but the simple quantum Ising gauge theory in (2+1) dimensions [89]. This theory is well-known to have a local $\mathcal{Z}_2$ symmetry and the degeneracy scales exactly equal to $2^{N_x+N_y+1}$ [174]. Also, it is shown that the addition of Ising-type intramolecular interaction given by J_1 extends the deconfined phase along the J_1 axis. The J_2 term in Eq. (4.2) denotes a dipole-dipole interactions between two sub-plaquettes A and B as shown in Fig. 4.1. The physical origin of dipole-dipole interactions arises naturally when the local ground-state or the zeroth-order electrostatic energy is perturbed by the vibrational modes of the ”SQ” molecules. Experimentally the existence of dipole-dipole interaction is indirectly confirmed by the existence

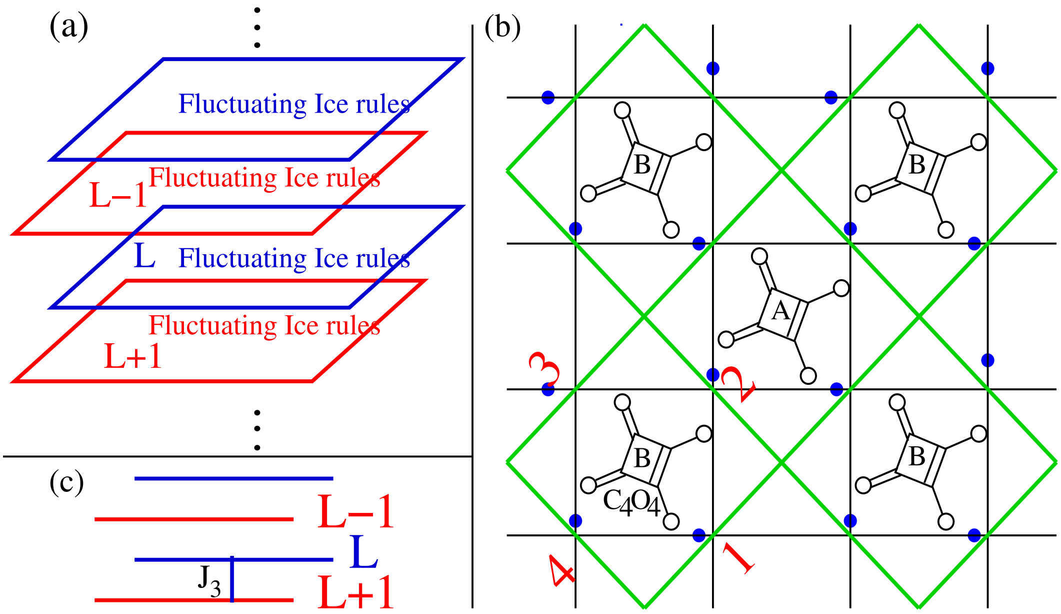

Figure 4.1: A 3D view of Squaric Acid crystal lattice showing two intermediate layers coupled through the Ising exchange coupling J_3 shown with the arrow in cyan color. The small colored dots (blue) mimic the protons while the compound C_4O_4 form a quasi-2D layered configuration with protons placed on the edges of a square lattice. The coloring of protons represents a different state of the local proton ordering which in the pseudo-spin language is $|\uparrow\rangle$, $|\downarrow\rangle$. Each square plaquette is occupied by exactly one square molecule where Ice rules are conserved by the gauge and Ising coupling, J_0, J_1.

of ferroelectric states. This dipole-dipole interaction yields a global stripe ordering with four-fold degeneracy [174].

4.2 Path integral formulation of partition function

We can decompose the Hamiltonian in Eq. (4.2) and (4.2) into two parts, convieniently separating off-diagonal and diagonal operators as,

$$\mathcal{H}_{\text{3D}} = H_D + H_{OD}, \tag{4.3}$$

here, H_{D} is the Hamiltonian comprising of diagonal operators in S^z-basis, that is, the J_0, J_1, J_2 operators and also the interlayer coupling J_3. The H_{OD} is the off-diagonal operator, that is, the magnetic field $-K\sum_i \sigma_i^x$. We have thus separated $\mathcal{H}_{\text{3D}}$ into two parts, each of which consists of commuting terms such that the relation $[H_D, H_{OD}] \neq 0$ holds true. Then the partition function for the model can be written as,

$$\mathcal{Z} \;=\; \mathrm{Tr}\exp\{\beta\mathcal{H}_{\mathrm{3D}}\} = \sum_{\{\sigma\}}\langle\sigma|\exp\{-\beta\mathcal{H}_{\mathrm{3D}}\}|\sigma\rangle = \sum_{\{\sigma\}}\langle\sigma|\exp\{-\beta(H_D + H_{OD})\}|\sigma\rangle. \quad (4.4)$$

Now, following the Suzuki-Trotter decomposition [178], we rewrite the exponential operator as a product of many terms, each with a small prefactor β/M in front of $\mathcal{H}_{\mathrm{3D}}$, that is,

$$\exp\{-\beta\mathcal{H}_{\mathrm{3D}}\} = \Big(\exp\{(-\beta/M)\mathcal{H}_{\mathrm{3D}}\}\Big)^M = \Big(\exp\{-\Delta\tau\mathcal{H}_{\mathrm{3D}}\}\Big)^M, \quad (4.5)$$

with a (large) integer number (called the Trotter number)M, and $\Delta\tau = \beta/M$. The Suzuki-Trotter decomposition now consists in approximating the exponential of H, expressed in terms of the two non-commuting pieces $\mathcal{H}_{3D} = H_D + H_{OD}$, by a product of exponentials. While many such decompositions are possible, the most commonly used approximations (also employed beyond QMC methods) are

$$\exp(-\Delta\tau\mathcal{H}_{\mathrm{3D}}) = \exp(-\Delta\tau(H_D + H_{OD})) = \begin{cases} \exp(-\Delta\tau H_D)\exp(\Delta\tau H_{OD}) + \mathcal{O}(\Delta^2), \\ \exp(-\Delta\tau H_{OD}/2)\exp(\Delta\tau H_D)\exp(-\Delta\tau H_{OD}/2) \\ +\mathcal{O}(\Delta^3). \end{cases} \quad (4.6)$$

Where the errors are also proportional to the commutator $[H_D, H_{OD}]$. Using either of the two approximations in Eq. (4.5), we obtain

$$\begin{aligned} \mathcal{Z} \;&=\; \mathrm{Tr}(e^{(\beta\mathcal{H}_{\mathrm{3D}})}), \\ &= \mathrm{Tr}(\underbrace{e^{(-\Delta\tau H_D)}e^{(\Delta\tau H_{OD})}}_{M}\underbrace{e^{(-\Delta\tau H_D)}e^{(\Delta\tau H_{OD})}}_{M-1}\ldots\underbrace{e^{(-\Delta\tau H_D)}e^{(\Delta\tau H_{OD})}}_{1}) + \mathcal{O}(\Delta^2). \quad (4.7)\end{aligned}$$

When using the second-order approximation from Eq. (4.6), the final expression is obvious. However, when using the third-order approximation, one actually obtains the same final expression, due to the cyclic invariance of the trace, which can be used to move the extreme left exponential to the very right, and then coalesce every other two consecutive terms. This also shows, that the systematic error in $\mathcal{Z}$ actually scales as $M\Delta\tau^3 \propto \Delta\tau^2$, even when using the second-order approximation, where one might have expected an $O(\Delta\tau)$ error in the final expression. Now, consider a basis of the Hilbert space, e.g., in terms of the local eigenstates of S_i^z, which we write as,

$$\begin{aligned}
|\sigma_1\rangle &= |\uparrow\uparrow\uparrow \ldots \uparrow\rangle, \\
|\sigma_2\rangle &= |\uparrow\uparrow\uparrow \ldots \downarrow\rangle, \\
&\vdots \\
|\sigma_{2^N}\rangle &= |\downarrow\downarrow\downarrow \ldots \downarrow\rangle.
\end{aligned} \tag{4.8}$$

Since this forms a complete set of basis, we obtain a completeness relation:

$$\sum_{\sigma} |\sigma\rangle\langle\sigma| = 1, \tag{4.9}$$

where $|\sigma\rangle\langle\sigma|$ is a projection operator onto the basis state $|\sigma\rangle$. Using the above basis, we can thus express the partition function as

$$\begin{aligned}
\mathcal{Z} &= \sum_{\sigma_0} \langle\sigma^0| e^{-\beta\mathcal{H}_{\mathrm{3D}}} |\sigma^0\rangle & (4.10) \\
&= \sum_{\sigma_0} \langle\sigma^0| \lim_{M\to\infty} (\underbrace{e^{(-\Delta\tau H_D)} e^{(-\Delta\tau H_{OD})}}_{M} \underbrace{e^{(-\Delta\tau H_D)} e^{(-\Delta\tau H_{OD})}}_{M-1} \ldots \underbrace{e^{(-\Delta\tau H_D)} e^{(-\Delta\tau H_{OD})}}_{1}) |\sigma^0\rangle & (4.11) \\
&= \lim_{M\to\infty} \sum_{\sigma_0} \langle\sigma^0| (e^{(-\Delta\tau H_D)} e^{(-\Delta\tau H_{OD})} \ldots e^{(-\Delta\tau H_D)} \left(\sum_{\sigma^1} |\sigma^1\rangle\langle\sigma^1| \right) e^{(-\Delta\tau H_{OD})}) |\sigma^0\rangle & (4.12) \\
&= \lim_{M\to\infty} \sum_{\sigma_0} \sum_{\sigma_1} \langle\sigma^0| (e^{(-\Delta\tau H_D)} \ldots \left(\sum_{\sigma^2} |\sigma^2\rangle\langle\sigma^1| \right) e^{(-\Delta\tau H_{OD})}) |\sigma^1\rangle\langle\sigma^1| e^{-\Delta\tau H_{OD}} |\sigma^0\rangle & (4.13) \\
&= \lim_{M\to\infty} \sum_{\sigma_0,\sigma_1,\sigma_2} \langle\sigma^0| e^{-\Delta\tau H_D} e^{-\Delta\tau H_{OD}} \ldots \left(\sum_{\sigma^3} |\sigma^3\rangle\langle\sigma^3| \right) e^{-\Delta\tau H_{OD}} |\sigma^2\rangle\langle\sigma^2| e^{-\Delta\tau H_D} |\sigma^1\rangle \times
\end{aligned}$$

$$\langle\sigma^1|e^{-\Delta\tau H_{OD}}|\sigma^0\rangle. \tag{4.14}$$

In the above summations, we have used the associative property of $limit$ function, we have also added a (superscript) label to distinguish the basis sets that arise from the trace ($|\sigma^0\rangle$) and from the various inserted partitions of unity ($|\sigma^1\rangle$, $|\sigma^2\rangle$, and $|\sigma^3\rangle$). Continuing this way, we eventually arrive at the following expression:

$$\begin{aligned}\mathcal{Z} &= \lim_{M\to\infty}\sum_{\{\sigma^i\}}\underbrace{\langle\sigma^0|e^{-\Delta\tau H_D}|\sigma^{2M-1}\rangle}_{2M}\underbrace{\langle\sigma^{2M-1}|e^{-\Delta\tau H_{OD}}|\sigma^{2M-2}\rangle}_{2M-1}\underbrace{\langle\sigma^{2M-2}|e^{-\Delta\tau H_D}|\sigma^{2M-3}\rangle}_{2M-2}\cdots\\ &\cdots\underbrace{\langle\sigma^3|e^{-\Delta\tau H_{OD}}|\sigma^2\rangle}_{3}\underbrace{\langle\sigma^2|e^{-\Delta\tau H_D}|\sigma^1\rangle}_{2}\underbrace{\langle\sigma^1|e^{-\Delta\tau H_{OD}}|\sigma^0\rangle}_{1}, \end{aligned}\tag{4.15}$$

This representation of $\mathcal{Z}$ is referred to as the “Suzuki-Trotter decomposition”. Furthermore, since H_D and H_{OD} each consists of commuting parts, we find that

$$e^{\Delta\tau H_D} = \prod_i e^{\Delta\tau H_{D_i}} = e^{\Delta\tau H_{D_1}}e^{\Delta\tau H_{D_2}}...e^{\Delta\tau H_{D_{N_D}}}, \tag{4.16}$$

$$e^{\Delta\tau H_{OD}} = \prod_i e^{\Delta\tau H_{OD_i}} = e^{\Delta\tau H_{OD_1}}e^{\Delta\tau H_{OD_2}}...e^{\Delta\tau H_{OD_{N_{OD}}}}, \tag{4.17}$$

and thus in the Suzuki-Trotter decomposition each exponential expression factorizes into exponentials for the plaquette (site) Hamiltonians for diagonal (off-diagonal) operators. One can represent a given contribution to $\mathcal{Z}$ graphically, as is shown for a specific example with $N = 6$, and $M = 3$ in Fig. 4.2. This two-dimensional picture appears like a space-time picture of spins propagating in discrete steps from the initial configuration $|\sigma^0\rangle$ to $|\sigma^1\rangle$,..., and finally from $|\sigma^{2M-1}\rangle$ back to $|\sigma^0\rangle$, since the configurations on the first and the last step are equal. This pictorial illustration also explains why the underlying partitioning of the Hamiltonian is often referred to as the “checkerboard decomposition”.

An important thing to notice is that at this point we have two possible ways of sampling $\mathcal{Z}$ (Eq. (4.15)) within a Monte Carlo scheme. One is directly sampling the Eq. (4.15) without any further

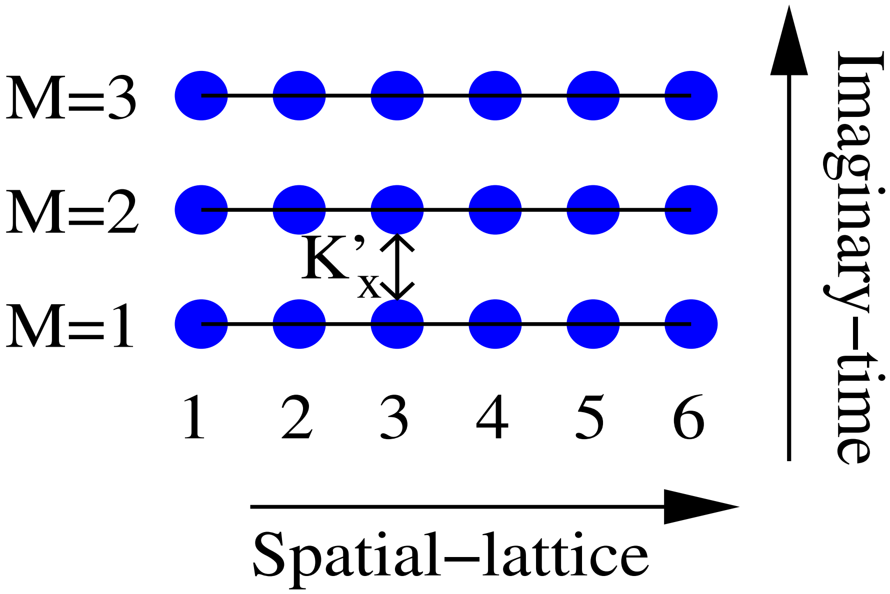

Figure 4.2: Schematic showing the propagation direction for case of N = 6 spins and a Trotter dimension of $M = 3$. K'_x denotes the couplng between the imaginary-time slices (see Eq. (4.14)).

simplification, and the other involves proceeding further in deriving an effective actions describing the same physics as the quantum Hamiltonian but with cost of extended configuration space along the imaginary-time direction, here it is the Trotter direction M. Next we proceed onto obtaining the effective classical action for our Hamiltonian in a path integral representation useful for sampling.

The approximation in the exponential can be made to an exact expression by taking the following limit as follows:

$$\exp\left(-\Delta\tau\mathcal{H}_{3\mathrm{D}}\right)^{M} = \left[\exp\left(-\Delta\tau(H_D + H_{OD})\right)\right]^{M} = \lim_{M\to\infty}\left[\exp\left(-\Delta\tau H_D\right)\exp(\Delta\tau H_{OD})\right]^{M} \tag{4.18}$$

$$\tag{4.19}$$

Now, the diagonal part of the Hamiltonian is also given as,:

$$\begin{aligned} e^{-\Delta\tau H_D}|\sigma^i\rangle &= e^{-\Delta\tau\left(-J_0\sum_{\square}\sigma_1^z\sigma_2^z\sigma_3^z\sigma_4^z + J_1\sum_{\square}(\sigma_1^z\sigma_3^z+\sigma_2^z\sigma_4^z) - J_2\sum_{\langle AB\rangle}\hat{P}_A\cdot\hat{P}_B - \sum_L J_3(L)\sigma_L^z\sigma_{L+1}^z\right)}|\sigma^i\rangle && (4.20)\\ &= e^{-\Delta\tau\left(-J_0\sum_{\square}S_1S_2S_3S_4 + J_1\sum_{\square}(S_1S_3+S_2S_4) - J_2\sum_{\langle AB\rangle}P_A\cdot P_B - \sum_L J_3(L)S_LS_{L+1}\right.}\Big)|\sigma^i\rangle && (4.21)\\ &= e^{-\Delta\tau E_{D_i}}|\sigma^i\rangle, && (4.22)\end{aligned}$$

where E_{D_i} is the configurational energy of any given configuration that is one among the states in Eq. (4.8). In such scenario the energy of the state is trivially given in terms of the eigenvalue as $E_{D_i} = -J_0 \sum_{\Box} S_1 S_2 S_3 S_4 + J_1 \sum_{\Box} (S_1 S_3 + S_2 S_4) - J_2 \sum_{\langle AB \rangle} P_A \cdot P_B - \sum_{L} J_3(L) S_L S_{L+1}$, here the S_i are the eigenvalues of the σ_i^z operator acting at site i, the partition function in Eq. (4.15) then can be simplified to,

$$
\begin{aligned}
\mathcal{Z} &= \lim_{M\to\infty} \sum_{\{\sigma^i\}} \underbrace{e^{-\Delta\tau E_{D_0}} \delta_{0,2M-1}}_{2M} \underbrace{\langle \sigma^{2M-1} | e^{-\Delta\tau H_{OD}} | \sigma^{2M-2} \rangle}_{2M-1} \underbrace{e^{-\Delta\tau E_{D_{2M-2}}} \delta_{2M-2,2M-3}}_{2M-2} \cdots \\
&\quad \ldots \underbrace{\langle \sigma^{3} | e^{-\Delta\tau H_{OD}} | \sigma^{2} \rangle}_{3} \underbrace{e^{-\Delta\tau E_{D_1}} \delta_{2,1}}_{2} \underbrace{\langle \sigma^{1} | e^{-\Delta\tau H_{OD}} | \sigma^{0} \rangle}_{1}, \qquad (4.23)
\end{aligned}
$$

further, summing the delta functions and replacing the dummy indices in the sum with i by $i-1$ leads to,

$$
\mathcal{Z} = \lim_{M\to\infty} \sum_{\{\sigma^i\}} \left(\left[\prod_{k=1}^{M} e^{-\Delta\tau E_{D_k}} \right] \underbrace{\langle \sigma^{0} | e^{-\Delta\tau H_{OD}} | \sigma^{M-1} \rangle}_{M} \ldots\ldots \underbrace{\langle \sigma^{1} | e^{-\Delta\tau H_{OD}} | \sigma^{0} \rangle}_{1} \right). \qquad (4.24)
$$

Now, one is left with the terms consisting of off-diagonal operators to evaluate, that is,

$$
\begin{aligned}
\langle \sigma^k | e^{-\Delta\tau H_{OD}} | \sigma^{k-1} \rangle &\equiv \langle \sigma^k | e^{-\Delta\tau[-K \sum_j \sigma_j^x]} | \sigma^{k-1} \rangle && (4.25) \\
&\equiv \prod_{i=1}^{N} \langle S_i^k | e^{\Delta\tau K \sigma_i^x} | s_i^{k-1} \rangle && (4.26) \\
&= \prod_{i=1}^{N} \left[\sinh(\Delta\tau K) \delta_{S_i^k, -S_i^{k-1}} + \cosh(\Delta\tau K) \delta_{S_i^k, S_i^{k-1}} \right] && (4.27) \\
&= \prod_{i=1}^{N} \left(\left[\frac{1}{2} \sinh(2\Delta\tau K) \right]^{1/2} e^{\frac{1}{2} \log[\coth(\Delta\tau K)] S_i^k S_i^{k-1}} \right). && (4.28)
\end{aligned}
$$

Substituting Eq. (4.28) into the Eq. (4.24) we obtain the partition function in the familiar representation of Feynmann path integral formalism and for that matter the following method is sometimes also called as imaginary-time Monte Carlo. Nevertheless, the simplified Eq. (4.24) after the substitution can be rewritten as,

$$
\begin{aligned}
\mathcal{Z} &= \lim_{M\to\infty} \sum_{\{\sigma^i\}} \left(\prod_{k=1}^{M} \left[e^{-\Delta\tau E_{D_k}} \prod_{i=1}^{N} \left[\frac{1}{2}\sinh\left(2\Delta\tau K\right)\right]^{1/2} e^{\frac{1}{2}\log\left[\coth\left(\Delta\tau K\right)\right] S_i^k S_i^{k-1}} \right] \right) && (4.29)\\
&= \lim_{M\to\infty} C_M \sum_{\{\sigma^i\}} \left(\prod_{k=1}^{M} \left[e^{-\Delta\tau E_{D_k}} \prod_{i=1}^{N} e^{\frac{1}{2}\log\left[\coth\left(\Delta\tau K\right)\right] S_i^k S_i^{k-1}} \right] \right) && (4.30)\\
&= \lim_{M\to\infty} C_M \sum_{\{\sigma^i\}} \left(\prod_{k=1}^{M} \left[e^{-\Delta\tau E_{D_k}} e^{\sum\limits_{i=1}^{N} \frac{1}{2}\log\left[\coth\left(\Delta\tau K\right)\right] S_i^k S_i^{k-1}} \right] \right) && (4.31)\\
&= \lim_{M\to\infty} C_M \sum_{\{\sigma^i\}} \left(\prod_{k=1}^{M} \left[e^{-\Delta\tau E_{D_k} + \sum\limits_{i=1}^{N} \frac{1}{2}\log\left[\coth\left(\Delta\tau K\right)\right] S_i^k S_i^{k-1}} \right] \right) && (4.32)\\
&= \lim_{M\to\infty} C_M \sum_{\{\sigma^i\}} \left(e^{-\beta H_{\text{eff}}} \right), && (4.33)
\end{aligned}
$$

here, in the second step, the constant C_M is pulled out of summation and is given as $C_M = \left[\frac{1}{2}\sinh\left(2\Delta\tau K\right)\right]^{N/2}$. Since the scalars commute, the third step involves the exponential being merged into one. The Eq. (4.32) is the important equation used in the importance-sampling. The Eq. 4.33 can be compared to the Euclidean path integral approach $\big(\mathcal{Z} = \int e^{iS[\mathbf{x}]}\mathcal{D}\mathbf{x}$. Where $S[\mathbf{x}]$ is the classical action being summed over all possible classical paths $\mathcal{D}\mathbf{x}$ in the Euclidean space-time$\big)$ after performing a Wick rotation $it = \tau$. Followed by the transformation $\tau/\hbar \to \beta$, the path integral then becomes the partition function as $\mathcal{Z} \sim e^{-\beta S}$. Therefore, the term inside the exponential must be equal to the negative of the classical action H_{eff} divided by inverse temperatures, and upto an irrelevant constant the expression for effective Hamiltonian is given by,

$$
H_{\text{eff}} = \frac{S}{\beta} = \sum_{k=1}^{M} \left[\frac{\Delta\tau}{\beta} E_{D_k} - \sum_{i=1}^{N} \frac{1}{2\beta} \log\left[\coth\left(\Delta\tau K\right)\right] S_i^k S_i^{k-1} \right], \tag{4.34}
$$

where we have successfully converted a quantum Hamiltonian into a classical theory but at the expense of compromising an addition of extended configurational space with the inclusion of imaginary-time dimension. Effectively the quantum system ($SU(2)$) with N spins is transformed into the classical system ($SO(3)$) with $M \times N$ spins. Note the periodic boundary condition along the "discrete imaginary-time" axis similar to the SSE QMC approach discussed in chapter 3. The Eq. (4.34) is quite general to a broad range of models that has off-diagonal operator acting on a single site such as the transverse field models with no other off-diagonal operators. The diagonal part (E_{D_i}) however strictly depends on the model considered. It is to be noted that to reduce the error due to discretization of the Trotter index $\Delta\tau$, one may take a continuous limit even before the Importance sampling to arrive at a robust continuous-time Monte Carlo scheme which however is not the motivation here as the discrete imaginary-time scheme paves easy access to the correlation function that is very much equivalent to the Matsubara imaginary-time approach. However, in practice one may tend to obtain better-converged results and reduce the error if the Trotter number M is chosen sufficiently large. Typically one uses the Trotter number proportional to system size and the inverse temperature. We do follow the same in our simulation, however, we see that the results tend to converge much smoothly up to the third decimal after $M = 400$. In the next section, we discuss the details of sampling the effective classical action obtained as in Eq. (4.34).

4.3 Observables

For a diagonal operator (S^z-basis), the ensemble average seems to be simply an average over all configurations including the extended configuration space spanned by the Trotter dimension M. However, the case of off-diagonal operators are different as we shall see below. We start with the same expression of partition function with an general operator ($\mathcal{O}$) expression as,

$$\begin{aligned} \langle\hat{\mathcal{O}}\rangle &= \frac{\mathrm{Tr}\big(\hat{\mathcal{O}}e^{(-\beta\mathcal{H}_{\mathrm{3D}})}\big)}{\mathrm{Tr}\big(e^{(-\beta\mathcal{H}_{\mathrm{3D}})}\big)} &(4.35)\\ &= \lim_{M\to\infty}\sum_{\{\sigma^i\}}\prod_{k=1}^{M} e^{-\Delta\tau E_{D_k}}\prod_{i,k}^{N,M}\langle\sigma_i^k|e^{(\Delta\tau K\sigma_i^x)}|\sigma_i^{k+1}\rangle, &(4.36)\end{aligned}$$

where we have used the expression as already derived in Eq. (4.14). Now, it is convienient to introduce a probability measure on the $N \times M$ Ising spins,

$$\begin{aligned} \mu(\{\sigma\}) &= \frac{1}{Z_M} e^{(-\beta \tilde{E}(\{\sigma\}))} \prod_{i=1}^{N} w(\{\sigma\}), && (4.37) \\ Z_M &= \sum_{\{\sigma\}} e^{(-\beta \tilde{E}(\{\sigma\}))} \prod_{i=1}^{N} w(\{\sigma\}), && (4.38) \end{aligned}$$

so that the normalization constant Z_M becomes the partition function $\mathcal{Z}$ in the limit $M \to \infty$. We have also for simplicity redefined our energy expression as,

$$\tilde{E}(\{\sigma\}) = \frac{1}{M} \sum_{k=1}^{M} E_D(\{\sigma^k\}), \tag{4.39}$$

which is nothing but the average of the classical energy on various Trotter intervals, and

$$w(\sigma) = \prod_{k=1}^{M} \langle \sigma^k | e^{\Delta\tau K \sigma^x} | \sigma^{k+1} \rangle = \prod_{k=1}^{M} \Big(\cosh(\Delta\tau K) \delta_{\sigma^k, \sigma^{k+1}} + \sinh(\Delta\tau K) \delta_{\sigma^k, -\sigma^{k+1}} \Big), \tag{4.40}$$

where $w(\sigma)$ is the coefficient obtained from the interaction (ferromagnetic) along the imaginary time axis because of the flipping operator σ^x. Then the ensemble average of an observable $\mathcal{O}$ in this scheme can be obtained from the Eq. (4.35) as follows:

$$\langle \mathcal{O} \rangle = \sum_{\{\sigma\}} \mu(\{\sigma\}) \frac{\langle \sigma^k | \mathcal{O} e^{(-\Delta\tau \mathcal{H}_{3\mathrm{D}})} | \sigma^{k+1} \rangle}{\langle \sigma^k | e^{(-\Delta\tau \mathcal{H}_{3\mathrm{D}})} | \sigma^{k+1} \rangle}, \tag{4.41}$$

here the Trotter index 'k' is arbitrary as the product containing the k is already hidden in the Eq. (4.37). This is possible only when there is cyclic invariance such as in the current scenario where the operator $\mathcal{O}$ can be moved inside the trace. Now the Eq. (4.41) can be further simplified for the operators diagonal in the S^z-basis and can be given as,

$$\langle\mathcal{O}\rangle = \sum_{\{\sigma\}} \mu(\{\sigma\}) O(\sigma^k) = \sum_{\{\sigma\}} \mu(\{\sigma\}) \frac{1}{M} \sum_{k=1}^{M} O(\sigma^k). \tag{4.42}$$

Similarly the expression for non-diagonal observable such as the transverse magnetization $\langle\sigma_i^x\rangle$ can be obtained as,

$$\begin{aligned}\langle\sigma_i^x\rangle &= \sum_{\{\sigma\}} \mu(\{\sigma\}) \frac{1}{M} \sum_{k=1}^{M} \frac{\langle\sigma^k|\sigma_i^x e^{(-\Delta\tau\mathcal{H}_{3\mathrm{D}})}|\sigma^{k+1}\rangle}{\langle\sigma^k|e^{(-\Delta\tau\mathcal{H}_{3\mathrm{D}})}|\sigma^{k+1}\rangle} && (4.43)\\ &= \sum_{\{\sigma\}} \mu(\{\sigma\}) \frac{1}{M} \sum_{k=1}^{M} \Big(\tanh(\Delta\tau K)\Big)^{\sigma_i^k\sigma_i^{k+1}}. && (4.44)\end{aligned}$$

4.4 Discrete-time loop and cluster algorithms

One of the biggest advantages of transforming the quantum Hamiltonian into the classical one is that we can now invoke powerful classical cluster (loop) algorithms that are already in the literature, for example, the Swendsen-Wang [165] updates. The other motive is to run parallel tempering straightforwardly with the transition probability simply given by,

$$P(i \rightarrow i+1) \sim \exp\Big((\beta_i - \beta_{i+1})(E_i - E_{i+1})\Big). \tag{4.45}$$

We note that the parallel tempering in SSE involves numerous MPI child processes to be invoked parallelly, as the intervals between two adjacent inverse temperatures β_i should be very small since the probability of acceptance of a move is $\propto (\beta_i/\beta_{i+1})^{n_{i+1}/n_i}$ and typically this number is very small (10^{-2}) if the intervals are not close enough. Therefore, mapping to a classical Hamiltonian gives an advantage in regards to parallel tempering algorithm by reducing the number of cores usage.

We use similar algorithms as in the SSE case discussed in chapter 3. However, a bit of modification in the implementation is needed as the imaginary-time slices in the present Monte Carlo scheme involve a fictional ferromagnetic interaction (J_3) among the adjacent layers. Noticeably, we identify that the energy landscape of the current Hamiltonian with such a large parameter space is not smooth, and we observe similar deviation of physical quantities at low temperatures (and or fields) due to apparent spin percolation and thereby freezing. Therefore, we invoke multiple cluster algorithms working together and simultaneously each satisfying the detailed balance principle. We first list out all the algorithms used for our case,

1. **Swendsen-Wang**: Along the imaginary-time direction we employ the Swendsen-Wang (SW) cluster algorithm [165] as the interaction between the layers are of nearest neighbor and include a ferromagnetic coupling. We know that whenever one encounters a ferromagnetic interaction of Ising spins, the probability of adding a bond (plaquette) connecting two adjacent spins i and $i + 1$ (i, j, k, l) to the SW cluster is $P_b = 1 - \exp(-2\beta J_b(J_{ijkl}))$, see Ref. [165]. This way one identifies all the clusters spanning the lattice (along the world-line). SW algorithm is renowned for its *rejection free* nature and its ability to suppress the critical slowing down.

2. **Heat-bath update**: Following the above step, once all the clusters are identified, we flip each of them with their corresponding heat-bath weights given by the neighboring spins surrounding the cluster with the following probability $P = 1/(1 + \exp(-2\beta))$.

3. **Loop-flip update**: This is purely a loop algorithm applied on one particular Trotter slice (or one world-line) and contains spins only within the spatial dimension of that particular slice. We note that the rules governing the identification of clusters are the same as in the case of SSE where the loops are formed connecting all the diagonal spins (or the spins that are interacting by J_1). For example, the loop-chain of spins along the x-direction starting from spin i, and then $i + l_x$, $i + 2l_x$,... with periodic boundary conditions until one again encounters the site i. Here l_x is the lattice dimension along x.

4. **Modified loop-flip algorithm**: Same as above, but here the loops are formed at one particular

quasi-2D slice of H_2SQ and all the spins connected accordingly just above the considered slice along the interlayer dimension are flipped. Also, other ways of implementing a similar algorithm are, instead of flipping all the spins along the interlayer axis, one can flip the spins at one quasi-2D slice with a Metropolis update proportional to its Boltzmann weight.

5. **Parallel tempering**: This is completely a local update but works on the principle of exchanging configurations of neighboring temperatures ranging from anywhere between 0, β_c, where β_c is the cut-off temperature one considers in the simulation. Typically, at first, till the temperatures where spin freezing is not visibly observed can be taken as the cut-off temperatures for exchanging. As mentioned the probability of transition for such exchanges is given simply as: $P(i \rightarrow i+1) = \exp\Bigg((\beta_i - \beta_{i+1})(E_i - E_{i+1})\Bigg)$ where i and $i+1$ corresponds to nearest neighbour indices of configurations with β_i and β_{i+1} inverse temperatures respectively.

Implementing these algorithms listed above comply with the rules of detailed balance and can be used anytime. The actual motive of implementing these algorithms in the simulation comes from the efficiency of them. And for faster convergence and better results, we use the trick of QMC which is to give a better trial state as the input. Though this is not an effective way of implementing a rigorous unbiased simulation, yet the present case offers such a scenario as the ground state for the quasi-2D case has been exactly known. Using this we give an input trial state obtained from the previous results on the quasi-2D lattice with ferroelectric ground states for $J_2 \neq 0$ and disordered state $J_2 = 0$. To testify our results we perform another individual simulation which is fed with the final state obtained from the mean-field analysis for $K_x = 0$ including the interlayer coupling. We match the results for energy with exact diagonalization to further validate our results. In the next section, we discuss the details of some of the above algorithms that are very useful in most of the H-bonded systems with ice-rule physics.

In an earlier study [13], we have investigated dipole-dipole induced phase transition for a quasi-2D H_2SQ crystal not accounting the interlayer interaction, J_3, that is, $J_3 = 0$. The study showed the presence of a ferroelectric phase at lower temperatures (and fields), a quantum paraelectric phase (or the liquid-like intermediate phase with finite-molecular polarization) at intermediate ranges of temperatures (and fields), and the conventional paraelectric phase at higher temperatures. We note that the ferroelectric phase corresponds to the long-range ordered dipole moments, and the quantum paraelectric (QP) phase containing molecules (subplaquettes) having finite dipole moments but are in one of the ice-rule states. We note that the QP phase continues to survive to a large range of temperatures (and field) indicating quantum coherence at a small length scale.

As evident from Fig. 4.1 in the absence of J_3, the ice-rule configuration or dipole-dipole interaction within a 2D layer are independent of each other (layers). However, when J_3 is turned on, a certain correlation between the ice-rule allowed states in adjacent 2D layers comes to exist.

4.4.1 Details of implementation procedure

Here we briefly outline the method and the details of implementation of the imaginary-time quantum Monte Carlo technique. We use the discretized version of the continuous time QMC algorithm developed by $Nakamura$ [177]. Using the Suzuki-Trotter decomposition scheme [178], the current three-dimensional quantum Hamiltonian is mapped on to an effective four-dimensional classical Hamiltonian with the additional fourth dimension extended along the imaginary-time (Trotter) axis τ where the effective classical action is given by,

$$\begin{aligned}\mathcal{S} &= \sum_p \Bigg(-\frac{\beta J_0}{M}\sum_{\square} A_{\square,p} + \frac{\beta J_1}{M}\sum_{\square} B_{\square,p} - \frac{\beta J_2}{M}\sum_{\langle AB\rangle} \vec{P}_{A_p}\cdot\vec{P}_{B_p} + \frac{\beta J_3}{M}\sum_{\langle L_p\rangle}\sigma_{L,p}\sigma_{L+1,p} \\ &\quad -K'\sum_i \sigma_{i,p}\sigma_{i,p+1}\Bigg), \end{aligned} \tag{4.46}$$

where at each Trotter index p the operators initially of the form $\hat{A}_{\square}$ are mapped to $A_{\square,p}$. Note that the quantum spins are now replaced by their classical Ising variables, for instance, $A_{\square,p} = \sigma_{1,p}\sigma_{2,p}\sigma_{3,p}\sigma_{4,p}$ and similarly the same is applied for all the remaining operators in the original Hamiltonian (Eq. (4.2)). Here, M is the cut-off length along Trotter axes and is fixed at the start of the simulation, while β is the inverse temperature and $K' = -\frac{1}{2}\ln\coth(\beta K/M)$ is the effective coupling (FM) along the newly added Trotter dimension τ.

We adopt the heat-bath algorithm along the spatial-axes and the Swendsen-Wang cluster update is applied in the imaginary-time direction. However, the case for $J_2 = 0$ is highly degenerate at smaller-fields, and to avoid apparent spin-freezing and to speed-up the relaxation process we employ the variant of the loop-flip update algorithm [179]. The loops are formed at a particular imaginary time slice along the vertical or horizontal chain of spins and are flipped all at once and overall Trotter slices to maintain detailed balance. We note that for the case of $J_2 \neq 0$ the loops are flipped with probability proportional to their Boltzmann weight since they are no more Iso-energetic though they form the subset of the restricted ice-rules. We consider systems sizes up to $N = 12 \times 12 \times 8$ block of spatial spins comprising the 3D lattice and the number of Trotter slices are fixed up to $M = 1000$. About $\sim 10^5$ Monte Carlo steps (MCS) were used for equilibration and 5×10^5 were used for measurements. Binning analyses were done by dividing results into six bins where statistical errors are estimated.

As we are interested in analyzing the system under both the quantum (fields) and thermal (temperature) fluctuations we, therefore, vary both the parameters taken along the contour that is parametrized by θ, such that $\theta = \tan^{-1}(K\beta)$. For small inverse temperatures, the system is subjected to strong thermal fluctuations and vice-versa. We now proceed to the next section 4.5 describing the details of physical quantities that will be estimated using the QMC simulations briefed here.

4.5 Physical quantities

We divide the cases based on the limiting ratios of J_2 and J_3. For the case $J_1 \ggg J_2$, we measure the gauge-invariant dipole-dipole correlation function c_τ [89] averaged over all molecules along the imaginary-time direction. The correlation function c_τ characterizing the deconfined phase is given by,

$$c_\tau = \frac{1}{N}\sum_i \langle P^x(i,0)P^x(i,\tau)\rangle, \tag{4.47}$$

where, τ denotes the imaginary-time index, N being the number of molecules/plaquettes. The correlation function contains terms that are gauge-invariant and is used to characterize the deconfined phase. For small J_2 other parameters of the Wilson-loop operator form could also be used to distinguish the corresponding strong-coupling limit and weak-coupling limit (within the deconfined regime) where the correlation function follows perimeter and area-law respectively [152]. However, for $J_{2,3} = 0$, the minimal Wilson-loop one can consider in spatial direction is the plaquette operator $\mathcal{P} = \sigma_1^z\sigma_2^z\sigma_3^z\sigma_4^z$ and the corresponding correlation would describe confinement-deconfinement transition. Taking advantage of the gauge-fixing along the temporal axes to be one, the dipole-dipole correlation c_τ along the imaginary-time axis is now gauge-invariant making us evaluate the non-vanishing correlation function c_τ. Next, for finite J_2 we measure the order parameter P along with the associated susceptibility given by χ_{zz} which characterizes the global ferroelectric ordering developed by the dipole-dipole interaction term. To concretize our results we also measure the off-diagonal expectation value of the magnetization along the transverse-field, m_x along with the associated susceptibility $\chi_{xx} = \frac{\partial m_x}{\partial K}$,

$$P = \frac{1}{N}[\mid S(0,\pi)\mid^2 + \mid S(\pi,0)\mid^2]^{1/2} \tag{4.48}$$

$$\frac{\chi_P}{N} = \beta\Big[\langle P^2\rangle - \langle P^2\rangle\Big], \tag{4.49}$$

where S($\mathbf{k}$) is the static spin-structure factor given by

$$S(\mathbf{k}) = \frac{1}{N}\sum_{i,j}^{N} S_i^z S_j^z \exp{(-\mathbf{k}\cdot\mathbf{r}_{ij})}, \tag{4.50}$$

(a) Ice–rule states (finite–dipole moment)

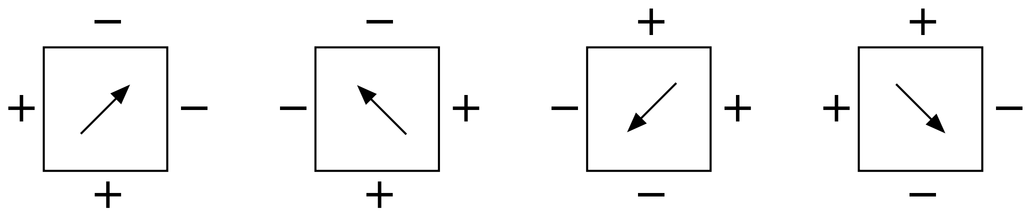

(b) non ice–rule states

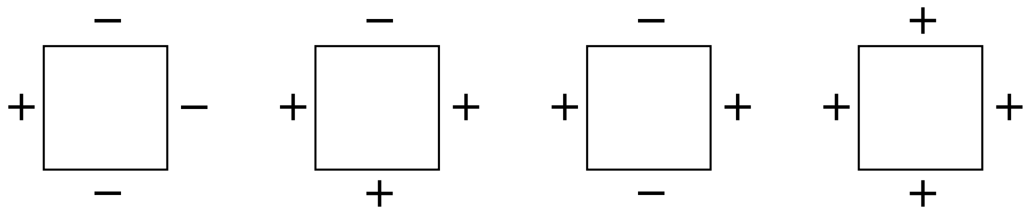

Figure 4.3: Illustration of the ice-rule (shown in (a)) and the non-ice-rule states (shown in (b)) for the current Hamiltonian.

here, $\mathbf{r}_{ij}$ is the relative vector between i^{th} and j^{th} spin on the lattice. We also measure parameter ρ which detects an ice-rule state locally and gives information about the amount of disordered dipole configurations in general. This along with P becomes crucial in understanding the local ordering of the protons. The relation for ρ is given as,

$$\tilde{\rho}_{\square} = \begin{cases} 1, & \text{if } \square \,\epsilon\, \text{ice-rule}, \\ \\ -1/3, & \text{otherwise}, \end{cases} \qquad \& \quad \rho = \sum_{\square} \tilde{\rho}_{\square}, \tag{4.51}$$

here, $\rho_{\square}$ probes the ordering in each plaquette such that $\rho_{\square}$ is equal to 1 if the local ordering in each plaquette is in any one of the four possible states with finite dipole moments as shown in Fig. 4.3(a). The values of ρ assigning to states belonging to two different sectors is to distinguish the states that obey ice-rules locally at each individual plaquette from the states that do not. This can be understood as follow:

1. There are four configurations which satisfy the ice-rules and that have finite dipole-moment. So, we fix the value of $\tilde{\rho}_{\square}$ to be equal to 1, that is,

$$\tilde{\rho}_{\Box} = 1, \qquad \text{if in any one of the four ice-rule states shown in Fig. 4.3(a).} \tag{4.52}$$

Now, by this assignment, we are leftover with 12 other configurations that do not satisfy the ice-rules constraint. Since 4 out of 16 satisfy the constraint, therefore the total value that can be assigned for these states can be given as

$$\tilde{\rho}_{\Box} \sim 4 : (16 - 4) = 4 : 12. \tag{4.53}$$

Since, they do not obey the ice-rules, they were also assigned a negative value. That is,

$$\tilde{\rho}_{\Box} = -4 : 12 = -1/3. \tag{4.54}$$

In simulations, for example, one can consider the chart shown in Fig. 1.4 with state 1 and energy -1. The four states that we are discussing correspond to the four states represented in the lowest panel of the figure in sec. 1.3 of chapter 1.1. Numerically what this means is that suppose on a 4×4 lattice, we have at each plaquette the configuration one among the eight states (ice-rule and non-ice-rule) states and also the other eight obtainable by the spins in each state. Let's say at plaquette indexed 1 has a configuration shown in Fig. 4.3(a), that means $\rho_{\Box_1} = 1$, similarly, at plaquette number 2 we have a configuration that is one among the Fig. 4.3(b), then the $\rho_{\Box_2} = -1/3$, similarly one iterates till the last plaquette of the lattice. Then to obtain the total configurational ordering we sum the $\rho_{\Box}$'s to obtain the parameter ρ, very similar to any other local order parameter such as magnetization, here one can understand that z-component spin $\hat{\sigma}_i$ is similar to the $\rho_{\Box_i}$. Although the parameters, ρ, and P would suffice in detecting any global ordering especially antiferroelectric it is useful to estimate other parameters such as uniform susceptibility and the correlation function. Finally, to locate the critical points accurately, we estimate the Binder cumulant which is given by [172],

$$Q = \frac{1}{2}\left(1 - \frac{\langle P^4\rangle}{3\langle P^2\rangle^2}\right). \tag{4.55}$$

4.6 Results

4.6.1 Mean-field and spin-wave analysis

To get an understanding of the role of interlayer coupling classically we here provide the analysis of classical groundstates. Later, the obtained groundstates are used to investigate their behavior under quantum fluctuations (field). Following Ref. [174], we notice that the 3D-model Hamiltonian can also be rewritten in the following form: $H = \sum_i (h_i^z S_i^z + h_i^x S_i^x)$, where for a given spin component S_i^α, h_i^α denotes the local-field component along α axis. The minimum energy configuration of spins is then obtained by aligning S_i^α to the negative α axis. Usually, one starts from a random configuration of $[S_{i,0}^\alpha]$ yielding a configurations of $[h_{i,0}^\alpha]$ and a total energy $E[S_{i,0}]$. The distribution $[h_{i,0}^\alpha]$ yields a new configuration of spins and new total energy of the system $E[S_{i,1}^\alpha]$. In the above, the index "0" or "1" denotes the steps in numerical iterations. We continue this process until $E[S_{i,n}] \equiv E[S_{i,n+1}]$. We have performed numerical simulations over a lattice of dimension 256×256 and checked for sufficient initial configurations. Noticeably, we have found that the ground state has a one-to- one corresponds to the ground-state configurations of the quasi-2D configurations. The only difference is that the spins have now a finite and constant value of S_i^x, which changes as a function of K, and other parameters similar to what has been found for the Kitaev model in the presence of transverse magnetic field in an earlier study [108, 174]. Thus the ground-state configurations can be written as,

$$\vec{S}_i = S(\lambda_i \cos\theta \mathbf{e_z} + \sin\theta \mathbf{e_x}), \tag{4.56}$$

where λ_i could be ± 1 in tune with the groundstate configurations of H_0 for $K = 0$. The equilibrium configuration, that is, the value of θ_{eq} depends on K, J_1, J_2, and J_3. For $K = 0$, we have $\theta = 0$ but λ's can still take either ± 1. The θ plays the role of order parameter. From the mean-field ansatz represented by Eq. (4.56), the groundstate energy of the system can be written as follows:

$$\begin{aligned} E_{cl} &= -\frac{1}{2} J_0 S^4 N \cos^4\theta - J_1 S^2 N \cos^2\theta \\ &\quad -KSN\sin\theta - 2J_2 S^2 N \cos^2\theta - J_3 N S^2 \cos^2\theta. \end{aligned} \tag{4.57}$$

Minimizing E_{cl} with respect to θ, we obtain θ_C, which minimizes the groundstate energy $E_{cl}(\theta_C)$. This groundstate energy has been compared with the $E_x = -KN$, which denotes the energy corresponding to the state where all spins are aligned along x-direction. For a given J_0, J_1, J_2, there exists a K_c such that if $K \leq K_c$ then $E_{cl} < E_x(\theta_C)$ with $\theta_C \leq \pi/2$. One can numerically solve for θ_C and obtain the classical phase diagram [174]. However, we are interested in the spin-wave spectrum both in low and high-fields. In the next section, we use the so obtained classical groundstates upon which we perform a Holstein-Primakoff (HP) transformation. For all the parameter values, there is a θ_C for $K \leq Kc$ that defines the groundstate configuration according to Eq. (4.56). The groundstate has finite degeneracy in the presence of J_0, J_1, and J_2 even when including interlayer coupling J_3. For finite interlayer coupling, that is, $J_3 > 0$ $J_1 = J_2 = 0$, the degeneracy is still $2^{N_x N_y + 1}$ and for $J_2 = 0$, the degeneracy is $2^{N_x + N_y}$. For both J_1 and J_2 nonzero, the degeneracy is reduced to four as in the case of 2D case [174]. For large $K > Kc$, all the spins get aligned along the x-axis corresponding to $\theta_C = \pi/2$. Even upon the introduction of J_3, the frustration is still there because not all the bonds can be satisfied (for example where a disordered interlayer coupling J_3 is considered). In the disorder case, even with a small strength, we see that the degeneracy is completely lifted. In the other two cases, that is, FM (AFM), we see that the quasi-2D configurations get extended along the interlayer with z-projections of spins in one layer aligned (anti-aligned) alternatively. However, the degeneracy in these cases is not lifted and in fact, we see that the degeneracy is the same as before in the quasi-2D case. This is seen in the simulations where the specific heat shows an anomalous peak whose height is proportional to this degeneracy.

4.6.2 Linear spin-wave theory

The classical groundstates obtained is strictly dependent on θ, that is, the local axis represented by $x'(z')$. One may have to rotate the axis to the global coordinate system $x(z)$. Hence, any spin can be decomposed as follows:

$$\vec{S}_r = \vec{\mathbf{e}}_x S_r^x + \vec{\mathbf{e}}_z S_r^z. \tag{4.58}$$

Here **r** represents the positions of a given site. Since the interactions are decomposed along x and z axes, we therefore, perform an orthogonal coordinate transformation (from x, z to x', z') around y-axis such that one axis of our new coordinate system gets aligned along the local moment direction at every site:

$$\mathbf{S_r^x} = \mathbf{S_r^{x'}} \cos\lambda_\mathbf{i}\theta - \mathbf{S_r^{z'}} \sin\lambda_\mathbf{i}\theta, \tag{4.59}$$

$$\mathbf{S_r^z} = \mathbf{S_r^{x'}} \sin\lambda_\mathbf{i}\theta + \mathbf{S_r^{z'}} \cos\lambda_\mathbf{i}\theta. \tag{4.60}$$

The expressions for $S'_{x/z}$ in terms of the bosonic operators are given below:

$$\mathbf{S_r^{x'}} = \mathbf{s} - \mathbf{a_r^\dagger a_r}, \;\; \mathbf{S_r^{z'}} = \sqrt{\mathbf{s/2}}(\mathbf{a_r^\dagger} + \mathbf{a_r}). \tag{4.61}$$

We have specifically chosen the above representation as our interest is to investigate the phase boundary where the spins align mostly along x direction, where $\mathbf{a_r^\dagger}$ and $\mathbf{a_r}$ represent the creation and annihilation operators of a magnon at site r.

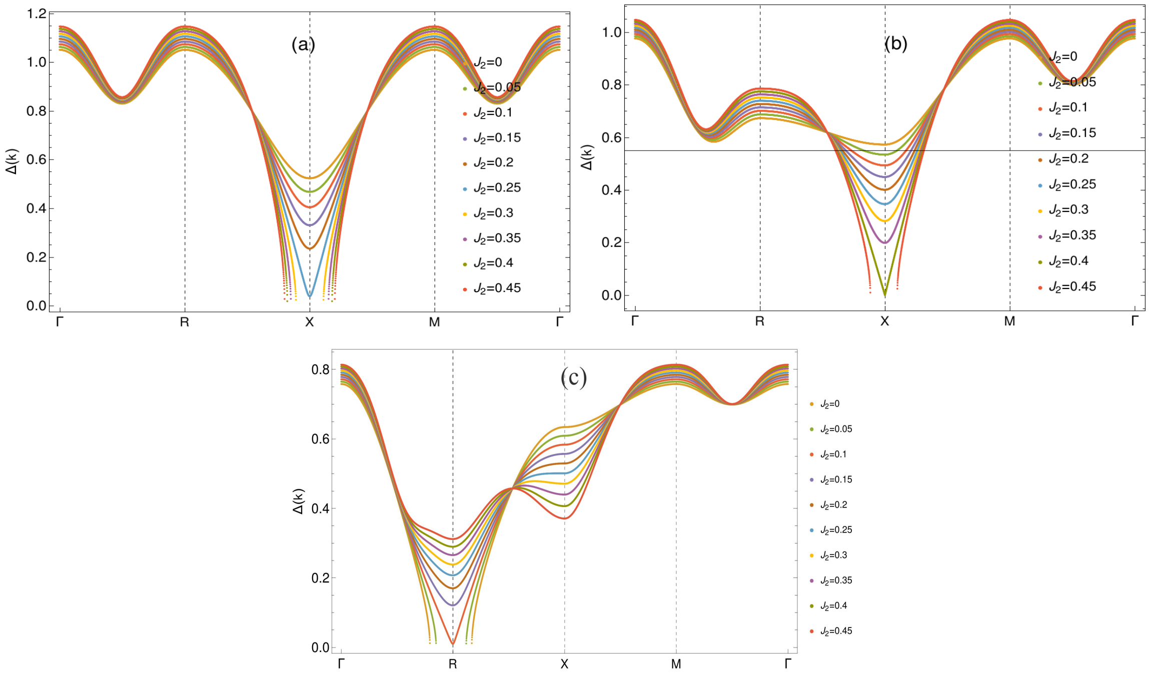

Figure 4.4: Plot showing the dispersion in the high-field case where quadratic behavior slowly converges to a linear behavior at the second-order critical line given by $K = 2sJ_1 + \frac{21}{8}sJ_2 + 2s|J_3|$. The spectrum is plotted for various values of J_2, the rest of the parameters used in plot (a) are: $J_3 = 0$, $K = 0.5$, $J_1 = 0.5$, $J_0 = 1.0$. Similarly for plot (b), $J_3 = 0.2$, $K = 0.5$, $J_1 = 0.5$, $J_0 = 1.0$. And for plot (c), $J_3 = 0.8$, $K = 0.5$, $J_1 = 0.5$, , $J_0 = 1.0$. The various symmetry point used in the above figure is as follows: Γ = $(0, 0, 0)$, R = (π, π, π), $X = (0, \pi, 0)$, and $M = (\pi, \pi, 0)$.

4.6.3 High-field limit, $K \gg J_0, J_1, J_2$ & $\theta_0 = \pi/2$

The groundstate in this limit is a trivial one with all the spins pointing towards the x-axis. To obtain the magnon-spectrum and to check the stability of the classical groundstates, the Holstein-Primakoff transformation Eq. (4.61) is substituted into the classical version of the Hamiltonian 4.2 with the groundstate Eq. (4.56) now being explicitly embedded into it. Since in the high-field case we invoke the translation invariance of the spin-configurations, we then can Fourier transform the a_i variables to a_k as $a_i = \frac{1}{N}\sum_{\vec{k}} a_{\vec{k}} \exp(-i\vec{k}\cdot\vec{r})$, substituting the transformed boson operators into the above equation yields a Hamiltonian of various orders in a. Within the linear regime we neglect the higher order terms beyond the order 2, the Hamiltonian then is given by,

$$\mathcal{H} = N\sum_k \left[\xi_k a_k a_k^\dagger + \frac{\gamma_k}{2}(a_k a_{-k} + a_k^\dagger a_k^\dagger)\right] + C_0 + \mathcal{O}(a^3) + \mathcal{O}(a^4), \tag{4.62}$$

where $C_0 = KSN$ and is the classical energy upon which the terms within the bracket has the information of the first dispersion in k-space, given by ξ_k. The ξ_k and γ_k is given below as,

$$\xi_k = \gamma_k + K - \frac{SJ_2}{8}, \tag{4.63}$$

$$\gamma_k = \frac{-s}{4}\left[J_2(2p_k^2 - 1) - 4(J_1 + J_2)p_k + 4|J_3|\cos(k_z)\right], \tag{4.64}$$

where $p_k = \cos(k_x + k_y)\cos(k_x - k_y)$. Now, the Hamiltonian is easily diagonalizable and upon doing that we obtain the eigen energies of the magnon spectra as given by,

$$E_k = \sqrt{\xi_k^2 - \gamma_k^2}. \tag{4.65}$$

In the Fig. 4.4 we show the spectrum plotted for parameters $J_1 = 0.2, K = 1.0$ and varying J_2 from 0.1 to 0.5. To qualitatively decipher the linearity seen in the dispersion curves obtained for $J_2 = 8/21$ we find the spectrum by extracting the low-energy behavior around the minima, that is, X (or R) high-symmetry point. We consider the following approximation $(k_x = -\pi/2 + \delta_x, k_y = \pi/2 + \delta_y, k_z = \pi + \delta_z)$ around R. Substituting these in Eq. (4.65) and expanding the terms γ_k, p_k, we get,

$$E_{\vec{\delta}} = \tilde{K}_1^{1/2}\sqrt{\tilde{K}_2 + 4(J_1 + 2J_2 + |J_3|)|\vec{\delta}|^2}, \tag{4.66}$$

here, $\tilde{K}_1 = K - \frac{sJ_2}{8}$, $\tilde{K}_2 = (K - 2sJ_1 - \frac{21}{8}sJ_2 + 2s|J_3|)$. From the Eq. (4.66) we can see that for all the values of $J_{1,2}, K$ the spectrum remains gapped with low-energy quadratic behavior in the dispersion curves except at the second-order transition point as obtained by $K_c = 2sJ_1 + 21/8J_2 + 2s|J_3|$. The spectrum at this point becomes linear and gapless, indicating a possible signature of with the underlying features of the groundstate for higher J_2, which is the antiferroelectric case. This also shows that the transition for smaller values of J_2 the system behaves quite differently from the one with relatively higher values of J_2. This can be attributed to the fact that the gapped spectrum is protecting the degeneracy in the groundstate manifold in the absence of dipole-dipole interaction J_2, with the excitations being gapped and discrete. When J_2 is increased and approaches the antiferroelectric ordered state, the spin-wave spectrum becomes linear and gapless as expected. And as one increases the value of J_2 further we see that the $\tilde{K}_2$ changes to negative in sign where the spectrum becomes imaginary (4.66). The same can be deciphered from the Fig. 4.4 shown in dotted lines near the $X(R)$ high-symmetry points where there are no states available with the gap $\Delta(k)$ being undefined. It is to be noted that for sufficiently large J_2 one needs to perform the SW analysis on a different groundstate. Importantly, from Eq. 4.66, we can see that the spin-wave velocity is independent of the nature of the coupling. Since,

$$\frac{\partial(E_{\vec{\delta}})}{\partial\vec{\delta}} \propto |J_3\vec{\delta}|\tilde{K}_1^{1/2}\sqrt{\tilde{K}_2 + 4(J_1 + 2J_2 + |J_3|)|\vec{\delta}|^2}. \tag{4.67}$$

The indistinguishability of the spin-wave velocity can be understood as follows: Let us consider a single layer, in a ground state of J_0, where each plaquette can take up to 8 different configurations with the same energy (four of them are shown in Fig. 4.3(a)). Now, if we pick any one of the eight states we see there exists one high-energy (from the rest of the seven states) state that appears at finite temperatures or fields. And, six of the low-energy choice where the system can exist at low-temperatures (from the remaining six other choices). Similarly, we do the same analysis for the AFM case and we see the same number of choices are available even for that case. That is even for AFM coupling there exists six low-energy choices and one high-energy choice the system can exist. Hence, we note that this choice of states is independent of the nature of the coupling, i.e, it does not distinguish whether the coupling is AFM or FM. This is reflected in the spin-wave spectrum and thus we obtain identical spin-wave velocity.

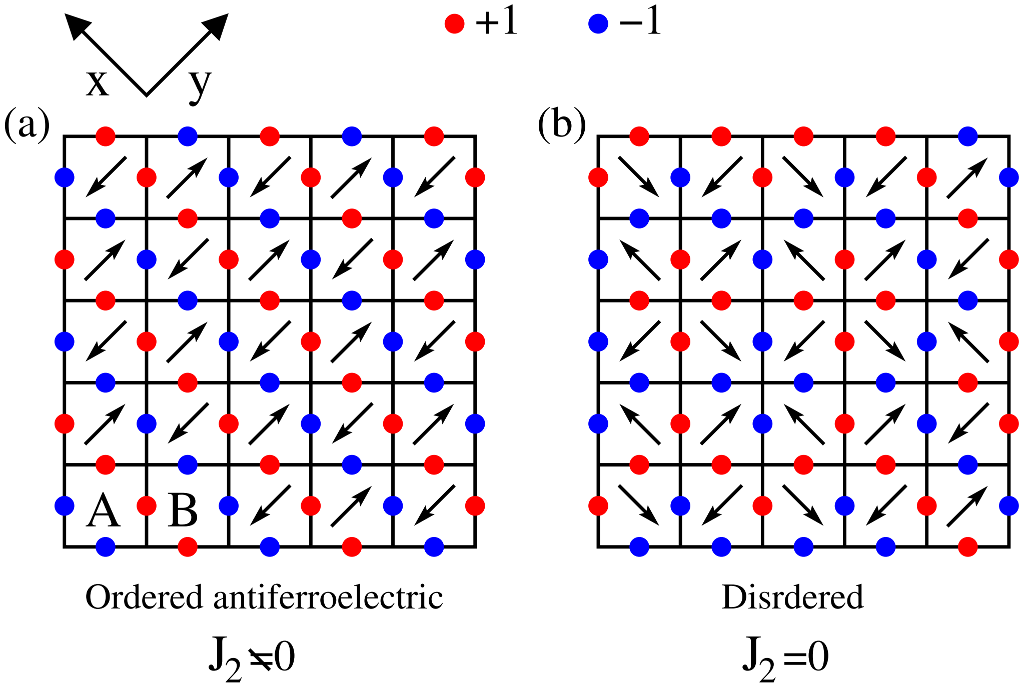

Figure 4.5: Illustration of a possible groundstate candidate in the regimes where $J_2 = 0$ (b) and $J_2 \neq 0$ (a).

4.6.4 Imaginary-time quantum Monte Carlo

First, we consider the confinement-deconfinement transition (CDT) where $J_2 = 0$. We vary the external field for various interlayer couplings, and calculate the imaginary-time correlation c_τ as a function of τ, as shown in Fig. 4.6. Similarly, in the next section, we provide the results for the order parameter P, ρ and specific heat C for $J_2 \neq 0$ where the material is believed to host the AFM phase.

4.6.5 Confinement-deconfinement transition

In Fig. 4.6(a-b), we plot $\log c_\tau$ versus τ for various values of field strengths. The plots are shown for J_3 where the coupling is taken as disordered type. We see that when the field strength is below a critical field of $K_c = 1.63$ (Fig. 4.6), the $\log c_\tau$ curve starts deviating from the power law decay (a behavior corresponding to a deconfined phase [89]). The functional form we fit is given by $c_\tau = r^{-n} \exp r/r_0$ (here, $n \sim 0.61$), that is, a behavior intermediate between a power law and exponential decay. We distinguish both phases by the fact that in the paraelectric phase the behavior one expects

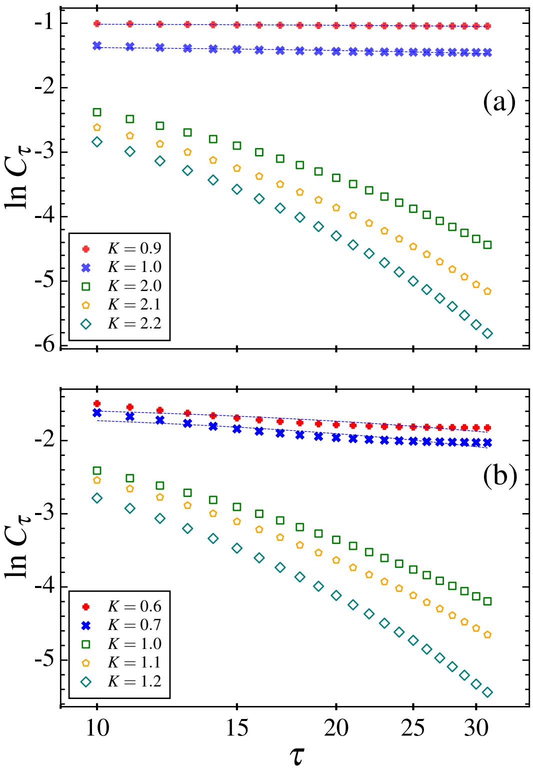

Figure 4.6: Plots showing the variation of the correlation function c_τ along the imaginary-time axis as estimated for different values of field strength. $J_0 = J_1 = 1.0$ is used in all the figures here. (a) Corresponds to the case where the strength of the interlayer coupling $J_3 = 0.1$ with a critical value of $K_c = 1.63$. Similarly, (b) for $J_3 = 0.3$. We see that the correlation function decays according to the power-law for low-field values, that is, for $K = 0.6, 0.7$ ($K < K_c = 0.94$) and then an exponential decay for $K = 1.0, 1.1, 1.2$ ($K > K_c$).

is purely exponential decay (cases where $K = 2.0, 2.1, 2.2$ in Fig. 4.6(a)). Similarly, in Fig. 4.6(b) where the strength of J_3 is now higher and is equal to 0.3, we see the function c_τ shows a lesser amount of long-range correlation for $K = 0.6, 0.7$ ($K < K_c$) decaying slowly away from the power-law $\sim 1/r^{\eta-d/2+\nu}$ compared to Fig. 4.6(a). This may be due to the reason that the quantum fluctuations in higher dimensions are much more pronounced leading to such a behavior. However, intutively, when the field strength is further increased we see that the c_τ deviates more and more away from the power-law (see the blue dot curve in Fig. 4.6) as it decays according to the exponential law corresponding to a confined phase. The critical point for $J_3 = 0.1$ is $K_c = 1.63$ and similarly for $J_3 = 0.3$ is $K_c = 0.94$.

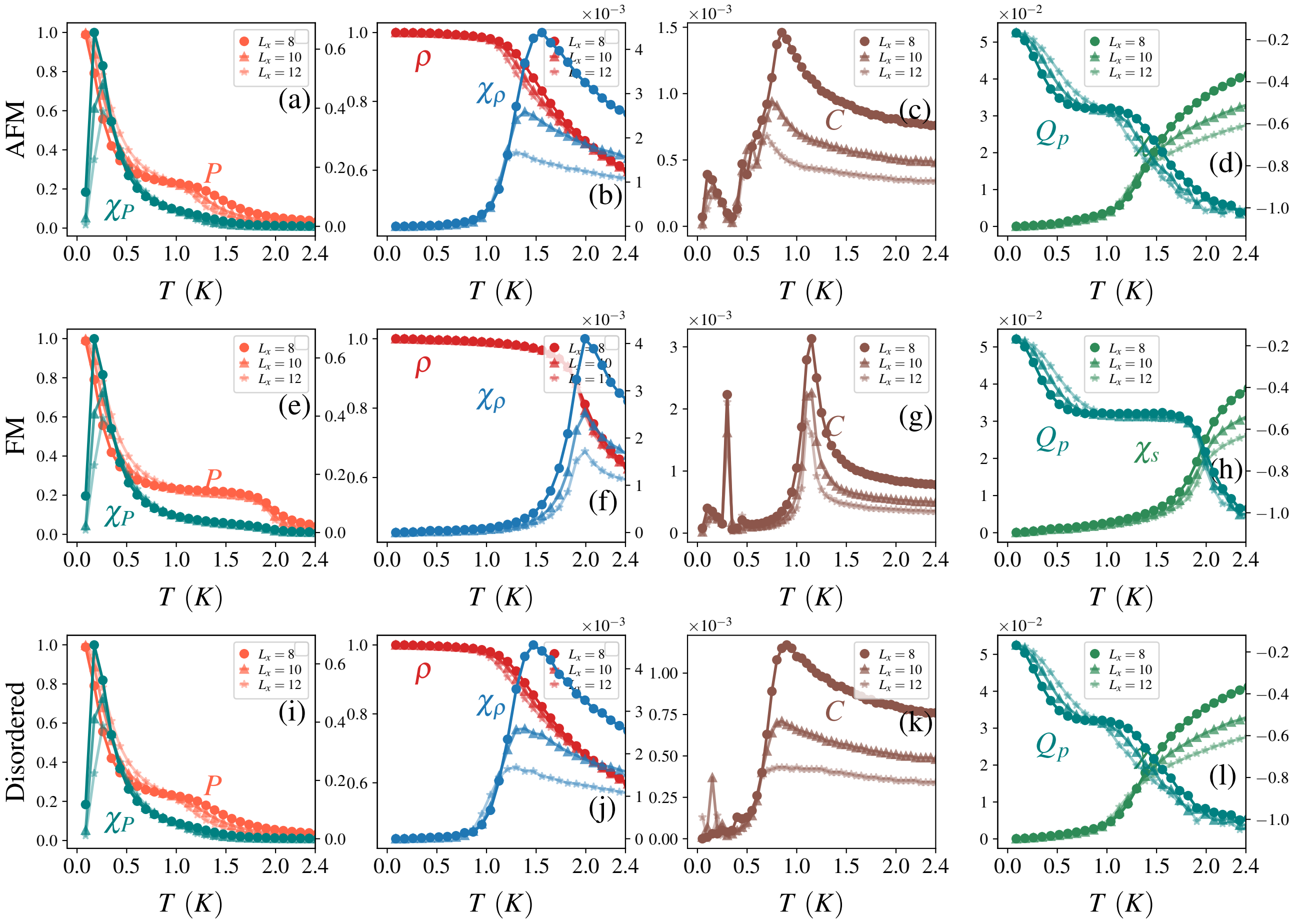

Figure 4.7: The variation of the order parameter P ((a), (e), (i)), the ice-rule detecting parameter ρ ((b), (f), (j)) and their corresponding susceptibilities χ_P ((a), (e), (i)) and and χ_ρ ((b), (f), (j)) as a function of temperature (and field) are shown for different lattice dimensions. Similarly, the specific heat over temperature, C/T is shown in (c), (g), (k) ppanels. Finally, the uniform magnetic susceptibility is shown in (d), (h), (l) correspondingly. The variation of all the parameters are estimated for three cases as labeled along the vertical axis, that is, AFM (antiferromagnet), FM (ferromagnet), Disorder. All the plots include the same, θ, that is, $\theta = \pi/6$. The values used in each of the cases are: $J_1 = 0.5$, $J_2 = 0.04$, $J_3 = 0.4$ with 8, 10, 12 lattice dimensions used along the interlayer axis, while we fix 12×12 as the intralayer dimensions.

4.6.6 Antiferroelectric phase transition

Antiferromagnet coupling: In Fig. 4.7(a-d) order parameters P, ρ and corresponding susceptibilities $\chi_P, \chi_\rho, C, \chi_s, Q_P$ are plotted against K. Note that not only the temperature is varied but also the field as dictated by the relation $K = T\tan\theta$. So, when a certain temperature value is mentioned, it is to be understood that the corresponding temperature value is $K = T\tan\theta$. Here for Fig. 4.7 θ is adjusted to $\pi/6$. We see that the P has a maximum value of 1 till the temperature of 0.3, indicating an antiferroelectric order. As the temperature is increased further, the P shows a plateau

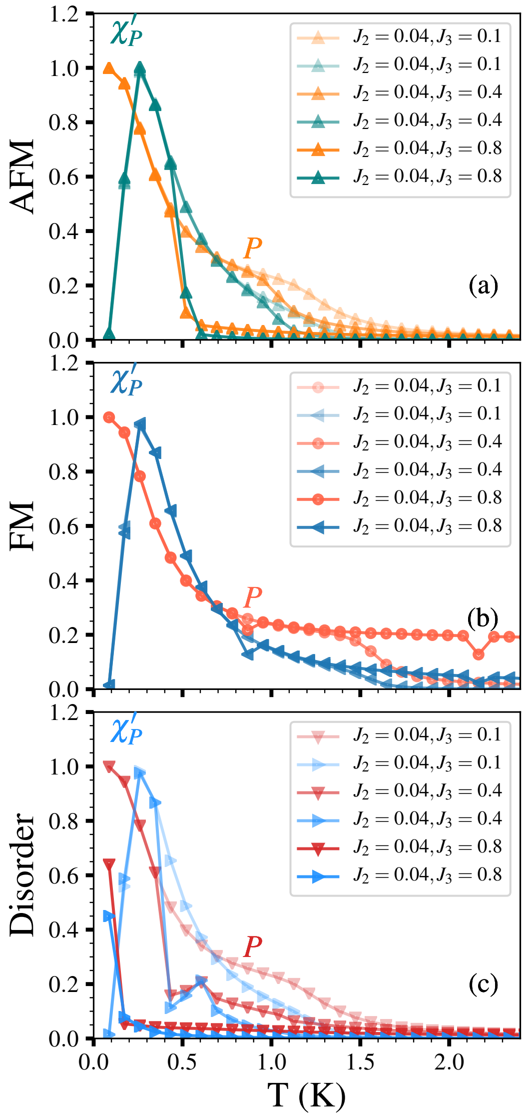

Figure 4.8: (Color Online) Variation of the order parameter P and the ice-rule parameter ρ versus field (temperature) are shown for different cases of J_3. The interlayer coupling values used are $J_3 = 0.1, 0.4, 0.8$ in the increasing trend of the color contrast of respective parameters (e.g: orange color corresponds to P and the increase in J_3 can be seen from the least to the highest contrast). a) Corresponds to the variation with AFM, b) FM and c) disordered interlayer couplings

behavior for intermediate temperatures (around $K \sim 0.2$ to 0.33) before vanishing to a conventional paraelectric state ($K > 1$). The plateau behavior can be identified as an intermediate state with strong quantum fluctuations [13, 103]. This is because the order parameter P gets vanished around these temperatures while the ice-rule parameter ρ continues to show a constant value of $\rho = 1$ till the temperatures of $K = 1.1$. So the region of temperatures where the P vanishes to the temperature where the value of ρ starts decreasing from 1 should correspond to a state which satisfies ice-rules. Also, these states should carry a zero net dipole-moment (molecular polarization). This is only possible when each plaquette has a finite dipole moment (molecular polarization) but is randomly oriented with respect to the neighboring plaquettes. The illustration of such a state can be understood from Fig. 4.5(b) where one possible groundstate is shown. The other states can be obtained by a gauge transformation which is already discussed in chapter 2. Similarly, the values for susceptibility, χ_P also corroborate the same as a peak around 0.25 seems to suggest a possible second-order transition at $K_c = 1.70(15), 1.85(27), 2.04(35)$ for $J_3 = 0.2, 0.3, 0.4$ respectively. Note that the scaling of parameters P, ρ shows a uniform behavior as we vary the linear size of the system from $L_x = 8$ to $L_x = 12$. For $L_x = 8$, the plateau is steeper than that for L_x =12. This is intuitive, as the higher sizes are understood to have fewer fluctuations with stable configurations.

Specific heat, C (see Fig. 4.7(c)), also shows a small anomalous peak similar to the behavior observed with no interlayer coupling. The susceptibility obtained due to P is shown in Fig. 4.7(a) and (b) by light red colored points which shows a jump at the transition from ferroelectric phase to quantum liquid-like states. This suggests that ferroelectricity is almost destroyed at this transition. However the susceptibility corresponding to ρ, that is χ_ρ is initially at lower temperatures it is almost zero, which gradually increases until the temperature reaches near the transition from quantum liquid-like states to the paraelectric states. At this transition the χ_ρ jumps at a higher value and remain almost constant up to a certain temperature which we call T_{χ_ρ} and after this, χ_ρ decreases monotonically. The specific heat at a very large temperature shows monotonically decreasing behavior characteristic to the usual paraelectric phase but at low temperature, it shows two peaks of different magnitude as seen in Fig. 4.7(c). The largest peak appears at the transition of quantum liquid-like state and we denote this temperature by $T^{\star}_{C/T}$. However, the sharp nature of the peak indicates a possible order-disorder phenomenon where the degeneracy seems to be uplifted to some extent. Below this temperature specific heat shows another small peak at where the P starts to decrease from the initial constant value for small T. This may be attributed to the fact that the increase of K results in more quantum fluctuations.

In Fig. 4.7(d), we plot the results for uniform susceptibility averaged over a single layer show an antiferromagnetic-like order along the orthogonal unit axes spanning the lattice. This shows that as the system size increases the peak height reduces and only vanishes in the thermodynamic limit.

Ferromagnet coupling: Similar to the AFM case, the results are shown accordingly in Fig. 4.7(e-h). Here also the order parameter P shows a value close to 1 at low temperatures (and temperatures) indicating an antiferroelectric phase. But unlike the AFM case, as we increase the temperatures further the intermediate liquid-like state seems to extend to much larger temperatures compared to the AFM case, indeed the intermediate-liquid-like extends from values of 0.3 to 1.2. This can be understood that because of FM type coupling, one expects a lesser amount of quantum fluctuations (compared to AFM and disordered case) across the interlayers. This trend is followed similarly by susceptibility since it shows a peak around the same value of K around 0.25. This is because we have used the same values of interlayer strength with just opposite signs and thus the peak around the same temperatures.

Specific heat curves plotted in Fig. 4.7(g) show that cross-over temperatures have slightly shifted to higher temperature values compared to the AFM case (see Fig. 4.7(c)). This is in favor of the finding that the intermediate state extends to much larger temperatures in the curves of order parameter P. The common aspect in AFM and FM case is about the peak at low temperatures (~ 0.3). The peak values are the same in both cases, unlike the peak appearing at higher temperatures. Which for the FM case is sharper than the AFM case. This may seem to suggest that a possible order-disorder phenomenon taking place driven by thermal energy.

Disordered coupling: In this case, we see that P shows a behavior that is very close to the AFM and unlike the FM case. The only difference that we see is in the specific heat curves. We observe that the anomalous peak almost vanishes and also the crossover peak at later temperatures gets broader than the rest of the two cases. This strongly suggests that the disorder completely lifts the degeneracy and there is no re-entrance of the intermediate-liquid-like as such. The values of the specific heat curves are intermediate to that of AFM and FM. In all the cases, the variation of χ_s is antiferromagnetic. Though for the disorder the antiferromagnetic nature is slightly perturbed (see Fig. 4.7(i-l)).

Variation with the interlayer interaction strength

Antiferromagnet coupling: We also plot the behavior of P and ρ for various values of J_3. In Fig. 4.8(a), we have shown the variation of χ_P and χ_ρ for J_3=$(0.1, 0.4, 0.8)$ in orange and navy blue colored points respectively. For large values of $J_3 = 0.8$, P and ρ have sharper peaks and decrease more rapidly compared to the case of small values of J_3. This could be due to the lowered stability of the intermediate liquid-like state as the coupling strength J_3 is increased. Also, though the plateau is diminishing, the value of P at low temperatures remains the same for all the cases of coupling. The AFE phase under the AFM type coupling is stable while for the intermediate liquid-like state this is not the case.

Ferromagnet coupling: In the Fig. 4.8(b), clearly the plateau region in order parameter P extends to much larger temperatures as the coupling is increased. This is in contrast to the AFM case. When the value of J_3 is equal to 0.1, the intermediate liquid-like state extends from $T = 0.42$ to $T = 0.94$. When $J_3 = 0.4$, it extends from $T = 0.45$ to $T = 1.4$. And for $J_3 = 0.8$, it is much higher. The reason could be because of the lesser quantum fluctuations in the FM case. Nevertheless, the order parameter P still shows a value of 1 for all the values of coupling strength, J_3. This is similar to the AFM case.

Disordered coupling: In the Fig. 4.8(c), when the value of J_3 is small, i.e, 0.1, the variation of order parameter resembles slightly that of AFM and FM case. The plateau region extends from $T = 0.25$ to $T = 0.75$. But when J_3 is increased to 0.4, we see that the intermediate liquid-like state only extends from $T = 0.25$ to 0.6. Similarly, when $J_3 = 0.8$, comparable to the energies of the intraplane interactions, the order parameter P has a lower value at lower temperatures. Also, there is no plateau behavior, instead, the abrupt vanishing of P is seen. This could be understood because of more quantum fluctuations induced by disorder type. However, for lower values of interlayer cou-

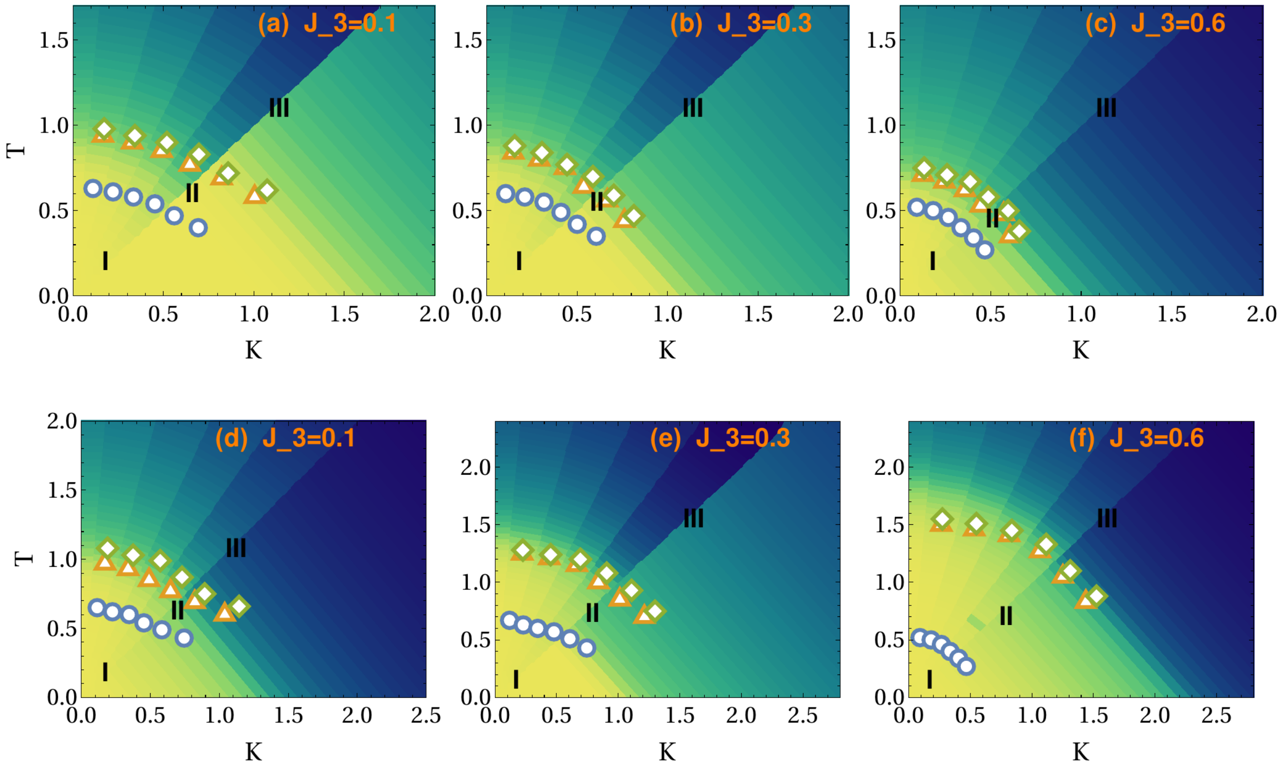

Figure 4.9: Phase diagram in T_K plane for both the cases, that is, AFM (Fig. (a)-(c)) and similarly for FM (Fig. (d)-(f)). In each row starting from the left (Fig. (a)), the cases correspond to $J_3 = 0.1, 0.3, 0.6$ of interlayer coupling strength. The labels **I**, **II**, **III** indicate the AFE phase, Intermediate liquid-like phase and conventional paraelectric phase respectively.

pling, even the disordered type coupling hosts both an AFE and intermediate liquid-like state. The variation of ice-rule parameter ρ is used to show that there exists an intermediate state with finite-molecular polarization since the value of ρ close to 1 indicates that the entire lattice is in an ice-rule state (apart from statistical fluctuations) and any deviation from it indicates a non-ice-rule state.

Phase diagram

Antiferromagnet coupling: In Fig. 4.9 (top row), we plot the critical points in the $T - K$ plane as obtained from the the Binder cumulant (see Eq. (4.55)). We also plot the peak values of the specific heat curve (T_C) and the peak in the susceptibility of ice rule order parameter T_{χ_ρ}. For the AFM case, the corresponding values are given in Table 4.10. Clearly, the values the gap between T_c and T_C (or T_{χ_ρ}) is decreasing with the strength of J_3.

(a)J_3=0.1

K	T_c	T_C	T_{χ_ρ}
0.1	0.67	1.25	1.28
0.2	0.63	1.21	1.24
0.3	0.6	1.15	1.2
0.4	0.57	1.	1.08
0.5	0.51	0.85	0.93
0.6	0.43	0.7	0.75

(b)J_3=0.4

K	T_c	T_C	T_{χ_ρ}
0.1	0.65	0.97	1.08
0.2	0.62	0.93	1.03
0.3	0.6	0.85	0.99
0.4	0.54	0.77	0.87
0.5	0.49	0.69	0.75
0.6	0.43	0.6	0.66

(c)J_3=0.8

K	T_c	T_C	T_{χ_ρ}
0.1	0.52	1.5	1.55
0.2	0.5	1.46	1.51
0.3	0.46	1.41	1.45
0.4	0.4	1.27	1.33
0.5	0.34	1.05	1.1
0.6	0.27	0.83	0.88

Figure 4.10: Table showing the critical points (T_c) and the points where the specific heat C and the susceptibility T_{χ_ρ} peaks. (a) For $J_3 = 0.1$ value of FM type coupling, (b) for $J_3 = 0.4$, (c) for $J_3 = 0.8$.

Ferromagnet coupling: In Fig. 4.9 (bottom row), we plot the critical points in the $T - K$ plane as obtained from the the Binder cumulant (see Eq. (4.55)). We also plot the peak values of the specific heat curve (T_C) and the peak in the susceptibility of ice rule order parameter T_{χ_ρ}. For the AFM case, the corresponding values are given in Table 4.10. Clearly, the values the gap between T_c and T_C (or T_{χ_ρ}) is increasing with the strength of J_3.

4.6.7 Dynamic structure factor

As mentioned, an earlier study that has not accounted for the interlayer coupling has shown three distinct phases as mentioned [103, 13]. Here, we numerically perform simple linear-spin wave dynamic structure calculations on a real space lattice over the classical ground states of the respective phases identified in a quasi-2D version. We do it on a quasi-2D structure because the interlayer coupling is shown to alter the critical points where the qualitative behavior is not changed. So, the dynamic structure factor can be qualitatively extrapolated from quasi-2D results when an interlayer coupling is introduced for the 3D case. Nevertheless, we note that the present study offers scope to get the low-lying excitations (that can be experimentally tractable) above the classical ground states [174]. Crucial information regarding the degree of fluctuations in the ice-rule physics could also be the best probed to validate certain underlying theories [89]. We know that in organic ferroelectrics each symmetric arrangement of the molecule posses an associated vibrational mode with it. We, therefore, expect that the amount of frustration mandated by its symmetry can be observed experimentally in

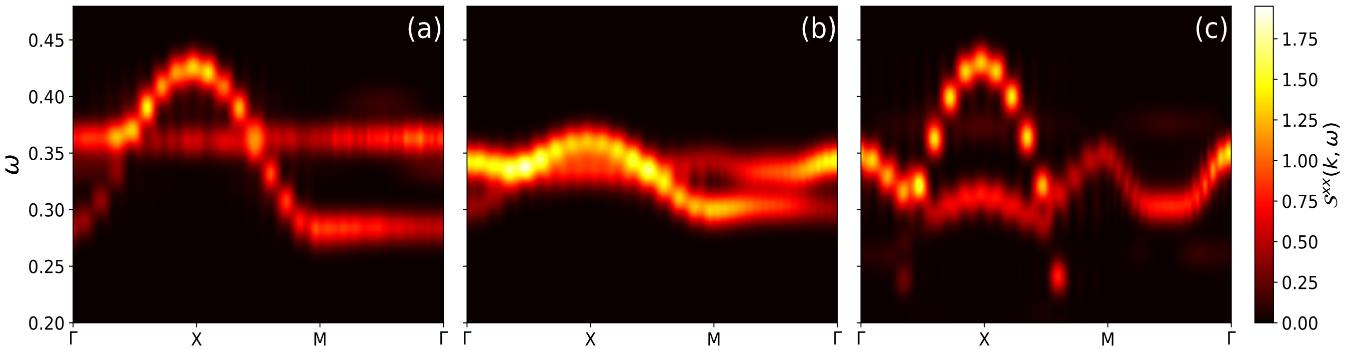

Figure 4.11: The dynamic structure factor, $\mathcal{S}^{xx}(k,\omega)$ within the realm of Real-space linear spin-wave theory (RS-LSWT) calculated for weak interlayer coupling limit. In all the plots, we fix the value of $J_0 = 1$. a) For the parameters $J_1 = 1.0$, $J_2 = 0$, $K_x = 0.3$. b) For $J_1 = 1.0$, $J_2 = 0.019$, $K_x = 0.3$. Similarly, c) For $J_1 = 1.0$, $J_2 = 0.3$, $K_x = 0.2$. Here, $\Gamma \equiv (0,0)$, $M \equiv (\pi,\pi)$, $X \equiv (0,\pi)$

the non-resonant Raman-scattering.

The brief details on the method and implementation of RS-LSWT are given in Appendix B. Fig. 4.11 shows the xx dynamical correlation function $S^{xx}(k,\omega)$ plotted for three different regimes under small magnetic fields. In Fig. 4.11(a), we see two bands, one of them is a flat one (no dispersion, see Fig. 4.11(a) at $\omega \sim 0.36(7)$) and the other with a dispersion. The flat band can be understood to be the excitations corresponding to the conserved quantities with a non-local gauge symmetry (as discussed in chapter 3). Within the linear-spin wave theory probing the excitations under the classical ground states, the gauge operator can be decomposed into non-interacting pairs of correlators, for example, $\sigma_1^z\sigma_2^z\sigma_3^z\sigma_4^z \sim \sigma_1^{x'}\sigma_2^{x'} + \sigma_3^{x'}\sigma_4^{x'} + \cdots$ in the transformed coordinates. Since, for $J_2 = 0$, the terms $\sigma_1^x\sigma_2^x$ will yield a dispersive term like $\cos k$ and since the further configurations along the unit vectors are independent, we see a $\sin k$ behavior is also likely possible. Therefore, ending with the net result being non-dispersive. Even if one considers a mean-field theory extension to the present scenario we might still see a similar flat band, because these terms do not vanish. Note that the minimum of the spectrum is at multiple k-points, i.e, $\omega \sim 0.28$ from M to Γ points. This could also reflect the underlying symmetry in the system.

Similarly, the optical mode that we see from Γ to X and X to M in Fig. 4.11(a) could be associated to the excitations of the correlators of the form $\sigma_1^{x'}\sigma_2^{x'} + \sigma_3^{x'}\sigma_4^{x'} + \cdots$ coming from the gauge operators and as well as the intramolecular interaction term. The decomposition can be understood like all the possible dimer coverings on a plaquette spanning the entire lattice. So then the excitations should correspond to these dimers. Now the reason for the appearance of the optical mode can be understood from ice-rule constraint. Since the configurations along the unit vector that spans the lattice are not completely independent. We expect that the net superposition of the spin-waves should be non-dispersive. That is why we see optical modes when only one component is varied (k_x from Γ to X or k_y from X to M). But when both the components are varied we see that the net result is flat (from M to Γ). When J_2 is turned on, due to the global ordering being established, we see that the excitations of these dimer coverings have a definite spectrum of the form $\cos k_x$ or $\sin k_y$. We thus see no flat band behavior in Fig. 4.11(a).

4.7 Chapter summary

We have simulated a three-dimensional model of squaric acid crystal considering the interlayer interaction (J_3) of protons that were not rigorously accounted earlier. We use the pseudo-spin formalism and introduce an additional interlayer interaction (J_3) of the Ising type. We aim at understanding the role played by the nature of the J_3 and the strength of it on the phases that have been found for quasi-2D case. Motivated by earlier works [42], in the present work, we use three different types of interlayer coupling (AFM, FM, Disorder). Our QMC analysis reveals interesting results for small J_2 strengths. Similar to the quasi-2D case [103, 13], we observe an intermediate-state appearing (around $T \sim 0.3$) where the order parameter, P, is found to exhibit a plateau behavior that vanishes with the system size. This is not the scenario for all the types of couplings considered. From Fig. 4.8(a), for an AFM case of interlayer coupling, we see that the AFE stacked configuration of layers seems to be more robust (see Fig. 4.7) as the value of $P(\sim 1)$ at low temperatures does not change even when J_3 is increased. Since the quantum fluctuations in the AFM case has more pronounced quantum fluctuations, therefore, the intermediate liquid-like states is found to vanish as the strength of J_3 is increased (see Fig. 4.8. The plateau starts getting narrowed and then disappears for large J_3). Secondly, when we consider the FM type of J_3, we observe that not only does the AFE stacked configuration is found to exist for large J_3 ($J_3 < 1.0$), but also the intermediate state was shown to extend to larger temperatures (and fields). In contrast to the AFM coupling of J_3, the anomalous peak seen at lower temperatures in the specific-heat curves is shown to have lesser entropy. As the peak height is lesser than in the case of AFM. We know that the entropy ($S \propto \ln(C/T)$). Therefore, the higher the peak the more degeneracy the system possesses. Nevertheless, in the last case of disordered coupling, we see neither of the AFE nor intermediate liquid-like state is shown to exist beyond a disorder strength of $J_3 = 0.4$. This is intuitive because the disorder case accounts for a large degree of quantum fluctuations compared to AFM and FM resulting in such behavior.

We note that previous studies [13, 103] has investigated the finite-temperature phase diagram in a related model with two body interactions [103] followed by a four-spin model [13, 89] motivated by the earlier studies [99]. Though it is known that the interlayer interaction is a weak one, some studies have reported that in H_2SQ interlayer interaction is more likely AFM in nature. Here, in the present work, we show that AFM type J_3 has a more robust anomalous peak compared to the others. And the stability of the intermediate state strictly depends on the strength. While this is the scenario for AFM, the FM coupling also hosts the AFE phase, but with the exception that unlike the AFM coupling the intermediate state extends to larger temperatures and pressures as the strength of J_3 is increased.

Further, apart from the ground state properties and static susceptibilities, to probe the nature of excitations that can be experimentally verified, we also calculate the dynamic structure factor in our calculations. We use a real-space linear spin-wave theory to obtain the spectrum. We see that the characteristic behavior of the deconfined phase can be seen in Fig. 4.11(a) when $J_{1,2}$ are absent. That is, apart from the flat spectrum in Fig. 4.11(a) the spectrum is highly asymmetric around the X, M high symmetry point. This is expected because in the deconfined phase the system along the two orthogonal directions has an independent configuration. The configuration along the unit vector x is independent of configuration along y. Due to this fact, we see that the spectrum until the $M-$high symmetry point is broader while the spectrum from M to Γ is flat. This explains the deconfined characteristic. Next, once we put the finite J_1 with small J_2, we see that a small deviation from the flat spectrum from M to Γ is seen. This is because the small J_2 is responsible for a global ordering in the system. And in the global ordering case, the ordering along the two orthogonal vectors spanning the lattice is no more independent. This can be further corroborated from the Fig. 4.11(c) when the J_2 is further increased a sinusoidal behavior in the spectrum is seen. We know that any ordering in the system manifests in the form of $\sim \cos(\vec{k})$ or $\sin(\vec{k})$. This explains the dynamic structure factor in three important regimes.

Appendices

APPENDIX A

Scheme for Extrapolation

Generally, perturbative series expansions are mostly well respected in the low-field regime or for small perturbing parameter strengths. To make a good approximation to higher fields or higher perturbing values, it is often useful to ascribe to extrapolation methods. Any finite series can be extrapolated to capture the analytic properties in the regimes where the perturbative approach deviates. Earlier, Domb and Sykes [180] used the extrapolation methods to obtain dynamical critical exponents using perturbative series. Similarly, various other robust methods have been introduced in the 1970s gained popularity is the one by Guttmann [181]. Often it seems there is no specific extrapolation method that works to all other perturbative series, it is up to us to determine which gives better convergence. Here, we briefly describe the method of Pade and DLog-Pade approximant that have been and are been used in the current pCUT methods and have been successfully applied in the past for similar problems.

Consider a function analytical over all regions of its domain, say, $f(x)$. The Taylor expansion at order N around $x = 0$ is given by,

$$S_N(x) = \sum_{i=0}^{N} a_i x^i. \tag{A.1}$$

Now we can introduce the function $P[L(x), M(x)]$ that extrapolates the series $S_N(x)$ by a rational functions which is nothing but the *Pade approximant*, defined as

$$P[L(x), M(x)] = \frac{P_L(x)}{Q_M(x)}, \tag{A.2}$$

here, the polynomials $P_L(x)$ and $Q_M(x)$ are of degree L and M respectively. They can be given as,

$$\begin{aligned} P_L(x) &= \sum_{i=0}^{L} p_i x^i, \\ Q_M(x) &= \sum_{i=0}^{M} q_i x^i. \end{aligned} \tag{A.3}$$

Here on the polynomial are notated by without the explicit x-dependence. The series expansion of the Pade approximant $P[L, M]$ at prder N must be equivalent to S_N. Now, by comparing the coefficients on both sides leads to set of N linear equations for p_i, q_i and a_i, with a unique solution for $L + M \leq N$. In our context, the coefficients a_i can be exactly found. While in the perturbative limit the Pade approximants are, by construction, very close to $f(x)$, for large L and M they are expected to give a better representation of $f(x)$ than the bare series, even though $P[L, M]$ can have upto M poles in the complex plane, which are usually spurious pole.

If $f(x)$ is a quantity with an algebraic divergence at the critical point x_c, then,

$$\lim_{x \to x_c} f(x) = A(x_c - x)^{-\theta}, \tag{A.4}$$

it is useful to approximate its logarithmic derivative as,

$$\frac{d}{dx}\ln\left[f(x)\right] = \frac{f'(x)}{f(x)} = \lim_{x\to x_c} \frac{\theta}{x_c - x}. \tag{A.5}$$

With this trick, a Pade extrapolation of the LHS in Eq. (A.5) can be used to approximate the critical point x_c through its poles and the critical exponent θ through its residues. Generally, a Dlog$P[L,M]$ yields up to M pole-residue pairs. To identify a physical pole one needs to have a basic knowledge about the system at hand. However, here we are interested in real-values functions $f(x)$ with positive x. If the approximant Dlog$P[L,M]$(or $P[L,M]$) features real poles close to the origin than the physical singularity, it is then a defective pole. One needs to be cautious when dealing with Pade analysis where the spurious poles appearance can lead to an apprehension of false converge. One good way to check the validity of the real nature of poles, one needs to perform consistently a Pade approximant analysis from smaller series to higher series (as high as possible). If the poles converge smoothly with no new information, then one may account for it to be the real pole. However, in practice, it is safer and easier to gather results from all approximants Dlog$P[L,M]$ with $L+M \leq N-1$ in a so called Pade table and try to find sequences of stable approximations to estimate the accuracy of the extrapolation. Often the best approximants are $[L-1,L]$, $[L,L]$ and $[L,L-1]$.

There are other versions of Pade approximations that have been generalized in different ways, a certain class of generations known under the name differential approximants (DA) and others that have been generalized by Guttmann and Joyce by adding a higher derivative of $f(x)$ can be found in Ref. [182]. Interested reader for further extrapolation methods used in the pCUT methods can refer to Ref. [183, 184, 185, 186]. In our present analysis, we have used only a simple DLog-pade approximation to arrive at our results. We, therefore, give the technical analysis that has been rigorously solved in Mathematica, the gap Δ was estimated and is presented term by term in the next subsection.

A.1 pCUT calculated dispersion in high-field limit & $J_2 = 0$

$$
\begin{aligned}
\Delta(k_x, k_y) \;=\; & K + \frac{541 J_0^5 J_1 \cos(k_x + k_y)}{1152} - \frac{15331 J_0^4 J_1^2 \cos(2k_x + 2k_y)}{13824} - \frac{15331 J_0^4 J_1^2 \cos(6k_x + 6k_y)}{13824} + \\
& \frac{67}{576} J_0^4 J_1 \cos(k_x + k_y) - \frac{891}{128} J_0^3 J_1^3 \cos(k_x + k_y) \\
& + \frac{521}{128} J_0^3 J_1^3 \cos(3k_x + 3k_y) + \frac{521}{128} J_0^3 J_1^3 \cos(5k_x + 5k_y) - \\
& \frac{13}{8} J_0^3 J_1^2 \cos(2k_x + 2k_y) - \frac{13}{8} J_0^3 J_1^2 \cos(5k_x + 5k_y) - \\
& \frac{3}{4} J_0^3 J_1 \cos(k_x + k_y) + \frac{129}{64} J_0^2 J_1^4 \cos(2k_x + 2k_y) - \frac{2497}{128} J_0^2 J_1^4 \cos(4k_x + 4k_y) + \\
& \frac{129}{64} J_0^2 J_1^4 \cos(6k_x + 6k_y) - \frac{57}{32} J_0^2 J_1^3 \cos(k_x + k_y) + \\
& \frac{545}{128} J_0^2 J_1^3 \cos(3k_x + 3k_y) + \frac{545}{128} J_0^2 J_1^3 \cos(4k_x + 4k_y) - \\
& \frac{15}{8} J_0^2 J_1^2 \cos(2k_x + 2k_y) - \frac{15}{8} J_0^2 J_1^2 \cos(4k_x + 4k_y) - \\
& \frac{1}{8} J_0^2 J_1 \cos(k_x + k_y) - \frac{5}{2} J_0 J_1^5 \cos(k_x + k_y) + 4 J_0 J_1^5 \cos(3k_x + 3k_y) + \\
& 4 J_0 J_1^5 \cos(5k_x + 5k_y) + 3 J_0 J_1^4 \cos(2k_x + 2k_y) - 5 J_0 J_1^4 \cos(3k_x + 3k_y) - \\
& 5 J_0 J_1^4 \cos(4k_x + 4k_y) + 3 J_0 J_1^4 \cos(5k_x + 5k_y) - 2 J_0 J_1^3 \cos(k_x + k_y) + \\
& 6 J_0 J_1^3 \cos(3k_x + 3k_y) - 2 J_0 J_1^2 \cos(2k_x + 2k_y) - 2 J_0 J_1^2 \cos(3k_x + 3k_y) + \\
& 2 J_0 J_1 \cos(k_x + k_y) - 2 J_1^6 \cos(2k_x + 2k_y) + \frac{7}{2} J_1^6 \cos(4k_x + 4k_y) - \\
& 2 J_1^6 \cos(6k_x + 6k_y) - \frac{1}{2} J_1^5 \cos(k_x + k_y) + \\
& \frac{7}{4} J_1^5 \cos(2k_x + 2k_y) - \frac{5}{4} J_1^5 \cos(3k_x + 3k_y) - \frac{5}{4} J_1^5 \cos(4k_x + 4k_y) + \frac{7}{4} J_1^5 \cos(5k_x + 5k_y) - \\
& \frac{1}{4} J_1^4 \cos(2k_x + 2k_y) - \frac{1}{4} J_1^4 \cos(4k_x + 4k_y) - J_1^3 \cos(k_x + k_y) + J_1^3 \cos(2k_x + \\
& 2k_y) + J_1^3 \cos(3k_x + 3k_y) - 2 J_1^2 \cos(2k_x + 2k_y) + 2 J_1 \cos(k_x + k_y) - \frac{31 J_0^6}{768} - \\
& \frac{9437 J_0^4 J_1^2}{4608} + \frac{3 J_0^4}{32} - \frac{15 J_0^3 J_1^2}{8} + \frac{145 J_0^2 J_1^4}{32} + \\
& \frac{9 J_0^2 J_1^2}{8} - \frac{J_0^2}{2} + 2 J_0 J_1^4 + 2 J_0 J_1^2 + \frac{J_1^6}{4} + \frac{J_1^4}{4} + J_1^2.
\end{aligned}
\tag{A.6}
$$

A.2 pCUT calculated dispersion in high-field limit & $J_2 \neq 0$

$$
\begin{aligned}
\Delta(k_x, k_y) \;=\; & K - \frac{31J_0^6}{768} + \frac{541J_1\cos(k_x+k_y)J_0^5}{1152} - \frac{9437J_1^2J_0^4}{4608} + \frac{67}{576}J_1J_0^4\cos(k_x+k_y) - \\
& \frac{15331J_1^2J_0^4\cos(2k_x+2k_y)}{13824} - \frac{15331J_1^2J_0^4\cos(6k_x+6k_y)}{13824} + \frac{3J_0^4}{32} - \frac{15J_1^2J_0^3}{8} - \\
& \frac{891}{128}J_0^3J_1^3\cos(k_x+k_y) - \frac{3}{4}J_0^3J_1\cos(k_x+k_y) - \frac{5}{8}J_0^3J_2\cos(k_x+k_y) - \\
& \frac{13}{8}J_0^3J_1^2\cos(2k_x+2k_y) + \frac{521}{128}J_0^3J_1^3\cos(3k_x+3k_y) + \frac{521}{128}J_0^3J_1^3\cos(5k_x+5k_y) - \\
& \frac{13}{8}J_0^3J_1^2\cos(5k_x+5k_y) + \frac{145J_0^2J_1^4}{32} + \frac{9J_1^2J_0^2}{8} + \frac{5J_2^2J_0^2}{1024} + \frac{67}{128}J_1J_2J_0^2 - \\
& \frac{169}{512}J_2^2\cos(2k_x)J_0^2 - \frac{7}{32}J_1J_2\cos(2k_x)J_0^2 - \frac{3}{64}J_2\cos(2k_x)J_0^2 - \frac{9J_2^2\cos(4k_x)J_0^2}{2048} - \\
& \frac{7}{256}J_2^2\cos(k_x-3k_y)J_0^2 - \frac{35}{512}J_2^2\cos(2k_x-2k_y)J_0^2 - \frac{11}{16}J_2^2\cos(k_x-k_y)J_0^2 - \\
& \frac{35}{64}J_1J_2\cos(k_x-k_y)J_0^2 - \frac{1}{16}J_2\cos(k_x-k_y)J_0^2 - \frac{7}{256}J_2^2\cos(3k_x-k_y)J_0^2 - \\
& \frac{169}{512}J_2^2\cos(2k_y)J_0^2 - \frac{7}{32}J_1J_2\cos(2k_y)J_0^2 - \frac{3}{64}J_2\cos(2k_y)J_0^2 - \frac{9J_0^2J_2^2\cos(4k_y)}{2048} - \\
& \frac{57}{32}J_1^3\cos(k_x+k_y)J_0^2 - \frac{273}{128}J_2^2\cos(k_x+k_y)J_0^2 - \frac{1}{8}J_1\cos(k_x+k_y)J_0^2 - \\
& \frac{229}{64}J_1J_2\cos(k_x+k_y)J_0^2 - \frac{1}{16}J_2\cos(k_x+k_y)J_0^2 - \frac{3}{128}J_2^2\cos(3k_x+k_y)J_0^2 - \\
& \frac{11}{256}J_1J_2\cos(3k_x+k_y)J_0^2 + \frac{129}{64}J_1^4\cos(2k_x+2k_y)J_0^2 - \frac{15}{8}J_1^2\cos(2k_x+2k_y)J_0^2 - \\
& \frac{35}{512}J_2^2\cos(2k_x+2k_y)J_0^2 - \frac{13}{64}J_1J_2\cos(2k_x+2k_y)J_0^2 - \frac{3}{32}J_2\cos(2k_x+2k_y)J_0^2 - \\
& \frac{1}{512}J_2^2\cos(4k_x+2k_y)J_0^2 - \frac{3}{128}J_2^2\cos(k_x+3k_y)J_0^2 - \frac{11}{256}J_1J_2\cos(k_x+3k_y)J_0^2 + \\
& \frac{545}{128}J_1^3\cos(3k_x+3k_y)J_0^2 - \frac{1}{64}J_2^2\cos(3k_x+3k_y)J_0^2 - \frac{1}{32}J_1J_2\cos(3k_x+3k_y)J_0^2 - \\
& \frac{1}{512}J_2^2\cos(2k_x+4k_y)J_0^2 - \frac{2497}{128}J_1^4\cos(4k_x+4k_y)J_0^2 + \frac{545}{128}J_1^3\cos(4k_x+4k_y)J_0^2 - \\
& \frac{15}{8}J_1^2\cos(4k_x+4k_y)J_0^2 + \frac{5J_2^2\cos(4k_x+4k_y)J_0^2}{1024} + \frac{129}{64}J_1^4\cos(6k_x+6k_y)J_0^2 - \\
& \frac{J_0^2}{2} + 2J_1^4J_0 - \frac{101J_2^3J_0}{128} + 2J_1^2J_0 - \frac{77}{32}J_1J_2^2J_0 + \\
& \frac{J_2^2J_0}{4} - \frac{53}{32}J_1^2J_2J_0 + J_1J_2J_0 + \frac{31}{64}J_2^3\cos(2k_x)J_0 + \\
& \frac{25}{16}J_1J_2^2\cos(2k_x)J_0 - \frac{1}{4}J_2^2\cos(2k_x)J_0 + \frac{19}{16}J_1^2J_2\cos(2k_x)J_0 -
\end{aligned}
$$

$$\frac{1}{2}J_1J_2\cos(2k_x)J_0 + \frac{19}{256}J_2^3\cos(4k_x)J_0 + \frac{19}{128}J_1J_2^2\cos(4k_x)J_0 +$$

$$\frac{67}{256}J_2^3\cos(k_x-3k_y)J_0 + \frac{67}{128}J_1J_2^2\cos(k_x-3k_y)J_0 + \frac{3}{8}J_2^3\cos(2k_x-2k_y)J_0 +$$

$$\frac{3}{4}J_1J_2^2\cos(2k_x-2k_y)J_0 + \frac{43}{64}J_2^3\cos(k_x-k_y)J_0 + \frac{43}{32}J_1J_2^2\cos(k_x-k_y)J_0 -$$

$$\frac{1}{2}J_2^2\cos(k_x-k_y)J_0 - J_1J_2\cos(k_x-k_y)J_0 + \frac{67}{256}J_2^3\cos(3k_x-k_y)J_0 +$$

$$\frac{67}{128}J_1J_2^2\cos(3k_x-k_y)J_0 + \frac{31}{64}J_2^3\cos(2k_y)J_0 + \frac{25}{16}J_1J_2^2\cos(2k_y)J_0 - \frac{1}{4}J_2^2\cos(2k_y)J_0 +$$

$$\frac{19}{16}J_1^2J_2\cos(2k_y)J_0 - \frac{1}{2}J_1J_2\cos(2k_y)J_0 + \frac{19}{256}J_2^3\cos(4k_y)J_0 +$$

$$\frac{19}{128}J_1J_2^2\cos(4k_y)J_0 - \frac{5}{2}J_1^5\cos(k_x+k_y)J_0 - 2J_1^3\cos(k_x+k_y)J_0 +$$

$$\frac{7}{16}J_2^3\cos(k_x+k_y)J_0 + \frac{5}{4}J_1J_2^2\cos(k_x+k_y)J_0 - \frac{5}{2}J_2^2\cos(k_x+k_y)J_0 +$$

$$2J_1\cos(k_x+k_y)J_0 + \frac{9}{8}J_1^2J_2\cos(k_x+k_y)J_0 - \frac{7}{2}J_1J_2\cos(k_x+k_y)J_0 +$$

$$2J_2\cos(k_x+k_y)J_0 + \frac{73}{256}J_0J_2^3\cos(3k_x+k_y) + \frac{111}{128}J_0J_1J_2^2\cos(3k_x+k_y) -$$

$$\frac{1}{4}J_2^2\cos(3k_x+k_y)J_0 + \frac{19}{32}J_1^2J_2\cos(3k_x+k_y)J_0 - \frac{1}{2}J_1J_2\cos(3k_x+k_y)J_0 +$$

$$\frac{7}{256}J_2^3\cos(5k_x+k_y)J_0 + \frac{7}{128}J_1J_2^2\cos(5k_x+k_y)J_0 + 3J_1^4\cos(2k_x+2k_y)J_0 +$$

$$\frac{1}{2}J_2^3\cos(2k_x+2k_y)J_0 - 2J_1^2\cos(2k_x+2k_y)J_0 + \frac{45}{32}J_1J_2^2\cos(2k_x+2k_y)J_0 -$$

$$J_2^2\cos(2k_x+2k_y)J_0 + \frac{13}{16}J_1^2J_2\cos(2k_x+2k_y)J_0 -$$

$$4J_1J_2\cos(2k_x+2k_y)J_0 + \frac{47}{256}J_2^3\cos(4k_x+2k_y)J_0 +$$

$$\frac{75}{128}J_1J_2^2\cos(4k_x+2k_y)J_0 +$$

$$\frac{7}{16}J_1^2J_2\cos(4k_x+2k_y)J_0 + \frac{73}{256}J_2^3\cos(k_x+3k_y)J_0 + \frac{111}{128}J_1J_2^2\cos(k_x+3k_y)J_0 -$$

$$\frac{1}{4}J_2^2\cos(k_x+3k_y)J_0 + \frac{19}{32}J_1^2J_2\cos(k_x+3k_y)J_0 - \frac{1}{2}J_1J_2\cos(k_x+3k_y)J_0 +$$

$$4J_1^5\cos(3k_x+3k_y)J_0 - 5J_1^4\cos(3k_x+3k_y)J_0 + 6J_1^3\cos(3k_x+3k_y)J_0 +$$

$$\frac{29}{64}J_2^3\cos(3k_x+3k_y)J_0 - 2J_1^2\cos(3k_x+3k_y)J_0 + \frac{57}{32}J_1J_2^2\cos(3k_x+3k_y)J_0 -$$

$$\frac{1}{2}J_2^2\cos(3k_x+3k_y)J_0 + \frac{21}{8}J_1^2J_2\cos(3k_x+3k_y)J_0 - J_1J_2\cos(3k_x+3k_y)J_0 +$$

$$\frac{7}{128}J_2^3\cos(5k_x+3k_y)J_0 + \frac{7}{64}J_1J_2^2\cos(5k_x+3k_y)J_0 +$$

$$\frac{47}{256}J_2^3\cos(2k_x+4k_y)J_0 + \frac{75}{128}J_1J_2^2\cos(2k_x+4k_y)J_0 + \frac{7}{16}J_1^2J_2\cos(2k_x+4k_y)J_0 -$$

$$5J_1^4\cos(4k_x+4k_y)J_0+\frac{7}{32}J_2^3\cos(4k_x+4k_y)J_0+\frac{7}{8}J_1J_2^2\cos(4k_x+4k_y)J_0+$$

$$\frac{7}{8}J_1^2J_2\cos(4k_x+4k_y)J_0+\frac{7}{256}J_2^3\cos(k_x+5k_y)J_0+\frac{7}{128}J_1J_2^2\cos(k_x+5k_y)J_0+$$

$$\frac{7}{128}J_2^3\cos(3k_x+5k_y)J_0+\frac{7}{64}J_1J_2^2\cos(3k_x+5k_y)J_0+4J_1^5\cos(5k_x+5k_y)J_0+$$

$$3J_1^4\cos(5k_x+5k_y)J_0+\frac{7}{128}J_2^3\cos(5k_x+5k_y)J_0+\frac{7}{64}J_1J_2^2\cos(5k_x+5k_y)J_0+$$

$$\frac{J_1^6}{4}+\frac{J_1^4}{4}+\frac{241J_2^4}{64}+10J_1J_2^3-\frac{21J_2^3}{16}+J_1^2+$$

$$\frac{119J_1^2J_2^2}{16}-3J_1J_2^2+\frac{J_2^2}{2}+K+\frac{J_1^3J_2}{2}-$$

$$\frac{3J_1^2J_2}{2}+J_1J_2-\frac{15}{32}J_2^4\cos(2k_x)-\frac{43}{32}J_1J_2^3\cos(2k_x)+$$

$$\frac{13}{32}J_2^3\cos(2k_x)-\frac{5}{4}J_1^2J_2^2\cos(2k_x)+\frac{9}{8}J_1J_2^2\cos(2k_x)-$$

$$\frac{3}{8}J_2^2\cos(2k_x)-\frac{1}{4}J_1^3J_2\cos(2k_x)+\frac{3}{4}J_1^2J_2\cos(2k_x)-$$

$$\frac{1}{2}J_1J_2\cos(2k_x)+\frac{1}{2}J_2\cos(2k_x)-\frac{561}{512}J_2^4\cos(4k_x)-$$

$$\frac{89}{32}J_1J_2^3\cos(4k_x)+\frac{21}{64}J_2^3\cos(4k_x)-\frac{59}{32}J_1^2J_2^2\cos(4k_x)+$$

$$\frac{3}{8}J_1J_2^2\cos(4k_x)-\frac{1}{16}J_2^2\cos(4k_x)-\frac{15}{64}J_2^4\cos(6k_x)-$$

$$\frac{15}{64}J_1J_2^3\cos(6k_x)+\frac{1}{64}J_2^3\cos(6k_x)-\frac{5J_2^4\cos(8k_x)}{1024}-$$

$$\frac{5}{256}J_2^4\cos(k_x-7k_y)-\frac{25}{512}J_2^4\cos(2k_x-6k_y)-\frac{105}{256}J_2^4\cos(k_x-5k_y)-$$

$$\frac{35}{64}J_1J_2^3\cos(k_x-5k_y)+\frac{3}{64}J_2^3\cos(k_x-5k_y)-$$

$$\frac{5}{64}J_2^4\cos(3k_x-5k_y)-\frac{135}{256}J_2^4\cos(2k_x-4k_y)-\frac{25}{32}J_1J_2^3\cos(2k_x-4k_y)+$$

$$\frac{3}{32}J_2^3\cos(2k_x-4k_y)-\frac{95}{512}J_2^4\cos(4k_x-4k_y)-\frac{79}{64}J_2^4\cos(k_x-3k_y)-$$

$$\frac{191}{64}J_1J_2^3\cos(k_x-3k_y)+\frac{15}{32}J_2^3\cos(k_x-3k_y)-\frac{29}{16}J_1^2J_2^2\cos(k_x-3k_y)+$$

$$\frac{3}{4}J_1J_2^2\cos(k_x-3k_y)-\frac{1}{8}J_2^2\cos(k_x-3k_y)-\frac{75}{64}J_2^4\cos(3k_x-3k_y)-$$

$$\frac{15}{8}J_1J_2^3\cos(3k_x-3k_y)+\frac{7}{32}J_2^3\cos(3k_x-3k_y)-\frac{5}{64}J_2^4\cos(5k_x-3k_y)-$$

$$\frac{157}{64}J_2^4\cos(2k_x-2k_y)-\frac{51}{8}J_1J_2^3\cos(2k_x-2k_y)+\frac{15}{16}J_2^3\cos(2k_x-2k_y)-$$

$$\frac{9}{2}J_1^2J_2^2\cos(2k_x-2k_y)+\frac{3}{2}J_1J_2^2\cos(2k_x-2k_y)-\frac{3}{8}J_2^2\cos(2k_x-2k_y)-$$

$$\frac{135}{256}J_2^4\cos(4k_x-2k_y)-\frac{25}{32}J_1J_2^3\cos(4k_x-2k_y)+\frac{3}{32}J_2^3\cos(4k_x-2k_y)-$$

$$\frac{25}{512}J_2^4\cos(6k_x-2k_y)-\frac{59}{64}J_2^4\cos(k_x-k_y)-\frac{15}{8}J_1J_2^3\cos(k_x-k_y)+$$

$$\frac{29}{32}J_2^3\cos(k_x-k_y)-\frac{3}{2}J_1^2J_2^2\cos(k_x-k_y)+\frac{3}{2}J_1J_2^2\cos(k_x-k_y)-$$

$$J_2^2\cos(k_x-k_y)-J_1^3J_2\cos(k_x-k_y)-3J_1^4\cos(5k_x+5k_y)J_0+$$

$$2J_1J_2\cos(k_x-k_y)+J_2\cos(k_x-k_y)-$$

$$\frac{79}{64}J_2^4\cos(3k_x-k_y)-\frac{191}{64}J_1J_2^3\cos(3k_x-k_y)+\frac{15}{32}J_2^3\cos(3k_x-k_y)-$$

$$\frac{29}{16}J_1^2J_2^2\cos(3k_x-k_y)+\frac{3}{4}J_1J_2^2\cos(3k_x-k_y)-\frac{1}{8}J_2^2\cos(3k_x-k_y)-$$

$$\frac{105}{256}J_2^4\cos(5k_x-k_y)-\frac{35}{64}J_1J_2^3\cos(5k_x-k_y)+\frac{3}{64}J_2^3\cos(5k_x-k_y)-$$

$$\frac{5}{256}J_2^4\cos(7k_x-k_y)-\frac{15}{32}J_2^4\cos(2k_y)-\frac{43}{32}J_1J_2^3\cos(2k_y)+$$

$$\frac{13}{32}J_2^3\cos(2k_y)-\frac{5}{4}J_1^2J_2^2\cos(2k_y)+\frac{9}{8}J_1J_2^2\cos(2k_y)-$$

$$\frac{3}{8}J_2^2\cos(2k_y)-\frac{1}{4}J_1^3J_2\cos(2k_y)+\frac{3}{4}J_1^2J_2\cos(2k_y)-$$

$$\frac{1}{2}J_1J_2\cos(2k_y)+\frac{1}{2}J_2\cos(2k_y)-\frac{561}{512}J_2^4\cos(4k_y)-$$

$$\frac{89}{32}J_1J_2^3\cos(4k_y)+\frac{21}{64}J_2^3\cos(4k_y)-\frac{59}{32}J_1^2J_2^2\cos(4k_y)+\frac{3}{8}J_1J_2^2\cos(4k_y)-$$

$$\frac{1}{16}J_2^2\cos(4k_y)-\frac{15}{64}J_2^4\cos(6k_y)-\frac{15}{64}J_1J_2^3\cos(6k_y)+\frac{1}{64}J_2^3\cos(6k_y)-$$

$$\frac{5J_2^4\cos(8k_y)}{1024}-\frac{1}{2}J_1^5\cos(k_x+k_y)-\frac{13}{64}J_2^4\cos(k_x+k_y)-J_1^3\cos(k_x+k_y)+$$

$$\frac{93}{32}J_1J_2^3\cos(k_x+k_y)+\frac{1}{2}J_2^3\cos(k_x+k_y)+\frac{23}{4}J_1^2J_2^2\cos(k_x+k_y)-$$

$$\frac{3}{4}J_1J_2^2\cos(k_x+k_y)-J_2^2\cos(k_x+k_y)+2J_1\cos(k_x+k_y)+2J_1^3J_2\cos(k_x+k_y)-$$

$$3J_1^2J_2\cos(k_x+k_y)-J_1J_2\cos(k_x+k_y)+2J_2\cos(k_x+k_y)-$$

$$\frac{85}{64}J_2^4\cos(3k_x+k_y)-\frac{27}{8}J_1J_2^3\cos(3k_x+k_y)+\frac{45}{64}J_2^3\cos(3k_x+k_y)-$$

$$\frac{25}{8}J_1^2J_2^2\cos(3k_x+k_y)+\frac{3}{2}J_1J_2^2\cos(3k_x+k_y)-\frac{3}{8}J_2^2\cos(3k_x+k_y)-$$

$$\frac{3}{2}J_1^3J_2\cos(3k_x+k_y)+\frac{3}{4}J_1^2J_2\cos(3k_x+k_y)-\frac{1}{2}J_1J_2\cos(3k_x+k_y)-$$

$$\frac{215}{256}J_2^4\cos(5k_x+k_y)-\frac{15}{8}J_1J_2^3\cos(5k_x+k_y)+\frac{3}{16}J_2^3\cos(5k_x+k_y)-$$

$$\frac{15}{16}J_1^2J_2^2\cos(5k_x+k_y)+\frac{3}{16}J_1J_2^2\cos(5k_x+k_y)-\frac{25}{256}J_2^4\cos(7k_x+k_y)-$$

$$\frac{5}{64}J_1J_2^3\cos(7k_x+k_y)-2J_1^6\cos(2k_x+2k_y)+\frac{7}{4}J_1^5\cos(2k_x+2k_y)-$$

$$\frac{1}{4}J_1^4\cos(2k_x+2k_y)-\frac{61}{64}J_2^4\cos(2k_x+2k_y)+J_1^3\cos(2k_x+2k_y)-$$

$$\frac{43}{16}J_1J_2^3\cos(2k_x+2k_y)+\frac{23}{32}J_2^3\cos(2k_x+2k_y)-2J_1^2\cos(2k_x+2k_y)-$$

$$\frac{11}{16}J_1^2J_2^2\cos(2k_x+2k_y)+\frac{3}{2}J_1J_2^2\cos(2k_x+2k_y)-$$

$$\frac{3}{4}J_2^2\cos(2k_x+2k_y)+4J_1^3J_2\cos(2k_x+2k_y)-2J_1J_2\cos(2k_x+2k_y)+$$

$$J_2\cos(2k_x+2k_y)-\frac{321}{256}J_2^4\cos(4k_x+2k_y)-\frac{59}{16}J_1J_2^3\cos(4k_x+2k_y)+$$

$$\frac{15}{32}J_2^3\cos(4k_x+2k_y)-\frac{59}{16}J_1^2J_2^2\cos(4k_x+2k_y)+\frac{9}{8}J_1J_2^2\cos(4k_x+2k_y)-$$

$$\frac{1}{8}J_2^2\cos(4k_x+2k_y)-\frac{5}{4}J_1^3J_2\cos(4k_x+2k_y)+\frac{3}{4}J_1^2J_2\cos(4k_x+2k_y)-$$

$$\frac{235}{512}J_2^4\cos(6k_x+2k_y)-\frac{15}{16}J_1J_2^3\cos(6k_x+2k_y)+\frac{3}{64}J_2^3\cos(6k_x+2k_y)-$$

$$\frac{15}{32}J_1^2J_2^2\cos(6k_x+2k_y)-\frac{5}{256}J_2^4\cos(8k_x+2k_y)-\frac{85}{64}J_2^4\cos(k_x+3k_y)-$$

$$\frac{27}{8}J_1J_2^3\cos(k_x+3k_y)+\frac{45}{64}J_2^3\cos(k_x+3k_y)-\frac{25}{8}J_1^2J_2^2\cos(k_x+3k_y)+$$

$$\frac{3}{2}J_1J_2^2\cos(k_x+3k_y)-\frac{3}{8}J_2^2\cos(k_x+3k_y)-\frac{3}{2}J_1^3J_2\cos(k_x+3k_y)+$$

$$\frac{3}{4}J_1^2J_2\cos(k_x+3k_y)-\frac{1}{2}J_1J_2\cos(k_x+3k_y)-\frac{5}{4}J_1^5\cos(3k_x+3k_y)-$$

$$\frac{1341}{512}J_2^4\cos(3k_x+3k_y)+J_1^3\cos(3k_x+3k_y)-\frac{205}{32}J_1J_2^3\cos(3k_x+3k_y)+$$

$$\frac{39}{32}J_2^3\cos(3k_x+3k_y)-$$

$$\frac{9}{2}J_1^2J_2^2\cos(3k_x+3k_y)+\frac{21}{8}J_1J_2^2\cos(3k_x+3k_y)-\frac{5}{8}J_2^2\cos(3k_x+3k_y)-$$

$$\frac{1}{2}J_1^3J_2\cos(3k_x+3k_y)+3J_1^2J_2\cos(3k_x+3k_y)-J_1J_2\cos(3k_x+3k_y)-$$

$$\frac{15}{16}J_2^4\cos(5k_x+3k_y)-\frac{165}{64}J_1J_2^3\cos(5k_x+3k_y)+$$

$$\frac{9}{32}J_2^3\cos(5k_x+3k_y)-\frac{45}{16}J_1^2J_2^2\cos(5k_x+3k_y)+\frac{3}{8}J_1J_2^2\cos(5k_x+3k_y)-$$

$$\frac{5}{4}J_1^3J_2\cos(5k_x+3k_y)-\frac{105}{512}J_2^4\cos(7k_x+3k_y)-\frac{15}{64}J_1J_2^3\cos(7k_x+3k_y)-$$

$$\frac{321}{256}J_2^4\cos(2k_x+4k_y)-\frac{59}{16}J_1J_2^3\cos(2k_x+4k_y)+\frac{15}{32}J_2^3\cos(2k_x+4k_y)-$$

$$\frac{59}{16}J_1^2J_2^2\cos(2k_x+4k_y)+\frac{9}{8}J_1J_2^2\cos(2k_x+4k_y)-\frac{1}{8}J_2^2\cos(2k_x+4k_y)-$$

$$\frac{5}{4}J_1^3J_2\cos(2k_x+4k_y)+\frac{3}{4}J_1^2J_2\cos(2k_x+4k_y)+\frac{7}{2}J_1^6\cos(4k_x+4k_y)-$$

$$\frac{5}{4}J_1^5\cos(4k_x+4k_y)-\frac{1}{4}J_1^4\cos(4k_x+4k_y)-\frac{531}{256}J_2^4\cos(4k_x+4k_y)-$$

$$
\begin{aligned}
&\frac{193}{32} J_1 J_2^3 \cos(4k_x + 4k_y) + \frac{3}{4} J_2^3 \cos(4k_x + 4k_y) - \frac{13}{2} J_1^2 J_2^2 \cos(4k_x + 4k_y) + \\
&\frac{15}{8} J_1 J_2^2 \cos(4k_x + 4k_y) - 5 J_1^3 J_2 \cos(4k_x + 4k_y) + \frac{3}{2} J_1^2 J_2 \cos(4k_x + 4k_y) - \\
&\frac{145}{256} J_2^4 \cos(6k_x + 4k_y) - \\
&\frac{45}{32} J_1 J_2^3 \cos(6k_x + 4k_y) - \frac{15}{16} J_1^2 J_2^2 \cos(6k_x + 4k_y) - \frac{215}{256} J_2^4 \cos(k_x + 5k_y) - \\
&\frac{15}{8} J_1 J_2^3 \cos(k_x + 5k_y) + \frac{3}{16} J_2^3 \cos(k_x + 5k_y) - \frac{15}{16} J_1^2 J_2^2 \cos(k_x + 5k_y) + \\
&\frac{3}{16} J_1 J_2^2 \cos(k_x + 5k_y) - \frac{15}{16} J_2^4 \cos(3k_x + 5k_y) - \frac{165}{64} J_1 J_2^3 \cos(3k_x + 5k_y) + \\
&\frac{9}{32} J_2^3 \cos(3k_x + 5k_y) - \frac{45}{16} J_1^2 J_2^2 \cos(3k_x + 5k_y) + \frac{3}{8} J_1 J_2^2 \cos(3k_x + 5k_y) - \\
&\frac{5}{4} J_1^3 J_2 \cos(3k_x + 5k_y) + \frac{7}{4} J_1^5 \cos(5k_x + 5k_y) - \frac{185}{128} J_2^4 \cos(5k_x + 5k_y) - \\
&\frac{125}{32} J_1 J_2^3 \cos(5k_x + 5k_y) - \frac{75}{16} J_1^2 J_2^2 \cos(5k_x + 5k_y) - \frac{5}{2} J_1^3 J_2 \cos(5k_x + 5k_y) - \\
&\frac{235}{512} J_2^4 \cos(2k_x + 6k_y) - \frac{15}{16} J_1 J_2^3 \cos(2k_x + 6k_y) + \frac{3}{64} J_2^3 \cos(2k_x + 6k_y) - \\
&\frac{15}{32} J_1^2 J_2^2 \cos(2k_x + 6k_y) - \frac{145}{256} J_2^4 \cos(4k_x + 6k_y) - \frac{45}{32} J_1 J_2^3 \cos(4k_x + 6k_y) - \\
&\frac{15}{16} J_1^2 J_2^2 \cos(4k_x + 6k_y) - 2 J_1^6 \cos(6k_x + 6k_y) - \frac{25}{256} J_2^4 \cos(k_x + 7k_y) - \\
&\frac{5}{64} J_1 J_2^3 \cos(k_x + 7k_y) - \\
&\frac{105}{512} J_2^4 \cos(3k_x + 7k_y) - \frac{15}{64} J_1 J_2^3 \cos(3k_x + 7k_y) - \frac{5}{256} J_2^4 \cos(2k_x + 8k_y).
\end{aligned}
\tag{A.7}
$$

A.3 Derivation of the spin-wave Hamiltonian in low-field regime

We continue the derivation of Hamiltonian under the low-field limit starting from Eq. (A.8). This is a case where J_2 is finite and the groundstate in this regime is a global ordered (anti)ferroelectric state. The Eq. (A.8) is given by,

$$
\begin{aligned}
\mathcal{H}_{lf}^{ferro} &= \sum_{\square} \Big[- J_0 \times \\
&((\lambda_1 \cos\theta (s - a_1^\dagger a_1) + \sqrt{s/2} \sin\theta (a_1^\dagger + a_1))(\lambda_2 \cos\theta (s - a_2^\dagger a_2) + \sqrt{s/2} \sin\theta (a_2^\dagger + a_2)) \\
&(\lambda_3 \cos\theta (s - a_3^\dagger a_3) + \sqrt{s/2} \sin\theta (a_3^\dagger + a_3))(\lambda_4 \cos\theta (s - a_4^\dagger a_4) + \sqrt{s/2} \sin\theta (a_4^\dagger + a_4)) +
\end{aligned}
$$

$$
\begin{aligned}
& J_1((\lambda_1 \cos\theta(s - a_1^\dagger a_1) + \sqrt{s/2}\sin\theta(a_1^\dagger + a_1))(\lambda_3 \cos\theta(s - a_3^\dagger a_3) + \sqrt{s/2}\sin\theta(a_3^\dagger + a_3)) \\
& +(\lambda_2 \cos\theta(s - a_2^\dagger a_2) + \sqrt{s/2}\sin\theta(a_2^\dagger + a_2))(\lambda_4 \cos\theta(s - a_4^\dagger a_4) + \sqrt{s/2}\sin\theta(a_4^\dagger + a_4))\Big] - \\
& \frac{J_2}{16}\sum_{\langle AB\rangle}\Big[\\
& (\lambda_1 \cos\theta(s - a_1^\dagger a_1) + \sqrt{s/2}\sin\theta(a_1^\dagger + a_1)) + \lambda_2 \cos\theta(s - a_2^\dagger a_2) + \sqrt{s/2}\sin\theta(a_2^\dagger + a_2)) \\
& -\lambda_3 \cos\theta(s - a_3^\dagger a_3) + \sqrt{s/2}\sin\theta(a_3^\dagger + a_3)) - \lambda_4 \cos\theta(s - a_4^\dagger a_4) + \sqrt{s/2}\sin\theta(a_4^\dagger + a_4))_A \\
& \times(\lambda_1 \cos\theta(s - a_1^\dagger a_1) + \sqrt{s/2}\sin\theta(a_1^\dagger + a_1)) + \lambda_4 \cos\theta(s - a_4^\dagger a_4) + \sqrt{s/2}\sin\theta(a_4^\dagger + a_4)) \\
& -\lambda_2 \cos\theta(s - a_2^\dagger a_2) + \sqrt{s/2}\sin\theta(a_2^\dagger + a_2)) - \lambda_3 \cos\theta(s - a_3^\dagger a_3) + \sqrt{s/2}\sin\theta(a_3^\dagger + a_3))_B\Big],
\end{aligned}
\tag{A.8}
$$

$$
\begin{aligned}
& s^4\lambda_i\lambda_{i_1}\lambda_{i_2}\lambda_{i_3}\cos^4(\theta) - s^3 a_i\lambda_i\lambda_{i_1}\lambda_{i_2}\lambda_{i_3}a_i^\dagger\cos^4(\theta) - s^3 a_{i_1}\lambda_i\lambda_{i_1}\lambda_{i_2}\lambda_{i_3}a_{i_1}^\dagger\cos^4(\theta) + \\
&\quad s^2 a_i a_{i_1}\lambda_i\lambda_{i_1}\lambda_{i_2}\lambda_{i_3}a_i^\dagger a_{i_1}^\dagger\cos^4(\theta) - s^3 a_{i_2}\lambda_i\lambda_{i_1}\lambda_{i_2}\lambda_{i_3}a_{i_2}^\dagger\cos^4(\theta) + \\
&\quad s^2 a_i a_{i_2}\lambda_i\lambda_{i_1}\lambda_{i_2}\lambda_{i_3}a_i^\dagger a_{i_2}^\dagger\cos^4(\theta) + s^2 a_{i_1}a_{i_2}\lambda_i\lambda_{i_1}\lambda_{i_2}\lambda_{i_3}a_{i_1}^\dagger a_{i_2}^\dagger\cos^4(\theta) - \\
&\quad s a_i a_{i_1}a_{i_2}\lambda_i\lambda_{i_1}\lambda_{i_2}\lambda_{i_3}a_i^\dagger a_{i_1}^\dagger a_{i_2}^\dagger\cos^4(\theta) - s^3 a_{i_3}\lambda_i\lambda_{i_1}\lambda_{i_2}\lambda_{i_3}a_{i_3}^\dagger\cos^4(\theta) + \\
&\quad s^2 a_i a_{i_3}\lambda_i\lambda_{i_1}\lambda_{i_2}\lambda_{i_3}a_i^\dagger a_{i_3}^\dagger\cos^4(\theta) + s^2 a_{i_1}a_{i_3}\lambda_i\lambda_{i_1}\lambda_{i_2}\lambda_{i_3}a_{i_1}^\dagger a_{i_3}^\dagger\cos^4(\theta) - \\
&\quad s a_i a_{i_1}a_{i_3}\lambda_i\lambda_{i_1}\lambda_{i_2}\lambda_{i_3}a_i^\dagger a_{i_1}^\dagger a_{i_3}^\dagger\cos^4(\theta) + s^2 a_{i_2}a_{i_3}\lambda_i\lambda_{i_1}\lambda_{i_2}\lambda_{i_3}a_{i_2}^\dagger a_{i_3}^\dagger\cos^4(\theta) - \\
&\quad s a_i a_{i_2}a_{i_3}\lambda_i\lambda_{i_1}\lambda_{i_2}\lambda_{i_3}a_i^\dagger a_{i_2}^\dagger a_{i_3}^\dagger\cos^4(\theta) - s a_{i_1}a_{i_2}a_{i_3}\lambda_i\lambda_{i_1}\lambda_{i_2}\lambda_{i_3}a_{i_1}^\dagger a_{i_2}^\dagger a_{i_3}^\dagger\cos^4(\theta) + \\
&\quad a_i a_{i_1}a_{i_2}a_{i_3}\lambda_i\lambda_{i_1}\lambda_{i_2}\lambda_{i_3}a_i^\dagger a_{i_1}^\dagger a_{i_2}^\dagger a_{i_3}^\dagger\cos^4(\theta) + \frac{s^{7/2}\sin(\theta)a_{i_3}\lambda_i\lambda_{i_1}\lambda_{i_2}\cos^3(\theta)}{\sqrt{2}} + \\
&\quad \frac{s^{7/2}\sin(\theta)a_{i_2}\lambda_i\lambda_{i_1}\lambda_{i_3}\cos^3(\theta)}{\sqrt{2}} + \frac{s^{7/2}\sin(\theta)a_{i_1}\lambda_i\lambda_{i_2}\lambda_{i_3}\cos^3(\theta)}{\sqrt{2}} + \\
&\quad \frac{s^{7/2}\sin(\theta)a_i\lambda_{i_1}\lambda_{i_2}\lambda_{i_3}\cos^3(\theta)}{\sqrt{2}} - \frac{s^{5/2}\sin(\theta)a_i a_{i_3}\lambda_i\lambda_{i_1}\lambda_{i_2}a_i^\dagger\cos^3(\theta)}{\sqrt{2}} - \\
&\quad \frac{s^{5/2}\sin(\theta)a_i a_{i_2}\lambda_i\lambda_{i_1}\lambda_{i_3}a_i^\dagger\cos^3(\theta)}{\sqrt{2}} - \frac{s^{5/2}\sin(\theta)a_i a_{i_1}\lambda_i\lambda_{i_2}\lambda_{i_3}a_i^\dagger\cos^3(\theta)}{\sqrt{2}} + \\
&\quad \frac{s^{7/2}\sin(\theta)\lambda_{i_1}\lambda_{i_2}\lambda_{i_3}a_i^\dagger\cos^3(\theta)}{\sqrt{2}} - \frac{s^{5/2}\sin(\theta)a_{i_1}a_{i_3}\lambda_i\lambda_{i_1}\lambda_{i_2}a_{i_1}^\dagger\cos^3(\theta)}{\sqrt{2}} - \\
&\quad \frac{s^{5/2}\sin(\theta)a_{i_1}a_{i_2}\lambda_i\lambda_{i_1}\lambda_{i_3}a_{i_1}^\dagger\cos^3(\theta)}{\sqrt{2}} + \frac{s^{7/2}\sin(\theta)\lambda_i\lambda_{i_2}\lambda_{i_3}a_{i_1}^\dagger\cos^3(\theta)}{\sqrt{2}} - \\
&\quad \frac{s^{5/2}\sin(\theta)a_i a_{i_1}\lambda_{i_1}\lambda_{i_2}\lambda_{i_3}a_{i_1}^\dagger\cos^3(\theta)}{\sqrt{2}} + \frac{s^{3/2}\sin(\theta)a_i a_{i_1}a_{i_3}\lambda_i\lambda_{i_1}\lambda_{i_2}a_i^\dagger a_{i_1}^\dagger\cos^3(\theta)}{\sqrt{2}} + \\
&\quad \frac{s^{3/2}\sin(\theta)a_i a_{i_1}a_{i_2}\lambda_i\lambda_{i_1}\lambda_{i_3}a_i^\dagger a_{i_1}^\dagger\cos^3(\theta)}{\sqrt{2}} - \frac{s^{5/2}\sin(\theta)a_i\lambda_i\lambda_{i_2}\lambda_{i_3}a_i^\dagger a_{i_1}^\dagger\cos^3(\theta)}{\sqrt{2}} - \\
&\quad \frac{s^{5/2}\sin(\theta)a_{i_1}\lambda_{i_1}\lambda_{i_2}\lambda_{i_3}a_i^\dagger a_{i_1}^\dagger\cos^3(\theta)}{\sqrt{2}} - \frac{s^{5/2}\sin(\theta)a_{i_2}a_{i_3}\lambda_i\lambda_{i_1}\lambda_{i_2}a_{i_2}^\dagger\cos^3(\theta)}{\sqrt{2}} + \\
&\quad \frac{s^{7/2}\sin(\theta)\lambda_i\lambda_{i_1}\lambda_{i_3}a_{i_2}^\dagger\cos^3(\theta)}{\sqrt{2}} - \frac{s^{5/2}\sin(\theta)a_{i_1}a_{i_2}\lambda_i\lambda_{i_2}\lambda_{i_3}a_{i_2}^\dagger\cos^3(\theta)}{\sqrt{2}} - \\
&\quad \frac{s^{5/2}\sin(\theta)a_i a_{i_2}\lambda_{i_1}\lambda_{i_2}\lambda_{i_3}a_{i_2}^\dagger\cos^3(\theta)}{\sqrt{2}} + \frac{s^{3/2}\sin(\theta)a_i a_{i_2}a_{i_3}\lambda_i\lambda_{i_1}\lambda_{i_2}a_i^\dagger a_{i_2}^\dagger\cos^3(\theta)}{\sqrt{2}} -
\end{aligned}
$$

$$\frac{s^{5/2}\sin(\theta)a_i\lambda_i\lambda_{i_1}\lambda_{i_3}a_i^\dagger a_{i_2}^\dagger\cos^3(\theta)}{\sqrt{2}}+\frac{s^{3/2}\sin(\theta)a_ia_{i_1}a_{i_2}\lambda_i\lambda_{i_2}\lambda_{i_3}a_i^\dagger a_{i_2}^\dagger\cos^3(\theta)}{\sqrt{2}}-$$

$$\frac{s^{5/2}\sin(\theta)a_{i_2}\lambda_{i_1}\lambda_{i_2}\lambda_{i_3}a_i^\dagger a_{i_2}^\dagger\cos^3(\theta)}{\sqrt{2}}+\frac{s^{3/2}\sin(\theta)a_{i_1}a_{i_2}a_{i_3}\lambda_i\lambda_{i_1}\lambda_{i_2}a_{i_1}^\dagger a_{i_2}^\dagger\cos^3(\theta)}{\sqrt{2}}-$$

$$\frac{s^{5/2}\sin(\theta)a_{i_1}\lambda_i\lambda_{i_1}\lambda_{i_3}a_{i_1}^\dagger a_{i_2}^\dagger\cos^3(\theta)}{\sqrt{2}}-\frac{s^{5/2}\sin(\theta)a_{i_2}\lambda_i\lambda_{i_2}\lambda_{i_3}a_{i_1}^\dagger a_{i_2}^\dagger\cos^3(\theta)}{\sqrt{2}}+$$

$$\frac{s^{3/2}\sin(\theta)a_ia_{i_1}a_{i_2}\lambda_{i_1}\lambda_{i_2}\lambda_{i_3}a_{i_1}^\dagger a_{i_2}^\dagger\cos^3(\theta)}{\sqrt{2}}-\frac{\sqrt{s}\sin(\theta)a_ia_{i_1}a_{i_2}a_{i_3}\lambda_i\lambda_{i_1}\lambda_{i_2}a_i^\dagger a_{i_1}^\dagger a_{i_2}^\dagger\cos^3(\theta)}{\sqrt{2}}+$$

$$\frac{s^{3/2}\sin(\theta)a_ia_{i_1}\lambda_i\lambda_{i_1}\lambda_{i_3}a_i^\dagger a_{i_1}^\dagger a_{i_2}^\dagger\cos^3(\theta)}{\sqrt{2}}+\frac{s^{3/2}\sin(\theta)a_ia_{i_2}\lambda_i\lambda_{i_2}\lambda_{i_3}a_i^\dagger a_{i_1}^\dagger a_{i_2}^\dagger\cos^3(\theta)}{\sqrt{2}}+$$

$$\frac{s^{3/2}\sin(\theta)a_{i_1}a_{i_2}\lambda_{i_1}\lambda_{i_2}\lambda_{i_3}a_i^\dagger a_{i_1}^\dagger a_{i_2}^\dagger\cos^3(\theta)}{\sqrt{2}}+\frac{s^{7/2}\sin(\theta)\lambda_i\lambda_{i_1}\lambda_{i_2}a_{i_3}^\dagger\cos^3(\theta)}{\sqrt{2}}-$$

$$\frac{s^{5/2}\sin(\theta)a_{i_2}a_{i_3}\lambda_i\lambda_{i_1}\lambda_{i_3}a_{i_3}^\dagger\cos^3(\theta)}{\sqrt{2}}-\frac{s^{5/2}\sin(\theta)a_{i_1}a_{i_3}\lambda_i\lambda_{i_2}\lambda_{i_3}a_{i_3}^\dagger\cos^3(\theta)}{\sqrt{2}}-$$

$$\frac{s^{5/2}\sin(\theta)a_ia_{i_3}\lambda_{i_1}\lambda_{i_2}\lambda_{i_3}a_{i_3}^\dagger\cos^3(\theta)}{\sqrt{2}}-\frac{s^{5/2}\sin(\theta)a_i\lambda_i\lambda_{i_1}\lambda_{i_2}a_i^\dagger a_{i_3}^\dagger\cos^3(\theta)}{\sqrt{2}}+$$

$$\frac{s^{3/2}\sin(\theta)a_ia_{i_2}a_{i_3}\lambda_i\lambda_{i_1}\lambda_{i_3}a_i^\dagger a_{i_3}^\dagger\cos^3(\theta)}{\sqrt{2}}+\frac{s^{3/2}\sin(\theta)a_ia_{i_1}a_{i_3}\lambda_i\lambda_{i_2}\lambda_{i_3}a_i^\dagger a_{i_3}^\dagger\cos^3(\theta)}{\sqrt{2}}-$$

$$\frac{s^{5/2}\sin(\theta)a_{i_3}\lambda_{i_1}\lambda_{i_2}\lambda_{i_3}a_i^\dagger a_{i_3}^\dagger\cos^3(\theta)}{\sqrt{2}}-\frac{s^{5/2}\sin(\theta)a_{i_1}\lambda_i\lambda_{i_1}\lambda_{i_2}a_{i_1}^\dagger a_{i_3}^\dagger\cos^3(\theta)}{\sqrt{2}}+$$

$$\frac{s^{3/2}\sin(\theta)a_{i_1}a_{i_2}a_{i_3}\lambda_i\lambda_{i_1}\lambda_{i_3}a_{i_1}^\dagger a_{i_3}^\dagger\cos^3(\theta)}{\sqrt{2}}-\frac{s^{5/2}\sin(\theta)a_{i_3}\lambda_i\lambda_{i_2}\lambda_{i_3}a_{i_1}^\dagger a_{i_3}^\dagger\cos^3(\theta)}{\sqrt{2}}+$$

$$\frac{s^{3/2}\sin(\theta)a_ia_{i_1}a_{i_3}\lambda_{i_1}\lambda_{i_2}\lambda_{i_3}a_{i_1}^\dagger a_{i_3}^\dagger\cos^3(\theta)}{\sqrt{2}}+\frac{s^{3/2}\sin(\theta)a_ia_{i_1}\lambda_i\lambda_{i_1}\lambda_{i_2}a_i^\dagger a_{i_1}^\dagger a_{i_3}^\dagger\cos^3(\theta)}{\sqrt{2}}-$$

$$\frac{\sqrt{s}\sin(\theta)a_ia_{i_1}a_{i_2}a_{i_3}\lambda_i\lambda_{i_1}\lambda_{i_3}a_i^\dagger a_{i_1}^\dagger a_{i_3}^\dagger\cos^3(\theta)}{\sqrt{2}}+\frac{s^{3/2}\sin(\theta)a_ia_{i_3}\lambda_i\lambda_{i_2}\lambda_{i_3}a_i^\dagger a_{i_1}^\dagger a_{i_3}^\dagger\cos^3(\theta)}{\sqrt{2}}+$$

$$\frac{s^{3/2}\sin(\theta)a_{i_1}a_{i_3}\lambda_{i_1}\lambda_{i_2}\lambda_{i_3}a_i^\dagger a_{i_1}^\dagger a_{i_3}^\dagger\cos^3(\theta)}{\sqrt{2}}-\frac{s^{5/2}\sin(\theta)a_{i_2}\lambda_i\lambda_{i_1}\lambda_{i_2}a_{i_2}^\dagger a_{i_3}^\dagger\cos^3(\theta)}{\sqrt{2}}-$$

$$\frac{s^{5/2}\sin(\theta)a_{i_3}\lambda_i\lambda_{i_1}\lambda_{i_3}a_{i_2}^\dagger a_{i_3}^\dagger\cos^3(\theta)}{\sqrt{2}}+\frac{s^{3/2}\sin(\theta)a_{i_1}a_{i_2}a_{i_3}\lambda_i\lambda_{i_2}\lambda_{i_3}a_{i_2}^\dagger a_{i_3}^\dagger\cos^3(\theta)}{\sqrt{2}}+$$

$$\frac{s^{3/2}\sin(\theta)a_ia_{i_2}a_{i_3}\lambda_{i_1}\lambda_{i_2}\lambda_{i_3}a_{i_2}^\dagger a_{i_3}^\dagger\cos^3(\theta)}{\sqrt{2}}+\frac{s^{3/2}\sin(\theta)a_ia_{i_2}\lambda_i\lambda_{i_1}\lambda_{i_2}a_i^\dagger a_{i_2}^\dagger a_{i_3}^\dagger\cos^3(\theta)}{\sqrt{2}}+$$

$$\frac{s^{3/2}\sin(\theta)a_ia_{i_3}\lambda_i\lambda_{i_1}\lambda_{i_3}a_i^\dagger a_{i_2}^\dagger a_{i_3}^\dagger\cos^3(\theta)}{\sqrt{2}}-\frac{\sqrt{s}\sin(\theta)a_ia_{i_1}a_{i_2}a_{i_3}\lambda_i\lambda_{i_2}\lambda_{i_3}a_i^\dagger a_{i_2}^\dagger a_{i_3}^\dagger\cos^3(\theta)}{\sqrt{2}}+$$

$$\frac{s^{3/2}\sin(\theta)a_{i_2}a_{i_3}\lambda_{i_1}\lambda_{i_2}\lambda_{i_3}a_i^\dagger a_{i_2}^\dagger a_{i_3}^\dagger\cos^3(\theta)}{\sqrt{2}}+\frac{s^{3/2}\sin(\theta)a_{i_1}a_{i_2}\lambda_i\lambda_{i_1}\lambda_{i_2}a_{i_1}^\dagger a_{i_2}^\dagger a_{i_3}^\dagger\cos^3(\theta)}{\sqrt{2}}+$$

$$\frac{s^{3/2}\sin(\theta)a_{i_1}a_{i_3}\lambda_i\lambda_{i_1}\lambda_{i_3}a_{i_1}^\dagger a_{i_2}^\dagger a_{i_3}^\dagger\cos^3(\theta)}{\sqrt{2}}+\frac{s^{3/2}\sin(\theta)a_{i_2}a_{i_3}\lambda_i\lambda_{i_2}\lambda_{i_3}a_{i_1}^\dagger a_{i_2}^\dagger a_{i_3}^\dagger\cos^3(\theta)}{\sqrt{2}}-$$

$$\frac{\sqrt{s}\sin(\theta)a_ia_{i_1}a_{i_2}a_{i_3}\lambda_{i_1}\lambda_{i_2}\lambda_{i_3}a_{i_1}^\dagger a_{i_2}^\dagger a_{i_3}^\dagger\cos^3(\theta)}{\sqrt{2}}-$$

$$\frac{\sqrt{s}\sin(\theta)a_ia_{i_1}a_{i_2}\lambda_i\lambda_{i_1}\lambda_{i_2}a_i^\dagger a_{i_1}^\dagger a_{i_2}^\dagger a_{i_3}^\dagger\cos^3(\theta)}{\sqrt{2}}-$$

$$\frac{\sqrt{s}\sin(\theta)a_ia_{i_1}a_{i_3}\lambda_i\lambda_{i_1}\lambda_{i_3}a_i^\dagger a_{i_1}^\dagger a_{i_2}^\dagger a_{i_3}^\dagger\cos^3(\theta)}{\sqrt{2}}-$$

$$\frac{\sqrt{s}\sin(\theta)a_i a_{i_2} a_{i_3}\lambda_i\lambda_{i_2}\lambda_{i_3}a_i^\dagger a_{i_1}^\dagger a_{i_2}^\dagger a_{i_3}^\dagger\cos^3(\theta)}{\sqrt{2}} -$$

$$\frac{\sqrt{s}\sin(\theta)a_{i_1}a_{i_2}a_{i_3}\lambda_{i_1}\lambda_{i_2}\lambda_{i_3}a_i^\dagger a_{i_1}^\dagger a_{i_2}^\dagger a_{i_3}^\dagger\cos^3(\theta)}{\sqrt{2}} + \frac{1}{2}s^3\sin^2(\theta)a_{i_2}a_{i_3}\lambda_i\lambda_{i_1}\cos^2(\theta) +$$

$$\frac{1}{2}s^3\sin^2(\theta)a_{i_1}a_{i_3}\lambda_i\lambda_{i_2}\cos^2(\theta) + \frac{1}{2}s^3\sin^2(\theta)a_i a_{i_3}\lambda_{i_1}\lambda_{i_2}\cos^2(\theta) +$$

$$\frac{1}{2}s^3\sin^2(\theta)a_{i_1}a_{i_2}\lambda_i\lambda_{i_3}\cos^2(\theta) + \frac{1}{2}s^3\sin^2(\theta)a_i a_{i_2}\lambda_{i_1}\lambda_{i_3}\cos^2(\theta) +$$

$$\frac{1}{2}s^3\sin^2(\theta)a_i a_{i_1}\lambda_{i_2}\lambda_{i_3}\cos^2(\theta) - \frac{1}{2}s^2\sin^2(\theta)a_i a_{i_2}a_{i_3}\lambda_i\lambda_{i_1}a_i^\dagger\cos^2(\theta) -$$

$$\frac{1}{2}s^2\sin^2(\theta)a_i a_{i_1}a_{i_3}\lambda_i\lambda_{i_2}a_i^\dagger\cos^2(\theta) + \frac{1}{2}s^3\sin^2(\theta)a_{i_3}\lambda_{i_1}\lambda_{i_2}a_i^\dagger\cos^2(\theta) -$$

$$\frac{1}{2}s^2\sin^2(\theta)a_i a_{i_1}a_{i_2}\lambda_i\lambda_{i_3}a_i^\dagger\cos^2(\theta) + \frac{1}{2}s^3\sin^2(\theta)a_{i_2}\lambda_{i_1}\lambda_{i_3}a_i^\dagger\cos^2(\theta) +$$

$$\frac{1}{2}s^3\sin^2(\theta)a_{i_1}\lambda_{i_2}\lambda_{i_3}a_i^\dagger\cos^2(\theta) - \frac{1}{2}s^2\sin^2(\theta)a_{i_1}a_{i_2}a_{i_3}\lambda_i\lambda_{i_1}a_{i_1}^\dagger\cos^2(\theta) +$$

$$\frac{1}{2}s^3\sin^2(\theta)a_{i_3}\lambda_i\lambda_{i_2}a_{i_1}^\dagger\cos^2(\theta) - \frac{1}{2}s^2\sin^2(\theta)a_i a_{i_1}a_{i_3}\lambda_{i_1}\lambda_{i_2}a_{i_1}^\dagger\cos^2(\theta) +$$

$$\frac{1}{2}s^3\sin^2(\theta)a_{i_2}\lambda_i\lambda_{i_3}a_{i_1}^\dagger\cos^2(\theta) - \frac{1}{2}s^2\sin^2(\theta)a_i a_{i_1}a_{i_2}\lambda_{i_1}\lambda_{i_3}a_{i_1}^\dagger\cos^2(\theta) +$$

$$\frac{1}{2}s^3\sin^2(\theta)a_i\lambda_{i_2}\lambda_{i_3}a_{i_1}^\dagger\cos^2(\theta) + \frac{1}{2}s\sin^2(\theta)a_i a_{i_1}a_{i_2}a_{i_3}\lambda_i\lambda_{i_1}a_i^\dagger a_{i_1}^\dagger\cos^2(\theta) -$$

$$\frac{1}{2}s^2\sin^2(\theta)a_i a_{i_3}\lambda_i\lambda_{i_2}a_i^\dagger a_{i_1}^\dagger\cos^2(\theta) - \frac{1}{2}s^2\sin^2(\theta)a_{i_1}a_{i_3}\lambda_{i_1}\lambda_{i_2}a_i^\dagger a_{i_1}^\dagger\cos^2(\theta) -$$

$$\frac{1}{2}s^2\sin^2(\theta)a_i a_{i_2}\lambda_i\lambda_{i_3}a_i^\dagger a_{i_1}^\dagger\cos^2(\theta) - \frac{1}{2}s^2\sin^2(\theta)a_{i_1}a_{i_2}\lambda_{i_1}\lambda_{i_3}a_i^\dagger a_{i_1}^\dagger\cos^2(\theta) +$$

$$\frac{1}{2}s^3\sin^2(\theta)\lambda_{i_2}\lambda_{i_3}a_i^\dagger a_{i_1}^\dagger\cos^2(\theta) + \frac{1}{2}s^3\sin^2(\theta)a_{i_3}\lambda_i\lambda_{i_1}a_{i_2}^\dagger\cos^2(\theta) -$$

$$\frac{1}{2}s^2\sin^2(\theta)a_{i_1}a_{i_2}a_{i_3}\lambda_i\lambda_{i_2}a_{i_2}^\dagger\cos^2(\theta) - \frac{1}{2}s^2\sin^2(\theta)a_i a_{i_2}a_{i_3}\lambda_{i_1}\lambda_{i_2}a_{i_2}^\dagger\cos^2(\theta) +$$

$$\frac{1}{2}s^3\sin^2(\theta)a_{i_1}\lambda_i\lambda_{i_3}a_{i_2}^\dagger\cos^2(\theta) + \frac{1}{2}s^3\sin^2(\theta)a_i\lambda_{i_1}\lambda_{i_3}a_{i_2}^\dagger\cos^2(\theta) -$$

$$\frac{1}{2}s^2\sin^2(\theta)a_i a_{i_1}a_{i_2}\lambda_{i_2}\lambda_{i_3}a_{i_2}^\dagger\cos^2(\theta) - \frac{1}{2}s^2\sin^2(\theta)a_i a_{i_3}\lambda_i\lambda_{i_1}a_i^\dagger a_{i_2}^\dagger\cos^2(\theta) +$$

$$\frac{1}{2}s\sin^2(\theta)a_i a_{i_1}a_{i_2}a_{i_3}\lambda_i\lambda_{i_2}a_i^\dagger a_{i_2}^\dagger\cos^2(\theta) - \frac{1}{2}s^2\sin^2(\theta)a_{i_2}a_{i_3}\lambda_{i_1}\lambda_{i_2}a_i^\dagger a_{i_2}^\dagger\cos^2(\theta) -$$

$$\frac{1}{2}s^2\sin^2(\theta)a_i a_{i_1}\lambda_i\lambda_{i_3}a_i^\dagger a_{i_2}^\dagger\cos^2(\theta) + \frac{1}{2}s^3\sin^2(\theta)\lambda_{i_1}\lambda_{i_3}a_i^\dagger a_{i_2}^\dagger\cos^2(\theta) -$$

$$\frac{1}{2}s^2\sin^2(\theta)a_{i_1}a_{i_2}\lambda_{i_2}\lambda_{i_3}a_i^\dagger a_{i_2}^\dagger\cos^2(\theta) - \frac{1}{2}s^2\sin^2(\theta)a_{i_1}a_{i_3}\lambda_i\lambda_{i_1}a_{i_1}^\dagger a_{i_2}^\dagger\cos^2(\theta) -$$

$$\frac{1}{2}s^2\sin^2(\theta)a_{i_2}a_{i_3}\lambda_i\lambda_{i_2}a_{i_1}^\dagger a_{i_2}^\dagger\cos^2(\theta) + \frac{1}{2}s\sin^2(\theta)a_i a_{i_1}a_{i_2}a_{i_3}\lambda_{i_1}\lambda_{i_2}a_{i_1}^\dagger a_{i_2}^\dagger\cos^2(\theta) +$$

$$\frac{1}{2}s^3\sin^2(\theta)\lambda_i\lambda_{i_3}a_{i_1}^\dagger a_{i_2}^\dagger\cos^2(\theta) - \frac{1}{2}s^2\sin^2(\theta)a_i a_{i_1}\lambda_{i_1}\lambda_{i_3}a_{i_1}^\dagger a_{i_2}^\dagger\cos^2(\theta) -$$

$$\frac{1}{2}s^2\sin^2(\theta)a_i a_{i_2}\lambda_{i_2}\lambda_{i_3}a_{i_1}^\dagger a_{i_2}^\dagger\cos^2(\theta) + \frac{1}{2}s\sin^2(\theta)a_i a_{i_1}a_{i_3}\lambda_i\lambda_{i_1}a_i^\dagger a_{i_1}^\dagger a_{i_2}^\dagger\cos^2(\theta) +$$

$$\frac{1}{2}s\sin^2(\theta)a_i a_{i_2}a_{i_3}\lambda_i\lambda_{i_2}a_i^\dagger a_{i_1}^\dagger a_{i_2}^\dagger\cos^2(\theta) + \frac{1}{2}s\sin^2(\theta)a_{i_1}a_{i_2}a_{i_3}\lambda_{i_1}\lambda_{i_2}a_i^\dagger a_{i_1}^\dagger a_{i_2}^\dagger\cos^2(\theta) -$$

$$\frac{1}{2}s^2\sin^2(\theta)a_i\lambda_i\lambda_{i_3}a_i^\dagger a_{i_1}^\dagger a_{i_2}^\dagger\cos^2(\theta) - \frac{1}{2}s^2\sin^2(\theta)a_{i_1}\lambda_{i_1}\lambda_{i_3}a_i^\dagger a_{i_1}^\dagger a_{i_2}^\dagger\cos^2(\theta) -$$

$$\frac{1}{2}s^2\sin^2(\theta)a_{i_2}\lambda_{i_2}\lambda_{i_3}a_i^\dagger a_{i_1}^\dagger a_{i_2}^\dagger\cos^2(\theta) + \frac{1}{2}s^3\sin^2(\theta)a_{i_2}\lambda_i\lambda_{i_1}a_{i_3}^\dagger\cos^2(\theta) +$$

$$\frac{1}{2}s^3\sin^2(\theta)a_{i_1}\lambda_i\lambda_{i_2}a_{i_3}^\dagger\cos^2(\theta) + \frac{1}{2}s^3\sin^2(\theta)a_i\lambda_{i_1}\lambda_{i_2}a_{i_3}^\dagger\cos^2(\theta) -$$

$$\frac{1}{2}s^2\sin^2(\theta)a_{i_1}a_{i_2}a_{i_3}\lambda_i\lambda_{i_3}a_{i_3}^\dagger\cos^2(\theta) - \frac{1}{2}s^2\sin^2(\theta)a_i a_{i_2}a_{i_3}\lambda_{i_1}\lambda_{i_3}a_{i_3}^\dagger\cos^2(\theta) -$$

$$\frac{1}{2}s^2\sin^2(\theta)a_ia_{i_1}a_{i_3}\lambda_{i_2}\lambda_{i_3}a_{i_3}^\dagger\cos^2(\theta)-\frac{1}{2}s^2\sin^2(\theta)a_ia_{i_2}\lambda_i\lambda_{i_1}a_i^\dagger a_{i_3}^\dagger\cos^2(\theta)-$$
$$\frac{1}{2}s^2\sin^2(\theta)a_ia_{i_1}\lambda_i\lambda_{i_2}a_i^\dagger a_{i_3}^\dagger\cos^2(\theta)+\frac{1}{2}s^3\sin^2(\theta)\lambda_{i_1}\lambda_{i_2}a_i^\dagger a_{i_3}^\dagger\cos^2(\theta)+$$
$$\frac{1}{2}s\sin^2(\theta)a_ia_{i_1}a_{i_2}a_{i_3}\lambda_i\lambda_{i_3}a_i^\dagger a_{i_3}^\dagger\cos^2(\theta)-\frac{1}{2}s^2\sin^2(\theta)a_{i_2}a_{i_3}\lambda_{i_1}\lambda_{i_3}a_i^\dagger a_{i_3}^\dagger\cos^2(\theta)-$$
$$\frac{1}{2}s^2\sin^2(\theta)a_{i_1}a_{i_3}\lambda_{i_2}\lambda_{i_3}a_i^\dagger a_{i_3}^\dagger\cos^2(\theta)-\frac{1}{2}s^2\sin^2(\theta)a_{i_1}a_{i_2}\lambda_i\lambda_{i_1}a_{i_1}^\dagger a_{i_3}^\dagger\cos^2(\theta)+$$
$$\frac{1}{2}s^3\sin^2(\theta)\lambda_i\lambda_{i_2}a_{i_1}^\dagger a_{i_3}^\dagger\cos^2(\theta)-\frac{1}{2}s^2\sin^2(\theta)a_ia_{i_1}\lambda_{i_1}\lambda_{i_2}a_{i_1}^\dagger a_{i_3}^\dagger\cos^2(\theta)-$$
$$\frac{1}{2}s^2\sin^2(\theta)a_{i_2}a_{i_3}\lambda_i\lambda_{i_3}a_{i_1}^\dagger a_{i_3}^\dagger\cos^2(\theta)+\frac{1}{2}s\sin^2(\theta)a_ia_{i_1}a_{i_2}a_{i_3}\lambda_{i_1}\lambda_{i_3}a_{i_1}^\dagger a_{i_3}^\dagger\cos^2(\theta)-$$
$$\frac{1}{2}s^2\sin^2(\theta)a_ia_{i_3}\lambda_{i_2}\lambda_{i_3}a_{i_1}^\dagger a_{i_3}^\dagger\cos^2(\theta)+\frac{1}{2}s\sin^2(\theta)a_ia_{i_1}a_{i_2}\lambda_i\lambda_{i_1}a_i^\dagger a_{i_1}^\dagger a_{i_3}^\dagger\cos^2(\theta)-$$
$$\frac{1}{2}s^2\sin^2(\theta)a_i\lambda_i\lambda_{i_2}a_i^\dagger a_{i_1}^\dagger a_{i_3}^\dagger\cos^2(\theta)-\frac{1}{2}s^2\sin^2(\theta)a_{i_1}\lambda_{i_1}\lambda_{i_2}a_i^\dagger a_{i_1}^\dagger a_{i_3}^\dagger\cos^2(\theta)+$$
$$\frac{1}{2}s\sin^2(\theta)a_ia_{i_2}a_{i_3}\lambda_i\lambda_{i_3}a_i^\dagger a_{i_1}^\dagger a_{i_3}^\dagger\cos^2(\theta)+\frac{1}{2}s\sin^2(\theta)a_{i_1}a_{i_2}a_{i_3}\lambda_{i_1}\lambda_{i_3}a_i^\dagger a_{i_1}^\dagger a_{i_3}^\dagger\cos^2(\theta)-$$
$$\frac{1}{2}s^2\sin^2(\theta)a_{i_3}\lambda_{i_2}\lambda_{i_3}a_i^\dagger a_{i_1}^\dagger a_{i_3}^\dagger\cos^2(\theta)+\frac{1}{2}s^3\sin^2(\theta)\lambda_i\lambda_{i_1}a_{i_2}^\dagger a_{i_3}^\dagger\cos^2(\theta)-$$
$$\frac{1}{2}s^2\sin^2(\theta)a_{i_1}a_{i_2}\lambda_i\lambda_{i_2}a_{i_2}^\dagger a_{i_3}^\dagger\cos^2(\theta)-\frac{1}{2}s^2\sin^2(\theta)a_ia_{i_2}\lambda_{i_1}\lambda_{i_2}a_{i_2}^\dagger a_{i_3}^\dagger\cos^2(\theta)-$$
$$\frac{1}{2}s^2\sin^2(\theta)a_{i_1}a_{i_3}\lambda_i\lambda_{i_3}a_{i_2}^\dagger a_{i_3}^\dagger\cos^2(\theta)-\frac{1}{2}s^2\sin^2(\theta)a_ia_{i_3}\lambda_{i_1}\lambda_{i_3}a_{i_2}^\dagger a_{i_3}^\dagger\cos^2(\theta)+$$
$$\frac{1}{2}s\sin^2(\theta)a_ia_{i_1}a_{i_2}a_{i_3}\lambda_{i_2}\lambda_{i_3}a_{i_2}^\dagger a_{i_3}^\dagger\cos^2(\theta)-\frac{1}{2}s^2\sin^2(\theta)a_i\lambda_i\lambda_{i_1}a_i^\dagger a_{i_2}^\dagger a_{i_3}^\dagger\cos^2(\theta)+$$
$$\frac{1}{2}s\sin^2(\theta)a_ia_{i_1}a_{i_2}\lambda_i\lambda_{i_2}a_i^\dagger a_{i_2}^\dagger a_{i_3}^\dagger\cos^2(\theta)-\frac{1}{2}s^2\sin^2(\theta)a_{i_2}\lambda_{i_1}\lambda_{i_2}a_i^\dagger a_{i_2}^\dagger a_{i_3}^\dagger\cos^2(\theta)+$$
$$\frac{1}{2}s\sin^2(\theta)a_ia_{i_1}a_{i_3}\lambda_i\lambda_{i_3}a_i^\dagger a_{i_2}^\dagger a_{i_3}^\dagger\cos^2(\theta)-\frac{1}{2}s^2\sin^2(\theta)a_{i_3}\lambda_{i_1}\lambda_{i_3}a_i^\dagger a_{i_2}^\dagger a_{i_3}^\dagger\cos^2(\theta)+$$
$$\frac{1}{2}s\sin^2(\theta)a_{i_1}a_{i_2}a_{i_3}\lambda_{i_2}\lambda_{i_3}a_i^\dagger a_{i_2}^\dagger a_{i_3}^\dagger\cos^2(\theta)-\frac{1}{2}s^2\sin^2(\theta)a_{i_1}\lambda_i\lambda_{i_1}a_{i_1}^\dagger a_{i_2}^\dagger a_{i_3}^\dagger\cos^2(\theta)-$$
$$\frac{1}{2}s^2\sin^2(\theta)a_{i_2}\lambda_i\lambda_{i_2}a_{i_1}^\dagger a_{i_2}^\dagger a_{i_3}^\dagger\cos^2(\theta)+\frac{1}{2}s\sin^2(\theta)a_ia_{i_1}a_{i_2}\lambda_{i_1}\lambda_{i_2}a_{i_1}^\dagger a_{i_2}^\dagger a_{i_3}^\dagger\cos^2(\theta)-$$
$$\frac{1}{2}s^2\sin^2(\theta)a_{i_3}\lambda_i\lambda_{i_3}a_{i_1}^\dagger a_{i_2}^\dagger a_{i_3}^\dagger\cos^2(\theta)+\frac{1}{2}s\sin^2(\theta)a_ia_{i_1}a_{i_3}\lambda_{i_1}\lambda_{i_3}a_{i_1}^\dagger a_{i_2}^\dagger a_{i_3}^\dagger\cos^2(\theta)+$$
$$\frac{1}{2}s\sin^2(\theta)a_ia_{i_2}a_{i_3}\lambda_{i_2}\lambda_{i_3}a_{i_1}^\dagger a_{i_2}^\dagger a_{i_3}^\dagger\cos^2(\theta)+\frac{1}{2}s\sin^2(\theta)a_ia_{i_1}\lambda_i\lambda_{i_1}a_i^\dagger a_{i_1}^\dagger a_{i_2}^\dagger a_{i_3}^\dagger\cos^2(\theta)+$$
$$\frac{1}{2}s\sin^2(\theta)a_ia_{i_2}\lambda_i\lambda_{i_2}a_i^\dagger a_{i_1}^\dagger a_{i_2}^\dagger a_{i_3}^\dagger\cos^2(\theta)+\frac{1}{2}s\sin^2(\theta)a_{i_1}a_{i_2}\lambda_{i_1}\lambda_{i_2}a_i^\dagger a_{i_1}^\dagger a_{i_2}^\dagger a_{i_3}^\dagger\cos^2(\theta)+$$
$$\frac{1}{2}s\sin^2(\theta)a_ia_{i_3}\lambda_i\lambda_{i_3}a_i^\dagger a_{i_1}^\dagger a_{i_2}^\dagger a_{i_3}^\dagger\cos^2(\theta)+\frac{1}{2}s\sin^2(\theta)a_{i_1}a_{i_3}\lambda_{i_1}\lambda_{i_3}a_i^\dagger a_{i_1}^\dagger a_{i_2}^\dagger a_{i_3}^\dagger\cos^2(\theta)+$$
$$\frac{1}{2}s\sin^2(\theta)a_{i_2}a_{i_3}\lambda_{i_2}\lambda_{i_3}a_i^\dagger a_{i_1}^\dagger a_{i_2}^\dagger a_{i_3}^\dagger\cos^2(\theta)+\frac{s^{5/2}\sin^3(\theta)a_{i_1}a_{i_2}a_{i_3}\lambda_i\cos(\theta)}{2\sqrt{2}}+$$
$$\frac{s^{5/2}\sin^3(\theta)a_ia_{i_2}a_{i_3}\lambda_{i_1}\cos(\theta)}{2\sqrt{2}}+\frac{s^{5/2}\sin^3(\theta)a_ia_{i_1}a_{i_3}\lambda_{i_2}\cos(\theta)}{2\sqrt{2}}+$$
$$\frac{s^{5/2}\sin^3(\theta)a_ia_{i_1}a_{i_2}\lambda_{i_3}\cos(\theta)}{2\sqrt{2}}-\frac{s^{3/2}\sin^3(\theta)a_ia_{i_1}a_{i_2}a_{i_3}\lambda_ia_i^\dagger\cos(\theta)}{2\sqrt{2}}+$$
$$\frac{s^{5/2}\sin^3(\theta)a_{i_2}a_{i_3}\lambda_{i_1}a_i^\dagger\cos(\theta)}{2\sqrt{2}}+\frac{s^{5/2}\sin^3(\theta)a_{i_1}a_{i_3}\lambda_{i_2}a_i^\dagger\cos(\theta)}{2\sqrt{2}}+$$
$$\frac{s^{5/2}\sin^3(\theta)a_{i_1}a_{i_2}\lambda_{i_3}a_i^\dagger\cos(\theta)}{2\sqrt{2}}+\frac{s^{5/2}\sin^3(\theta)a_{i_2}a_{i_3}\lambda_ia_{i_1}^\dagger\cos(\theta)}{2\sqrt{2}}-$$
$$\frac{s^{3/2}\sin^3(\theta)a_ia_{i_1}a_{i_2}a_{i_3}\lambda_{i_1}a_{i_1}^\dagger\cos(\theta)}{2\sqrt{2}}+\frac{s^{5/2}\sin^3(\theta)a_ia_{i_3}\lambda_{i_2}a_{i_1}^\dagger\cos(\theta)}{2\sqrt{2}}+$$

$$\frac{s^{5/2}\sin^3(\theta)a_ia_{i_2}\lambda_{i_3}a_{i_1}^\dagger\cos(\theta)}{2\sqrt{2}}-\frac{s^{3/2}\sin^3(\theta)a_ia_{i_2}a_{i_3}\lambda_ia_i^\dagger a_{i_1}^\dagger\cos(\theta)}{2\sqrt{2}}-$$

$$\frac{s^{3/2}\sin^3(\theta)a_{i_1}a_{i_2}a_{i_3}\lambda_{i_1}a_i^\dagger a_{i_1}^\dagger\cos(\theta)}{2\sqrt{2}}+\frac{s^{5/2}\sin^3(\theta)a_{i_3}\lambda_{i_2}a_i^\dagger a_{i_1}^\dagger\cos(\theta)}{2\sqrt{2}}+$$

$$\frac{s^{5/2}\sin^3(\theta)a_{i_2}\lambda_{i_3}a_i^\dagger a_{i_1}^\dagger\cos(\theta)}{2\sqrt{2}}+\frac{s^{5/2}\sin^3(\theta)a_{i_1}a_{i_3}\lambda_ia_{i_2}^\dagger\cos(\theta)}{2\sqrt{2}}+$$

$$\frac{s^{5/2}\sin^3(\theta)a_ia_{i_3}\lambda_{i_1}a_{i_2}^\dagger\cos(\theta)}{2\sqrt{2}}-\frac{s^{3/2}\sin^3(\theta)a_ia_{i_1}a_{i_2}a_{i_3}\lambda_{i_2}a_{i_2}^\dagger\cos(\theta)}{2\sqrt{2}}+$$

$$\frac{s^{5/2}\sin^3(\theta)a_ia_{i_1}\lambda_{i_3}a_{i_2}^\dagger\cos(\theta)}{2\sqrt{2}}-\frac{s^{3/2}\sin^3(\theta)a_ia_{i_1}a_{i_3}\lambda_ia_i^\dagger a_{i_2}^\dagger\cos(\theta)}{2\sqrt{2}}+$$

$$\frac{s^{5/2}\sin^3(\theta)a_{i_3}\lambda_{i_1}a_i^\dagger a_{i_2}^\dagger\cos(\theta)}{2\sqrt{2}}-\frac{s^{3/2}\sin^3(\theta)a_{i_1}a_{i_2}a_{i_3}\lambda_{i_2}a_i^\dagger a_{i_2}^\dagger\cos(\theta)}{2\sqrt{2}}+$$

$$\frac{s^{5/2}\sin^3(\theta)a_{i_1}\lambda_{i_3}a_i^\dagger a_{i_2}^\dagger\cos(\theta)}{2\sqrt{2}}+\frac{s^{5/2}\sin^3(\theta)a_{i_3}\lambda_ia_{i_1}^\dagger a_{i_2}^\dagger\cos(\theta)}{2\sqrt{2}}-$$

$$\frac{s^{3/2}\sin^3(\theta)a_ia_{i_1}a_{i_3}\lambda_{i_1}a_{i_1}^\dagger a_{i_2}^\dagger\cos(\theta)}{2\sqrt{2}}-\frac{s^{3/2}\sin^3(\theta)a_ia_{i_2}a_{i_3}\lambda_{i_2}a_{i_1}^\dagger a_{i_2}^\dagger\cos(\theta)}{2\sqrt{2}}+$$

$$\frac{s^{5/2}\sin^3(\theta)a_i\lambda_{i_3}a_{i_1}^\dagger a_{i_2}^\dagger\cos(\theta)}{2\sqrt{2}}-\frac{s^{3/2}\sin^3(\theta)a_ia_{i_3}\lambda_ia_i^\dagger a_{i_1}^\dagger a_{i_2}^\dagger\cos(\theta)}{2\sqrt{2}}-$$

$$\frac{s^{3/2}\sin^3(\theta)a_{i_1}a_{i_3}\lambda_{i_1}a_i^\dagger a_{i_1}^\dagger a_{i_2}^\dagger\cos(\theta)}{2\sqrt{2}}-\frac{s^{3/2}\sin^3(\theta)a_{i_2}a_{i_3}\lambda_{i_2}a_i^\dagger a_{i_1}^\dagger a_{i_2}^\dagger\cos(\theta)}{2\sqrt{2}}+$$

$$\frac{s^{5/2}\sin^3(\theta)\lambda_{i_3}a_i^\dagger a_{i_1}^\dagger a_{i_2}^\dagger\cos(\theta)}{2\sqrt{2}}+\frac{s^{5/2}\sin^3(\theta)a_{i_1}a_{i_2}\lambda_ia_{i_3}^\dagger\cos(\theta)}{2\sqrt{2}}+$$

$$\frac{s^{5/2}\sin^3(\theta)a_ia_{i_2}\lambda_{i_1}a_{i_3}^\dagger\cos(\theta)}{2\sqrt{2}}+\frac{s^{5/2}\sin^3(\theta)a_ia_{i_1}\lambda_{i_2}a_{i_3}^\dagger\cos(\theta)}{2\sqrt{2}}-$$

$$\frac{s^{3/2}\sin^3(\theta)a_ia_{i_1}a_{i_2}a_{i_3}\lambda_{i_3}a_{i_3}^\dagger\cos(\theta)}{2\sqrt{2}}-\frac{s^{3/2}\sin^3(\theta)a_ia_{i_1}a_{i_2}\lambda_ia_i^\dagger a_{i_3}^\dagger\cos(\theta)}{2\sqrt{2}}+$$

$$\frac{s^{5/2}\sin^3(\theta)a_{i_2}\lambda_{i_1}a_i^\dagger a_{i_3}^\dagger\cos(\theta)}{2\sqrt{2}}+\frac{s^{5/2}\sin^3(\theta)a_{i_1}\lambda_{i_2}a_i^\dagger a_{i_3}^\dagger\cos(\theta)}{2\sqrt{2}}-$$

$$\frac{s^{3/2}\sin^3(\theta)a_{i_1}a_{i_2}a_{i_3}\lambda_{i_3}a_i^\dagger a_{i_3}^\dagger\cos(\theta)}{2\sqrt{2}}+\frac{s^{5/2}\sin^3(\theta)a_{i_2}\lambda_ia_{i_1}^\dagger a_{i_3}^\dagger\cos(\theta)}{2\sqrt{2}}-$$

$$\frac{s^{3/2}\sin^3(\theta)a_ia_{i_1}a_{i_2}\lambda_{i_1}a_{i_1}^\dagger a_{i_3}^\dagger\cos(\theta)}{2\sqrt{2}}+\frac{s^{5/2}\sin^3(\theta)a_i\lambda_{i_2}a_{i_1}^\dagger a_{i_3}^\dagger\cos(\theta)}{2\sqrt{2}}-$$

$$\frac{s^{3/2}\sin^3(\theta)a_ia_{i_2}a_{i_3}\lambda_{i_3}a_{i_1}^\dagger a_{i_3}^\dagger\cos(\theta)}{2\sqrt{2}}-\frac{s^{3/2}\sin^3(\theta)a_ia_{i_2}\lambda_ia_i^\dagger a_{i_1}^\dagger a_{i_3}^\dagger\cos(\theta)}{2\sqrt{2}}-$$

$$\frac{s^{3/2}\sin^3(\theta)a_{i_1}a_{i_2}\lambda_{i_1}a_i^\dagger a_{i_1}^\dagger a_{i_3}^\dagger\cos(\theta)}{2\sqrt{2}}+\frac{s^{5/2}\sin^3(\theta)\lambda_{i_2}a_i^\dagger a_{i_1}^\dagger a_{i_3}^\dagger\cos(\theta)}{2\sqrt{2}}-$$

$$\frac{s^{3/2}\sin^3(\theta)a_{i_2}a_{i_3}\lambda_{i_3}a_i^\dagger a_{i_1}^\dagger a_{i_3}^\dagger\cos(\theta)}{2\sqrt{2}}+\frac{s^{5/2}\sin^3(\theta)a_{i_1}\lambda_ia_{i_2}^\dagger a_{i_3}^\dagger\cos(\theta)}{2\sqrt{2}}+$$

$$\frac{s^{5/2}\sin^3(\theta)a_i\lambda_{i_1}a_{i_2}^\dagger a_{i_3}^\dagger\cos(\theta)}{2\sqrt{2}}-\frac{s^{3/2}\sin^3(\theta)a_ia_{i_1}a_{i_2}\lambda_{i_2}a_{i_2}^\dagger a_{i_3}^\dagger\cos(\theta)}{2\sqrt{2}}-$$

$$\frac{s^{3/2}\sin^3(\theta)a_ia_{i_1}a_{i_3}\lambda_{i_3}a_{i_2}^\dagger a_{i_3}^\dagger\cos(\theta)}{2\sqrt{2}}-\frac{s^{3/2}\sin^3(\theta)a_ia_{i_1}\lambda_ia_i^\dagger a_{i_2}^\dagger a_{i_3}^\dagger\cos(\theta)}{2\sqrt{2}}+$$

$$\frac{s^{5/2}\sin^3(\theta)\lambda_{i_1}a_i^\dagger a_{i_2}^\dagger a_{i_3}^\dagger\cos(\theta)}{2\sqrt{2}}-\frac{s^{3/2}\sin^3(\theta)a_{i_1}a_{i_2}\lambda_{i_2}a_i^\dagger a_{i_2}^\dagger a_{i_3}^\dagger\cos(\theta)}{2\sqrt{2}}-$$

$$\frac{s^{3/2}\sin^3(\theta)a_{i_1}a_{i_3}\lambda_{i_3}a_i^\dagger a_{i_2}^\dagger a_{i_3}^\dagger\cos(\theta)}{2\sqrt{2}}+\frac{s^{5/2}\sin^3(\theta)\lambda_i a_{i_1}^\dagger a_{i_2}^\dagger a_{i_3}^\dagger\cos(\theta)}{2\sqrt{2}}-$$

$$\frac{s^{3/2}\sin^3(\theta)a_i a_{i_1}\lambda_{i_1}a_{i_1}^\dagger a_{i_2}^\dagger a_{i_3}^\dagger\cos(\theta)}{2\sqrt{2}}-\frac{s^{3/2}\sin^3(\theta)a_i a_{i_2}\lambda_{i_2}a_{i_1}^\dagger a_{i_2}^\dagger a_{i_3}^\dagger\cos(\theta)}{2\sqrt{2}}-$$

$$\frac{s^{3/2}\sin^3(\theta)a_i a_{i_3}\lambda_{i_3}a_{i_1}^\dagger a_{i_2}^\dagger a_{i_3}^\dagger\cos(\theta)}{2\sqrt{2}}-\frac{s^{3/2}\sin^3(\theta)a_i\lambda_i a_i^\dagger a_{i_1}^\dagger a_{i_2}^\dagger a_{i_3}^\dagger\cos(\theta)}{2\sqrt{2}}-$$

$$\frac{s^{3/2}\sin^3(\theta)a_{i_1}\lambda_{i_1}a_i^\dagger a_{i_1}^\dagger a_{i_2}^\dagger a_{i_3}^\dagger\cos(\theta)}{2\sqrt{2}}-\frac{s^{3/2}\sin^3(\theta)a_{i_2}\lambda_{i_2}a_i^\dagger a_{i_1}^\dagger a_{i_2}^\dagger a_{i_3}^\dagger\cos(\theta)}{2\sqrt{2}}-$$

$$\frac{s^{3/2}\sin^3(\theta)a_{i_3}\lambda_{i_3}a_i^\dagger a_{i_1}^\dagger a_{i_2}^\dagger a_{i_3}^\dagger\cos(\theta)}{2\sqrt{2}}+\frac{1}{4}s^2\sin^4(\theta)a_i a_{i_1}a_{i_2}a_{i_3}+\frac{1}{4}s^2\sin^4(\theta)a_{i_1}a_{i_2}a_{i_3}a_i^\dagger+$$

$$\frac{1}{4}s^2\sin^4(\theta)a_i a_{i_2}a_{i_3}a_{i_1}^\dagger+\frac{1}{4}s^2\sin^4(\theta)a_{i_2}a_{i_3}a_i^\dagger a_{i_1}^\dagger+\frac{1}{4}s^2\sin^4(\theta)a_i a_{i_1}a_{i_3}a_{i_2}^\dagger+$$

$$\frac{1}{4}s^2\sin^4(\theta)a_{i_1}a_{i_3}a_i^\dagger a_{i_2}^\dagger+\frac{1}{4}s^2\sin^4(\theta)a_i a_{i_3}a_{i_1}^\dagger a_{i_2}^\dagger+\frac{1}{4}s^2\sin^4(\theta)a_{i_3}a_i^\dagger a_{i_1}^\dagger a_{i_2}^\dagger+$$

$$\frac{1}{4}s^2\sin^4(\theta)a_i a_{i_1}a_{i_2}a_{i_3}^\dagger+\frac{1}{4}s^2\sin^4(\theta)a_{i_1}a_{i_2}a_i^\dagger a_{i_3}^\dagger+\frac{1}{4}s^2\sin^4(\theta)a_i a_{i_2}a_{i_1}^\dagger a_{i_3}^\dagger+$$

$$\frac{1}{4}s^2\sin^4(\theta)a_{i_2}a_i^\dagger a_{i_1}^\dagger a_{i_3}^\dagger+\frac{1}{4}s^2\sin^4(\theta)a_i a_{i_1}a_{i_2}^\dagger a_{i_3}^\dagger+\frac{1}{4}s^2\sin^4(\theta)a_{i_1}a_i^\dagger a_{i_2}^\dagger a_{i_3}^\dagger+$$

$$\frac{1}{4}s^2\sin^4(\theta)a_i a_{i_1}^\dagger a_{i_2}^\dagger a_{i_3}^\dagger+\frac{1}{4}s^2\sin^4(\theta)a_i^\dagger a_{i_1}^\dagger a_{i_2}^\dagger a_{i_3}^\dagger$$

$$+\quad\sum_i\frac{J_1}{2}\Bigg(s^2\lambda_i\lambda_{i_2}\cos^2(\theta)+s^2\lambda_{i_1}\lambda_{i_3}\cos^2(\theta)-sa_i\lambda_i\lambda_{i_2}a_i^\dagger\cos^2(\theta)$$

$$-sa_{i_1}\lambda_{i_1}\lambda_{i_3}a_{i_1}^\dagger\cos^2(\theta)-sa_{i_2}\lambda_i\lambda_{i_2}a_{i_2}^\dagger\cos^2(\theta)+a_i a_{i_2}\lambda_i\lambda_{i_2}a_i^\dagger a_{i_2}^\dagger\cos^2(\theta)$$

$$-sa_{i_3}\lambda_{i_1}\lambda_{i_3}a_{i_3}^\dagger\cos^2(\theta)+a_{i_1}a_{i_3}\lambda_{i_1}\lambda_{i_3}a_{i_1}^\dagger a_{i_3}^\dagger\cos^2(\theta)$$

$$+\frac{s^{3/2}\sin(\theta)a_{i_2}\lambda_i\cos(\theta)}{\sqrt{2}}+\frac{s^{3/2}\sin(\theta)a_{i_3}\lambda_{i_1}\cos(\theta)}{\sqrt{2}}$$

$$+\frac{s^{3/2}\sin(\theta)a_i\lambda_{i_2}\cos(\theta)}{\sqrt{2}}+\frac{s^{3/2}\sin(\theta)a_{i_1}\lambda_{i_3}\cos(\theta)}{\sqrt{2}}-\frac{\sqrt{s}\sin(\theta)a_i a_{i_2}\lambda_i a_i^\dagger\cos(\theta)}{\sqrt{2}}$$

$$+\frac{s^{3/2}\sin(\theta)\lambda_{i_2}a_i^\dagger\cos(\theta)}{\sqrt{2}}-\frac{\sqrt{s}\sin(\theta)a_{i_1}a_{i_3}\lambda_{i_1}a_{i_1}^\dagger\cos(\theta)}{\sqrt{2}}$$

$$+\frac{s^{3/2}\sin(\theta)\lambda_{i_3}a_{i_1}^\dagger\cos(\theta)}{\sqrt{2}}+\frac{s^{3/2}\sin(\theta)\lambda_i a_{i_2}^\dagger\cos(\theta)}{\sqrt{2}}$$

$$-\frac{\sqrt{s}\sin(\theta)a_i a_{i_2}\lambda_{i_2}a_{i_2}^\dagger\cos(\theta)}{\sqrt{2}}-\frac{\sqrt{s}\sin(\theta)a_i\lambda_i a_i^\dagger a_{i_2}^\dagger\cos(\theta)}{\sqrt{2}}$$

$$-\frac{\sqrt{s}\sin(\theta)a_{i_2}\lambda_{i_2}a_i^\dagger a_{i_2}^\dagger\cos(\theta)}{\sqrt{2}}+\frac{s^{3/2}\sin(\theta)\lambda_{i_1}a_{i_3}^\dagger\cos(\theta)}{\sqrt{2}}$$

$$-\frac{\sqrt{s}\sin(\theta)a_{i_1}a_{i_3}\lambda_{i_3}a_{i_3}^\dagger\cos(\theta)}{\sqrt{2}}-\frac{\sqrt{s}\sin(\theta)a_{i_1}\lambda_{i_1}a_{i_1}^\dagger a_{i_3}^\dagger\cos(\theta)}{\sqrt{2}}$$

$$-\frac{\sqrt{s}\sin(\theta)a_{i_3}\lambda_{i_3}a_{i_1}^\dagger a_{i_3}^\dagger\cos(\theta)}{\sqrt{2}}+\frac{1}{2}s\sin^2(\theta)a_i a_{i_2}$$

$$+\frac{1}{2}s\sin^2(\theta)a_{i_1}a_{i_3}+\frac{1}{2}s\sin^2(\theta)a_{i_2}a_i^\dagger+\frac{1}{2}s\sin^2(\theta)a_{i_3}a_{i_1}^\dagger$$

$$
\begin{aligned}
&+\frac{1}{2}s\sin^2(\theta)a_i a^\dagger_{i_2}+\frac{1}{2}s\sin^2(\theta)a^\dagger_i a^\dagger_{i_2}+\frac{1}{2}s\sin^2(\theta)a_{i_1}a^\dagger_{i_3}\\
&+\frac{1}{2}s\sin^2(\theta)a^\dagger_{i_1}a^\dagger_{i_3}\Bigg)
\end{aligned}
\tag{A.9}
$$

$$
\begin{aligned}
+\sum_{i_{\langle AB\rangle}}\frac{J_2}{16}\Bigg(&\frac{1}{2}s\sin^2(\theta)a_{i_A}a_{i_B}c^2-\frac{1}{2}s\sin^2(\theta)a_{i_B}a_{i_{A_1}}c^2-\frac{1}{2}s\sin^2(\theta)a_{i_B}a_{i_{A_2}}c^2+\\
&\frac{1}{2}s\sin^2(\theta)a_{i_B}a_{i_{A_3}}c^2-\frac{1}{2}s\sin(\theta)a_{i_A}a_{i_{B_1}}c^2+\frac{1}{2}s\sin(\theta)a_{i_{A_1}}a_{i_{B_1}}c^2+\frac{1}{2}s\sin(\theta)a_{i_{A_2}}a_{i_{B_1}}c^2-\\
&\frac{1}{2}s\sin(\theta)a_{i_{A_3}}a_{i_{B_1}}c^2-\frac{1}{2}s\sin^2(\theta)a_{i_A}a_{i_{B_2}}c^2+\frac{1}{2}s\sin^2(\theta)a_{i_{A_1}}a_{i_{B_2}}c^2+\frac{1}{2}s\sin^2(\theta)a_{i_{A_2}}a_{i_{B_2}}c^2-\\
&\frac{1}{2}s\sin^2(\theta)a_{i_{A_3}}a_{i_{B_2}}c^2+\frac{1}{2}s\sin^2(\theta)a_{i_A}a_{i_{B_3}}c^2-\frac{1}{2}s\sin^2(\theta)a_{i_{A_1}}a_{i_{B_3}}c^2-\frac{1}{2}s\sin^2(\theta)a_{i_{A_2}}a_{i_{B_3}}c^2+\\
&\frac{1}{2}s\sin^2(\theta)a_{i_{A_3}}a_{i_{B_3}}c^2+\frac{1}{2}s\sin^2(\theta)a_{i_B}a^\dagger_{i_A}c^2-\frac{1}{2}s\sin(\theta)a_{i_{B_1}}a^\dagger_{i_A}c^2-\frac{1}{2}s\sin^2(\theta)a_{i_{B_2}}a^\dagger_{i_A}c^2+\\
&\frac{1}{2}s\sin^2(\theta)a_{i_{B_3}}a^\dagger_{i_A}c^2-\frac{\sqrt{s}\cos(\theta)\sin(\theta)a_{i_A}a_{i_B}\lambda_{i_A}a^\dagger_{i_A}c^2}{\sqrt{2}}+\frac{\sqrt{s}\cos(\theta)a_{i_A}a_{i_{B_1}}\lambda_{i_A}a^\dagger_{i_A}c^2}{\sqrt{2}}+\\
&\frac{\sqrt{s}\cos(\theta)\sin(\theta)a_{i_A}a_{i_{B_2}}\lambda_{i_A}a^\dagger_{i_A}c^2}{\sqrt{2}}-\frac{\sqrt{s}\cos(\theta)\sin(\theta)a_{i_A}a_{i_{B_3}}\lambda_{i_A}a^\dagger_{i_A}c^2}{\sqrt{2}}+\\
&\frac{\sqrt{s}\cos(\theta)\sin(\theta)a_{i_A}a_{i_B}\lambda_{i_{A_1}}a^\dagger_{i_A}c^2}{\sqrt{2}}-\frac{\sqrt{s}\cos(\theta)a_{i_A}a_{i_{B_1}}\lambda_{i_{A_1}}a^\dagger_{i_A}c^2}{\sqrt{2}}-\\
&\frac{\sqrt{s}\cos(\theta)\sin(\theta)a_{i_A}a_{i_{B_2}}\lambda_{i_{A_1}}a^\dagger_{i_A}c^2}{\sqrt{2}}+\frac{\sqrt{s}\cos(\theta)\sin(\theta)a_{i_A}a_{i_{B_3}}\lambda_{i_{A_1}}a^\dagger_{i_A}c^2}{\sqrt{2}}+\\
&\frac{\sqrt{s}\cos(\theta)\sin(\theta)a_{i_A}a_{i_B}\lambda_{i_{A_2}}a^\dagger_{i_A}c^2}{\sqrt{2}}-\frac{\sqrt{s}\cos(\theta)a_{i_A}a_{i_{B_1}}\lambda_{i_{A_2}}a^\dagger_{i_A}c^2}{\sqrt{2}}-\\
&\frac{\sqrt{s}\cos(\theta)\sin(\theta)a_{i_A}a_{i_{B_2}}\lambda_{i_{A_2}}a^\dagger_{i_A}c^2}{\sqrt{2}}+\frac{\sqrt{s}\cos(\theta)\sin(\theta)a_{i_A}a_{i_{B_3}}\lambda_{i_{A_2}}a^\dagger_{i_A}c^2}{\sqrt{2}}-\\
&\frac{\sqrt{s}\cos(\theta)\sin(\theta)a_{i_A}a_{i_B}\lambda_{i_{A_3}}a^\dagger_{i_A}c^2}{\sqrt{2}}+\frac{\sqrt{s}\cos(\theta)a_{i_A}a_{i_{B_1}}\lambda_{i_{A_3}}a^\dagger_{i_A}c^2}{\sqrt{2}}+\\
&\frac{\sqrt{s}\cos(\theta)\sin(\theta)a_{i_A}a_{i_{B_2}}\lambda_{i_{A_3}}a^\dagger_{i_A}c^2}{\sqrt{2}}-\frac{\sqrt{s}\cos(\theta)\sin(\theta)a_{i_A}a_{i_{B_3}}\lambda_{i_{A_3}}a^\dagger_{i_A}c^2}{\sqrt{2}}+\\
&\frac{1}{2}s\sin^2(\theta)a_{i_A}a^\dagger_{i_B}c^2-\frac{1}{2}s\sin^2(\theta)a_{i_{A_1}}a^\dagger_{i_B}c^2-\frac{1}{2}s\sin^2(\theta)a_{i_{A_2}}a^\dagger_{i_B}c^2+\frac{1}{2}s\sin^2(\theta)a_{i_{A_3}}a^\dagger_{i_B}c^2-\\
&\frac{\sqrt{s}\cos(\theta)\sin(\theta)a_{i_A}a_{i_B}\lambda_{i_B}a^\dagger_{i_B}c^2}{\sqrt{2}}+\frac{\sqrt{s}\cos(\theta)\sin(\theta)a_{i_B}a_{i_{A_1}}\lambda_{i_B}a^\dagger_{i_B}c^2}{\sqrt{2}}+\\
&\frac{\sqrt{s}\cos(\theta)\sin(\theta)a_{i_B}a_{i_{A_2}}\lambda_{i_B}a^\dagger_{i_B}c^2}{\sqrt{2}}-\frac{\sqrt{s}\cos(\theta)\sin(\theta)a_{i_B}a_{i_{A_3}}\lambda_{i_B}a^\dagger_{i_B}c^2}{\sqrt{2}}+\\
&\frac{1}{2}s\sin^2(\theta)a^\dagger_{i_A}a^\dagger_{i_B}c^2-\frac{\sqrt{s}\cos(\theta)\sin(\theta)a_{i_A}\lambda_{i_A}a^\dagger_{i_A}a^\dagger_{i_B}c^2}{\sqrt{2}}-\\
&\frac{\sqrt{s}\cos(\theta)\sin(\theta)a_{i_B}\lambda_{i_B}a^\dagger_{i_A}a^\dagger_{i_B}c^2}{\sqrt{2}}+\cos^2(\theta)a_{i_A}a_{i_B}\lambda_{i_A}\lambda_{i_B}a^\dagger_{i_A}a^\dagger_{i_B}c^2+\\
&\frac{\sqrt{s}\cos(\theta)\sin(\theta)a_{i_A}\lambda_{i_{A_1}}a^\dagger_{i_A}a^\dagger_{i_B}c^2}{\sqrt{2}}-\cos^2(\theta)a_{i_A}a_{i_B}\lambda_{i_B}\lambda_{i_{A_1}}a^\dagger_{i_A}a^\dagger_{i_B}c^2+\\
&\frac{\sqrt{s}\cos(\theta)\sin(\theta)a_{i_A}\lambda_{i_{A_2}}a^\dagger_{i_A}a^\dagger_{i_B}c^2}{\sqrt{2}}-\cos^2(\theta)a_{i_A}a_{i_B}\lambda_{i_B}\lambda_{i_{A_2}}a^\dagger_{i_A}a^\dagger_{i_B}c^2-
\end{aligned}
$$

$$\frac{\sqrt{s}\cos(\theta)\sin(\theta)a_{i_A}\lambda_{i_{A_3}}a^\dagger_{i_A}a^\dagger_{i_B}c^2}{\sqrt{2}}+\cos^2(\theta)a_{i_A}a_{i_B}\lambda_{i_B}\lambda_{i_{A_3}}a^\dagger_{i_A}a^\dagger_{i_B}c^2-\frac{1}{2}s\sin^2(\theta)a_{i_B}a^\dagger_{i_{A_1}}c^2+$$

$$\frac{1}{2}s\sin(\theta)a_{i_{B_1}}a^\dagger_{i_{A_1}}c^2+\frac{1}{2}s\sin^2(\theta)a_{i_{B_2}}a^\dagger_{i_{A_1}}c^2-\frac{1}{2}s\sin^2(\theta)a_{i_{B_3}}a^\dagger_{i_{A_1}}c^2-\frac{1}{2}s\sin^2(\theta)a^\dagger_{i_B}a^\dagger_{i_{A_1}}c^2+$$

$$\frac{\sqrt{s}\cos(\theta)\sin(\theta)a_{i_B}\lambda_{i_B}a^\dagger_{i_B}a^\dagger_{i_{A_1}}c^2}{\sqrt{2}}-\frac{1}{2}s\sin^2(\theta)a_{i_B}a^\dagger_{i_{A_2}}c^2+\frac{1}{2}s\sin(\theta)a_{i_{B_1}}a^\dagger_{i_{A_2}}c^2+$$

$$\frac{1}{2}s\sin^2(\theta)a_{i_{B_2}}a^\dagger_{i_{A_2}}c^2-\frac{1}{2}s\sin^2(\theta)a_{i_{B_3}}a^\dagger_{i_{A_2}}c^2-\frac{1}{2}s\sin^2(\theta)a^\dagger_{i_B}a^\dagger_{i_{A_2}}c^2+$$

$$\frac{\sqrt{s}\cos(\theta)\sin(\theta)a_{i_B}\lambda_{i_B}a^\dagger_{i_B}a^\dagger_{i_{A_2}}c^2}{\sqrt{2}}+\frac{1}{2}s\sin^2(\theta)a_{i_B}a^\dagger_{i_{A_3}}c^2-\frac{1}{2}s\sin(\theta)a_{i_{B_1}}a^\dagger_{i_{A_3}}c^2-$$

$$\frac{1}{2}s\sin^2(\theta)a_{i_{B_2}}a^\dagger_{i_{A_3}}c^2+\frac{1}{2}s\sin^2(\theta)a_{i_{B_3}}a^\dagger_{i_{A_3}}c^2+\frac{1}{2}s\sin^2(\theta)a^\dagger_{i_B}a^\dagger_{i_{A_3}}c^2-$$

$$\frac{\sqrt{s}\cos(\theta)\sin(\theta)a_{i_B}\lambda_{i_B}a^\dagger_{i_B}a^\dagger_{i_{A_3}}c^2}{\sqrt{2}}-\frac{1}{2}s\sin(\theta)a_{i_A}a^\dagger_{i_{B_1}}c^2+\frac{1}{2}s\sin(\theta)a_{i_{A_1}}a^\dagger_{i_{B_1}}c^2+$$

$$\frac{1}{2}s\sin(\theta)a_{i_{A_2}}a^\dagger_{i_{B_1}}c^2-\frac{1}{2}s\sin(\theta)a_{i_{A_3}}a^\dagger_{i_{B_1}}c^2+\frac{\sqrt{s}\cos(\theta)\sin(\theta)a_{i_A}a_{i_{B_1}}\lambda_{i_{B_1}}a^\dagger_{i_{B_1}}c^2}{\sqrt{2}}-$$

$$\frac{\sqrt{s}\cos(\theta)\sin(\theta)a_{i_{A_1}}a_{i_{B_1}}\lambda_{i_{B_1}}a^\dagger_{i_{B_1}}c^2}{\sqrt{2}}-\frac{\sqrt{s}\cos(\theta)\sin(\theta)a_{i_{A_2}}a_{i_{B_1}}\lambda_{i_{B_1}}a^\dagger_{i_{B_1}}c^2}{\sqrt{2}}+$$

$$\frac{\sqrt{s}\cos(\theta)\sin(\theta)a_{i_{A_3}}a_{i_{B_1}}\lambda_{i_{B_1}}a^\dagger_{i_{B_1}}c^2}{\sqrt{2}}-\frac{1}{2}s\sin(\theta)a^\dagger_{i_A}a^\dagger_{i_{B_1}}c^2+\frac{\sqrt{s}\cos(\theta)a_{i_A}\lambda_{i_A}a^\dagger_{i_A}a^\dagger_{i_{B_1}}c^2}{\sqrt{2}}-$$

$$\frac{\sqrt{s}\cos(\theta)a_{i_A}\lambda_{i_{A_1}}a^\dagger_{i_A}a^\dagger_{i_{B_1}}c^2}{\sqrt{2}}-\frac{\sqrt{s}\cos(\theta)a_{i_A}\lambda_{i_{A_2}}a^\dagger_{i_A}a^\dagger_{i_{B_1}}c^2}{\sqrt{2}}+\frac{\sqrt{s}\cos(\theta)a_{i_A}\lambda_{i_{A_3}}a^\dagger_{i_A}a^\dagger_{i_{B_1}}c^2}{\sqrt{2}}+$$

$$\frac{\sqrt{s}\cos(\theta)\sin(\theta)a_{i_{B_1}}\lambda_{i_{B_1}}a^\dagger_{i_A}a^\dagger_{i_{B_1}}c^2}{\sqrt{2}}-\cos^2(\theta)a_{i_A}a_{i_{B_1}}\lambda_{i_A}\lambda_{i_{B_1}}a^\dagger_{i_A}a^\dagger_{i_{B_1}}c^2+$$

$$\cos^2(\theta)a_{i_A}a_{i_{B_1}}\lambda_{i_{A_1}}\lambda_{i_{B_1}}a^\dagger_{i_A}a^\dagger_{i_{B_1}}c^2+\cos^2(\theta)a_{i_A}a_{i_{B_1}}\lambda_{i_{A_2}}\lambda_{i_{B_1}}a^\dagger_{i_A}a^\dagger_{i_{B_1}}c^2-$$

$$\cos^2(\theta)a_{i_A}a_{i_{B_1}}\lambda_{i_{A_3}}\lambda_{i_{B_1}}a^\dagger_{i_A}a^\dagger_{i_{B_1}}c^2+\frac{1}{2}s\sin(\theta)a^\dagger_{i_{A_1}}a^\dagger_{i_{B_1}}c^2-$$

$$\frac{\sqrt{s}\cos(\theta)\sin(\theta)a_{i_{B_1}}\lambda_{i_{B_1}}a^\dagger_{i_{A_1}}a^\dagger_{i_{B_1}}c^2}{\sqrt{2}}+\frac{1}{2}s\sin(\theta)a^\dagger_{i_{A_2}}a^\dagger_{i_{B_1}}c^2-$$

$$\frac{\sqrt{s}\cos(\theta)\sin(\theta)a_{i_{B_1}}\lambda_{i_{B_1}}a^\dagger_{i_{A_2}}a^\dagger_{i_{B_1}}c^2}{\sqrt{2}}-\frac{1}{2}s\sin(\theta)a^\dagger_{i_{A_3}}a^\dagger_{i_{B_1}}c^2+$$

$$\frac{\sqrt{s}\cos(\theta)\sin(\theta)a_{i_{B_1}}\lambda_{i_{B_1}}a^\dagger_{i_{A_3}}a^\dagger_{i_{B_1}}c^2}{\sqrt{2}}-\frac{1}{2}s\sin^2(\theta)a_{i_A}a^\dagger_{i_{B_2}}c^2+\frac{1}{2}s\sin^2(\theta)a_{i_{A_1}}a^\dagger_{i_{B_2}}c^2+$$

$$\frac{1}{2}s\sin^2(\theta)a_{i_{A_2}}a^\dagger_{i_{B_2}}c^2-\frac{1}{2}s\sin^2(\theta)a_{i_{A_3}}a^\dagger_{i_{B_2}}c^2+\frac{\sqrt{s}\cos(\theta)\sin(\theta)a_{i_A}a_{i_{B_2}}\lambda_{i_{B_2}}a^\dagger_{i_{B_2}}c^2}{\sqrt{2}}-$$

$$\frac{\sqrt{s}\cos(\theta)\sin(\theta)a_{i_{A_1}}a_{i_{B_2}}\lambda_{i_{B_2}}a^\dagger_{i_{B_2}}c^2}{\sqrt{2}}-\frac{\sqrt{s}\cos(\theta)\sin(\theta)a_{i_{A_2}}a_{i_{B_2}}\lambda_{i_{B_2}}a^\dagger_{i_{B_2}}c^2}{\sqrt{2}}+$$

$$\frac{\sqrt{s}\cos(\theta)\sin(\theta)a_{i_{A_3}}a_{i_{B_2}}\lambda_{i_{B_2}}a^\dagger_{i_{B_2}}c^2}{\sqrt{2}}-\frac{1}{2}s\sin^2(\theta)a^\dagger_{i_A}a^\dagger_{i_{B_2}}c^2+$$

$$\frac{\sqrt{s}\cos(\theta)\sin(\theta)a_{i_A}\lambda_{i_A}a^\dagger_{i_A}a^\dagger_{i_{B_2}}c^2}{\sqrt{2}}-\frac{\sqrt{s}\cos(\theta)\sin(\theta)a_{i_A}\lambda_{i_{A_1}}a^\dagger_{i_A}a^\dagger_{i_{B_2}}c^2}{\sqrt{2}}-$$

$$\frac{\sqrt{s}\cos(\theta)\sin(\theta)a_{i_A}\lambda_{i_{A_2}}a^\dagger_{i_A}a^\dagger_{i_{B_2}}c^2}{\sqrt{2}}+\frac{\sqrt{s}\cos(\theta)\sin(\theta)a_{i_A}\lambda_{i_{A_3}}a^\dagger_{i_A}a^\dagger_{i_{B_2}}c^2}{\sqrt{2}}+$$

$$\frac{\sqrt{s}\cos(\theta)\sin(\theta)a_{i_{B_2}}\lambda_{i_{B_2}}a^\dagger_{i_A}a^\dagger_{i_{B_2}}c^2}{\sqrt{2}}-\cos^2(\theta)a_{i_A}a_{i_{B_2}}\lambda_{i_A}\lambda_{i_{B_2}}a^\dagger_{i_A}a^\dagger_{i_{B_2}}c^2+$$

$$\cos^2(\theta)a_{i_A}a_{i_{B_2}}\lambda_{i_{A_1}}\lambda_{i_{B_2}}a^\dagger_{i_A}a^\dagger_{i_{B_2}}c^2+\cos^2(\theta)a_{i_A}a_{i_{B_2}}\lambda_{i_{A_2}}\lambda_{i_{B_2}}a^\dagger_{i_A}a^\dagger_{i_{B_2}}c^2-$$
$$\cos^2(\theta)a_{i_A}a_{i_{B_2}}\lambda_{i_{A_3}}\lambda_{i_{B_2}}a^\dagger_{i_A}a^\dagger_{i_{B_2}}c^2+\frac{1}{2}s\sin^2(\theta)a^\dagger_{i_{A_1}}a^\dagger_{i_{B_2}}c^2-$$
$$\frac{\sqrt{s}\cos(\theta)\sin(\theta)a_{i_{B_2}}\lambda_{i_{B_2}}a^\dagger_{i_{A_1}}a^\dagger_{i_{B_2}}c^2}{\sqrt{2}}+\frac{1}{2}s\sin^2(\theta)a^\dagger_{i_{A_2}}a^\dagger_{i_{B_2}}c^2-$$
$$\frac{\sqrt{s}\cos(\theta)\sin(\theta)a_{i_{B_2}}\lambda_{i_{B_2}}a^\dagger_{i_{A_2}}a^\dagger_{i_{B_2}}c^2}{\sqrt{2}}-\frac{1}{2}s\sin^2(\theta)a^\dagger_{i_{A_3}}a^\dagger_{i_{B_2}}c^2+$$
$$\frac{\sqrt{s}\cos(\theta)\sin(\theta)a_{i_{B_2}}\lambda_{i_{B_2}}a^\dagger_{i_{A_3}}a^\dagger_{i_{B_2}}c^2}{\sqrt{2}}+\frac{1}{2}s\sin^2(\theta)a_{i_A}a^\dagger_{i_{B_3}}c^2-\frac{1}{2}s\sin^2(\theta)a_{i_{A_1}}a^\dagger_{i_{B_3}}c^2-$$
$$\frac{1}{2}s\sin^2(\theta)a_{i_{A_2}}a^\dagger_{i_{B_3}}c^2+\frac{1}{2}s\sin^2(\theta)a_{i_{A_3}}a^\dagger_{i_{B_3}}c^2-\frac{\sqrt{s}\cos(\theta)\sin(\theta)a_{i_A}a_{i_{B_3}}\lambda_{i_{B_3}}a^\dagger_{i_{B_3}}c^2}{\sqrt{2}}+$$
$$\frac{\sqrt{s}\cos(\theta)\sin(\theta)a_{i_{A_1}}a_{i_{B_3}}\lambda_{i_{B_3}}a^\dagger_{i_{B_3}}c^2}{\sqrt{2}}+\frac{\sqrt{s}\cos(\theta)\sin(\theta)a_{i_{A_2}}a_{i_{B_3}}\lambda_{i_{B_3}}a^\dagger_{i_{B_3}}c^2}{\sqrt{2}}-$$
$$\frac{\sqrt{s}\cos(\theta)\sin(\theta)a_{i_{A_3}}a_{i_{B_3}}\lambda_{i_{B_3}}a^\dagger_{i_{B_3}}c^2}{\sqrt{2}}+\frac{1}{2}s\sin^2(\theta)a^\dagger_{i_A}a^\dagger_{i_{B_3}}c^2-$$
$$\frac{\sqrt{s}\cos(\theta)\sin(\theta)a_{i_A}\lambda_{i_A}a^\dagger_{i_A}a^\dagger_{i_{B_3}}c^2}{\sqrt{2}}+\frac{\sqrt{s}\cos(\theta)\sin(\theta)a_{i_A}\lambda_{i_{A_1}}a^\dagger_{i_A}a^\dagger_{i_{B_3}}c^2}{\sqrt{2}}+$$
$$\frac{\sqrt{s}\cos(\theta)\sin(\theta)a_{i_A}\lambda_{i_{A_2}}a^\dagger_{i_A}a^\dagger_{i_{B_3}}c^2}{\sqrt{2}}-\frac{\sqrt{s}\cos(\theta)\sin(\theta)a_{i_A}\lambda_{i_{A_3}}a^\dagger_{i_A}a^\dagger_{i_{B_3}}c^2}{\sqrt{2}}-$$
$$\frac{\sqrt{s}\cos(\theta)\sin(\theta)a_{i_{B_3}}\lambda_{i_{B_3}}a^\dagger_{i_A}a^\dagger_{i_{B_3}}c^2}{\sqrt{2}}+\cos^2(\theta)a_{i_A}a_{i_{B_3}}\lambda_{i_A}\lambda_{i_{B_3}}a^\dagger_{i_A}a^\dagger_{i_{B_3}}c^2-$$
$$\cos^2(\theta)a_{i_A}a_{i_{B_3}}\lambda_{i_{A_1}}\lambda_{i_{B_3}}a^\dagger_{i_A}a^\dagger_{i_{B_3}}c^2-\cos^2(\theta)a_{i_A}a_{i_{B_3}}\lambda_{i_{A_2}}\lambda_{i_{B_3}}a^\dagger_{i_A}a^\dagger_{i_{B_3}}c^2+$$
$$\cos^2(\theta)a_{i_A}a_{i_{B_3}}\lambda_{i_{A_3}}\lambda_{i_{B_3}}a^\dagger_{i_A}a^\dagger_{i_{B_3}}c^2-\frac{1}{2}s\sin^2(\theta)a^\dagger_{i_{A_1}}a^\dagger_{i_{B_3}}c^2+$$
$$\frac{\sqrt{s}\cos(\theta)\sin(\theta)a_{i_{B_3}}\lambda_{i_{B_3}}a^\dagger_{i_{A_1}}a^\dagger_{i_{B_3}}c^2}{\sqrt{2}}-\frac{1}{2}s\sin^2(\theta)a^\dagger_{i_{A_2}}a^\dagger_{i_{B_3}}c^2+$$
$$\frac{\sqrt{s}\cos(\theta)\sin(\theta)a_{i_{B_3}}\lambda_{i_{B_3}}a^\dagger_{i_{A_2}}a^\dagger_{i_{B_3}}c^2}{\sqrt{2}}+\frac{1}{2}s\sin^2(\theta)a^\dagger_{i_{A_3}}a^\dagger_{i_{B_3}}c^2-$$
$$\frac{\sqrt{s}\cos(\theta)\sin(\theta)a_{i_{B_3}}\lambda_{i_{B_3}}a^\dagger_{i_{A_3}}a^\dagger_{i_{B_3}}c^2}{\sqrt{2}}+\frac{s^{3/2}\cos(\theta)\sin(\theta)a_{i_B}\lambda_{i_A}c}{\sqrt{2}}-\frac{s^{3/2}\cos(\theta)a_{i_{B_1}}\lambda_{i_A}c}{\sqrt{2}}-$$
$$\frac{s^{3/2}\cos(\theta)\sin(\theta)a_{i_{B_2}}\lambda_{i_A}c}{\sqrt{2}}+\frac{s^{3/2}\cos(\theta)\sin(\theta)a_{i_{B_3}}\lambda_{i_A}c}{\sqrt{2}}+\frac{s^{3/2}\cos(\theta)\sin(\theta)a_{i_A}\lambda_{i_B}c}{\sqrt{2}}-$$
$$\frac{s^{3/2}\cos(\theta)\sin(\theta)a_{i_{A_1}}\lambda_{i_B}c}{\sqrt{2}}-\frac{s^{3/2}\cos(\theta)\sin(\theta)a_{i_{A_2}}\lambda_{i_B}c}{\sqrt{2}}+\frac{s^{3/2}\cos(\theta)\sin(\theta)a_{i_{A_3}}\lambda_{i_B}c}{\sqrt{2}}-$$
$$\frac{s^{3/2}\cos(\theta)\sin(\theta)a_{i_B}\lambda_{i_{A_1}}c}{\sqrt{2}}+\frac{s^{3/2}\cos(\theta)a_{i_{B_1}}\lambda_{i_{A_1}}c}{\sqrt{2}}+\frac{s^{3/2}\cos(\theta)\sin(\theta)a_{i_{B_2}}\lambda_{i_{A_1}}c}{\sqrt{2}}-$$
$$\frac{s^{3/2}\cos(\theta)\sin(\theta)a_{i_{B_3}}\lambda_{i_{A_1}}c}{\sqrt{2}}-\frac{s^{3/2}\cos(\theta)\sin(\theta)a_{i_B}\lambda_{i_{A_2}}c}{\sqrt{2}}+\frac{s^{3/2}\cos(\theta)a_{i_{B_1}}\lambda_{i_{A_2}}c}{\sqrt{2}}+$$
$$\frac{s^{3/2}\cos(\theta)\sin(\theta)a_{i_{B_2}}\lambda_{i_{A_2}}c}{\sqrt{2}}-\frac{s^{3/2}\cos(\theta)\sin(\theta)a_{i_{B_3}}\lambda_{i_{A_2}}c}{\sqrt{2}}+\frac{s^{3/2}\cos(\theta)\sin(\theta)a_{i_B}\lambda_{i_{A_3}}c}{\sqrt{2}}-$$
$$\frac{s^{3/2}\cos(\theta)a_{i_{B_1}}\lambda_{i_{A_3}}c}{\sqrt{2}}-\frac{s^{3/2}\cos(\theta)\sin(\theta)a_{i_{B_2}}\lambda_{i_{A_3}}c}{\sqrt{2}}+\frac{s^{3/2}\cos(\theta)\sin(\theta)a_{i_{B_3}}\lambda_{i_{A_3}}c}{\sqrt{2}}-$$
$$\frac{s^{3/2}\cos(\theta)\sin(\theta)a_{i_A}\lambda_{i_{B_1}}c}{\sqrt{2}}+\frac{s^{3/2}\cos(\theta)\sin(\theta)a_{i_{A_1}}\lambda_{i_{B_1}}c}{\sqrt{2}}+\frac{s^{3/2}\cos(\theta)\sin(\theta)a_{i_{A_2}}\lambda_{i_{B_1}}c}{\sqrt{2}}-$$

$$\frac{s^{3/2}\cos(\theta)\sin(\theta)a_{i_{A_3}}\lambda_{i_{B_1}}c}{\sqrt{2}}-\frac{s^{3/2}\cos(\theta)\sin(\theta)a_{i_A}\lambda_{i_{B_2}}c}{\sqrt{2}}+\frac{s^{3/2}\cos(\theta)\sin(\theta)a_{i_{A_1}}\lambda_{i_{B_2}}c}{\sqrt{2}}+$$

$$\frac{s^{3/2}\cos(\theta)\sin(\theta)a_{i_{A_2}}\lambda_{i_{B_2}}c}{\sqrt{2}}-\frac{s^{3/2}\cos(\theta)\sin(\theta)a_{i_{A_3}}\lambda_{i_{B_2}}c}{\sqrt{2}}+\frac{s^{3/2}\cos(\theta)\sin(\theta)a_{i_A}\lambda_{i_{B_3}}c}{\sqrt{2}}-$$

$$\frac{s^{3/2}\cos(\theta)\sin(\theta)a_{i_{A_1}}\lambda_{i_{B_3}}c}{\sqrt{2}}-\frac{s^{3/2}\cos(\theta)\sin(\theta)a_{i_{A_2}}\lambda_{i_{B_3}}c}{\sqrt{2}}+\frac{s^{3/2}\cos(\theta)\sin(\theta)a_{i_{A_3}}\lambda_{i_{B_3}}c}{\sqrt{2}}+$$

$$\frac{s^{3/2}\cos(\theta)\sin(\theta)\lambda_{i_B}a^{\dagger}_{i_A}c}{\sqrt{2}}-s\cos^2(\theta)a_{i_A}\lambda_{i_A}\lambda_{i_B}a^{\dagger}_{i_A}c+s\cos^2(\theta)a_{i_A}\lambda_{i_B}\lambda_{i_{A_1}}a^{\dagger}_{i_A}c+$$

$$s\cos^2(\theta)a_{i_A}\lambda_{i_B}\lambda_{i_{A_2}}a^{\dagger}_{i_A}c-s\cos^2(\theta)a_{i_A}\lambda_{i_B}\lambda_{i_{A_3}}a^{\dagger}_{i_A}c-\frac{s^{3/2}\cos(\theta)\sin(\theta)\lambda_{i_{B_1}}a^{\dagger}_{i_A}c}{\sqrt{2}}+$$

$$s\cos^2(\theta)a_{i_A}\lambda_{i_A}\lambda_{i_{B_1}}a^{\dagger}_{i_A}c-s\cos^2(\theta)a_{i_A}\lambda_{i_{A_1}}\lambda_{i_{B_1}}a^{\dagger}_{i_A}c-s\cos^2(\theta)a_{i_A}\lambda_{i_{A_2}}\lambda_{i_{B_1}}a^{\dagger}_{i_A}c+$$

$$s\cos^2(\theta)a_{i_A}\lambda_{i_{A_3}}\lambda_{i_{B_1}}a^{\dagger}_{i_A}c-\frac{s^{3/2}\cos(\theta)\sin(\theta)\lambda_{i_{B_2}}a^{\dagger}_{i_A}c}{\sqrt{2}}+s\cos^2(\theta)a_{i_A}\lambda_{i_A}\lambda_{i_{B_2}}a^{\dagger}_{i_A}c-$$

$$s\cos^2(\theta)a_{i_A}\lambda_{i_{A_1}}\lambda_{i_{B_2}}a^{\dagger}_{i_A}c-s\cos^2(\theta)a_{i_A}\lambda_{i_{A_2}}\lambda_{i_{B_2}}a^{\dagger}_{i_A}c+s\cos^2(\theta)a_{i_A}\lambda_{i_{A_3}}\lambda_{i_{B_2}}a^{\dagger}_{i_A}c+$$

$$\frac{s^{3/2}\cos(\theta)\sin(\theta)\lambda_{i_{B_3}}a^{\dagger}_{i_A}c}{\sqrt{2}}-s\cos^2(\theta)a_{i_A}\lambda_{i_A}\lambda_{i_{B_3}}a^{\dagger}_{i_A}c+s\cos^2(\theta)a_{i_A}\lambda_{i_{A_1}}\lambda_{i_{B_3}}a^{\dagger}_{i_A}c+$$

$$s\cos^2(\theta)a_{i_A}\lambda_{i_{A_2}}\lambda_{i_{B_3}}a^{\dagger}_{i_A}c-s\cos^2(\theta)a_{i_A}\lambda_{i_{A_3}}\lambda_{i_{B_3}}a^{\dagger}_{i_A}c+\frac{s^{3/2}\cos(\theta)\sin(\theta)\lambda_{i_A}a^{\dagger}_{i_B}c}{\sqrt{2}}-$$

$$s\cos^2(\theta)a_{i_B}\lambda_{i_A}\lambda_{i_B}a^{\dagger}_{i_B}c-\frac{s^{3/2}\cos(\theta)\sin(\theta)\lambda_{i_{A_1}}a^{\dagger}_{i_B}c}{\sqrt{2}}+s\cos^2(\theta)a_{i_B}\lambda_{i_B}\lambda_{i_{A_1}}a^{\dagger}_{i_B}c-$$

$$\frac{s^{3/2}\cos(\theta)\sin(\theta)\lambda_{i_{A_2}}a^{\dagger}_{i_B}c}{\sqrt{2}}+s\cos^2(\theta)a_{i_B}\lambda_{i_B}\lambda_{i_{A_2}}a^{\dagger}_{i_B}c+\frac{s^{3/2}\cos(\theta)\sin(\theta)\lambda_{i_{A_3}}a^{\dagger}_{i_B}c}{\sqrt{2}}-$$

$$s\cos^2(\theta)a_{i_B}\lambda_{i_B}\lambda_{i_{A_3}}a^{\dagger}_{i_B}c-\frac{s^{3/2}\cos(\theta)\sin(\theta)\lambda_{i_B}a^{\dagger}_{i_{A_1}}c}{\sqrt{2}}+\frac{s^{3/2}\cos(\theta)\sin(\theta)\lambda_{i_{B_1}}a^{\dagger}_{i_{A_1}}c}{\sqrt{2}}+$$

$$\frac{s^{3/2}\cos(\theta)\sin(\theta)\lambda_{i_{B_2}}a^{\dagger}_{i_{A_1}}c}{\sqrt{2}}-\frac{s^{3/2}\cos(\theta)\sin(\theta)\lambda_{i_{B_3}}a^{\dagger}_{i_{A_1}}c}{\sqrt{2}}-\frac{s^{3/2}\cos(\theta)\sin(\theta)\lambda_{i_B}a^{\dagger}_{i_{A_2}}c}{\sqrt{2}}+$$

$$\frac{s^{3/2}\cos(\theta)\sin(\theta)\lambda_{i_{B_1}}a^{\dagger}_{i_{A_2}}c}{\sqrt{2}}+\frac{s^{3/2}\cos(\theta)\sin(\theta)\lambda_{i_{B_2}}a^{\dagger}_{i_{A_2}}c}{\sqrt{2}}-\frac{s^{3/2}\cos(\theta)\sin(\theta)\lambda_{i_{B_3}}a^{\dagger}_{i_{A_2}}c}{\sqrt{2}}+$$

$$\frac{s^{3/2}\cos(\theta)\sin(\theta)\lambda_{i_B}a^{\dagger}_{i_{A_3}}c}{\sqrt{2}}-\frac{s^{3/2}\cos(\theta)\sin(\theta)\lambda_{i_{B_1}}a^{\dagger}_{i_{A_3}}c}{\sqrt{2}}-\frac{s^{3/2}\cos(\theta)\sin(\theta)\lambda_{i_{B_2}}a^{\dagger}_{i_{A_3}}c}{\sqrt{2}}+$$

$$\frac{s^{3/2}\cos(\theta)\sin(\theta)\lambda_{i_{B_3}}a^{\dagger}_{i_{A_3}}c}{\sqrt{2}}-\frac{s^{3/2}\cos(\theta)\lambda_{i_A}a^{\dagger}_{i_{B_1}}c}{\sqrt{2}}+\frac{s^{3/2}\cos(\theta)\lambda_{i_{A_1}}a^{\dagger}_{i_{B_1}}c}{\sqrt{2}}+$$

$$\frac{s^{3/2}\cos(\theta)\lambda_{i_{A_2}}a^{\dagger}_{i_{B_1}}c}{\sqrt{2}}-\frac{s^{3/2}\cos(\theta)\lambda_{i_{A_3}}a^{\dagger}_{i_{B_1}}c}{\sqrt{2}}+s\cos^2(\theta)a_{i_{B_1}}\lambda_{i_A}\lambda_{i_{B_1}}a^{\dagger}_{i_{B_1}}c-$$

$$s\cos^2(\theta)a_{i_{B_1}}\lambda_{i_{A_1}}\lambda_{i_{B_1}}a^{\dagger}_{i_{B_1}}c-s\cos^2(\theta)a_{i_{B_1}}\lambda_{i_{A_2}}\lambda_{i_{B_1}}a^{\dagger}_{i_{B_1}}c+s\cos^2(\theta)a_{i_{B_1}}\lambda_{i_{A_3}}\lambda_{i_{B_1}}a^{\dagger}_{i_{B_1}}c-$$

$$\frac{s^{3/2}\cos(\theta)\sin(\theta)\lambda_{i_A}a^{\dagger}_{i_{B_2}}c}{\sqrt{2}}+\frac{s^{3/2}\cos(\theta)\sin(\theta)\lambda_{i_{A_1}}a^{\dagger}_{i_{B_2}}c}{\sqrt{2}}+\frac{s^{3/2}\cos(\theta)\sin(\theta)\lambda_{i_{A_2}}a^{\dagger}_{i_{B_2}}c}{\sqrt{2}}-$$

$$\frac{s^{3/2}\cos(\theta)\sin(\theta)\lambda_{i_{A_3}}a^{\dagger}_{i_{B_2}}c}{\sqrt{2}}+s\cos^2(\theta)a_{i_{B_2}}\lambda_{i_A}\lambda_{i_{B_2}}a^{\dagger}_{i_{B_2}}c-s\cos^2(\theta)a_{i_{B_2}}\lambda_{i_{A_1}}\lambda_{i_{B_2}}a^{\dagger}_{i_{B_2}}c-$$

$$s\cos^2(\theta)a_{i_{B_2}}\lambda_{i_{A_2}}\lambda_{i_{B_2}}a^{\dagger}_{i_{B_2}}c+s\cos^2(\theta)a_{i_{B_2}}\lambda_{i_{A_3}}\lambda_{i_{B_2}}a^{\dagger}_{i_{B_2}}c+\frac{s^{3/2}\cos(\theta)\sin(\theta)\lambda_{i_A}a^{\dagger}_{i_{B_3}}c}{\sqrt{2}}-$$

$$\frac{s^{3/2}\cos(\theta)\sin(\theta)\lambda_{i_{A_1}}a^{\dagger}_{i_{B_3}}c}{\sqrt{2}}-\frac{s^{3/2}\cos(\theta)\sin(\theta)\lambda_{i_{A_2}}a^{\dagger}_{i_{B_3}}c}{\sqrt{2}}+\frac{s^{3/2}\cos(\theta)\sin(\theta)\lambda_{i_{A_3}}a^{\dagger}_{i_{B_3}}c}{\sqrt{2}}-$$

$$
\begin{aligned}
&s\cos^2(\theta)a_{i_{B_3}}\lambda_{i_A}\lambda_{i_{B_3}}a^\dagger_{i_{B_3}}c + s\cos^2(\theta)a_{i_{B_3}}\lambda_{i_{A_1}}\lambda_{i_{B_3}}a^\dagger_{i_{B_3}}c + s\cos^2(\theta)a_{i_{B_3}}\lambda_{i_{A_2}}\lambda_{i_{B_3}}a^\dagger_{i_{B_3}}c - \\
&s\cos^2(\theta)a_{i_{B_3}}\lambda_{i_{A_3}}\lambda_{i_{B_3}}a^\dagger_{i_{B_3}}c + s^2\cos^2(\theta)\lambda_{i_A}\lambda_{i_B} - s^2\cos^2(\theta)\lambda_{i_B}\lambda_{i_{A_1}} - s^2\cos^2(\theta)\lambda_{i_B}\lambda_{i_{A_2}} + \\
&s^2\cos^2(\theta)\lambda_{i_B}\lambda_{i_{A_3}} - s^2\cos^2(\theta)\lambda_{i_A}\lambda_{i_{B_1}} + s^2\cos^2(\theta)\lambda_{i_{A_1}}\lambda_{i_{B_1}} + s^2\cos^2(\theta)\lambda_{i_{A_2}}\lambda_{i_{B_1}} - \\
&s^2\cos^2(\theta)\lambda_{i_{A_3}}\lambda_{i_{B_1}} - s^2\cos^2(\theta)\lambda_{i_A}\lambda_{i_{B_2}} + s^2\cos^2(\theta)\lambda_{i_{A_1}}\lambda_{i_{B_2}} + s^2\cos^2(\theta)\lambda_{i_{A_2}}\lambda_{i_{B_2}} - \\
&s^2\cos^2(\theta)\lambda_{i_{A_3}}\lambda_{i_{B_2}} + s^2\cos^2(\theta)\lambda_{i_A}\lambda_{i_{B_3}} - s^2\cos^2(\theta)\lambda_{i_{A_1}}\lambda_{i_{B_3}} - s^2\cos^2(\theta)\lambda_{i_{A_2}}\lambda_{i_{B_3}} + \\
&s^2\cos^2(\theta)\lambda_{i_{A_3}}\lambda_{i_{B_3}}\Bigg).
\end{aligned}
$$

Clearly, looking at the equation one can see that the Hamiltonian has terms that go upto an order of 8 in the terms of interaction of bosons, that is to say, it contains terms such as, $aa^\dagger a^\dagger aaa^\dagger a^\dagger a$. However, here, we approximate the Hamiltonian by only considering the terms upto bilinear order (aa or $a^\dagger a$). After this approximation, the Hamiltonian reduces to,

$$
\begin{aligned}
\mathcal{H}_{lf}^{ferro} \;=\; & \sum_i \frac{-J_0}{4}\Bigg(\frac{1}{2}s^3\cos^2(\theta)((a_{i_3}\sin^2(\theta)\lambda_{i_1}\lambda_{i_2}a^\dagger_i + a_{i_3}\sin^2(\theta)\lambda_i\lambda_{i_2}a^\dagger_{i_1} \\
& +a_i\sin^2(\theta)\lambda_{i_2}\lambda_{i_3}a^\dagger_{i_1} + \sin^2(\theta)\lambda_{i_2}\lambda_{i_3}a^\dagger_i a^\dagger_{i_1} \\
& +a_{i_3}\sin^2(\theta)\lambda_i\lambda_{i_1}a^\dagger_{i_2} + a_i\sin^2(\theta)\lambda_{i_1}\lambda_{i_3}a^\dagger_{i_2} + \sin^2(\theta)\lambda_{i_1}\lambda_{i_3}a^\dagger_i a^\dagger_{i_2} \\
& +\sin^2(\theta)\lambda_i\lambda_{i_3}a^\dagger_{i_1}a^\dagger_{i_2} + a_i\sin^2(\theta)\lambda_{i_1}\lambda_{i_2}a^\dagger_{i_3} \\
& +\sin^2(\theta)\lambda_{i_1}\lambda_{i_2}a^\dagger_i a^\dagger_{i_3} + \sin^2(\theta)\lambda_i\lambda_{i_2}a^\dagger_{i_1}a^\dagger_{i_3} \\
& +\sin^2(\theta)\lambda_i\lambda_{i_1}a^\dagger_{i_2}a^\dagger_{i_3} \\
& -2a_i\cos^2(\theta)\lambda_i\lambda_{i_1}\lambda_{i_2}\lambda_{i_3}a^\dagger_i - 2a_{i_3}\cos^2(\theta)\lambda_i\lambda_{i_1}\lambda_{i_2}\lambda_{i_3}a^\dagger_{i_3} \\
& +a_{i_2}((\sin^2(\theta)\lambda_{i_1}\lambda_{i_3}a^\dagger_i + \sin^2(\theta)\lambda_i\lambda_{i_3}a^\dagger_{i_1} + \sin^2(\theta)\lambda_i\lambda_{i_1}a^\dagger_{i_3} \\
& -2\cos^2(\theta)\lambda_i\lambda_{i_1}\lambda_{i_2}\lambda_{i_3}a^\dagger_{i_2} + a_{i_3}\sin^2(\theta)\lambda_i\lambda_{i_1} + a_{i_1}\sin^2(\theta)\lambda_i\lambda_{i_3} \\
& +a_i\sin^2(\theta)\lambda_{i_1}\lambda_{i_3}) + a_{i_1}((\sin^2(\theta)\lambda_{i_2}\lambda_{i_3}a^\dagger_i + \sin^2(\theta)\lambda_i\lambda_{i_3}a^\dagger_{i_2} \\
& +\sin^2(\theta)\lambda_i\lambda_{i_2}a^\dagger_{i_3} - 2\cos^2(\theta)\lambda_i\lambda_{i_1}\lambda_{i_2}\lambda_{i_3}a^\dagger_{i_1} + a_{i_3}\sin^2(\theta)\lambda_i\lambda_{i_2} \\
& +a_i\sin^2(\theta)\lambda_{i_2}\lambda_{i_3}) + a_i a_{i_3}\sin^2(\theta)\lambda_{i_1}\lambda_{i_2})\Bigg) \\
& +\sum_i \frac{J_1}{2}\Bigg(\frac{1}{2}s(-2a_{i_2}\cos^2(\theta)\lambda_i\lambda_{i_2}a^\dagger_{i_2} - 2a_{i_3}\cos^2(\theta)\lambda_{i_1}\lambda_{i_3}a^\dagger_{i_3} + a_i(-2\cos^2(\theta)\lambda_i\lambda_{i_2}a^\dagger_i \\
& +\sin^2(\theta)a^\dagger_{i_2} + a_{i_2}\sin^2(\theta)) + a_{i_1}(-2\cos^2(\theta)\lambda_{i_1}\lambda_{i_3}a^\dagger_{i_1} + \sin^2(\theta)a^\dagger_{i_3} \\
& +a_{i_3}\sin^2(\theta)) + a_{i_2}\sin^2(\theta)a^\dagger_i + a_{i_3}\sin^2(\theta)a^\dagger_{i_1} + \sin^2(\theta)a^\dagger_i a^\dagger_{i_2} + \sin^2(\theta)a^\dagger_{i_1}a^\dagger_{i_3})\Bigg)
\end{aligned}
$$

$$+\frac{J_2}{16}\Bigg(\frac{1}{2}s(2a_{i_{B_1}}\lambda_{i_A}\lambda_{i_{B_1}}a^\dagger_{i_{B_1}}\cos^2(\theta)-2a_{i_{B_1}}\lambda_{i_{A_1}}\lambda_{i_{B_1}}a^\dagger_{i_{B_1}}\cos^2(\theta)$$

$$-2a_{i_{B_1}}\lambda_{i_{A_2}}\lambda_{i_{B_1}}a^\dagger_{i_{B_1}}\cos^2(\theta)+2a_{i_{B_1}}\lambda_{i_{A_3}}\lambda_{i_{B_1}}a^\dagger_{i_{B_1}}\cos^2(\theta)$$

$$+2a_{i_{B_2}}\lambda_{i_A}\lambda_{i_{B_2}}a^\dagger_{i_{B_2}}\cos^2(\theta)-2a_{i_{B_2}}\lambda_{i_{A_1}}\lambda_{i_{B_2}}a^\dagger_{i_{B_2}}\cos^2(\theta)$$

$$-2a_{i_{B_2}}\lambda_{i_{A_2}}\lambda_{i_{B_2}}a^\dagger_{i_{B_2}}\cos^2(\theta)+2a_{i_{B_2}}\lambda_{i_{A_3}}\lambda_{i_{B_2}}a^\dagger_{i_{B_2}}\cos^2(\theta)$$

$$-2a_{i_{B_3}}\lambda_{i_A}\lambda_{i_{B_3}}a^\dagger_{i_{B_3}}\cos^2(\theta)+2a_{i_{B_3}}\lambda_{i_{A_1}}\lambda_{i_{B_3}}a^\dagger_{i_{B_3}}\cos^2(\theta)$$

$$+2a_{i_{B_3}}\lambda_{i_{A_2}}\lambda_{i_{B_3}}a^\dagger_{i_{B_3}}\cos^2(\theta)-2a_{i_{B_3}}\lambda_{i_{A_3}}\lambda_{i_{B_3}}a^\dagger_{i_{B_3}}\cos^2(\theta)+\sin(\theta)a_{i_{A_1}}a_{i_{B_1}}$$

$$+\sin(\theta)a_{i_{A_2}}a_{i_{B_1}}-\sin(\theta)a_{i_{A_3}}a_{i_{B_1}}+\sin^2(\theta)a_{i_{A_1}}a_{i_{B_2}}+\sin^2(\theta)a_{i_{A_2}}a_{i_{B_2}}-\sin^2(\theta)a_{i_{A_3}}a_{i_{B_2}}$$

$$-\sin^2(\theta)a_{i_{A_1}}a_{i_{B_3}}-\sin^2(\theta)a_{i_{A_2}}a_{i_{B_3}}+\sin^2(\theta)a_{i_{A_3}}a_{i_{B_3}}-\sin(\theta)a_{i_{B_1}}a^\dagger_{i_A}$$

$$-\sin^2(\theta)a_{i_{B_2}}a^\dagger_{i_A}+\sin^2(\theta)a_{i_{B_3}}a^\dagger_{i_A}-\sin^2(\theta)a_{i_{A_1}}a^\dagger_{i_B}-\sin^2(\theta)a_{i_{A_2}}a^\dagger_{i_B}$$

$$+\sin^2(\theta)a_{i_{A_3}}a^\dagger_{i_B}+\sin^2(\theta)a^\dagger_{i_A}a^\dagger_{i_B}+\sin(\theta)a_{i_{B_1}}a^\dagger_{i_{A_1}}+\sin^2(\theta)a_{i_{B_2}}a^\dagger_{i_{A_1}}$$

$$-\sin^2(\theta)a_{i_{B_3}}a^\dagger_{i_{A_1}}-\sin^2(\theta)a^\dagger_{i_B}a^\dagger_{i_{A_1}}+\sin(\theta)a_{i_{B_1}}a^\dagger_{i_{A_2}}$$

$$+\sin^2(\theta)a_{i_{B_2}}a^\dagger_{i_{A_2}}-\sin^2(\theta)a_{i_{B_3}}a^\dagger_{i_{A_2}}-\sin^2(\theta)a^\dagger_{i_B}a^\dagger_{i_{A_2}}-\sin(\theta)a_{i_{B_1}}a^\dagger_{i_{A_3}}$$

$$-\sin^2(\theta)a_{i_{B_2}}a^\dagger_{i_{A_3}}+\sin^2(\theta)a_{i_{B_3}}a^\dagger_{i_{A_3}}+\sin^2(\theta)a^\dagger_{i_B}a^\dagger_{i_{A_3}}$$

$$-a_{i_B}(2\lambda_{i_A}\lambda_{i_B}a^\dagger_{i_B}\cos^2(\theta)-2\lambda_{i_B}\lambda_{i_{A_1}}a^\dagger_{i_B}\cos^2(\theta)-2\lambda_{i_B}\lambda_{i_{A_2}}a^\dagger_{i_B}\cos^2(\theta)$$

$$+2\lambda_{i_B}\lambda_{i_{A_3}}a^\dagger_{i_B}\cos^2(\theta)+\sin^2(\theta)a_{i_{A_1}}+\sin^2(\theta)a_{i_{A_2}}$$

$$-\sin^2(\theta)a_{i_{A_3}}-\sin^2(\theta)a^\dagger_{i_A}+\sin^2(\theta)a^\dagger_{i_{A_1}}+\sin^2(\theta)a^\dagger_{i_{A_2}}-\sin^2(\theta)a^\dagger_{i_{A_3}})$$

$$+\sin(\theta)a_{i_{A_1}}a^\dagger_{i_{B_1}}+\sin(\theta)a_{i_{A_2}}a^\dagger_{i_{B_1}}-\sin(\theta)a_{i_{A_3}}a^\dagger_{i_{B_1}}-\sin(\theta)a^\dagger_{i_A}a^\dagger_{i_{B_1}}$$

$$+\sin(\theta)a^\dagger_{i_{A_1}}a^\dagger_{i_{B_1}}+\sin(\theta)a^\dagger_{i_{A_2}}a^\dagger_{i_{B_1}}-\sin(\theta)a^\dagger_{i_{A_3}}a^\dagger_{i_{B_1}}$$

$$+\sin^2(\theta)a_{i_{A_1}}a^\dagger_{i_{B_2}}+\sin^2(\theta)a_{i_{A_2}}a^\dagger_{i_{B_2}}-\sin^2(\theta)a_{i_{A_3}}a^\dagger_{i_{B_2}}$$

$$-\sin^2(\theta)a^\dagger_{i_A}a^\dagger_{i_{B_2}}+\sin^2(\theta)a^\dagger_{i_{A_1}}a^\dagger_{i_{B_2}}+\sin^2(\theta)a^\dagger_{i_{A_2}}a^\dagger_{i_{B_2}}$$

$$-\sin^2(\theta)a^\dagger_{i_{A_3}}a^\dagger_{i_{B_2}}-\sin^2(\theta)a_{i_{A_1}}a^\dagger_{i_{B_3}}-\sin^2(\theta)a_{i_{A_2}}a^\dagger_{i_{B_3}}$$

$$+\sin^2(\theta)a_{i_{A_3}}a^\dagger_{i_{B_3}}+\sin^2(\theta)a^\dagger_{i_A}a^\dagger_{i_{B_3}}-\sin^2(\theta)a^\dagger_{i_{A_1}}a^\dagger_{i_{B_3}}$$

$$-\sin^2(\theta)a^\dagger_{i_{A_2}}a^\dagger_{i_{B_3}}+\sin^2(\theta)a^\dagger_{i_{A_3}}a^\dagger_{i_{B_3}}+a_{i_A}(-2\lambda_{i_A}\lambda_{i_B}a^\dagger_{i_A}\cos^2(\theta)$$

$$
\begin{aligned}
&+2\lambda_{i_B}\lambda_{i_{A_1}}a^\dagger_{i_A}\cos^2(\theta)+2\lambda_{i_B}\lambda_{i_{A_2}}a^\dagger_{i_A}\cos^2(\theta)-2\lambda_{i_B}\lambda_{i_{A_3}}a^\dagger_{i_A}\cos^2(\theta)\\
&+2\lambda_{i_A}\lambda_{i_{B_1}}a^\dagger_{i_A}\cos^2(\theta)-2\lambda_{i_{A_1}}\lambda_{i_{B_1}}a^\dagger_{i_A}\cos^2(\theta)\\
&-2\lambda_{i_{A_2}}\lambda_{i_{B_1}}a^\dagger_{i_A}\cos^2(\theta)+2\lambda_{i_{A_3}}\lambda_{i_{B_1}}a^\dagger_{i_A}\cos^2(\theta)+2\lambda_{i_A}\lambda_{i_{B_2}}a^\dagger_{i_A}\cos^2(\theta)\\
&-2\lambda_{i_{A_1}}\lambda_{i_{B_2}}a^\dagger_{i_A}\cos^2(\theta)-2\lambda_{i_{A_2}}\lambda_{i_{B_2}}a^\dagger_{i_A}\cos^2(\theta)\\
&+2\lambda_{i_{A_3}}\lambda_{i_{B_2}}a^\dagger_{i_A}\cos^2(\theta)-2\lambda_{i_A}\lambda_{i_{B_3}}a^\dagger_{i_A}\cos^2(\theta)+2\lambda_{i_{A_1}}\lambda_{i_{B_3}}a^\dagger_{i_A}\cos^2(\theta)\\
&+2\lambda_{i_{A_2}}\lambda_{i_{B_3}}a^\dagger_{i_A}\cos^2(\theta)-2\lambda_{i_{A_3}}\lambda_{i_{B_3}}a^\dagger_{i_A}\cos^2(\theta)+\sin^2(\theta)a_{i_B}-\sin(\theta)a_{i_{B_1}}\\
&-\sin^2(\theta)a_{i_{B_2}}+\sin^2(\theta)a_{i_{B_3}}+\sin^2(\theta)a^\dagger_{i_B}-\sin(\theta)a^\dagger_{i_{B_1}}-\sin^2(\theta)a^\dagger_{i_{B_2}}+\sin^2(\theta)a^\dagger_{i_{B_3}}))\Bigg),
\end{aligned}
\tag{A.10}
$$

upto a constant given by,

$$
\begin{aligned}
\mathcal{C} \;=\; \sum_i \Bigg(& -J_0 s^4\cos^4(\theta)\lambda_i\lambda_{i_1}\lambda_{i_2}\lambda_{i_3}+J_2 s^2\cos^2(\theta)\lambda_i\lambda_{i_2}+s^2\cos^2(\theta)\lambda_{i_1}\lambda_{i_3}\\
&-\frac{J_2}{16}(s^2\cos^2(\theta)\lambda_{i_A}\lambda_{i_B}-s^2\cos^2(\theta)\lambda_{i_{A_1}}\lambda_{i_B}-s^2\cos^2(\theta)\lambda_{i_{A_2}}\lambda_{i_B}+s^2\cos^2(\theta)\lambda_{i_{A_3}}\lambda_{i_B}\\
&-s^2\cos^2(\theta)\lambda_{i_A}\lambda_{i_{B_1}}+s^2\cos^2(\theta)\lambda_{i_{A_1}}\lambda_{i_{B_1}}+s^2\cos^2(\theta)\lambda_{i_{A_2}}\lambda_{i_{B_1}}\\
&-s^2\cos^2(\theta)\lambda_{i_{A_3}}\lambda_{i_{B_1}}-s^2\cos^2(\theta)\lambda_{i_A}\lambda_{i_{B_2}}+s^2\cos^2(\theta)\lambda_{i_{A_1}}\lambda_{i_{B_2}}+s^2\cos^2(\theta)\lambda_{i_{A_2}}\lambda_{i_{B_2}}\\
&-s^2\cos^2(\theta)\lambda_{i_{A_3}}\lambda_{i_{B_2}}+s^2\cos^2(\theta)\lambda_{i_A}\lambda_{i_{B_3}}-s^2\cos^2(\theta)\lambda_{i_{A_1}}\lambda_{i_{B_3}}\\
&-s^2\cos^2(\theta)\lambda_{i_{A_2}}\lambda_{i_{B_3}}+s^2\cos^2(\theta)\lambda_{i_{A_3}}\lambda_{i_{B_3}})\Bigg),
\end{aligned}
\tag{A.11}
$$

substituting λ^i's obtained from the mean-field ansatz from Eq. (2.15) in chapter 2, we get,

$$
\mathcal{C}=-\frac{1}{2}J_0 s^4 N\mathcal{C}_\theta^4-(J_1+2J_2)s^2 N\mathcal{C}_\theta^2. \tag{A.12}
$$

APPENDIX B

Appendix

B.1 The toric code model limit

Here, we aim to obtain the equivalence of our current model that is already discussed in the chapter 1 2. It was presented that the current Hamiltonian 3.13 can be mapped Kitaev's Toric Code Model [111] in the absence of any other couplings such as the intramolecular coupling term (J_1) and the dipole-dipole coupling (J_2). Here we show that even in the presence of intramolecular interaction, the system can still be mapped to TCM [111]. However, the mapping or equivalence can only be established at specific points that we find below using a simple preliminary analysis of pCUT. Indeed, we show that the physics of the current model can be exactly described by the TCM under $K_x \neq 0$, $K_{y,z} = 0$. First, in the low field limit $J_{0,1} \ggg K$, for quasi-2D intraplane structure and in the absence of dipole-dipole interaction, we calculate the one-particle dispersion within the perturbative Continuous Unitary Transformation (pCUT) formalism. Here we shall outline the implementation details of pCUT and give the ground state energy and the corresponding one-quasiparticle gap up to order 6. From the earlier studies we know that the low-field case hosts a deconfined phase with gauge charge excitations coming from the gauge term J_0 similar to the excitations in the Toric-code model (TCM). However with an exception that in TCM there are two kinds of excitations, one is the magnetic charge and the other being the gauge charge corresponding to the gauge term (J_0 term). It should be noted that the true one-particle excitation on a lattice can be achieved only in the open boundary conditions where one can separate the excitation pairs ideally without any additional energy cost to infinite distance, effectively becoming a one-particle sector. Our above analysis relies on the fact that the spectrum when J_1 is turned is no more equidistant as we shall see, and it is to be noted that in order to make pCUT applicable we, therefore, choose the parameters so that within the set of parameters (J_0, J_1) chosen we see the current problem reduces to TCM.

$$
\begin{aligned}
e_1 = 1 &+ K(-2\cos(q_x - q_y) - 2\cos(q_x + q_y)) + \\
&K^2(2 - 2\cos(2q_x) - \cos(q_x - q_y) - 2\cos(2q_y) - \\
&\cos(q_x + q_y)) + \\
&K^3(-3\cos(q_x - 3q_y) - 3\cos(3q_x - q_y) - 3\cos(3q_x + q_y) \\
&- 3\cos(q_x + 3q_y)) \\
&K^4(\frac{35}{2} - 2\cos(2q_x) - \frac{15}{2}\cos(4q_x) - 5\cos(q_x - 3q_y) \\
&- \frac{25}{4}\cos(2q_x - 2q_y) - \cos(q_x - q_y) - 5\cos(3q_x - q_y) - \\
&2\cos(2q_y) - \frac{15}{2}\cos(4q_y) - \cos(q_x + q_y) \\
&- 5\cos(3q_x + q_y) - \frac{25}{4}\cos(2q_x + 2q_y) - 5\cos(q_x + 3q_y)).
\end{aligned} \tag{B.1}
$$

The configurational energy sets for a single given plaquette (four spins) in the absence of magnetic field K are $-J_0 + 2J_1$, $-J_0 + 2J_1$, J_0, Clearly, only for two cases the spectrum is equidistant per plaquette, i.e, for $J_1 = 0$ and $J_1 = J_0$ with corresponding $-3J_0$, J_0 energy sets. One may shift the energy or renormalize it to give the energies that are $-J_0$ and J_0 respectively. Thus, we finally get an equidistant unperturbed spectrum. Inorder to validate that the current model maps to TCM, we evaluate the pCUT calculation using a single periodic cluster ($L \geq n+2$, where L is the 1D lattice dimension and n is the expansion order) method and arrive at the following results of groundstate energy and gap per particle: In other words,

The ground state energy per spin e_{GS} up to order 6 is given by,

$$e_{GS} = -J_0 - 2J_1 - \frac{1}{2}K^2 - \frac{15}{8}K^4 - \frac{147}{8}K^6, \tag{B.2}$$

and similarly we give the one particle dispersion e_1 up to order 4, order 5 and 6 are too lengthy to be given here but will be effectively given when the one particle gap is obtained at the minimum K-point, i.e, Γ. The important point to note, however, is that the groundstate energy matches exactly with the TCM groundstate energy at the value of $J_1 = J_0$ thus establishing the TCM limit point.

B.1.1 Real-space linear spin-wave theory

The parameter space of J_2=0 has groundstates that does not conserve translational symmetry and it is therefore the only choice to work in the real-space version. Here, we derive the result of $S^{xx}(k,\omega)$ within the linear spin-wave theory regime and give the brief details used in our simulation to arrive at the result for $s^{xx}(k,\omega)$. From the earlier works [174] we have the classical ground states in the respective parameter regime. However, we start our analysis generally and consider the classical spins s_i located at each site in it's equilibrium state. The discussion in this section parallels the discussion taken from Ref. [187]. It is very useful to define unit vectors $\mathbf{u}_i, \mathbf{v}_i, \mathbf{w}_i$ such that $\mathbf{u}_i = \mathbf{s}_i/S$ with $\mathbf{s}_i$ in it's equilibrium state. Fluctuations in the equilibrium state can be parametrized by the variables say x_i, y_i as,

$$\mathbf{s}_i = \sqrt{S^2 - S(x_i^2 + y_i^2)}\mathbf{u}_i + \sqrt{S}(x_i\mathbf{v}_i + y_i\mathbf{w}_i), \tag{B.3}$$

which can be approximated as,

$$\approx (S - \frac{x_i^2 + y_i^2}{2})\mathbf{u}_i + \sqrt{S}(x_i \mathbf{v}_i + y_i \mathbf{w}_i). \tag{B.4}$$

The variables satisfy the Lagrangian equations of motion as

$$\mathcal{L} = \sum_i \frac{1}{2}(y_i \frac{dx_i}{dt} - x_i \frac{dy_i}{dt}) - U, \tag{B.5}$$

here U is the Hamiltonian consisting of only spin-spin interactions. Taylor expanding the above equation around the equilibrium position in terms of the variables x_i, y_i, one gets the Eq.,

$$\mathcal{L} = \frac{1}{2} z^T \Gamma \frac{d}{dt} z - \frac{1}{2} z^T \mathcal{H} z. \tag{B.6}$$

Here, $\mathcal{H}$ is a symmetric matrix while Γ is skew-symmetric, and z is a column vector given as:

$$z \equiv \begin{pmatrix} x_1 \\ y_1 \\ x_2 \\ y_2 \\ \vdots \end{pmatrix}$$

,

$$z \equiv \begin{pmatrix} 0 & -1 & \cdots & 0 & 0 \\ 1 & 0 & \cdots & 0 & 0 \\ \vdots & \vdots & \cdots & \vdots & \vdots \\ 0 & 0 & \cdots & 0 & -1 \\ 0 & 0 & \cdots & 1 & 0 \end{pmatrix}$$

.

B.1.2 Classical Version

Here, we derive the expression for dynamic structure factor (DSF) considering that the spins are classical orthogonal vectors based on the above formalism. The DSF is defined as,

$$\mathcal{S}^{\mu\nu}(\mathbf{q},\omega)_{\text{classical}} = \frac{1}{2\pi N}\sum_{i,j=1}^{N}\int_{-\infty}^{\infty} dt e^{-i\mathbf{q}\cdot(\mathbf{r}_i-\mathbf{r}_j)+i\omega t} \times \langle s_i^{\mu}(t) s_j^{\nu}(0)\rangle, \tag{B.7}$$

with N being the total no. of lattice sites with i, j denoting the indices of the spins on located on the lattice sites/edges. μ, ν correspond to the spin projections along the cartesian coordinates. From Eq. (B.5), one finds the classical equation describing the precession of spins as,

$$\Gamma\frac{d}{dt}z = \mathcal{H}z. \tag{B.8}$$

The general solution to the above Eq. (B.8) can be given as,

$$z(t) = \sum_{\alpha} c_{\alpha}\psi_{\alpha}e^{-i\omega t}, \tag{B.9}$$

where C_{α} represent the amplitudes for the normal modes ψ_{α} with the solution to the equation given below:

$$(i\omega_{\alpha}\Gamma + \mathcal{H})\psi_{\alpha} = 0. \tag{B.10}$$

It can be clearly seen that $\omega_{\alpha} = -\omega_{-\alpha}$ with eigenvectors satisfying the equation,

$$\psi_{-\alpha}^{\dagger}(-i\Gamma)\psi_{-\alpha} = \text{sgn}(\omega)_{\alpha}\delta_{\alpha\beta}, \tag{B.11}$$

resulting in,

$$\psi_\beta^\dagger \mathcal{H}\psi_\alpha = \text{sgn}(\omega_\alpha)\omega_\alpha\delta_{\alpha\beta} = |\omega_\alpha\delta_{\alpha\beta}|, \tag{B.12}$$

where the spin-spin interaction energy should be diagonalized as,

$$U = \frac{1}{2}\sum_\alpha \omega_\alpha c_\alpha^\star c_\alpha, \tag{B.13}$$

where $\langle c_\beta^\star c_\alpha\rangle = \delta_{\alpha\beta}/\beta|\omega_\alpha|$ is nothing but the boltmann distribution average. Further using this the above equation can be simplified to,

$$\langle z_k(t) z_l(0)\rangle = \sum_\alpha \frac{[\psi_\alpha]_k[\psi_\alpha]_l}{\beta|\omega_\alpha|} e^{-i\omega_\alpha t}, \tag{B.14}$$

here $k, l = 1, 2, ..., 2N$. While $\psi_\alpha^i \equiv ([\psi_\alpha]_{2i}, [\psi_\alpha]_{2i+1})^T$ and $\eta_i^\mu \equiv (v_i^\mu, w_i^\mu)$. Using the above equations, one obtains the expression for DSF as,

$$\mathcal{S}^{\mu\nu}_{\text{classical}}(\mathbf{q}, \omega) = \frac{S}{N}\sum_{i,j=1}^{N} e^{-i\mathbf{q}\cdot(\mathbf{r}_i - \mathbf{r}_j)} \times \sum_\alpha \frac{(\eta_i^\mu \cdot \psi_\alpha^i)(\eta_j^\mu \cdot \psi_\alpha^j)^\star}{\beta|\omega_\alpha|}\delta(\omega - \omega_\alpha). \tag{B.15}$$

This result is however only valid for small fluctuations from the equilibrium state of $\mathbf{s}_i$. But the above analysis is very helpful in deriving a similar expression for DSF within the semi-classical or quantum approach. Interested reader can refer to Ref. [187] for further analysis on quantum statistics. Here in the next subsection we provide the brief details of the practical implementation of the DSF in our code.

Bibliography

[1] John C Slater. "Theory of the transition in KH2PO4". In: *The Journal of Chemical Physics* 9.1 (1941), pp. 16–33.

[2] GA Samara. "Vanishing of the Ferroelectric and Antiferroelectric States in K H 2 P O 2-Type Crystals at High Pressure". In: *Physical Review Letters* 27.2 (1971), p. 103.

[3] George A Samara. "Ferroelectricity revisited—advances in materials and physics". In: *Solid State Physics*. Vol. 56. Elsevier, 2001, pp. 239–458.

[4] Masaharu Tokunaga and Takeo Matsubara. "Theory of ferroelectric phase transition in KH2PO4 type crystals. I". In: *Progress of Theoretical Physics* 35.4 (1966), pp. 581–599.

[5] Robert Blinc and Bostjan Zeks. "Dynamics of order-disorder-type ferroelectrics and antiferroelectrics". In: *Advances in Physics* 21.93 (1972), pp. 693–757.

[6] FJ Hollander, D Semmingsen, and TF Koetzle. "The molecular and crystal structure of squaric acid (3, 4-dihydroxy-3-cyclobutene-1, 2-dione) at 121° C: A neutron diffraction study". In: *The Journal of Chemical Physics* 67.11 (1977), pp. 4825–4831.

[7] Eiko Matsushita and Takeo Matsubara. "Note on isotope effect in hydrogen bonded crystals". In: *Progress of Theoretical Physics* 67.1 (1982), pp. 1–19.

[8] J. D. Bernal and R. H. Fowler. “A Theory of Water and Ionic Solution, with Particular Reference to Hydrogen and Hydroxyl Ions”. In: *The Journal of Chemical Physics* 1.8 (1933), pp. 515–548.

[9] Nic Shannon et al. “Quantum ice: a quantum Monte Carlo study”. In: *Physical review letters* 108.6 (2012), p. 067204.

[10] Claudio Castelnovo, Roderich Moessner, and Shivaji L Sondhi. “Magnetic monopoles in spin ice”. In: *Nature* 451.7174 (2008), pp. 42–45.

[11] F. J. Hollander, D. Semmingsen, and T. F. Koetzle. “The molecular and crystal structure of squaric acid (3,4-dihydroxy-3-cyclobutene-1,2-dione) at $121°C$: A neutron diffraction study”. In: *The Journal of Chemical Physics* 67.11 (1977), pp. 4825–4831.

[12] GA Samara. “Pressure dependence of the static and dynamic properties of KH2PO4 and related ferroelectric and antiferroelectric crystals”. In: *Ferroelectrics* 71.1 (1987), pp. 161–182.

[13] Vikas Vijigiri and Saptarshi Mandal. “Dipole–dipole interaction induced phases in hydrogen-bonded squaric acid crystal”. In: *Journal of Physics: Condensed Matter* 32.28 (2020), p. 285802.

[14] Gerald Mathias and Dominik Marx. “Structures and spectral signatures of protonated water networks in bacteriorhodopsin”. In: *Proceedings of the National Academy of Sciences* 104.17 (2007), pp. 6980–6985.

[15] Mark L Brewer, Udo W Schmitt, and Gregory A Voth. “The formation and dynamics of proton wires in channel environments”. In: *Biophysical Journal* 80.4 (2001), pp. 1691–1702.

[16] Jorge J Kohanoff* and Raul E Cachau. “Multiple proton translocation in biomolecular systems: Concerted to stepwise transition in a simple model”. In: *Molecular Physics* 102.9-10 (2004), pp. 1007–1014.

[17] Christoph Dellago, Mor M Naor, and Gerhard Hummer. “Proton transport through water-filled carbon nanotubes”. In: *Physical review letters* 90.10 (2003), p. 105902.

[18] Ji Chen et al. “Nature of proton transport in a water-filled carbon nanotube and in liquid water”. In: *Physical Chemistry Chemical Physics* 15.17 (2013), pp. 6344–6349.

[19] LE Bove et al. “Anomalous proton dynamics in ice at low temperatures”. In: *Physical review letters* 103.16 (2009), p. 165901.

[20] JF Scott. “Applications of modern ferroelectrics”. In: *science* 315.5814 (2007), pp. 954–959.

[21] Sachio Horiuchi et al. “Above-room-temperature ferroelectricity in a single-component molecular crystal”. In: *Nature* 463.7282 (2010), pp. 789–792.

[22] PS Peercy and GA Samara. “Pressure and Temperature Dependences of the Dielectric Properties and Raman Spectra of Rb H 2 P O 4”. In: *Physical Review B* 8.5 (1973), p. 2033.

[23] Robert Blinc. “On the isotopic effects in the ferroelectric behaviour of crystals with short hydrogen bonds”. In: *Journal of Physics and Chemistry of Solids* 13.3-4 (1960), pp. 204–211.

[24] D Semmingsen, FJ Hollander, and TF Koetzle. “A neutron diffraction study of squaric acid (3, 4-dihydroxy-3-cyclobutene-1, 2-dione)”. In: *The Journal of Chemical Physics* 66.10 (1977), pp. 4405–4412.

[25] D Semmingsen. “The crystal structure of squaric acid”. In: *Acta Chem. Scand* 27 (1973), pp. 3961–3972.

[26] Julia M Wesselinowa and MS Marinov. “On the theory of first-order phase transition in order-disorder ferroelectrics”. In: *International Journal of Modern Physics B* 6.08 (1992), pp. 1181–1192.

[27] JM Wesselinowa, AT Apostolov, and MS Marinov. “The Green’s function technique for spin-phonon interactions in squaric acid”. In: *Journal of Physics: Condensed Matter* 7.8 (1995), p. 1701.

[28] Michael Mehring and Joachim D Becker. “Observation of Electronic Structure Change at the First-Order Phase Transition in Quasi-Two-Dimensional Squaric Acid (H 2 C 4 O 4) by C 13 NMR”. In: *Physical Review Letters* 47.5 (1981), p. 366.

[29] W Kuhn, H-D Maier, and J Petersson. “Temperature dependence of the order parameter of the two dimensional antiferroelectric squaric acid as determined from birefringence measurements”. In: *Solid State Communications* 32.3 (1979), pp. 249–252.

[30] W Rehwald and A Vonlanthen. “Ultrasonic studies of the structural phase transition in squaric acid”. In: *physica status solidi (b)* 90.1 (1978), pp. 61–66.

[31] CL Wang, ZK Qin, and DL Lin. “First-order phase transition in order-disorder ferroelectrics”. In: *Physical Review B* 40.1 (1989), p. 680.

[32] E Barth et al. “Specific heat of the two dimensional antiferroelectric squaric acid”. In: *Zeitschrift fur Physik B Condensed Matter* 34.4 (1979), pp. 393–397.

[33] WJ Kuhn, J Petersson, and HE Müser. “Phase transition fronts in single crystals of the antiferroelectric squaric acid”. In: *physica status solidi (a)* 71.2 (1982), pp. 483–492.

[34] N Dalal, A Klymachyov, and A Bussmann-Holder. “Coexistence of order-disorder and displacive features at the phase transitions in hydrogen-bonded solids: squaric acid and its analogs”. In: *Physical review letters* 81.26 (1998), p. 5924.

[35] R Fu et al. “Temperature-Jump 2D NMR Spectroscopy in Crystalline Solids: A Technique for Correlating Molecular Reorientation across the Phase Boundaries of an Order- Disorder Lattice”. In: *The Journal of Physical Chemistry B* 102.44 (1998), pp. 8732–8735.

[36] SP Gabuda, SG Kozlova, and NS Dalal. “Vibronic model for antiferroelectric phase transition in squaric acid, H2C4O4”. In: *Solid state communications* 130.11 (2004), pp. 729–733.

[37] Annette Bussmann-Holder and Naresh Dalal. "Order/disorder versus or with displacive dynamics in ferroelectric systems". In: *Ferro-and Antiferroelectricity*. Springer, 2006, pp. 1–21.

[38] Se Hun Kim et al. "Experimental observation of hydrogen in a mixed state of order-disorder and displacive behavior in squaric acid". In: *Journal of the Korean Physical Society* 57.5 (2010), pp. 1253–1256.

[39] Dag Semmingsen and Jens Feder. "A structural phase transition in squaric acid". In: *Solid State Communications* 15.8 (1974), pp. 1369–1372.

[40] Jens Feder. "Two dimensional ferroelectricity". In: *Ferroelectrics* 12.1 (1976), pp. 71–83.

[41] STUCKYG WANGY and WILLIAMS J M. In: *J.C.S.* Vol. 2. perkin, 1974, p. 35.

[42] Eiko Matsushita and Takeo Matsubara. "Cluster Theory of Phase Transition in Squaric Acid. I: Formulation and General Discussion". In: *Progress of Theoretical Physics* 68.6 (1982), pp. 1811–1826.

[43] AR Ubbelohde and KJ Gallagher. "Acid-base effects in hydrogen bonds in crystals". In: *Acta Crystallographica* 8.2 (1955), pp. 71–83.

[44] Xin-Zheng Li, Brent Walker, and Angelos Michaelides. "Quantum nature of the hydrogen bond". In: *Proceedings of the National Academy of Sciences* 108.16 (2011), pp. 6369–6373.

[45] MI McMahon et al. "The effect of deuteration on the crystal structure of squaric acid (H2C4O4) in its ordered phase". In: *Zeitschrift fur Kristallographie-Crystalline Materials* 195.3-4 (1991), pp. 231–239.

[46] MI McMahon et al. "The effect of deuteration on the crystal structure of squaric acid (H sub 2 C sub 4 O sub 4) in its ordered phase". In: (1991).

[47] Emil J Samuelsen and Dag Semmingsen. “The phase transition of two-dimensional squaric acid H2C4O4 studied by neutron scattering”. In: *Journal of Physics and Chemistry of Solids* 38.11 (1977), pp. 1275–1283.

[48] Emil J Samuelsen, E Fjaer, and D Semmingsen. “The phase transition of two-dimensional squaric acid H2C4O4 studied by Raman scattering”. In: *Journal of Physics C: Solid State Physics* 12.11 (1979), p. 2007.

[49] N Yasuda et al. “Hydrostatic pressure effect on the phase transition of squaric acid H2C4O4”. In: *Journal of Physics C: Solid State Physics* 11.8 (1978), p. L299.

[50] K Betzler and D Bäuerle. “Second harmonic generation in squaric acid”. In: *Physics Letters A* 70.2 (1979), pp. 153–154.

[51] K-D Ehrhardt et al. “One-dimensional molecular correlations in squaric acid as observed by neutron scattering”. In: *Physical Review B* 29.2 (1984), p. 996.

[52] Kwang-Sei Lee et al. “Polymorphic phase transition and thermal stability in squaric acid (H2C4O4)”. In: *Journal of Physics and Chemistry of Solids* 73.7 (2012), pp. 890–895.

[53] A Katrusiak and RJ Nelmes. “On the pressure dependence of the crystal structure of squaric acid (H2C4O4)”. In: *Journal of Physics C: Solid State Physics* 19.32 (1986), p. L765.

[54] GA Samara and Dag Semmingsen. “Effects of pressure on the dielectric properties and phase transitions of the 2-D antiferroelectric squaric acid:(H2C4O4 and D2C4O4)”. In: *The Journal of Chemical Physics* 71.3 (1979), pp. 1401–1407.

[55] G Fischer and L Genzel. “Dielectric relaxation near the antiferroelectric phase transition of squaric acid”. In: *Zeitschrift fur Physik B Condensed Matter* 71.4 (1988), pp. 509–514.

[56] Akio Yamanaka and Itaru Tatsuzaki. “Temperature and uniaxial stress dependence of rigid layer mode in squaric acid (H2C4O4)”. In: *Journal of the Physical Society of Japan* 53.7 (1984), pp. 2316–2325.

[57] S Nakashima and M Balkanski. “Raman study of squaric acid”. In: *Solid State Communications* 19.12 (1976), pp. 1225–1228.

[58] Claudio Puebla and Tae-Kyu Ha. “A theoretical study of electronic structures and vibrational frequencies of deltic and squaric acids, CnOnH2 (n= 3 and 4)”. In: *Journal of Molecular Structure: THEOCHEM* 148.1-2 (1986), pp. 163–174.

[59] FG Baglin and Charles B Rose. “The infrared and Raman spectra of crystalline squaric acid”. In: *Spectrochimica Acta Part A: Molecular Spectroscopy* 26.12 (1970), pp. 2293–2304.

[60] DPC Thackeray. “The structure and spectra of squaric acid and its potassium salts.” PhD thesis. University of Surrey, 1973.

[61] D Bougeard and A Novak. “Vibrational study of squaric acid”. In: *Solid State Communications* 27.4 (1978), pp. 453–457.

[62] Michael Mehring and Dirk Suwelack. “NMR observation of static low-temperature clusters above the phase transition in the H-bonded antiferroelectric Squaric acid (C 4 O 4 H 2)”. In: *Physical Review Letters* 42.5 (1979), p. 317.

[63] Janez Seliger, V Zagar, and Robert Blinc. “Oxygen-17 NQR study of the phase transition in squaric acid”. In: *Journal of Magnetic Resonance (1969)* 58.3 (1984), pp. 359–369.

[64] Cheol Eui Lee, CH Lee, and MW Park. “Observation of critical behaviors in squaric acid by 1H nuclear magnetic resonance”. In: *Solid state communications* 129.9 (2004), pp. 565–567.

[65] Sidney Cohen, John R Lacher, and Joseph D Park. “Diketocyclobutenediol”. In: *Journal of the American Chemical Society* 81.13 (1959), pp. 3480–3480.

[66] EJ Samuelsen and Dag Semmingsen. “Squaric acid, a two-dimensional hydrogen-bonded material with a phase transition”. In: *Solid State Communications* 17.2 (1975), pp. 217–219.

[67] Alexandr A Levin and Sergey P Dolin. “Molecular Models and Calculations in Microscopic Theory of Order- Disorder Structural Phase Transitions: Application to KH2PO4 and Related Compounds”. In: *The Journal of Physical Chemistry* 100.15 (1996), pp. 6258–6261.

[68] RJ Mayer and JL Bjorkstam. “Dielectric properties of KD2PO4”. In: *Journal of Physics and Chemistry of Solids* 23.6 (1962), pp. 619–620.

[69] A Bussmann-Holder and KH Michel. “Bond geometry and phase transition mechanism of H-bonded ferroelectrics”. In: *Physical review letters* 80.10 (1998), p. 2173.

[70] Dongdong Kang et al. “Quantum simulation of thermally-driven phase transition and oxygen K-edge x-ray absorption of high-pressure ice”. In: *Scientific reports* 3.1 (2013), pp. 1–7.

[71] PG De Gennes. “Collective motions of hydrogen bonds”. In: *Solid State Communications* 1.6 (1963), pp. 132–137.

[72] Y Moritomo et al. “Quantum paraelectricity and subsequent disappearance of bond alternation of molecule caused by proton dynamics in squaric acid crystal”. In: *Physical review letters* 67.15 (1991), p. 2041.

[73] Nic Shannon, Gregoire Misguich, and Karlo Penc. “Cyclic exchange, isolated states, and spinon deconfinement in an X X Z Heisenberg model on the checkerboard lattice”. In: *Physical Review B* 69.22 (2004), p. 220403.

[74] Eiko Matsushita, $K \neq o$ ji Yoshimitsu, and Takeo Matsubara. “Theory of Phase Transition in Squaric Acid”. In: *Progress of Theoretical Physics* 64.4 (1980), pp. 1176–1192.

[75] JF Stilck and SR Salinas. “Vertex models for the antiferroelectric transition in squaric acid”. In: *The Journal of Chemical Physics* 75.3 (1981), pp. 1368–1378.

[76] VE Schneider and EE Tornau. “The model of the phase transition in squaric acid”. In: *physica status solidi (b)* 107.2 (1981), pp. 491–496.

[77] Colin J Thompson, Akira Nakanishi, and Takeo Matsubara. “A unified model for hydrogen bonded crystals”. In: *Physica A: Statistical Mechanics and its Applications* 217.3-4 (1995), pp. 393–406.

[78] KT Wikfeldt and A Michaelides. *Communication: Ab initio simulations of hydrogen-bonded ferroelectrics: Collective tunneling and the origin of geometrical isotope effects*. 2014.

[79] KT Wikfeldt. “Nuclear quantum effects in a 1-D model of hydrogen bonded ferroelectrics”. In: *J. Phys.* 571 (2014), p. 012012.

[80] Takayoshi Ishimoto and Masanori Tachikawa. “Theoretical Analysis of Phase-Transition Temperature of Hydrogen-Bonded Dielectric Materials Induced by H/D Isotope Effect”. In: *Advances in Quantum Methods and Applications in Chemistry, Physics, and Biology*. Springer, 2013, pp. 303–329.

[81] Carme Rovira, Juan J Novoa, and Pietro Ballone. “Hydrogen bonding and collective proton modes in clusters and periodic layers of squaric acid: A density functional study”. In: *The Journal of Chemical Physics* 115.14 (2001), pp. 6406–6417.

[82] Shoji Ishibashi, Sachio Horiuchi, and Reiji Kumai. “Computational findings of metastable ferroelectric phases of squaric acid”. In: *Physical Review B* 97.18 (2018), p. 184102.

[83] Fumiyuki Ishii et al. “Covalent ferroelectricity in hydrogen-bonded organic molecular systems”. In: *Physical Review B* 73.21 (2006), p. 212105.

[84] Nic Shannon et al. “Quantum ice: a quantum Monte Carlo study”. In: *Physical review letters* 108.6 (2012), p. 067204.

[85] Kate A Ross et al. “Quantum excitations in quantum spin ice”. In: *Physical Review X* 1.2 (2011), p. 021002.

[86] Olav F Syljuasen and Sudip Chakravarty. “Resonating plaquette phase of a quantum six-vertex model”. In: *Physical review letters* 96.14 (2006), p. 147004.

[87] Eddy Ardonne, Paul Fendley, and Eduardo Fradkin. “Topological order and conformal quantum critical points”. In: *Annals of Physics* 310.2 (2004), pp. 493–551.

[88] Linus Pauling. “The structure and entropy of ice and of other crystals with some randomness of atomic arrangement”. In: *Journal of the American Chemical Society* 57.12 (1935), pp. 2680–2684.

[89] Chyh-Hong Chern and Naoto Nagaosa. “Gauge Field and the Confinement-Deconfinement Transition in Hydrogen-Bonded Ferroelectrics”. In: *Physical Review Letters* 112.24 (2014), p. 247602.

[90] JS Valverde. “Two-dimensional XXZ-Ising model with quartic interactions”. In: *Physical Review E* 85.5 (2012), p. 051135.

[91] Bo-Jie Huang and Chyh-Hong Chern. “Deconfinement of electric charges in hydrogen-bonded ferroelectrics”. In: *International Journal of Modern Physics B* 31.20 (2017), p. 1750130.

[92] Horst E. Müser. “Calculation of the Parameters for the Vertex Model of Squaric Acid”. In: *Japanese Journal of Applied Physics* 24.S2 (1985), p. 938. DOI: `10.7567/jjaps.24s2.938`. URL: `https://doi.org/10.7567%2Fjjaps.24s2.938`.

[93] D B Abraham and O J Heilmann. “Phase transition in squaric acid”. In: *Journal of Physics C: Solid State Physics* 9.15 (1976), pp. L393–L396. DOI: `10.1088/0022-3719/9/15/002`. URL: `https://doi.org/10.1088%2F0022-3719%2F9%2F15%2F002`.

[94] J F Stilck. “Proof of long range order for a class of ferroelectric vertex models”. In: *Journal of Physics A: Mathematical and General* 16.16 (1983), pp. L629–L633. DOI: `10.1088/0305-4470/16/16/008`. URL: `https://doi.org/10.1088%2F0305-4470%2F16%2F16%2F008`.

[95] J. F. Stilck, M. J. de Oliveira, and S. R. Salinas. “Phenomenological renormalization-group calculations for 12- and 16-vertex models on a square lattice”. In: *Phys. Rev. B* 30 (9 1984),

pp. 5326–5333. DOI: `10.1103/PhysRevB.30.5326`. URL: `https://link.aps.org/doi/10.1103/PhysRevB.30.5326`.

[96] Uwe Deininghaus. “Squaric acid—a realization of the baxter model?” In: *Zeitschrift fr Physik B Condensed Matter* 45.1 (1981), pp. 71–78.

[97] M Karayanni et al. “Protonic inter-H-bond motion and ionic conductivity in hydrogen-bonded proton glasses”. In: *Physical Review B* 59.5 (1999), p. 3534.

[98] Cheol E Lee and JR Gaines. “Pulsed-NMR study of the long-range order in solid H 2 and D 2”. In: *Physical Review B* 50.21 (1994), p. 15602.

[99] H-D Maier, HE Muser, and J Petersson. “Interacting one dimensional Ising spin chains as a model of the layered antiferroelectric squaric acid”. In: *Zeitschrift fur Physik B Condensed Matter* 46.3 (1982), pp. 251–260.

[100] Robert Savit. “Duality in field theory and statistical systems”. In: *Reviews of Modern Physics* 52.2 (1980), p. 453.

[101] GF Reiter, J Mayers, and P Platzman. “Direct observation of tunneling in KDP using neutron Compton scattering”. In: *Physical review letters* 89.13 (2002), p. 135505.

[102] C Castelnovo, R Moessner, and Shivaji Lal Sondhi. “Spin ice, fractionalization, and topological order”. In: *Annu. Rev. Condens. Matter Phys.* 3.1 (2012), pp. 35–55.

[103] Hiroaki Ishizuka et al. “Quantum Monte Carlo study of molecular polarization and antiferroelectric ordering in squaric acid crystals”. In: *Physical Review B* 84.6 (2011), p. 064120.

[104] Elliott H Lieb. “Exact solution of the problem of the entropy of two-dimensional ice”. In: *Physical Review Letters* 18.17 (1967), p. 692.

[105] JM Luttinger and L Tisza. “Theory of dipole interaction in crystals”. In: *Physical Review* 70.11-12 (1946), p. 954.

[106] S. Mandal et al. “Incommensurate helical spin ground states on the hollandite lattice”. In: *Phys. Rev. B* 90 (10 2014), p. 104420.

[107] Sophia R Sklan and Christopher L Henley. “Nonplanar ground states of frustrated antiferromagnets on an octahedral lattice”. In: *Physical Review B* 88.2 (2013), p. 024407.

[108] Julien Vidal, Kai Phillip Schmidt, and Sébastien Dusuel. “Perturbative approach to an exactly solved problem: Kitaev honeycomb model”. In: *Physical Review B* 78.24 (2008), p. 245121.

[109] Ming-wen Xiao. “Theory of transformation for the diagonalization of quadratic Hamiltonians”. In: *arXiv preprint arXiv:0908.0787* (2009).

[110] JHP Colpa. “Diagonalization of the quadratic boson Hamiltonian”. In: *Physica A: Statistical Mechanics and its Applications* 93.3-4 (1978), pp. 327–353.

[111] Julien Vidal et al. “Self-duality and bound states of the toric code model in a transverse field”. In: *Physical Review B* 80.8 (2009), p. 081104.

[112] Eduardo Fradkin. “Jordan-Wigner transformation for quantum-spin systems in two dimensions and fractional statistics”. In: *Physical review letters* 63.3 (1989), p. 322.

[113] Xiao-Gang Wen. “Quantum orders and symmetric spin liquids”. In: *Physical Review B* 65.16 (2002), p. 165113.

[114] A Yu Kitaev. “Fault-tolerant quantum computation by anyons”. In: *Annals of Physics* 303.1 (2003), pp. 2–30.

[115] Alexei Kitaev. “Anyons in an exactly solved model and beyond”. In: *Annals of Physics* 321.1 (2006), pp. 2–111.

[116] Saptarshi Mandal and Naveen Surendran. “Exactly solvable Kitaev model in three dimensions”. In: *Physical Review B* 79.2 (2009), p. 024426.

[117] Götz S Uhrig and B Normand. “Magnetic properties of $VO_2P_2O_7$ from frustrated interchain coupling”. In: *Physical Review B* 58.22 (1998), R14705.

[118] Christian Knetter and Götz S Uhrig. “Perturbation theory by flow equations: dimerized and frustrated S= 1/2 chain”. In: *The European Physical Journal B-Condensed Matter and Complex Systems* 13.2 (2000), pp. 209–225.

[119] Christian Knetter, Kai P Schmidt, and Götz S Uhrig. “High order perturbation theory for spectral densities of multi-particle excitations: $\frac{S=1}{2}$ two-leg Heisenberg ladder”. In: *The European Physical Journal B-Condensed Matter and Complex Systems* 36.4 (2003), pp. 525–544.

[120] Franz J Wegner. “Duality in generalized Ising models and phase transitions without local order parameters”. In: *Journal of Mathematical Physics* 12.10 (1971), pp. 2259–2272.

[121] Franz Wegner. “Flow-equations for Hamiltonians”. In: *Annalen der physik* 506.2 (1994), pp. 77–91.

[122] Stanisław D Głazek and Kenneth G Wilson. “Renormalization of hamiltonians”. In: *Physical Review D* 48.12 (1993), p. 5863.

[123] Jürgen Stein. “Flow equations and the strong-coupling expansion for the Hubbard model”. In: *Journal of statistical physics* 88.1-2 (1997), pp. 487–511.

[124] Andreas Mielke. “Flow equations for band-matrices”. In: *The European Physical Journal B-Condensed Matter and Complex Systems* 5.3 (1998), pp. 605–611.

[125] Christian Knetter, Kai P Schmidt, and Götz S Uhrig. “The structure of operators in effective particle-conserving models”. In: *Journal of Physics A: Mathematical and General* 36.29 (2003), p. 7889.

[126] Michael Kamfor. “Robustness and spectroscopy of the toric code in a magnetic field”. In: (2013).

[127] K Coester and KP Schmidt. “Optimizing linked-cluster expansions by white graphs”. In: *Physical Review E* 92.2 (2015), p. 022118.

[128] Stefan K Kehrein, Andreas Mielke, and Peter Neu. "Flow equations for the spin-boson problem". In: *Zeitschrift fur Physik B Condensed Matter* 99.2 (1995), pp. 269–280.

[129] Caspar P Heidbrink and Götz S Uhrig. "Landau's quasiparticle mapping: Fermi liquid approach and luttinger liquid behavior". In: *Physical review letters* 88.14 (2002), p. 146401.

[130] Tim Fischer, Sébastian Duffe, and Götz S Uhrig. "Adapted continuous unitary transformation to treat systems with quasi-particles of finite lifetime". In: *New Journal of Physics* 12.3 (2010), p. 033048.

[131] Nils A Drescher, Tim Fischer, and Götz S Uhrig. "Truncation errors in self-similar continuous unitary transformations". In: *The European Physical Journal B* 79.2 (2011), pp. 225–240.

[132] H Krull, NA Drescher, and Götz S Uhrig. "Enhanced perturbative continuous unitary transformations". In: *Physical Review B* 86.12 (2012), p. 125113.

[133] Marc Daniel Schulz et al. "Breakdown of a perturbed topological phase". In: *New Journal of Physics* 14.2 (2012), p. 025005.

[134] Julien Vidal, Sébastien Dusuel, and Kai Phillip Schmidt. "Low-energy effective theory of the toric code model in a parallel magnetic field". In: *Physical Review B* 79.3 (2009), p. 033109.

[135] Kai Phillip Schmidt, Sébastien Dusuel, and Julien Vidal. "Emergent fermions and anyons in the Kitaev model". In: *Physical review letters* 100.5 (2008), p. 057208.

[136] Charles Nash and Denjoe O'Connor. "Zero temperature phase diagram of the Kitaev model". In: *Physical review letters* 102.14 (2009), p. 147203.

[137] Christian Knetter et al. "Dispersion and symmetry of bound states in the Shastry-Sutherland model". In: *Physical review letters* 85.18 (2000), p. 3958.

[138] Christian Knetter et al. "Fractional and integer excitations in quantum antiferromagnetic spin 1/2 ladders". In: *Physical review letters* 87.16 (2001), p. 167204.

[139] Sébastien Dusuel and Julien Vidal. “Continuous unitary transformations and finite-size scaling exponents in the Lipkin-Meshkov-Glick model”. In: *Physical Review B* 71.22 (2005), p. 224420.

[140] Kai P Schmidt et al. “Supersolid phase induced by correlated hopping in spin-1/2 frustrated quantum magnets”. In: *Physical review letters* 100.9 (2008), p. 090401.

[141] M Kargarian, H Bombin, and MA Martin-Delgado. “Topological color codes and two-body quantum lattice Hamiltonians”. In: *New Journal of Physics* 12.2 (2010), p. 025018.

[142] Sébastien Dusuel et al. “Robustness of a perturbed topological phase”. In: *Physical review letters* 106.10 (2011), p. 107203.

[143] Sébastian Fey and Kai Phillip Schmidt. “Critical behavior of quantum magnets with long-range interactions in the thermodynamic limit”. In: *Physical Review B* 94.7 (2016), p. 075156.

[144] Sébastian Fey, Sébastian C Kapfer, and Kai Phillip Schmidt. “Quantum criticality of two-dimensional quantum magnets with long-range interactions”. In: *Physical review letters* 122.1 (2019), p. 017203.

[145] Jan Koziol et al. “Quantum criticality of the transverse-field Ising model with long-range interactions on triangular-lattice cylinders”. In: *Physical Review B* 100.14 (2019), p. 144411.

[146] Patrick Adelhardt et al. “Quantum criticality and excitations of a long-range anisotropic XY chain in a transverse field”. In: *Physical Review B* 102.17 (2020), p. 174424.

[147] Sébastien Dusuel et al. “Bound states in two-dimensional spin systems near the Ising limit: A quantum finite-lattice study”. In: *Physical Review B* 81.6 (2010), p. 064412.

[148] Jaan Oitmaa, Chris Hamer, and Weihong Zheng. *Series expansion methods for strongly interacting lattice models*. Cambridge University Press, 2006.

[149] IG Enting. “Series expansions from the finite lattice method”. In: *Nuclear Physics B-Proceedings Supplements* 47.1-3 (1996), pp. 180–187.

[150] IG Enting. “Finite lattice series expansions for the triangular lattice”. In: *Journal of Physics A: Mathematical and General* 13.8 (1980), p. L279.

[151] H Arisue, T Fujiwara, and K Tabata. “Higher orders of the high-temperature expansion for the Ising model in three dimensions”. In: *Nuclear Physics B-Proceedings Supplements* 129 (2004), pp. 774–776.

[152] John B. Kogut. “An introduction to lattice gauge theory and spin systems”. In: *Rev. Mod. Phys.* 51 (4 1979), pp. 659–713.

[153] Anders W Sandvik. “Stochastic series expansion method for quantum Ising models with arbitrary interactions”. In: *Physical Review E* 68.5 (2003), p. 056701.

[154] Olav F Syljuasen and Anders W Sandvik. “Quantum Monte Carlo with directed loops”. In: *Physical Review E* 66.4 (2002), p. 046701.

[155] Anders W Sandvik and Juhani Kurkijarvi. “Quantum Monte Carlo simulation method for spin systems”. In: *Physical Review B* 43.7 (1991), p. 5950.

[156] Anders W Sandvik. “Stochastic series expansion method with operator-loop update”. In: *Physical Review B* 59.22 (1999), R14157.

[157] Anders W Sandvik. “Computational studies of quantum spin systems”. In: *AIP Conference Proceedings*. Vol. 1297. 1. American Institute of Physics. 2010, pp. 135–338.

[158] Stephan Humeniuk. “Quantum Monte Carlo studies of strongly correlated systems for quantum simulators”. In: (2018).

[159] DC Handscomb. “The Monte Carlo method in quantum statistical mechanics”. In: *Mathematical Proceedings of the Cambridge Philosophical Society*. Vol. 58. 4. Cambridge University Press. 1962, pp. 594–598.

[160] DC Handscomb. “A Monte Carlo method applied to the Heisenberg ferromagnet”. In: *Mathematical Proceedings of the Cambridge Philosophical Society*. Vol. 60. 1. Cambridge University Press. 1964, pp. 115–122.

[161] AW Sandvik. “A generalization of Handscomb’s quantum Monte Carlo scheme-application to the 1D Hubbard model”. In: *Journal of Physics A: Mathematical and General* 25.13 (1992), p. 3667.

[162] Anders W Sandvik, Rajiv RP Singh, and David K Campbell. “Quantum Monte Carlo in the interaction representation: Application to a spin-Peierls model”. In: *Physical Review B* 56.22 (1997), p. 14510.

[163] Franz Michel and Hans-Gerd Evertz. “Lattice dynamics of the Heisenberg chain coupled to finite frequency bond phonons”. In: *arXiv preprint arXiv:0705.0799* (2007).

[164] Sounak Biswas and Kedar Damle. “Efficient quantum cluster algorithms for frustrated transverse field Ising antiferromagnets and Ising gauge theories”. In: *arXiv preprint arXiv:1812.05326* (2018).

[165] Robert H Swendsen, Jian-Sheng Wang, and Alan M Ferrenberg. “New Monte Carlo methods for improved efficiency of computer simulations in statistical mechanics”. In: *The Monte Carlo method in condensed matter physics*. Springer, 1992, pp. 75–91.

[166] Robert H Swendsen and Jian-Sheng Wang. “Nonuniversal critical dynamics in Monte Carlo simulations”. In: *Physical review letters* 58.2 (1987), p. 86.

[167] Ulli Wolff. “Collective Monte Carlo updating for spin systems”. In: *Physical Review Letters* 62.4 (1989), p. 361.

[168] Junwei Liu et al. “Self-learning Monte Carlo method”. In: *Phys. Rev. B* 95 (2017), p. 041101. DOI: `10.1103/PhysRevB.95.041101`. URL: `https://link.aps.org/doi/10.1103/PhysRevB.95.041101`.

[169] Li Huang and Lei Wang. “Accelerated Monte Carlo simulations with restricted Boltzmann machines”. In: *Physical Review B* 95.3 (2017), p. 035105.

[170] Junwei Liu et al. “Self-learning Monte Carlo method and cumulative update in fermion systems”. In: *Physical Review B* 95.24 (2017), p. 241104.

[171] Xiao Yan Xu et al. “Self-learning quantum Monte Carlo method in interacting fermion systems”. In: *Physical Review B* 96.4 (2017), p. 041119.

[172] Kurt Binder. “Finite size scaling analysis of Ising model block distribution functions”. In: *Zeitschrift fur Physik B Condensed Matter* 43.2 (1981), pp. 119–140.

[173] Chyh-Hong Chern and Naoto Nagaosa. “Gauge Field and the Confinement-Deconfinement Transition in Hydrogen-Bonded Ferroelectrics”. In: *Physical review letters* 112.24 (2014), p. 247602.

[174] Vikas Vijigiri and Saptarshi Mandal. “Classical mean-field, spin-wave, and perturbative continuous unitary transformation analyses of the squaric acid system H 2 SQ”. In: *Physical Review B* 98.22 (2018), p. 224425.

[175] S. P. Dolin et al. “Quantum-chemical modeling of squaric acid ferroelectric behavior”. In: *International Journal of Quantum Chemistry* 111.11 (2011), pp. 2671–2676. DOI: `https://doi.org/10.1002/qua.22743`. URL: `https://onlinelibrary.wiley.com/doi/abs/10.1002/qua.22743`.

[176] H. D. Maier and J. Petersson. “Phenomenological Behaviour and Phase Transition Mechanism of the Layered Antiferroelectric Squaric Acid”. In: *physica status solidi (b)* 100.1 (1980), pp. 171–178. DOI: `https://doi.org/10.1002/pssb.2221000117`. URL: `https://onlinelibrary.wiley.com/doi/abs/10.1002/pssb.2221000117`.

[177] Tota Nakamura. “Efficient Monte Carlo algorithm in quasi-one-dimensional Ising spin systems”. In: *Physical review letters* 101.21 (2008), p. 210602.

[178] Masuo Suzuki. “Improved Trotter-like formula”. In: *Physics Letters A* 180.3 (1993), pp. 232 –234. ISSN: 0375-9601. DOI: https://doi.org/10.1016/0375-9601(93)90701-Z. URL: http://www.sciencedirect.com/science/article/pii/037596019390701Z.

[179] Aneesur Rahman and Frank H. Stillinger. “Proton Distribution in Ice and the Kirkwood Correlation Factor”. In: *The Journal of Chemical Physics* 57.9 (1972), pp. 4009–4017. DOI: 10.1063/1.1678874. eprint: https://doi.org/10.1063/1.1678874. URL: https://doi.org/10.1063/1.1678874.

[180] Cyril Domb and Martin F Sykes. “On the susceptibility of a ferromagnetic above the Curie point”. In: *Proceedings of the Royal Society of London. Series A. Mathematical and Physical Sciences* 240.1221 (1957), pp. 214–228.

[181] C Domb and AJ Guttmann. “Low-temperature series for the Ising model”. In: *Journal of Physics C: Solid State Physics* 3.8 (1970), p. 1652.

[182] Anthony J Guttmann and GS Joyce. “On a new method of series analysis in lattice statistics”. In: *Journal of Physics A: General Physics* 5.9 (1972), p. L81.

[183] George A Baker Jr. “Further applications of the Pade approximant method to the Ising and Heisenberg models”. In: *Physical Review* 129.1 (1963), p. 99.

[184] JSR Chisholm. “Generalisations of Pade approximants”. In: *Rational Approximation in Systems Engineering*. Springer, 1982, pp. 279–287.

[185] Michael E. Fisher. “Series Expansion Approximants for Singular Functions of Many Variables”. In: *Statistical Mechanics and Statistical Methods in Theory and Application*. Ed. by Uzi Landman. Boston, MA: Springer US, 1977, pp. 3–31. ISBN: 978-1-4613-4166-6. DOI: 10.1007/978-1-4613-4166-6_2. URL: https://doi.org/10.1007/978-1-4613-4166-6_2.

[186] GA Baker. “Pade Approximant and Related Material”. In: *Cargese Lectures in Physics* 5 (1971), p. 349.

[187] Shu Zhang et al. “Dynamical Structure Factor of the Three-Dimensional Quantum Spin Liquid Candidate $NaCaNi_2F_7$”. In: *Phys. Rev. Lett.* 122 (2019), p. 167203. DOI: 10.1103/PhysRevLett.122.167203. URL: https://link.aps.org/doi/10.1103/PhysRevLett.122.167203.